Understanding the Influence of Non-gravitational Forces on the Physical Evolution of Near-Earth Asteroids and Comets

A thesis submitted for the degree of
Doctor of Philosophy

by

Agata Barbara Makieła
(Agata Rożek)

School of Physical Sciences

University of Kent
Canterbury
United Kingdom

2017

There are neither beginnings nor endings to the turning of the Wheel of Time.
But it was a beginning.

– Robert Jordan

Declaration

This thesis has not been submitted as an exercise for a degree at any other university.

Except where stated, the work described therein was carried out by me alone.

I give permission for the Library to lend or copy this thesis upon request.

SIGNED:

Abstract

Near-Earth asteroids are the small rocky bodies orbiting the Sun in the vicinity of Earth's orbit. They are remnants of the planetesimals formed in the young Solar System, which repeatedly collided and underwent disruption. They form loosely-bound aggregates dubbed 'rubble piles'. Their dynamical and physical evolution is expected to be affected by a non-gravitational torque called the YORP effect.

The YORP effect is a torque due to the anisotropic emission of thermal photons on minor bodies in the Solar System. For small asteroids the radiation recoil torques can systematically modify rotational rates or shift spin axis orientations (Rubincam, 2000). The effect is crucial to understanding the dynamical and physical evolution of near-Earth asteroids, like the alignment of spin-axes (Slivan, 2002), the peculiar spin-top shapes observed for a few targets (Ostro et al., 2006; Scheeres et al., 2006), or rotational fission and evolution of asteroid binaries (Walsh et al., 2008; Pravec et al., 2010; Jacobson and Scheeres, 2011; Jacobson et al., 2016). The first direct detection of the asteroidal YORP effect on asteroid (54509) 2000 PH_5 was possible thanks to the combination of radar and photometric lightcurve observations (Lowry et al., 2007; Taylor et al., 2007). Since then, YORP spin-up has also been detected on several other asteroids. However, the sample is still very small, and further observational data is needed to refine the YORP theories.

The asteroids (1917) Cuyo and (85990) 1999 JV_6, discussed here, were selected from a sample of nearly 40 YORP-detection candidates that were monitored photometrically, and in infra-red, through an ESO Large Programme (ESO LP) led by S. C. Lowry at the ESO New Technology Telescope and Very Large Telescope telescopes, and at other facilities with associated programmes.

The ESO LP has been used to acquire photometric lightcurves of the asteroid (1917) Cuyo spanning the period between 2010 and 2013, which, combined with the 1989-2008 archive lightcurves, should provide a large enough time-base to constrain a possible YORP strength. However, the distribution of observations in time results in effectively having observations from just two epochs. This produces potential YORP values in the range of -0.7×10^{-8} rad/d^2 (radians per day squared) and 1.5×10^{-8} rad/d^2. The rotation pole of the object is most likely located at $\lambda = 46°$, $\beta = -62°$. The sidereal period was refined relative to earlier lightcurve estimates, to be $(2.689\,764\,2 \pm 0.000\,003\,5)$ h (hours). The shape of the object suggests the presence of an 'equatorial bulge', typical for an evolved system close to shedding mass due to fast rotation.

For asteroid (85990) 1999 JV_6, the data in the ESO LP span the period between 2007 and 2016. Additionally, the author has secured radar spectra and imaging observations with Arecibo and Goldstone planetary radars. Having radar observations permitted additional constraints on the shape and spin-state, but YORP spin-up was not detected. The asteroid is shown to have a bi-lobed shape, likely a result of two ellipsoidal components collapsing onto each other. The smaller lobe is close to spherical and has diameters (345 ± 9) m, (281 ± 8) m and (291 ± 9) m, and the larger is more elongated, with (580 ± 10) m, (322 ± 5) m and (332 ± 7) m. The rotation pole resides at negative latitudes in a circle of a 10° radius, close to the southern pole of the celestial sphere. The refined sidereal rotation period is $(6.536\,787 \pm 0.000\,006)$ h. No YORP-induced change in period was detected using the phase offset measurement using the radar model, however the global lightcurve-only analysis shows the object could be experiencing a spin-up of up to 7×10^{-8} rad/d^2.

The shapes and spin-states developed here were used in further studies, beyond the scope of this thesis. Combined with the infra red observations the outcome of this work was used for thermophysical analysis by ESO LP collaborator B. Rozitis to constrain physical properties of both targets. The shape and rotation state of (1917) Cuyo can be used to

investigate cohesive forces as a way to explain why some targets survive rotation rates faster than the fission limit. The detection of non-gravitational acceleration in the orbital motion of the asteroid (85990) 1999 JV_6 combined with thermophysical modelling suggest a low, cometary-like density.

The shape modelling and spin-state analysis tools were also applied to a Jupiter family comet, and the Rosetta mission target, 67P/Churyumov-Gerasimenko. The author contributed to the confirmation of the seminal measurement of spin-rate change between previous perihelion approach and the arrival of Rosetta (Mottola et al., 2014, incl. A. Rożek). The detected 20 min decrease in the sidereal period, from $\approx$12.7 h to $\approx$12.4 h, was later linked to cometary activity (Keller et al., 2015b; Bertaux, 2015). Tools were also developed to assess the mean insolation of the comet's surface, useful in calculations of nucleus dust production rates (Guilbert-Lepoutre et al., 2014, incl. A. Rożek), establish jet-activity source regions on the surface of the nucleus (Lara et al., 2015; Lin et al., 2015, 2016, incl. A. Rożek), and calibrate ground-based photometry using the spacecraft shape model (Snodgrass et al., 2016, incl. A. Rożek).

Acknowledgements

Special thanks to my supervisor Stephen C. Lowry who provided this amazing opportunity for me to investigate all the different aspects of small-body planetary science. Thanks, Stephen, for your guidance and encouragement, and for sending me out to complete my 'telescope bucket list'!

Thanks to the ESO Large Programme team for providing data to be used in my research, feedback on conference abstract and proposals, and scientific support throughout my work. Especially Ben Rozitis, who was the first one to use my results, Colin Snodgrass, Simon Green, Sam Duddy, Paul Weissman and Mike Hicks.

To M. Nolan, E. Howell, P. Taylor and the Arecibo Planetary Radar team for providing help with all aspects of Arecibo observations, hospitality at the site and countless e-mails patiently answering all of my questions. L. Benner, S. Naidu and the Goldstone Solar System Radar team for providing radar observations of (85990) 1999 JV_6 and invaluable help with their interpretation and modelling. The software package `SHAPE`, used here, was kindly provided by C. Magri.

Thank you to the gigantic team behind the Rosetta spacecraft, OSIRIS instrument, and associated ground-based campaigns, especially OSIRIS PI H. Sierks, and A. Guilbert-Lepoutre, S. Mottola, L. Lara, and Z.-Y. Lin for including me in the work on the comet 67P/Churyumov-Gerasimenko.

I would also like to thank T. Michałowski and A. Erikson for providing the archived lightcurve data for asteroid (1917) Cuyo.

Thank you to the academic and administrative staff at the School of Physical Sciences at the University of Kent. To my co-students and officemates, thanks for expanding my knowledge by the fields of forensic science and chemistry, and for coming over to play board games! This includes a thanks to Timothy Kinnear, Kathryn Harriss, Joe Mist, Jacob Deller, Justin Donohoe, Sally Makin, Marine Riesemney, Mathew Cumber, Lucy Morgan et al.

Thank you to the scientists and staff at the Poznań Astronomical Observatory, for encouragement to leave familiar grounds and go to Kent to pursue my degree here. Special thanks to Sławomir Breiter, my former supervisor, for being an example of focus and science drive.

To the Almukantarat Astronomy Club, all its members and people associated with it, I want to say 'thank you' for showing me astronomy is not only the pretty pictures. You guys are an inspiration. Amongst others, I owe a special thanks to Aleksandra Woźniak (it's all your fault), Teresa Kubacka, Ola Gospodarczyk, Łukasz Zatorski, Wojciech Rutkowski, Agata Karska, and Piotr Ligęza.

The Image Reduction and Analysis Facility software was used for data reduction. The asteroid ephemeris were generated using JPL's Horizons service. The `CONVEXINV` and `SHAPE` software packages were used in shape modelling of the small bodies. This research has made use of data and/or services provided by the International Astronomical Union's Minor Planet Center.

And last, but not least, a huge 'thank you' has to go to my husband, Piotr Makieła, for supporting me and being an awesome partner. Thanks to our extended families for countless hours on on-line calls.

Mum and dad, thanks for showing me that learning is fun.

This thesis was typeset using the LaTeX typesetting system originally developed by Leslie Lamport, based on TeX created by Donald Knuth.

Contents

List of Tables

List of Figures

Publications

Publications resulting from this thesis work

The author of this thesis, Agata Barbara Makieła is publishing under the name Agata Rożek and will be referred to as A. Rożek throughout this work.

Refereed papers

1. Lin, Z.-Y., and 50 colleagues (incl. **A. Rożek**), 4/2016. Observations and analysis of a curved jet in the coma of comet 67P/Churyumov-Gerasimenko. A&A, 588, L3 *(14 citations)*.

2. Snodgrass, C., and 16 colleagues (incl. **A. Rożek**), 4/2016. Distant activity of 67P/Churyumov-Gerasimenko in 2014: Ground-based results during the Rosetta pre-landing phase. A&A, 588, A80 *(15 citations)*.

3. Lin, Z.-Y., and 49 colleagues (incl. **A. Rożek**), 11/2015. Morphology and dynamics of the jets of comet 67P/Churyumov-Gerasimenko: Early-phase development. A&A, 583, A11 *(23 citations)*.

4. Lara, L. M., and 56 colleagues (incl. **A. Rożek**), 11/2015. Large-scale dust jets in the coma of 67P/Churyumov-Gerasimenko as seen by the OSIRIS instrument onboard Rosetta. A&A583, A9 *(24 citations)*.

5. Mottola, S., Lowry, S., Snodgrass, C., Lamy, P. L., Toth, I., **Rożek, A.** and 43 colleagues, 9/2014. The rotation state of 67P/Churyumov-Gerasimenko from approach observations with the OSIRIS cameras on Rosetta. A&A, 569, L2 *(50 citations)*.

6. Guilbert-Lepoutre, A., Schulz, R., **Rożek, A.**, Lowry, S. C., Tozzi, G. P. and Stüwe, J. A., 7/2014. Pre-perihelion activity of comet 67P/Churyumov-Gerasimenko. A&A, 567, L2 *(10 citations)*.

Conference abstracts and other

- **A. Rożek**, and 25 colleagues, 2016. Shape and spin-state modelling of the NEA (85990) 1999 JV_6 from radar and optical observations, Binaries in The Solar System 4, held 20-23 June in Prague, Czech Republic. *(abstract)*

- J. D. Giorgini, P. A. Taylor, L. A. Rodriguez-Ford, **A. Rożek**, S. C. Lowry, M. C. Nolan, M. Brozovic, L. A. M. Benner, 2016, (85990) 1999 JV_6, CBAT Electronic Telegram No. 4279 `http://www.cbat.eps.harvard.edu/iau/cbet/004200/CBET004279.txt`. *(short announcement)*

- Rozitis, B., Emery, J., Lowry, S., **Rożek, A.**, Wolters, S., Snodgrass, C., Green, S, 2016. Thermal Emission Light-Curves of Rapidly Rotating Asteroids. Lunar and Planetary Science Conference 47, 1447. *(abstract)*

- Benner, L. A., and 15 colleagues (incl. **A. Rożek**), 2015. Radar Imaging of Binary Near-Earth Asteroid (357439) 2004 BL86. IAU General Assembly 22, 2257549. *(abstract)*

- Lin, Z.-Y., and 18 colleagues (incl. **A. Rożek**), 2015. Morphology and Dynamics of Jets of Comet 67P Churyumov-Gerasimenko: Early Phase Development. EGU General Assembly Conference Abstracts 17, 8899. *(abstract)*

- Ip, W. H., and 13 colleagues (incl. **A. Rożek**), 2014. Jets of 67P/Churyumov-Gerasimenko as Observed by Rosetta/OSIRIS. AGU Fall Meeting Abstracts. *(abstract)*
- **Rożek, A.**, and 9 colleagues, 2014. Spin-state and thermophysical analysis of the near-Earth asteroid (8567) 1996 HW1. Asteroids, Comets, Meteors 2014. *(abstract)*
- Weissman, Paul R., Lowry, S. C., **Rożek, A.**, Duddy, S. R., Rozitis, B., Wolters, S. D., Snodgrass, C., Fitzsimmons, A.; Green, S. and Hicks, M. D. 2013. Shape and Rotation Modeling and Thermophysical Analysis of Near-Earth Asteroid (1917) Cuyo. AAS/-Division for Planetary Sciences Meeting Abstracts 45, 112.15. *(abstract)*
- **Rożek, A.**, and 9 colleagues, 2013. Physical Properties of Asteroid (1917) Cuyo. European Planetary Science Congress 2013, held 8-13 September in London, UK, EPSC2013-943. *(abstract)*

Publications in preparation

- **A. Rożek**, S.C. Lowry, et al., Physical model of a Near-Earth Asteroid (1917) Cuyo
- **A. Rożek**, S. C. Lowry, et al., Physical model of the NEA (85990) 1999 JV_6
- **A. Rożek**, S.C. Lowry, et al., Spin state analysis and thermophysical analysis of the near-Earth asteroid (8567) 1996 HW_1

Publications resulting from earlier work

Refereed articles in planetary science

7. Breiter, S., **Rożek, A.**, Vokrouhlický, D. 2012. Stress field and spin axis relaxation for inelastic triaxial ellipsoids. MNRAS, 427, 755-769.
8. Breiter, S., **Rożek, A.**, Vokrouhlický, D. 2011. Yarkovsky-O'Keefe-Radzievskii-Paddack effect on tumbling objects. MNRAS, 417, 2478-2499.
9. **Rożek, A.**, Breiter, S., Jopek, T. J. 2011. Orbital similarity functions - application to asteroid pairs. MNRAS, 412, 987-994.

Refereed articles in spectroscopy of variable stars

10. Dimitrov, W., Fagas, M., Kamiński, K., Kolev, D., Kwiatkowski, T., Bąkowska, K., **Rożek, A.**, A., Bartczak, P., Borczyk, W., Schwarzenberg-Czerny, A. 2014. Spectroscopy of HD 86222 - a quintuple system with an eclipsing component. Astronomy and Astrophysics 564, A26.
11. Ratajczak, M., and 11 colleagues (incl. **A. Rożek**) 2010. Absolute properties of the main-sequence eclipsing binary FM Leo. MNRAS, 402, 2424-2428.
12. Baranowski, R., and 11 colleagues (incl. **A. Rożek**) 2009. V440 Per: the longest-period overtone Cepheid. MNRAS, 396, 2194-2200.
13. Handler, G., and 28 colleagues (incl. **A. Rożek**) 2009. Asteroseismology of Hybrid Pulsators Made Possible: Simultaneous MOST Space Photometry and Ground-Based Spectroscopy of γ Peg. The Astrophysical Journal 698, L56-L59.

Conference abstracts and other

- **Rożek, A.**; Breiter, S. and Vokrouhlický, D. 2011: YORP on tumbling asteroids, EPSC-DPS Joint Meeting 2011 *(abstract)*
- Sekalska, J., and 14 colleagues (incl. **A. Rożek**) 2010. Spectroscopy of Eclipsing Binary DY Lyncis Third Component Detected. Information Bulletin on Variable Stars 5954, 1. *(short announcement)*
- **Rożek, A.**; Breiter, S. and Jopek, T.J. 2009: Comparison of various orbital similarity functions, EPSC 2009. *(abstract)*
- Ratajczak, M.; Kwiatkowski, T.; Schwarzenberg-Czerny, A. et al. (incl. **A. Rożek**), 2010: FM Leo: the Tale of Twins, Binaries - Key to Comprehension of the Universe. Proceedings of a conference held June 8-12, 2009 in Brno, Czech Republic, San Francisco: Astronomical Society of the Pacific, 2010., p.95 *(abstract)*
- Fagas, M., Baranowski, R., Bartczak, P., Borczyk, W., Dimitrow, W., Kaminski, K., Kwiatkowski, T., Ratajczak, R., **Rożek, A.**, Schwarzenberg-Czerny, A. 2009. Preliminary results of V440 Per and α UMi observations with the Poznan Spectroscopic Telescope. Communications in Asteroseismology 159, 48-50. *(proceedings paper)*
- **Rożek, A.**, Baranowski, R., Bartczak, P., Borczyk, W., Dimitrov, W., Fagas, M., Kaminski, K., Kwiatkowski, T., Ratajczak, R., Schwarzenberg-Czerny, A. 2008. Spectroscopy of pulsating stars at Poznan Spectroscopic Telescope - data reduction and radial velocity measurements. Communications in Asteroseismology 157, 361-362. *(proceedings paper)*
- **Rożek, A.** et al 2008: Radial Velocity Measurements for Pulsating Stars with Poznan Spectroscopic Telescope: First Results, Kyiv University, YSC'15 2008. *(proceedings paper)*

Observing proposals submitted

Principal Investigator

- **Rożek, A.**, Lowry, S. C, Virkki A., Rozitis B., 2017. Observations of a near-Earth asteroid (6053) 1993 BW3 with Arecibo Planetary Radar. Approved Arecibo programme R3186, awarded 5 nights.
- **Rożek, A.**, Nolan, M. C., Lowry S. C., 2015. Observations of a near-Earth asteroid (85990) 1999 JV6 with Arecibo Planetary Radar. Approved Arecibo programme R3036, awarded 6 nights.
- **Rożek, A.**, Nolan, M. C., Lowry S. C., 2014. Observations of a near-Earth asteroid (85990) 1999 JV6 with Arecibo Planetary Radar. Approved Arecibo programme R2959, awarded 5 nights.

Co-Investigator

- Lowry S. C., Fitzsimmons A. , Green S., **Makieła A.**, Rozitis B., Snodgrass C., Zegmott T. J., 2016, near infra-red observations of near-Earth asteroids with VISIR instrument at VLT, Paranal Observatory, Chile, ESO Large Programme 197.C-0816.
- Lowry S. C., **Rożek, A.**, Zegmott T. J., Physical Characterization of the Bilobate Near-Earth Asteroid (85990) 1999 JV6, and Detection of the YORP Effect, Isaac Newton Telescope proposal I/2016A/10, awarded 4 nights

- Rozitis, B., Emery, J., Lowry, S. C., **Rożek, A.**, Wolters, S., Snodgrass, C., Green, S. 2014. Thermal Emission Light-Curves of Rapidly Rotating Asteroids. Spitzer Proposal 11097

Chapter 1

Thermal response of asteroid surfaces, the YORP and Yarkovsky effects

1.1 The dynamical classification of small Solar System bodies

The Solar System formed from a spinning cloud of dust and gas about 4.6 billion years ago. As the Sun formed and the proto-planetary disc around it collapsed, the dust particles began coagulating to form planetesimals that later formed planets. The current Solar System is made up of four rocky planets, Mercury, Venus, Earth and Mars, and four gaseous giants, Jupiter, Saturn, Uranus, and Neptune. According to the current understanding, the giant planets migrated from where they originally formed (Tsiganis et al., 2005; Morbidelli et al., 2005; Gomes et al., 2005; Walsh et al., 2011; Morbidelli et al., 2015). Not all the material of the proto-planetary disc ended up forming planets. The interactions with migrating bodies, especially Jupiter and Saturn, led to orbit scattering of small Solar System bodies (SSSBs). Some of those SSSBs were perturbed by gravitational interactions, their orbits moved closer to Earth in the process, and eventually formed the asteroid belt and near-Earth populations (Gomes et al., 2005; Raymond and Izidoro, 2017).

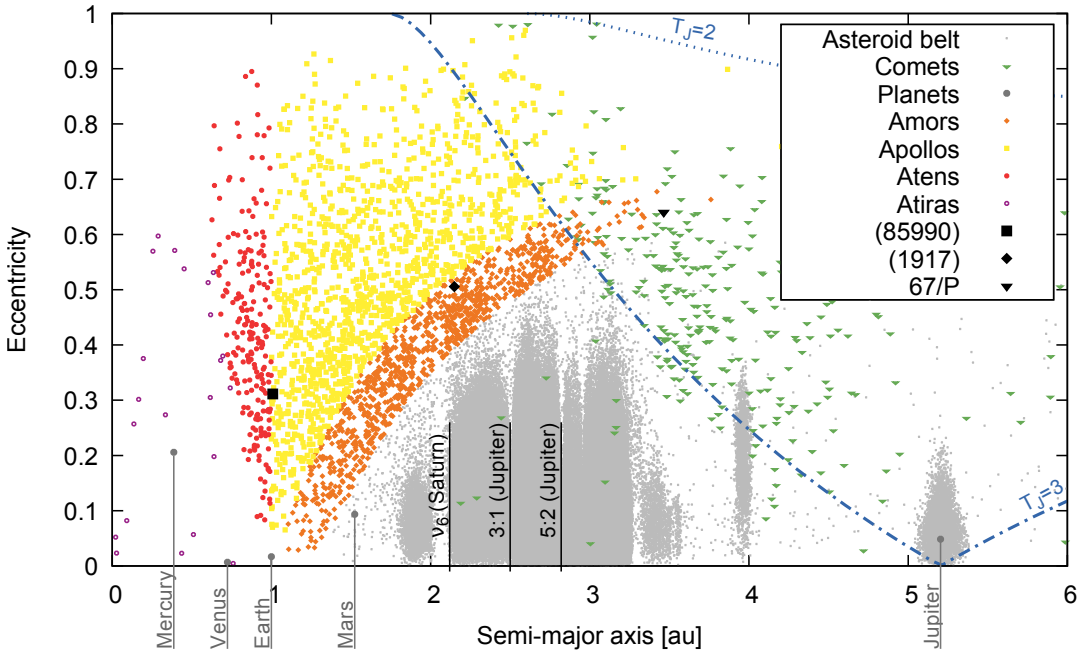

Figure 1.1: The distribution of osculating orbital elements of small Solar System bodies within the inner Solar System and up to the orbit of Jupiter. Coloured symbols are used to mark different dynamic classes of near-Earth objects. There are four types of near-Earth asteroids: Amors (marked with orange diamonds), Apollos (yellow squares), Atens (red circles), and Atiras (purple open circles). The periodic comets are included, marked with green triangles. The positions of objects discussed in this work are indicated with black symbols. The Mars crossers, main-belt asteroids and Jupiter Trojans are marked with grey dots. Lines marking two values of Tisserand invariants for Jupiter, $T_J = 2$ and 3 assuming inclination 0°, are included in the plot. Lastly, the positions of planets are marked with dark grey symbols, and positions of some of the important resonances in the asteroid belt are indicated with black lines. The osculating orbital elements used in the graph were taken from the NASA Solar System Dynamics site[b] (accessed 25th September 2017).

[b] https://ssd.jpl.nasa.gov/?sb_elem

The dynamical classification of the inner Solar System is illustrated in Figure 1.1. The graph represents the distribution of orbital elements of the Solar System bodies within 6 AU from the Sun. The x-axis of the graph corresponds to semi-major axes of the orbits, a (in AU). The y-dimension of the plot is the eccentricity, e. Combined, semi-major axis and eccentricity provide information about the perihelion distance, $q = (1 - e)a$, which is the minimum distance of target to the Sun, and the aphelion, $Q = (1 + e)a$, which is the maximum distance to the Sun for objects in elliptical orbits, with $e \in (0,1)$. The elements considered here are osculating elements, valid for a certain epoch, in this case 25$^{\text{th}}$ September 2017, whose values constantly change due to gravitational interactions and non-gravitational effects.

The planets are shown with dark grey symbols. The pale grey dots show all the asteroids which have perihelion distances larger than 1.3 AU, and are therefore not classified as near-Earth asteroids (NEAs), belonging mostly in the asteroid belt. The same representation is given to the members of Jupiter trojan family, objects close to the 1:1 mean motion resonance with Jupiter. The NEAs in the figure are divided into four traditional dynamical groups. The name of each class is derived from one of the first named bodies which orbit belonged to it. The orange diamonds mark the Amors, with orbits entirely outside the Earth's orbit, perihelia larger then aphelion distance of Earth ($q \geq 1.017$ AU), but smaller than 1.3 AU. The Amor asteroid (1917) Cuyo is marked here with a black diamond, as it is the subject of Chapter 4. The yellow squares mark the Apollos, objects crossing Earth's orbit, with $a > 1$ AU and $q \leq 1.017$ AU. The asteroid (85990) 1999 JV_6 is a member of this group, marked here with a black square, and discussed in detail in Chapter 5. The red circles are Atens, the orbits of which are smaller than Earth's, with $a < 1$ AU and $Q \geq 0.983$ AU. The final and least numerous group of NEAs is formed by the Atiras, with orbits entirely within the orbit of Earth, $Q \leq 0.983$ AU, and marked with open purple circles. Some of the Apollo and Aten objects can occasionally come to within 0.05 AU of Earth's orbit. If they are larger than $\approx$140 m, these objects can pose a risk of collision with Earth and are therefore called potentially hazardous asteroids.

The last group of bodies included in the illustration are periodic comets, marked with green triangles. Comets are icy small bodies with dark (low reflectance) surfaces recognised traditionally by their activity. Volatile frozen substances sublimate as the bodies approach the Sun producing dusty coma and gaseous and dusty tails. The comets are expected to occupy mostly the outer reaches of the Solar System with large semi-major axes and strongly elongated, almost parabolic or hyperbolic orbits. However, encounters with giant planets sometimes bring those bodies into the inner Solar System. A particular group of those bodies can be found within the dynamical region of the main asteroid belt normally attributed to asteroids. The so-called main-belt comets, are interesting as they provoke questions of whether dynamical classification of asteroid and comets is really valid (Binzel et al., 2015). They display comet-like activity normally associated with sublimation of surface ices on comets and one of them, 288/P (300163), was recently discovered to be a binary, consisting of two bodies in close orbit around each other (Agarwal et al., 2017). Most of the comets in Figure 1.1 belong to a group called the Jupiter family comets (JFCs). The class definition

is a bit ambiguous (Marsden, 2009), however it is usually accepted to include targets with Jupiter Tisserand invariant value, T_J, between 2 and 3. The Tisserand invariant is a dynamical property of the orbit. It combines the semi-major axis, eccentricity, and orbital inclination, i, of the small body with the semi-major axis of the perturbing body, a_J in case of Jupiter. The invariant for Jupiter is thus defined as follows

$$T_J = \frac{a_J}{a} + 2\sqrt{\frac{a}{a_J}(1-e^2)}\cos i. \tag{1.1}$$

The blue lines in Figure 1.1 mark the values of $T_J = 2$ and $T_J = 3$, assuming orbit inclination $i = 0°$. Some of the comets within the JFC class can have perihelia smaller than 1.3 AU, and thus qualify as near-Earth objects. One of such targets, comet 67P/Churyumov-Gerasimenko, is marked in the image with a black triangle. It was recently investigated extensively by the Rosetta mission, and some of the results are presented in Chapter 6.

The black lines on the figure mark the locations of some of the important resonant zones in the main belt. As the collisions, encounters and non-gravitational forces cause the orbits to change, the bodies arrive in the resonant zones where their elements are strongly perturbed, and they are swung towards NEA population through certain 'escape paths' that changed as the Solar System evolved (Morbidelli et al., 2015; Granvik et al., 2017). The ν_6 secular resonance with Saturn, together with the 3:1 and 5:2 mean motion resonances with Jupiter, all marked in the plot, are considered to be the main sources of the near-Earth population (Binzel et al., 2015).

1.2 Investigation of near-Earth asteroids

The study of NEAs has a range of motivations, to list a few:

- The asteroids provide markers of various stages of the evolution of the Solar System (Johansen et al., 2015; Morbidelli et al., 2015). Understanding their chemical composition and formation mechanisms allows for a better understanding the origin of our planet. The NEAs might be responsible for delivering water and pre-biotic materials to Earth (for example Chyba et al., 1989; Rivkin and Emery, 2010; Raymond and Izidoro, 2017). Additionally the frequent asteroid collisions with the young planet are linked to a series of extinction events that might have strongly influenced the evolution of life on Earth (Maher and Stevenson, 1988). Traces of those events can be found in geological strata and in form of craters, like the Chicxulub crater linked to the impact that led to the extinction of dinosaurs (Schulte et al., 2010).

- The NEAs are the closest Solar System bodies to Earth, easiest to reach with a spacecraft. The potential to reach a body is usually quantified by the ΔV, the minimum velocity impulse required to transfer a spacecraft from Earth's orbit into a rendezvous orbit (Shoemaker and Helin, 1978). The low ΔV objects are thus considered to be good

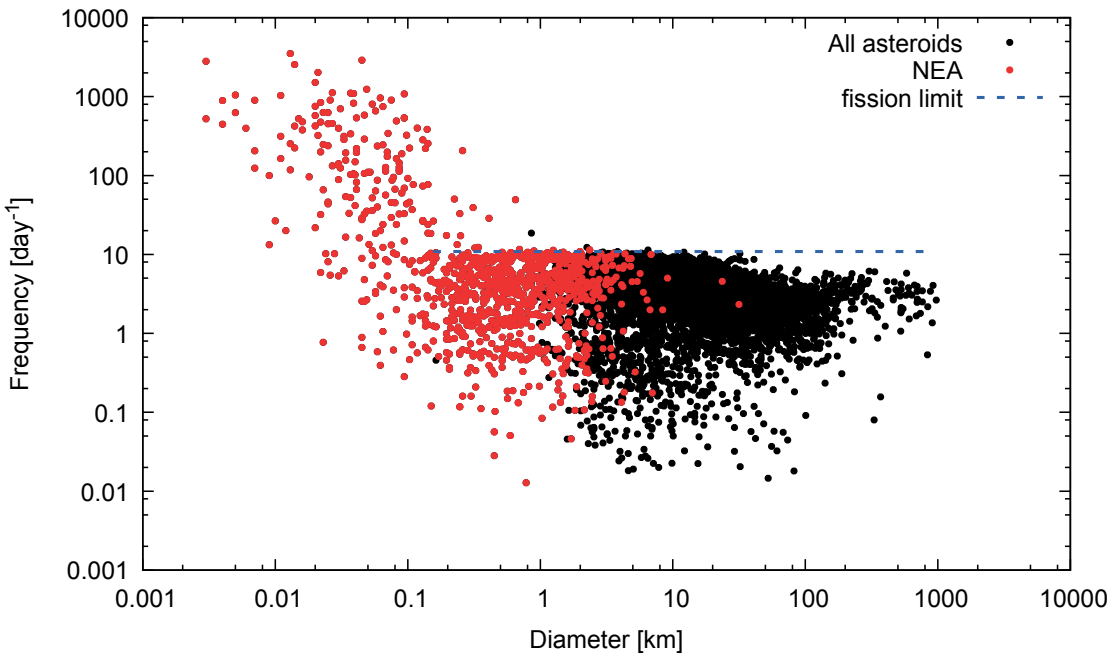

Figure 1.2: The size and frequency distribution of asteroids with published parameters. The diameters of the targets are given in km on the horizontal axis. The sidereal frequency is given in rotations per day on vertical axis. The black circles on the plot mark 6320 asteroids in the data base, including 1060 NEAs, highlighted in red. The blue line is an approximate location of the spin-induced fission limit, corresponding to the 2.2 h value adopted from Pravec and Harris (2000). Data used to produce the graph was downloaded from LCDB (Warner et al., 2009, 2017 annual release).

targets for in-situ investigation, sample-return and mining missions.

- Some of the NEAs might pose a risk of collision with Earth. Successful planning of asteroid deflection requires precise knowledge not only of orbital parameters, but also of physical properties of the bodies (Harris et al., 2015). The shape and spin-state modelling play crucial roles in designing deflection missions. Combined with detailed physical models of surface properties and study of asteroid internal structure they are essential in planning, and, in the future, execution of successful missions.

The bulk of this thesis is dedicated to observations of small bodies for the purpose of shape modelling (Chapter 2), and spin-state analysis (Chapter 3). The investigation of NEAs calls for precise physical modelling of the population members. Some important characteristics are the sizes and rotation rates, illustrated in Figure 1.2. The figure shows the known spin-rates (measured in rotations per day) against the diameters of asteroids (in km). Blue line marks approximately the rotational fission limit for a rubble-pile object, corresponding to the rotational period of 2.2 h. Following the derivation by Pravec and Harris (2000), for an asteroid rotating faster than this limit the centrifugal forces acting on boulders at the equator due to the objects intrinsic rotation outweigh the gravitational pull causing material to detach from the surface. The fission limit is independent on an asteroids size, but rather weakly depends on the bulk density with the fission-limit frequency proportional to a square of

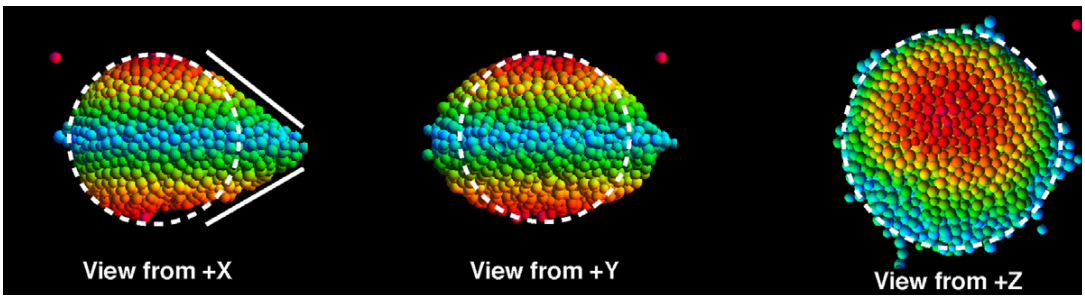

Figure 1.3: A rubble pile model of a small asteroid, used in simulation of rotational fission and demonstrate different parameters controlling it, image copied from Sánchez and Scheeres (2016, their Figure 5). Colours mark asteroid-centric latitudes, and the target is made-up of closely packed spheres. The picture illustrates the idea of an asteroid being a loosely bound pile of rubble with spherical pebbles, while it is accepted that the asteroids are made of fragments of different shapes and sizes. The object shown is a result of one of the recent simulations of a spin-up of an initially spherical aggregate (studied initially by Walsh et al., 2008). The object formed a characteristic 'equatorial bulge' and begins shedding mass (small particles floating around). The shapes strongly resembles real asteroids observed in the near-Earth population, for example (66391) 1994 KW_4 (Ostro et al., 2006).

density for a sphere. The abundant small and quickly rotating asteroids are likely monolithic bodies held together by forces stronger than self-gravity, but that issue is still investigated (Scheeres et al., 2015).

Currently, the only known differentiated bodies in the asteroid belt are asteroid (4) Vesta (Binzel and Xu, 1993) and dwarf planet Ceres (Thomas et al., 2005). The rapidly rotating smallest asteroids are considered to be monolithic fragments of larger parent bodies. The collisions between planetesimals, with cycles of disruption and re-formation, led to formation of a population of small fragmented rubble-piles (Johansen et al., 2015). The term is used to describe the asteroids that are generally believed to be gravitational aggregates of rock fragments and pebbles of a range of sizes, usually residing below the fission limit (see Figure 1.2). As an asteroid's rotation speeds up the loosely bound material can get moved towards the equator, forming an equatorial bulge (see for example Figure 1.3). When the rotation rate is quick enough the body can start shedding mass and eventually get disrupted, forming a binary system. The components of a binary system either drift away, or are slowed down by mutual tides and non-gravitational forces, eventually collapsing to form a single body (Jacobson and Scheeres, 2011).

It is currently accepted that the dynamics of SSSBs are greatly affected by non-gravitational effects resulting from sunlight being reflected and absorbed by asteroid surfaces (Bottke et al., 2006; Vokrouhlický et al., 2015a). The interaction with thermal photons has two aspects. One aspect is a force, called the Yarkovsky effect, non-negligible in predicting long-term evolution of asteroid orbits, and is discussed in Section 1.3. The other aspect, called YORP and discussed in Section 1.4, is a torque that affects long-term evolution of spin state, changing both the rotation rate and orientation of spin axis. Both effects have a seminal role in modern studies of small bodies of the solar system (Bottke et al., 2002; Bottke et al., 2006;

Vokrouhlický et al., 2015a). Those effects scale with size and distance to the Sun, acting most efficiently in the near-Earth area and on relatively small bodies.

The initial drive of this thesis was to focus on the YORP effect, nominally the new direct detections of the YORP-induced period change. While the effect has been intently studied ever since its modern definition (Rubincam, 2000), and first detection (Lowry et al., 2007; Taylor et al., 2007), there is still scope to improve and expand the theories by providing observational constraints. Before presenting the results, it is important for the reader to gain some understanding of how the thermal response of asteroidal surfaces affect their motion. In other words, how the Yarkovsky and YORP effects work, which will be the focus of the rest of this chapter. Later, the observational methods used to examine the near-Earth asteroids will be discussed in Chapter 2, followed by the description of modelling methods in Chapter 3. The results of detailed shape modelling and spin-state analysis of NEAs (1917) Cuyo and (85990) 1999 JV_6 are presented in Chapters 4 and 5 respectively. The same tools were used to analyse early data from the Rosetta spacecraft, on comet 67P/Churyumov-Gerasimenko, as shown in Chapter 6.

1.3 The Yarkovsky effect

The Yarkovsky effect was developed from an idea presented by a Polish-Russian engineer, Ivan O. Yarkovsky in 1888 (Beekman, 2006). He tried to explain why the friction of æther, that was believed to be filling the outer space, does not slow down planetary motion. According to Yarkovsky, the quintessence would be absorbed by a planet in the course of the orbital motion, and then heated up when the surface was illuminated by the Sun. The heat would cause the æther to expand and escape the planet, producing a small recoil force that would act against the predicted drag. After the idea of æther was abandoned by science, the Yarkovsky effect was re-formulated as the influence that thermal radiation has on orbital motion (see for example Beekman, 2006, for a detailed discussion of how the idea evolved). The solar radiation absorbed by a small body is later emitted as thermal infra-red photons. The momentum carried by the photons produces a tiny recoil force called the Yarkovsky effect.

The Yarkovsky effect can systematically change the orbit of a small body, most notably the semi-major axis. The mathematical formulation of the Yarkovsky effect comes from computation of the surface temperature distribution (the basic formulation is presented in Appendix C). The effect depends on the lag between receiving and emitting the radiation, in other words on how the temperature of the moving body changes. In terms of its influence on the semi-major axis, it has two aspects – one connected to the day-night cycle, called the diurnal effect, and second related to the change of seasons on the body, called the seasonal effect. Both aspects of the Yarkovsky effect depend highly on the spin-axis orientation.

The diurnal component of the effect comes from the difference of temperature between day and night on the body, as is illustrated in Figure 1.4. In the ideal case, shown

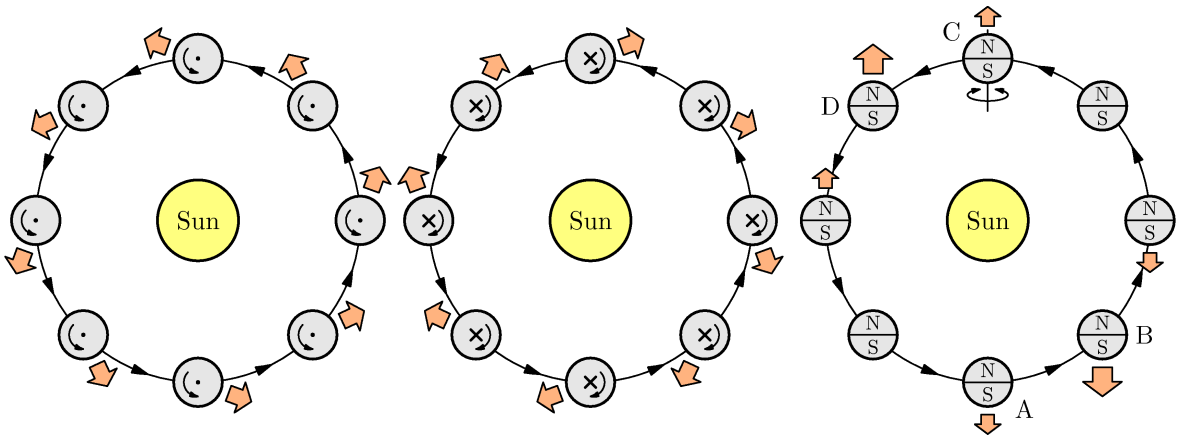

(a) Diurnal component (prograde)

(b) Diurnal component (retrograde)

(c) Seasonal component

Figure 1.4: The Yarkovsky effect has two components, diurnal (panels a and b) and seasonal (panel c, on the right). All three panels illustrate a spherical object on a circular orbit around the Sun, with the yellow Sun in the centre, different positions of the body in the orbit indicated by the grey circles and directions of orbital and rotational motion indicated by black arrows. The orange arrows show the direction in which the object would be moved by the Yarkovsky forces. In panels (a) and (b) the targets spin-axis is perpendicular to the orbital plane. In panel (a) the body is in a pro-grade rotation, and the Yarkovsky forces are causing the body to spiral outwards. In panel (b) the body is in retrograde rotation, spiralling inwards. In panel (c) the spin axis is in the orbital plane and the seasonal change in temperature between northern (N) and southern (S) hemisphere is causing the semi-major axis to decrease. The image is taken from Vokrouhlicky and Bottke (2012, Figure 2), and adopted to show the retrograde diurnal effect, see also Bottke et al. (2002, Figure 1).

here, a small spherical object is put on a circular orbit around the Sun (Bottke et al., 2006; Vokrouhlický et al., 2015a). The spin-axis is perpendicular to the orbital plane. The rotation period and thermal inertia of the surface are just right, so that the surface is warmest on the afternoon side of the body. The radiated heat produces a small thrust in the direction indicated by the broad orange arrows. For the rotation in the same direction as the orbital motion (prograde, Figure 1.4a), the Yarkovsky force acts to expand the orbit. When the target rotates in the retrograde sense, the thermal recoil acts against the orbital motion and effectively shrinks the orbit, see Figure 1.4b.

The seasonal effect is correlated with orbital rather than rotational motion, but it still does depend highly on the spin-axis orientation relative to the orbit. Again, in an idealised example, a small spherical body is on a circular orbit, but this time the spin-axis is in the orbital plane, see Figure 1.4c. The surface is divided into two hemispheres, N (northern) and S (southern), and is heated up by the Sun, with the biggest difference of insolation during either of the polar summers (points A and C on the orbit in Figure 1.4c). Once again, because of the delay between irradiation and the time when maximum temperature is reached, due to thermal inertia, the biggest thrust is produced in early autumn (as the polar day ends) on either hemisphere. Figure 1.4c shows that heat escaping the hemisphere S produces biggest recoil in point B on the orbit, and similarly most heat is emitted in point D from

N-hemisphere. The seasonal part of Yarkovsky effect is independent on the sense of rotation and always leads to orbit spiralling 'inwards'.

1.3.1 Applications of the Yarkovsky effect

The Yarkovsky effect is considered an important factor in the dynamics of small Solar System bodies, essential in explaining the distribution of asteroid family orbits, delivery of asteroids and meteors to the vicinity of Earth, assessing the impact hazards for NEAs and useful in determining physical properties of asteroids (Bottke et al., 2006; Vokrouhlický et al., 2015a).

The effect is a major factor in dynamical evolution of asteroid families. The asteroid families are formed in collisions, that lead to disruption of the parent bodies. The ejected fragments drift away due to the initial velocity impulse from the disruption event combined with the influence of the Yarkovsky effect (Vokrouhlický et al., 2006a). Due to the dependency on the body size, the effect produces a characteristic V-shaped spread in the distribution of absolute magnitudes (which translate to inverse of asteroid size) against the semi-major axis. In fact this V-shaped arrangement of asteroid family members is prominent enough that it allows for estimates of family age (Vokrouhlický et al., 2015a) and even for identification of new asteroid families (Bolin et al., 2017).

The near-Earth population originates mostly from the asteroid belt. The main sources of near-Earth asteroids and meteors are in the dynamical resonances with Jupiter and Saturn (Binzel et al., 2015; Morbidelli et al., 2015). It has been confirmed by numerical studies that the Yarkovsky effect is essential as a mechanism to deliver the meteors produced in asteroid collisions (Vokrouhlický and Farinella, 2000), and larger bodies from other regions in the asteroid belt to the resonant zones (Morbidelli and Vokrouhlický, 2003). The current numerical studies of asteroid dynamical evolution routinely take the non-gravitational forces into account (Granvik et al., 2017).

The impact hazard estimates rely on precise orbit determination. The Yarkovsky effect is one of the major factors in assessment of collision probabilities, especially for bodies with high accuracy astrometric measurements that distinguish between purely gravitational and Yarkovsky-influenced orbit predictions (Farnocchia et al., 2015). For potentially hazardous asteroids the Yarkovsky drift in orbital elements is either inferred from earlier measurements on members of the population, or precisely modelled for an accurate prediction (Vokrouhlický et al., 2000; Chesley et al., 2003). As was shown in case of the asteroid (99942) Apophis, the estimate of Yarkovsky magnitude can considerably change impact probabilities (Vokrouhlický et al., 2015b).

The determination of physical parameters of the asteroid surfaces is possible thanks to the infra-red observations and development of thermophysical analysis methods, like the Advanced Thermophysical Model (ATPM) (Rozitis and Green, 2011, 2012, 2013). The methods use shape and spin-state coupled with thermophysical model to infer surface parameters.

However, some of the parameters are coupled and impossible to disentangle without an additional resource, for example the thermal inertia, Γ, and density, ρ. The direct measurement of Yarkovsky strength can provide constraints to the modelled values, as was done for example for asteroid (107955) Bennu (Chesley et al., 2014). While thermophysical modelling is beyond the scope of this thesis the two NEAs analysed here were the subject of infra-red observations. The shape and spin-state models developed by the author were later used to determine the precise size of asteroid (1917) Cuyo (Chapter 4) and, coupled with a non-gravitational force detection, constrain the density of (85990) 1999 JV_6 (Chapter 5). This thesis makes use of the ESO LP observing campaign, an effort to provide observational ground-truth for YORP theory through physical characterisation of NEAs by means of optical and infra-red observations (it is discussed in Section 2.1.2). The ATPM modelling was performed by collaborator in the ESO LP, B. Rozitis.

1.3.2 Recent theoretical developments

Efforts are made to improve models of thermal properties of the asteroid surfaces (Delbo et al., 2015) and create robust models of the thermal recoil forces (Vokrouhlický et al., 2015a). Both analytical and numerical models have been developed over the past few decades that tackle the assumptions in the basic mathematical formulation, introduced in Appendix C in Equations (C.1) and (C.2), including derivations exploring the influence of physical parameters of the bodies, heat transfer laws, orbital dynamics, and coupling Yarkovsky with YORP effect and tumbling (Vokrouhlický et al., 2015a).

A comprehensive review of those models can be found in the recent Asteroids IV book (Vokrouhlický et al., 2015a), while a list of models and their underlying assumptions is neatly summarised in Rozitis and Green (2012, Table 1). For example, the investigation of non-linear boundary conditions for the surface temperature distribution of spherical bodies was performed using iterative semi-analytical methods (Sekiya and Shimoda, 2013, 2014). For bodies in circular orbits the linear approximation was found to give good estimates of the Yarkovsky semi-major axis drift despite the difference in the mean surface temperature. For eccentric orbits the authors developed not only the Yarkovsky drift for the semi-major axis, but also for eccentricity and the longitude of the periapsis. The iterative methods yield high accuracy of predictions, are in good agreement with earlier numerical studies, and expand the calculations to fast rotators when compared to earlier studies. In another example, the influence of surface roughness on the Yarkovsky effect was examined using the ATPM (Rozitis and Green, 2012). It was shown that the small-scale features of the surface lead to non-Lambertian (asymmetrical) scattering of the thermal infra-red radiation (beaming) and can alter the Yarkovsky drift predictions by a few tens of percent. Recently, a generalised model of the diurnal component of Yarkovsky torque was derived for an arbitrary convex body (Golubov et al., 2016).

1.3.3 Measurements of Yarkovsky effect for NEAs

The influence of Yarkovsky effect on the asteroid orbits on the time-scale of years was first studied by Vokrouhlický et al. (2000). The orbital uncertainties of a few objects were analysed along with a range of possible semi-major drift magnitudes, to predict potential future detection. The effect was first directly detected on asteroid (6489) Golevka (Chesley et al., 2003). During the 2003 approach, the orbit was known well enough to enable determination of a non-gravitational orbital drift (Vokrouhlický et al., 2000). The plot in Figure 1.5 shows the error ellipse of the ephemeris based solely on gravitational perturbances (labelled *SUM1*). An astrometry measurement performed in May 2003 (marked in the figure with a diamond) lays away from the predicted trajectory. Taking into account Yarkovsky effect shifts the error ellipse, so that the orbit prediction resides inside *SUM2*, and is consistent with the presented radar astrometry. The calculations based on a non-linear model of Yarkovsky effect, along with radar-derived size, spin-state and shape model, constrained the bulk density to be $2.5\,\mathrm{g/cm^3}$ and thermal conductivity of the surface to be $0.01\,\mathrm{W\,m^{-1}\,K^{-1}}$.

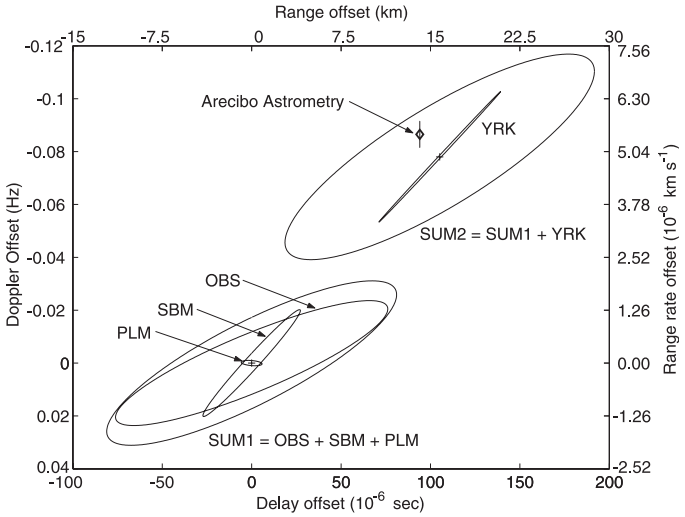

Figure 1.5: The first direct detection of Yarkovsky effect was possible thanks to astrometry using radar images. The image shows the orbital prediction for the asteroid (6489) Golevka. The horizontal axis is the offset in signal delay, marked on the lower axis and measured in 10^{-6} s (µs), which can be interpreted as the offset in range, marked on the upper axis and measured in km. The vertical axis marks the measured offset in signal frequency or the Doppler offset, marked on the left axis and measured in Hz. This can be translated to the offset in radial velocity or range rate, marked on the right and measured in $10^{-6}\,\mathrm{km\,s^{-1}}$. The offsets are measured relative to the nominal orbital prediction from the 1991-1999 radar data, marked with '+' at the point (0,0). The orbital prediction taking into account Yarkovsky offset is also marked with a '+'. The various labelled ellipses correspond to different sources of uncertainties: *OBS* comes from the uncertainties in the astrometric measurements, *SBM* from gravitational perturbations from other small bodies, *PLM* from gravitational influence of planets, *YRK* from the errors in Yarkovsky models. The big ellipse *SUM1* is the sum of the first three, and finally *SUM2* includes the Yarkovsky forces. The radar astrometry from 26$^{\mathrm{th}}$ May 2003 is marked with a diamond symbol. The image is taken from Chesley et al. (2003, Figure 2).

While a semi-major axis drift detected for a small Solar System body can be only due to a non-gravitational force, a thermophysical model is essential to confirm it is linked to the Yarkovsky effect. However, a signature of the effect can be found in the astrometric data without detailed modelling. This method is based on an orbital ephemeris calculated with an arbitrary transverse acceleration, described with a single parameter labelled A_2. The parameter A_2, like any other orbital parameter, has an associated uncertainty, σ_{A_2}. The ratio between the parameter and its uncertainty is then a measure of reliability of the detection of a non-gravitational force, with larger value interpreted as a better signal-to-noise ratio of the detection. The value of the parameter A_2 can be compared to expected maximum Yarkovsky acceleration, taking into account extreme obliquity and scaled by diameter of the body, $A_{2_{max}}$. The ratio of the two parameters, $A_2/A_{2_{max}}$ has to be close to 1 for the detection to be attributed to the Yarkovsky effect. This method allows for a pre-selection of candidates for a more involved study. This approach was used to confirm Yarkovsky detections for a few asteroids to date, see detailed list in Farnocchia et al. (2013); Vokrouhlický et al. (2015a) and on-line*.

1.4 The YORP effect

The term Yarkovsky, O'Keefe, Radzievskii, and Paddack (YORP) comes from the names of researchers who advanced studies on the effect that sunlight reflected off the minor bodies of the Solar System might have on their dynamics (Rubincam, 2000). Similar to the effect postulated by Yarkovsky, the YORP effect is a result of thermal re-radiation of absorbed sunlight. However, the Yarkovsky effect is connected to the lag between the absorption and re-emission of radiation and can work even on spherical bodies. The YORP effect depends on the asymmetry of the body, and it is extremely sensitive to the shape details. While the YORP effect can be produced by reflection of the radiation, its main driver is usually the thermal component. The contribution of thermal and reflected components depends on the Bond albedo (A) of target's surface and can be further enhanced for high surface roughness (Rozitis and Green, 2012).

To introduce the principle of the YORP effect, one often uses a simplified model that exaggerates the required asymmetry of the shape, presented here in Figure 1.6 (copied from Rubincam, 2000, Figure 1). Solar radiation heats up surfaces of an asteroid represented by a black-body shaped into a sphere with two prismatic wedges attached to its equator. The body is on a circular orbit, has the spin-axis perpendicular to the orbit (obliquity $\varepsilon = 0°$), and the surface has no thermal conductivity ($K = 0\,\mathrm{W\,m^{-1}\,K^{-1}}$). Thanks to the windmill-like shape, the thermal radiation creates a net torque, $\bar{\tau}$ (letter τ is adopted here to denote torque following Rubincam (2000)), when averaged over rotational and orbital motion. The $\bar{\tau}$ is traditionally divided in two components, τ_ω and τ_ε. The first one is just a projection on to the direction of spin-axis, defined as $\tau_\omega = \bar{\tau} \cdot \hat{\omega}$. The torque, τ_ω, can speed up as well as slow down an asteroid's rotation. The torque component τ_ε acts orthogonally to the spin axis,

*ftp://ssd.jpl.nasa.gov/pub/ssd/yarkovsky/

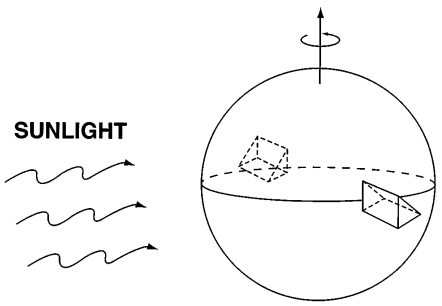

Figure 1.6: A simple model used in the explanation of the YORP effect (taken from Rubincam, 2000, Figure 1). The small body is put in a circular orbit with the spin-axis perpendicular to the orbital plane. The wedges to the sides of the body have the same projected cross-section, so absorb and emit the same amount of radiation albeit in different directions. The asymmetry in re-emission of the light creates a small torque that doesn't disappear after rotational and orbital averaging. The torque affects both the speed of rotation and the obliquity of the spin axis. *NOTE: the reflective component of YORP is omitted in this example, as the target is assumed to be a blackbody.*

defined by $\tau_\varepsilon = \bar{\tau} \cdot \left(\left(\hat{\omega} \cos\varepsilon - \hat{N} \right) / \sin\varepsilon \right)$ (for a drawing showing the relation between spin axis and orbital momentum, please see Appendix Figure B.2). It can change the orientation of rotational axis relative to the orbital plane, (Rubincam, 2000; Vokrouhlický and Čapek, 2002). The change in spin rate, $\dot{\omega}$, can be directly detected by investigation of the asteroid's rotation-induced brightness modulation (see Chapters 2 and 3). The change in spin-axis orientation, $\dot{\varepsilon}$, is more subtle, acting on longer time scales hence not possible to detect directly. Both aspects of the YORP effect can be expressed with reference to the torque components, divided by the largest moment of inertia, C, as

$$\dot{\omega} = \frac{\tau_\omega}{C}, \tag{1.2}$$

$$\dot{\varepsilon} = \frac{\tau_\varepsilon}{C\omega}. \tag{1.3}$$

To illustrate a 'typical' YORP behaviour, numerical studies were conducted by Rubincam (2000) and Vokrouhlický and Čapek (2002), who calculated values of both $\dot{\omega}$ and $\dot{\varepsilon}$ for a series of objects shaped like real asteroids, but scaled to different sizes. They found that the objects would asymptotically approach certain preferred values of obliquity, where they would be either spun up until their break-up or slowed down until a minor perturbation could trigger a tumbling state. Another finding was the identification of critical values of obliquity for which the influence of YORP on spin rate would vanish. Two examples are copied here from Vokrouhlický and Čapek (2002) to illustrate these findings. The two panels in Figure 1.7 show two objects shaped like NEAs (433) Eros (panel a) and Mars' moon Deimos (panel b), placed on circular orbits at 2.5 AU around the Sun.

The graphs in Figure 1.7a show the two components of YORP torque, scaled by the moment of inertia. The torques computed for the (433) Eros-shaped object correspond to a situation where the body obliquity would be driven to 90° with positive τ_ε for $\varepsilon < 90°$ and negative τ_ε for $\varepsilon > 90°$. The object would then slow down, with negative τ_ω at $\varepsilon = 90°$ until likely entering a tumbling state. The two critical values of obliquity, for which the rotational

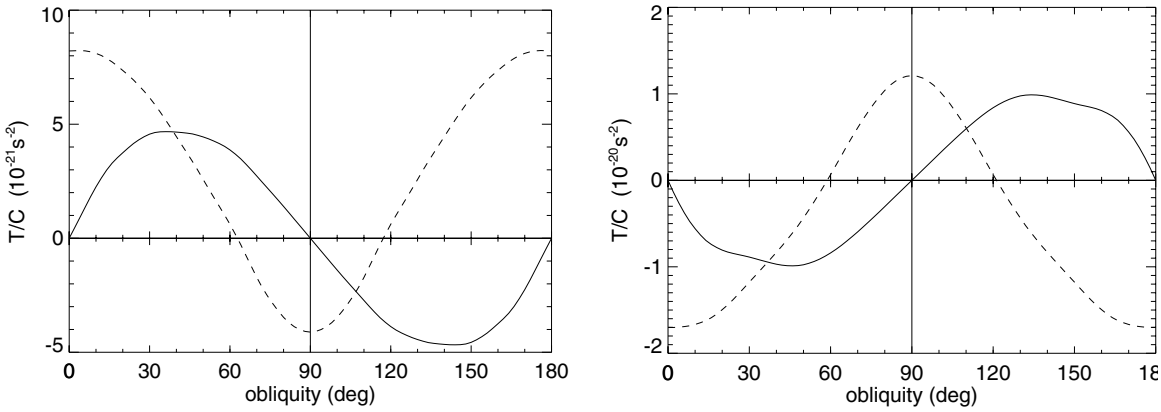

(a) (433) Eros-shaped object. **(b)** Deimos-shaped object.

Figure 1.7: Two examples of a dependence of YORP torques on obliquity in Rubincam's approximation (Vokrouhlický and Čapek, 2002, panel a is Fig. 4 and panel b is Fig. 6). The obliquity of the simulated spin axis, in degrees, is marked on the horizontal axis. The lines represent magnitude of torques, labelled here as T, scaled by the principal moment of inertia, C. The two components of YORP torque are discussed in the main text. The spin-rate torque, τ_ω / C, is marked with a dashed line, and the torque acting on the obliquity, τ_ε / C, with a solid line. The two panels show results for objects on circular orbits, approximately 2.5 AU radius, shaped like the real small bodies.

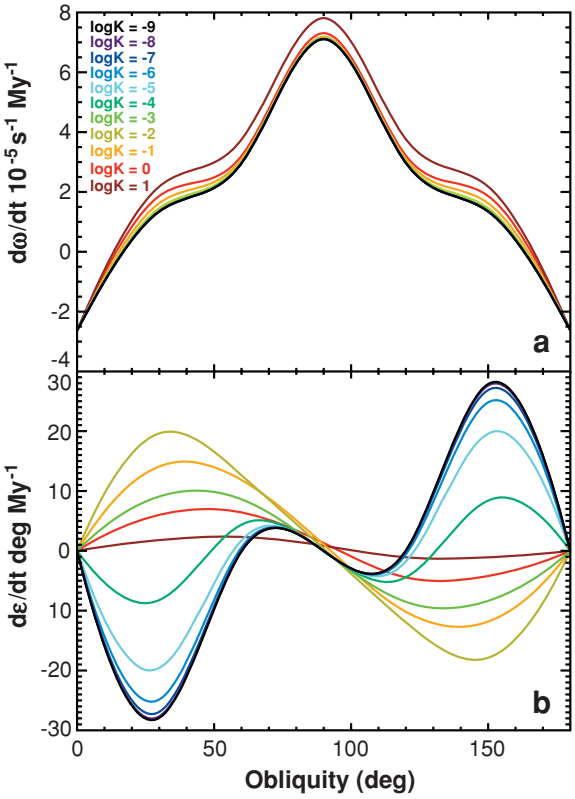

Figure 1.8: In this example, the YORP torques were simulated for a family of asteroids shaped like (6489) Golevka, but having varying thermal conductivity, assuming circular orbits with a radius of 2.5 AU. The horizontal axis on both panel is the obliquity (the angle between spin-axis and orbital plane of the body) in degrees. On panel (a) the vertical axis shows the change in rotation rate, $\mathrm{d}\omega / \mathrm{d}t$, averaged over rotational and orbital motion. Panel (b) shows the modelled mean change in obliquity, labelled ε. The different colours of the solid lines show the mean rates of change for both parameters for different values of thermal conductivity $\log K$. The figure is taken from Bottke et al. (2006, Fig. 6), which is a coloured version of Čapek and Vokrouhlický (2004, Figure 2).

component of the torque disappear are located around $\varepsilon \approx 60°$ and $\varepsilon \approx 120°$. Curiously, the 'mirror' shape (with the direction of the z-axis of the body reversed) displays a 'mirror' YORP behaviour, with the reversed sign of both torques. This type of YORP behaviour can be illustrated with the torques calculated for the shape of Deimos, Figure 1.7b. In this case the body would asymptotically approach $\varepsilon = 0°$ or $\varepsilon = 180°$, once again slowing the rotation. The two cases discussed are the two most common YORP evolution types according to the numerical studies under the Rubincam approximation (Vokrouhlický and Čapek, 2002).

Some more unusual behaviour is expected as well, see for example the torques simulated for a (6489) Golevka-like shaped body in Figure 1.8 (marked with black lines). In this case there are two possible critical values of obliquity, with $\tau_\omega = 0$ for obliquity values $\varepsilon \approx 10°$ and 170°, and three, rather than two, asymptotic values of obliquity to which the rotation would evolve. For $\varepsilon = 0°$ or 180° the rotation would slow down, similar to the previously discussed example, while for the $\varepsilon = 90°$ the body would be locked into being spun up until the rotationally-induced breakup. The situation gets more complicated when thermal conductivity, K, is accounted for in the simulations (Čapek and Vokrouhlický, 2004). The torque responsible for tilting the spin axis is the most affected, with the torques changing magnitude and sign. The coloured lines in Figure 1.8 illustrate the torques acting on (6489) Golevka-shaped object, but with a range of values of K.

1.4.1 Mathematical formulation

Both numerical and analytical studies were conducted to better understand these phenomena. In a simple approximation of a circular orbit, principal-axis rotation, no thermal conductivity, and small deviations from a spherical shape (Breiter and Michalska, 2008), an expression for the YORP-derived spin-up $\dot{\omega}$ can be formulated using Legendre polynomials

$$\dot{\omega} = \frac{\Lambda}{C} \sum_{i \geq 1} \mathcal{A}_i P_{2i}(\cos\varepsilon) \tag{1.4}$$

(Vokrouhlický et al., 2015a, Eq. 4), compare to (Breiter and Michalska, 2008, Eq. 109). Similarly the change in obliquity can be expressed as

$$\dot{\varepsilon} = \frac{\Lambda}{C\omega} \sum_{i \geq 1} \mathcal{B}_i P^1_{2i}(\cos\varepsilon) \tag{1.5}$$

(Vokrouhlický et al., 2015a, Eq. 5), compare to (Breiter and Michalska, 2008, Eq. 107)

Λ	a convenience factor, $\Lambda = 2(1-A)FR^3/3c$, with symbols defined below,
$\mathcal{A}_i$, $\mathcal{B}_i$	shape-specific coefficients,
$P_{2i}(\cos\varepsilon)$	Legendre polynomial of even degree of the cosine of obliquity,
$P^1_{2i}(\cos\varepsilon)$	associated Legendre polynomial of first order and even degree.

Some conclusions can be drawn from this formulation. Most simply, the YORP torque is inversely proportional to the density of the target, through the moment of inertia C, and also inversely proportional to the distance to the Sun via the solar flux, F. Similarly, through the Λ/C factor, the force is inversely proportional to the R^2, where R is the radius of the target. This leads to the effect becoming virtually negligible for large bodies, or bodies that are sufficiently far from the Sun. This is also what makes it especially important for small NEAs. For very small meteoroid fragments the $\dot{\omega}$ term should become increasingly strong, however this issue is still under investigation (Vokrouhlický et al., 2015a). It is also worth noting that while $\dot{\omega}$ is independent of ω, $\dot{\varepsilon}$ is inversely proportional to the rotation rate. This indicates the obliquity evolution considerably slows down for very fast rotators.

The dependence of YORP on obliquity is expressed via the Legendre polynomials of $\cos\varepsilon$. This implies a symmetry of $\dot{\omega}$ around $\varepsilon = 90°$, as the Legendre polynomials of even degree are symmetric, $P_{2i}(-x) = P_{2i}(x)$. Similarly the dependence of $\dot{\omega}$ on ε will be anti-symmetric around $\varepsilon = 90°$ due to the properties of associated Legendre polynomials of first order, $P^1_{2i}(-x) = -P^1_{2i}(x)$. This symmetry was earlier observed in numerical studies (Rubincam, 2000; Vokrouhlický and Čapek, 2002), see also Figures 1.7 and 1.8. The exact functional dependence of both components of YORP on ε is down to the coefficients $\mathcal{A}_i$ and $\mathcal{B}_i$. Those are computed based on the shape of the target, with the formulation above implying that the YORP torques would be sensitive to arbitrarily fine surface detail. This was indeed confirmed by numerical studies (Statler, 2009). The presence of certain critical values of ε for which YORP can be expected from the formulae in Equations (1.4) and (1.5), as those would be the roots of low-order Legendre polynomials.

1.4.2 Applications of YORP

The YORP effect was initially considered to be of importance for spin-state evolution only of small <5 km, asteroids (Rubincam, 2000). However, the first observational indication of YORP was found indirectly in the spin-state alignment of Koronis family members, which were considerably larger, 20 km to 40 km in diameter (Slivan, 2002; Slivan et al., 2003). The members of the family all had obliquities around 160° or 50°, and such clustering could not be explained by gravitationally-driven, or collisionally-driven, spin-state evolution. The obliquity values are close to the critical obliquities in the predicted YORP-driven evolution of the spin-states. It was shown that the distributions of both the pole orientations and rotational periods can be explained using the thermal recoil torques. Follow-up studies showed that YORP was more effective in shaping the spin-state distributions than collisions (Vokrouhlický et al., 2003). Currently the YORP effect models are used in concert with Yarkovsky to estimate ages of the asteroid families (Carruba et al., 2017).

The changes in spin-axis orientation lead to so-called YORP 'cycles' where an object experiences deceleration after reaching one of the aforementioned asymptotic states (Rubincam, 2000). The slow rotation can eventually lead to a tumbling state, then to reorientation of the

spin-axis and then, through the internal energy dissipation back to principal-axis rotation with the YORP-induced spin-axis evolution starting all over again. The YORP cycles are additionally affected by rearranged material on the body surface. The coupling between the YORP effect and shape has been closely investigated using multi-particle simulations (Sánchez and Scheeres, 2012). The effect was shown to change as the object is reshaped by the spin-up, due to the high sensitivity of YORP torques to surface detail. Recently the coupling was shown to act as a 'self-limitation' mechanism that narrows down expected ranges of rotation periods, and preserving the asteroids sense of rotation for longer than could be predicted for a rigid body (Cotto-Figueroa et al., 2015).

The YORP-induced spin-up of asteroid rotation is considered to be responsible for peculiar spin-top shape of many asteroids (Ostro et al., 2006; Scheeres et al., 2006). Numerical studies using the asteroid simulated as an aggregate of gravitationally-bound spheres show an equatorial bulge being formed as the object spins up. The centrifugal force acts against gravity, pushing material radially along the equator, forming a shape that has been observed on a few asteroids (Walsh et al., 2008; Sánchez and Scheeres, 2016).

Eventually the YORP induced spin-up leads to asteroid break up and creation of a binary asteroid system (Walsh et al., 2008, 2012). There are a few evolutionary paths an asteroid binary could take after rotational break up (Jacobson and Scheeres, 2011). One is the creation of asteroid pairs. That is, pairs of objects of the same dynamical origins, with similar orbital elements, but not gravitationally bound to each other (Pravec et al., 2010). Another is the slow degeneration of mutual orbit, which eventually leads to a contact binary, like (25143) Itokawa (Demura et al., 2006; Lowry et al., 2014), or asteroid (85990) 1999 JV_6 which is the subject of Chapter 5. Recently the distributions of different flavours of asteroid binaries, including contact binaries and fast-rotating binaries, in the NEA population was shown to be consistent with the YORP-induced fission theory (Jacobson et al., 2016).

Finally YORP might be coupled with Yarkovsky effect and influence orbital evolution of the small asteroids. As the Yarkovsky effect is sensitive to the rotation period and obliquity, the YORP-induced change in spin-state will affect the semi-major axis drift of the orbit. Excluding YORP from simulations of asteroid migration leads to an overestimation of the NEA influx from main belt. However, including the YORP effect in the model leads to the predicted fluxes being about 5 times lower than the observed (Granvik et al., 2017), showing there is scope for further development of all related theoretical models.

1.4.3 Recent theoretical developments

The principal aim of the initial formulation of the YORP effect was to analyse its possible importance in the spin-state evolution of the small Solar System bodies (Rubincam, 2000). It was stressed that the study treats the problem in a highly simplified way and the drawbacks of such an approach were addressed in later studies. To list a few examples:

- The asteroid surfaces were treated as blackbodies and the YORP torque as coming solely from the thermal radiation of a heated surface. In a more realistic case of a non-zero albedo the YORP torque would have a reflected radiation component as well as the thermal. This issue was addressed by newer models (e.g. Breiter et al., 2007; Rozitis and Green, 2012) .

- All computation was done for spherical-harmonics approximations of asteroid shape, an approach which already indicates the sensitivity of YORP to shape. An in-depth analysis has shown that surface details have major influence on YORP-torque strength and sign (Statler, 2009).

- The densities of asteroids used in simulations are assumed to be homogeneous. With a non-homogeneous density distribution the location of centre of mass as well as moments of inertia would change, affecting the position of rotational axis and the computation of YORP torques. Recently, the detection of YORP spin-up allowed the investigation of the internal structure of asteroid (25143) Itokawa (Lowry et al., 2014). The theoretical predictions of the YORP strength could not be reconciled with observations until an assumption of density inhomogeneity was made regarding the two lobes that comprise the asteroid.

- It was stated that the high temperature difference between the day and night sides of the object with poor surface thermal conductivity is incurring very efficient action of the YORP effect. It was implied that the YORP effect was much stronger for the analysed cases than it would be for objects with higher thermal conductivity or simply faster rotation rates. The influence of thermal conductivity on the YORP torques was investigated by Čapek and Vokrouhlický (2004), see Figure 1.8.

An important branch of the theoretical development of the effect is the investigation of its impact on orbits of binary asteroids, dubbed the binary-YORP or the B-YORP effect (Ćuk and Burns, 2005). The B-YORP effect requires at least one of the binary components to be synchronous (have the same spin and orbital period). The effect was postulated to affect the semi-major axis and eccentricity of the orbit, contributing to possible break-up of a binary into an asteroid pair, or collapse into a contact binary. However, no direct observation of the effect has been made to date (Vokrouhlický et al., 2015a). To explain the discrepancy between theory and observations, it was recently postulated that YORP and B-YORP effects might balance each other, stabilising a doubly synchronous binary system (Golubov and Scheeres, 2016).

Modelling of non-principal axis rotation, so-called 'tumbling', is one of the challenges in YORP modelling. Early attempts brought seemingly conflicting results. Numerical studies suggested that the spin-state could evolve in 'asymptotic states'. The asteroid rotation would be trapped in a tumbling motion with obliquity close to 55° or 125°, and rotational momentum increasing infinitely (Vokrouhlický et al., 2007). In the semi-analytical approach the authors also obtained a stable tumbling state, but with obliquity, spin-rate, and location

of the rotation axis within the body oscillating (Cicalò and Scheeres, 2010). The dispute was resolved by Breiter, Rożek, and Vokrouhlický (2011), who showed that both earlier results can be reproduced by using different order of approximation for the insolation. Additionally, a new type of behaviour was shown, a 'limiting cycle', where the obliquity and location of the spin-axis within the body oscillate, and the rotational momentum increases indefinitely. The result stays in conflict with the observations. The principal-axis rotation observed for most asteroids would require an additional effect working in concert with YORP and the YORP torques alone seem to induce stable tumbling states. The energy dissipation for inelastic ellipsoids was discussed later (Breiter, Rożek, and Vokrouhlický, 2012), and eventually coupled with YORP (Breiter and Murawiecka, 2015). However, the coupling fails to damp the tumbling, but rather a introduces a new stable non-principal axis rotation, albeit with constant period. There is a strong need for further development in this field (Vokrouhlický et al., 2015a).

Thermophysical models of asteroid surfaces and detailed shape models are essential for correct prediction of the YORP strength. The state-of-the-art approach takes into account small-scale surface roughness and self-heating of surface elements in modelling the infra-red data (Rozitis and Green, 2011). The surface roughness can significantly alter the direction in which the thermal radiation is re-emitted from the surface of the body, decreasing the magnitude of the rotational YORP torque (Rozitis and Green, 2012). The global self-heating and self-shadowing produce a vertical offset in the $\dot{\omega}$ as a function of obliquity, yet with opposite signs (Rozitis and Green, 2013). At the length-scales between surface roughness and large-scale concavities there are the stones covering asteroid surfaces. The asymmetric re-radiation from different sides of the stones can produce a small component of the YORP torque tangential to the surface, a so-called T-YORP (Golubov and Krugly, 2012; Golubov et al., 2014). This is why developing robust physical models is essential in calibrating the theoretical predictions of YORP strength.

1.4.4 Direct detections of YORP-induced spin-up on NEAs

The lightcurves obtained from measurements of changes in the brightness are an important tool in the study of small Solar System bodies. As the irregularly shaped object rotates, the illuminated and observed areas change. Therefore, the intensity of light reflected from the object and detected on Earth varies. The differences between the object's brightness at different moments in time can be quantified using photometric techniques. The resulting optical lightcurves provide the means to explore the spin-states, shapes and surface properties of small Solar System bodies. It is in these type of observations that the signature of YORP-induced period change can be found. The optical lightcurves are discussed in detail in Chapter 2 (explaining how they are collected) and Chapter 3 (dealing with how they are used in asteroid shape and spin-state modelling).

The first direct detection of a YORP-induced spin-rate acceleration was reported by

Lowry et al. (2007) and Taylor et al. (2007) for a near-Earth asteroid (54509) YORP (initial designation 2000 PH_5). The small, $\sim$57 m, asteroid is in a near 1:1 mean-motion resonance with Earth, making regular close approaches. The particular orbital configuration made it a convenient target for Earth-based observations. Additionally the asteroid is a fast rotator, with a period around 12 min, which allows observers to take a few full rotational lightcurves in a single night.

The optical data for the YORP-detection purposes was gathered between July 2001 and August 2005. Thanks to a nearly constant aspect of the observations, the lightcurves' amplitudes and shapes remained almost constant. This could be inconvenient for the purpose of reliable shape modelling (see Chapter 3 for details on asteroid shape determination), but allowed the authors to group observations from year-long intervals to form individual sets. Fourier analysis was used on the lightcurves across each set to find a sidereal rotation period, P (Harris et al., 1989). For each set of lightcurves the period was compared with a reference period P_0. A linear decrease of the period was detected between the subsequent years, with a fractional change in period, $(P - P_0)/P_0$, measured, as shown in Figure 1.9a. The object was found spinning up by -1.7×10^{-6} of the reference rotation period per year (see Figure 1.9a). Traditionally the YORP torque is presented as inducing the change in the rotation rate rather than period, and for this object it was measured to be $(2.0 \pm 0.2) \times 10^{-4}\,^\circ/\,\mathrm{d}^2$ or $(3.49 \pm 0.35) \times 10^{-6}\,\mathrm{rad}/\mathrm{d}^2$.

Close encounters with Earth might enable rotation period changes by gravitational torques. A dynamical simulation was performed that ruled out this possibility. The interaction with Earth's gravitational field was also deemed too irregular to cause a systematic decrease in period. Detailed analysis using a radar-derived shape model confirmed that YORP effect was the most likely cause to the period change (Taylor et al., 2007).

The measurement of YORP-induced spin-up was confirmed by phase-offset measurement performed using the radar shape model (Taylor et al., 2007). For each observed data set a synthetic lightcurve was generated. The lightcurves were then fitted to the observed data points with a constant period. To obtain a fit of the model lightcurve to the data, an additional phase shift was required, as illustrated in Figure 1.9b. The quadratic trend observed in the phase shifts required for the lightcurves over four years correspond to the linear decrease in period reported by Lowry et al. (2007).

The first example of a YORP-affected object to be found was also deemed to be a very evolved system. The rotational axis orientation, with a high obliquity, close to one of the stable YORP states ($\sim 180^\circ$) led to that conclusion. Dynamical simulations had shown that the asteroid could reach a rotational period as low as 20 s before braking up. Such a rapid spin rate is possible thanks to the, most likely, monolithic nature of the body.

The YORP-induced spin-up was confirmed for only four more objects to date: (1862) Apollo (Kaasalainen et al., 2007), (1620) Geographos (Ďurech et al., 2008), (3103) Eger (Ďurech et al., 2012), and most recently on (25143) Itokawa (Lowry et al., 2014). The de-

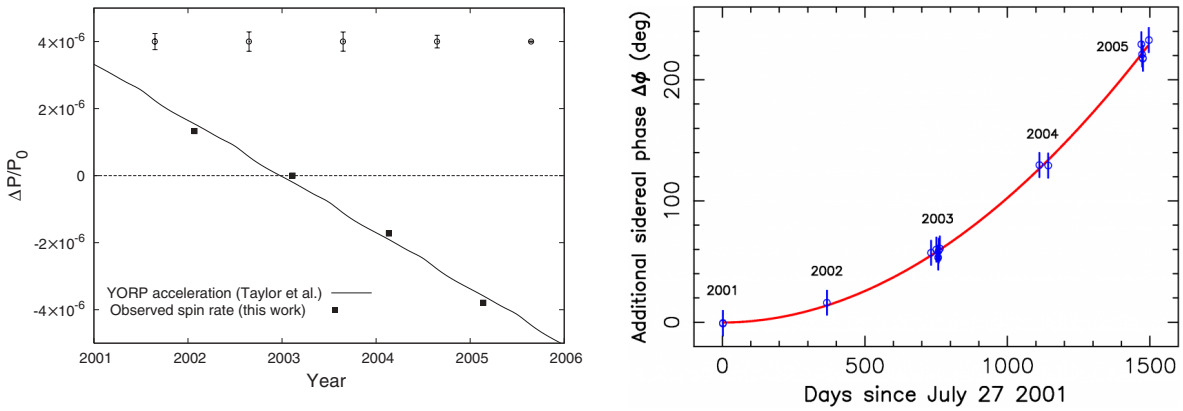

(a) Period change measurements.

(b) Phase offset measurements.

Figure 1.9: The two plots show the two ways the spin-rate change due to YORP effect can be measured. The left panel (a) is copied from Lowry et al. (2007, Figure 2), and represents direct measurements of observed change in sidereal period. The period change is dimensionless, defined as $\Delta P/P_0 \equiv (P - P_0)/P_0$. The lightcurve observations are gathered into year-long bins, with the year observations were taken marked on horizontal axis. The vertical axis shows period change relative to nominal period measured in 2002-2003 observations' bin. The filled square symbols marked measured period change (see Table 1 in Lowry et al., 2007, for details), while the empty circles show effect of the Earth's gravitational pull on the spin-period during close encounters. The points are shifted arbitrarily for clarity, but those changes are negligible compared to the YORP-induced spin-up. The horizontal dashed line corresponds to a constant period, while the black line in the numerical prediction of the YORP strength. The change of rotation period can be also measured as a quadratic trend in phase offsets, as shown in the right panel (b), copied from Vokrouhlicky and Bottke (2012, Figure 7), reproducing Taylor et al. (2007, Figure 2). The measured additional shift required to phase the lightcurve model with observations (in degrees) is on the vertical axis. The days elapsed since first lightcurve was acquired are plotted on the horizontal axis. The open circles mark the measured rotational phase offset and each cluster of observations is marked with the year data was gathered (compare to panel a). The red solid line is the quadratic trend fitted to the observed points, corresponding to the linear change in rotation rate.

tails of spin-states and sizes of the asteroids for which those detections were made, along with some more spurious cases are given in Table 1.2. The notable feature is that all of those reported values are YORP-induced spin-ups. Given the abundance of indirect evidence of YORP-induced evolution of the asteroid spin-states, there should be more objects for which the effect would be detectable, including the slow-down scenarios predicted by the theory. To improve agreement between the models and observations, more direct detections are needed. The following two chapters detail the observing methods (Chapter 2) analysis tools (Chapter 3) that were utilised and developed for the purpose of search for new YORP detections. Two individual NEA targets are then discussed, the asteroids (1917) Cuyo (Chapter 4) and (85990) 1999 JV_6 (Chapter 5). The detailed spin-state analysis did not yield a YORP detection from either target. However, the detected limits to the YORP strength for both objects are consistent with the predictions from ATPM modelling performed by my collaborator, B. Rozitis.

Asteroid	Period [h]	$d\omega/dt$ [rad/d^2]	λ [°]	β [°]	d [km]	Reference
(54509) YORP – 2000 PH_5	0.202 833 33 ± 0.000 000 01	3.49 ± 0.35 × 10^{-6}				Lowry et al. (2007)
			180 ± 10	−85 ± 10	0.113	Taylor et al. (2007)
(1862) Apollo	3.065 447 6 ± 0.000 003 0	5.3 ± 1.3 × 10^{-8}	50 ± 7	−71 ± 7	1.4	Kaasalainen et al. (2007)
(1620) Geographos	5.223 336 ± 0.000 002	1.15 ± 0.15 × 10^{-8}	58 ± 6	−49 ± 7	2.56	Ďurech et al. (2008)
(3103) Eger	5.710 156 ± 0.000 007	1.4 ± 0.6 × 10^{-8}	226 ± 15	−70 ± 4	∼ 1.5	Ďurech et al. (2012)
(25143) Itokawa	12.132 371 ± 0.000 006	3.54 ± 0.38 × 10^{-8}	128.5 ± 6.9	−89.7 ± 6.9	0.33	Lowry et al. (2014)
(1865) Cerberus•	6.803	< 8 × 10^{-9}				Ďurech et al. (2012)
(2100) Ra-Shalom•		< 3 × 10^{-8}				Ďurech et al. (2012)
(161989) Cacus⋆	3.7538	1.9 ± 0.3 × 10^{-8}			1.0 ± 0.2	Ďurech et al. (2016)
(101955) Bennu⋆	4.297 ± 0.002		−88 ± 4	45 ± 4	0.49 ± 0.02	Nolan et al. (2013)
	4.296 045 ± 0.000 002	4.0 × 10^{-8}				Nolan et al. (2016)

Table 1.2: Summary of the YORP-induced period change detections before 30th August 2017. The 6th column contains the diameter of a sphere with equivalent volume to the asteroid, as a rough size estimate, however most detections are made on quite elongated objects. The • symbol denotes the yet-unconfirmed detections with only the upper limit of YORP determined. The ⋆ symbol denotes results presented in conference abstracts, but yet to be confirmed.

Chapter 2

Observations of near-Earth asteroids

Understanding the physical evolution of small Solar System bodies requires knowing their physical state. Putting that state in context of general population properties helps to improve models of physical processes such as YORP-induced spin-state evolution, and Yarkovsky-driven orbital dynamics. Developing shapes and spin-states of small bodies are the focus of this work. This chapter is dedicated to the data sources utilised in this work. Section 2.1 talks about acquiring the visual lightcurve observations that were the primary data source used in this work (see Chapters 4 to 6), while Section 2.2 regards the radar observations (used in Chapter 5).

2.1 Lightcurve observations

2.1.1 Overview of asteroid lightcurve observations

The most reliable source of information about the shape of a body would be of course from direct imaging, but it is rare to have spatially-resolved images of an asteroid available. Even considering the biggest observatories and recent advances of adaptive optics, it is estimated that about 200 asteroids are currently resolvable and only up to 7000 largest objects will be possible to target after the European Extremely Large Telescope (40 m diameter) and the Thirty Meter Telescope (30 m) are finished (Merline et al., 2013). The space missions provide very high resolution imaging albeit for a very small sample of bodies. The in-situ observations with spacecraft flybys and orbiters had investigated only 12 asteroids to date and among those only three are NEA, (433) Eros, (25143) Itokawa, and (4179) Toutatis (Sears, 2015).

Currently, there are two sample return missions en route to NEAs. Japanese JAXA mission Hayabusa-2 will arrive at its target (162173) Ryugu in 2018, and come back to Earth in 2020. The mission is expected to launch a small explosive impactor to create an artificial crater on the asteroid's surface, and later collect samples of the ejecta (Saiki et al., 2017). The NASA mission OSIRIS-REx is planned to arrive at asteroid (101955) Bennu in 2018. It will stay in the vicinity of the target for almost two years and extend a robotic arm to acquire a sample. The mission will arrive back at Earth in 2023 (Lauretta et al., 2017). To put the number of NEA spacecraft visits into perspective, there are nearly 740 000 minor planets known and nearly 17 000 of them classified as near-Earth asteroids (as of October 2017*).

The lightcurves (as mentioned in Section 1.4.4) have the advantage that most of the near-Earth and main-belt asteroids can be reached even with small-aperture telescopes. Photometric monitoring of small bodies is done on a regular basis by various research groups. This thesis utilises results from one such program, the ESO Large Programme (ESO LP, see Section 2.1.2). Lightcurves of small bodies that were used to produce shape models of asteroid, are later available as supplementary material and can be accessed for example through the Database of Asteroid Models from Inversion Techniques (DAMIT) website (Ďurech et al.,

*http://www.minorplanetcenter.net/

2010). Sometimes the lightcurves are only used to determine a rotation periods, and are made available in on-line archives, one of those, the LCDB, accessible via the Minor Planet Centre, contains lightcurves for over 13 000 objects (Warner et al., 2009, as of October 2017). There is thus an abundance of asteroid lightcurves, and the past few decades have seen a dynamic development of the tools used to model them (Magnusson et al., 1989; Kaasalainen et al., 2002; Ďurech et al., 2015). Details of shape and spin-state modelling methods applied in this thesis are covered in Chapter 3.

2.1.2 The ESO Large Programme

The observations of NEAs (1917) Cuyo and (85990) 1999 JV_6 were carried out as a part of the ESO Large Programme (ESO LP), and supporting campaign, led by S. Lowry. The ESO LP is aimed at providing ground truth for the models of YORP-driven spin-state evolution, by combining new spin-rate-change detections with precise physical models. The means to achieve those goals were shape and spin-state modelling, and physical characterisation of near-Earth asteroids using optical and infra-red observations. Precise long-term lightcurve monitoring with optical facilities enables detections of YORP-induced period changes. The lightcurves are also used for shape modelling when a radar or spacecraft model is not available. The infra-red observations are complementary to the lightcurve studies, and allow to better constrain the non-gravitational forces predictions for any target by deriving thermophysical parameters such as surface roughness or thermal inertia. A selection of over 40 low ΔV asteroids has been investigated between April 2010 and present. The objects selected for the programme fulfil three conditions that make them likely candidates for new YORP detections: have short rotation periods, sizes sufficiently small, and orbits close to the Sun. The quick rotations also make them convenient photometry targets. A full rotational phase coverage can usually be obtained during a few consecutive days of observations. Orbital geometries of those objects on the other hand allows for revisiting each target a few times over the years.

Facilities used by ESO LP

The ESO LP was designed to make use of the facilities of the European Southern Observatory. ESO is an international organisation that brings together 15 European countries, including the United Kingdom, and Chile, which is the host of the ESO's observatories. The organisation was founded in 1962 with the aim to create innovative facilities to conduct the highest quality ground-based astronomical observations*. Ever since its founding the astronomers have used the ESO facilities for ground-breaking research, including monitoring of stellar motion around Galactic centre to provide evidence of a central black hole (Schödel et al., 2002), directly imaging an extrasolar planet for the first time (Chauvin et al., 2004), or first detection of a kilo-nova, an event observed at multiple wavelengths of the electromagnetic

*https://www.eso.org/

Figure 2.1: A view of La Silla observatory in Chile from the base of the ESO 3.6m. The angular dome on the right is the home of NTT telescope, one of the main facilities of the ESO LP discussed in subsection 2.1.2. The silvery dome near the centre houses the ESO 2.2m telescope. Picture taken by A. Rożek during her observations at NTT in February 2013.

spectrum that followed a neutron star merger producing a gravitational wave (Smartt et al., 2017). The Observatory currently operates on three sites in the dessert mountains of Chile, selected for their low light pollution and excellent astronomical climate with low humidity, rare cloud cover and stable seeing (see Figure 2.6). The telescopes used in the ESO LP are the New Technology Telescope located in La Silla, and the Very Large Telescope in Paranal.

ESO New Technology Telescope (NTT) – observatory code 809

The ESO LP observing campaign was carried out mainly at visible wavelengths with the 3.58 m New Technology Telescope (NTT). The telescope was built, as the name suggests, to prove new ideas in telescope design. The telescope is the first one in the world to be equipped with active optics (Tarenghi and Wilson, 1989). The monolithic primary mirror is thin enough to be flexible. It is supported by a series of small motors controlled by a computer to maintain the optimal shape of the reflecting surface regardless of the mount position. The enclosure of the NTT was an innovative design in itself (Murtagh, 1988, see Figure 2.1). The dome is angular which is a more compact design than the traditional semi-spherical shape, with windscreens allowing to reduce the adverse effects of high wind speeds, and a series of flaps providing ventilation and temperature control that reduce the air turbulence.

The NTT is a 3.58 m Ritchey-Chrétien (R-C) telescope with an altitude-azimuth mount. The telescope has operated a suite of instruments since its first light in 1989, and is currently equipped with two, installed in the Nasmyth foci. One of them is the ESO Faint Object Spectrograph and Camera (version 2) (EFOSC), used by the ESO LP. The instrument is fitted with a filter wheel, a grism wheel, and a slit wheel. It can be used in spectroscopy and imaging modes, and different variants of both. In the ESO LP both the imaging, mostly in the Bessel V and R filters, and long slit spectroscopy mode were used. The CCD detector of the instrument has 2048×2048 pixels and a field of view of $4.1' \times 4.1'$.

The 72 nights of observing time awarded at the NTT were divided into three-night segments, which are conventionally referred to as 'observing runs'. Over the four years of ESO LP a total of 24 observing runs were conducted at the NTT to monitor the selected targets photometrically and spectroscopically. Two observing runs at NTT, in February 2013 and April 2014, had been performed by the author of this thesis.

ESO Very Large Telescope (VLT) – observatory code 309

Observations from the NTT were supplemented with infra-red observations from the VLT Imager and Spectrometer for mid-InfraRed (VISIR) instrument at the VLT in ESO's Paranal observatory in Chile. The VLT is actually a set of four 8.2 m R-C Unit Telescopes (UTs), as shown in Figure 2.2a. The telescopes are equipped with monolithic active mirrors, and situated in angular domes that are an improvement on the NTT design (the dome is shown in Figure 2.2b). The four telescopes are accompanied by four smaller, 1.8 m, mobile Auxiliary Telescopes. A maximum of three Unit Telescopes and three Auxiliary Telescopes can be combined in an advanced optical interferometer.

Each Unit Telescope was built to accommodate up to three instruments, two in the Nasmyth foci, and one in the Cassegrain focus. The ESO LP made use one of the Units, UT3, Melipal. The Programme primarily used the VISIR instrument is mounted in Cassegrain focus of Melipal for infra-red photometry. For each object observed with VISIR a series of images was taken, using a wide range of narrow-band filters, to obtain information about thermal properties of asteroid surfaces. One of the ESO LP targets was also observed optically with VIMOS, another instrument on UT3.

The observations with VISIR were initially planned to parallel the optical campaign with the NTT. However, the collection of infra-red data was interrupted when the instrument was temporarily decommissioned during the original ESO LP. Recently, more time has been awarded at the VLT to compensate for the earlier disruption (PI: S. Lowry, A. Rożek is a Co-I). Therefore, the author of this work performed one of the observing runs with VISIR, in March 2017.

(a) Paranal mountain

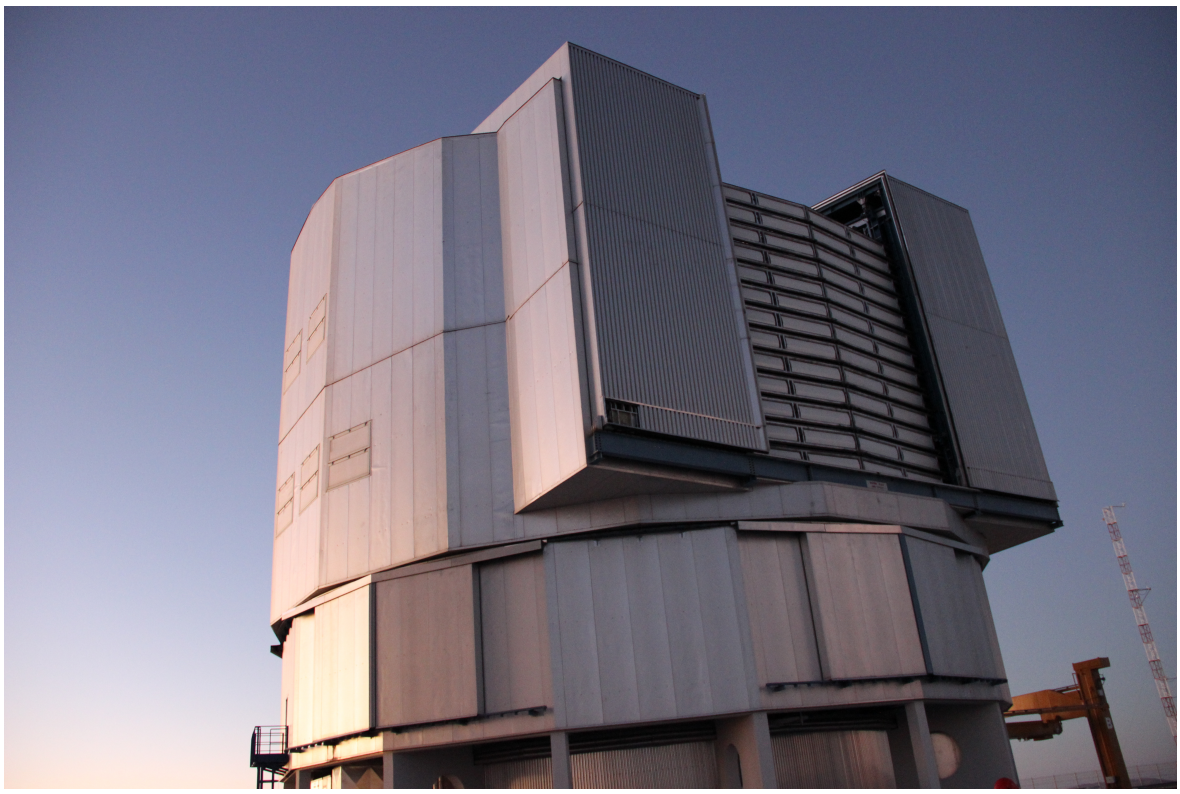

(b) VLT Unit Telescope 3 - Melipal

Figure 2.2: The upper panel (a) shows the view of Paranal telescope platform as seen from the astronomers' hotel Residencia. The positions of telescope control room and VLT Unit Telescope 3, Melipal, are marked. The Very Large Telescope is a set of four identical large Unit Telescopes, and four smaller Auxiliary Telescopes. All telescopes can be connected in an optical interferometer. The lower panel (b) shows Melipal dome opening up for an observing night. The modular windscreen is visible from under the dome slit. The flaps on the side of the dome, visible to the left, and the gates below the movable part of the dome can also be opened for improved air circulation. Pictures taken by A. Rożek during her observations at VLT in March 2017.

Facilities used by supporting campaigns

The photometric monitoring was conducted at other ground-based facilities in concert with the ESO LP observations allowing to broaden the lightcurve coverage for some objects. The term 'YORP programme' can be used when referring to the extended campaign. Presented below are the main instruments that provided observations included in this thesis work. A complete list of facilities and instruments used, with a rough estimate of the total length of

time utilised at each facility to obtain data, can be found in Table 2.1.

Table Mountain Observatory (TMO) – observatory code 673

A primary source for the lightcurves of (1917) Cuyo, besides NTT, has been the Jet Propulsion Laboratory (JPL)'s 0.6 m telescope at the Table Mountain Observatory in the Angeles National Forest, Wrightwood, USA. The telescope is a R-C telescope with instruments mounted in the Cassegrain focus. The telescope is equipped with a with a 1k $\times$ 1k CCD detector that has a 8.9° $\times$ 8.9° field of view.

Palomar Observatory, Hale Telescope – observatory code 675

Another important telescope is the 5.1 m Hale Telescope at the Palomar Observatory in the Cleveland National Forest on Palomar Mountain in the USA. The telescope has a Cassegrain optical design on an equatorial mount and is operated by the California Institute of Technology (Caltech). The YORP programme lightcurves had been acquired using the Large Format Camera (LFC) set in the prime focus of the telescope. The detector is a mosaic of six CCDs, but only one of them was used in the observations presented. The single CCD has the dimensions of 2048 $\times$ 4096 pixels and a field of view $6' \times 12.3'$ and the lightcurve were usually collected using the Bessel R filter.

Isaac Newton Telescope (INT) – observatory code 950

The biggest contribution to the (85990) 1999 JV_6 optical observing campaign comes from another Cassegrain telescope set on an equatorial mount, the 2.5 m Isaac Newton Telescope (INT) at Roque de Los Muchachos Observatory on La Palma, Spain. The telescope is part of the Isaac Newton Group of telescopes (ING) operated jointly by three institutions, British Science and Technology Facilities Council, Dutch Nederlanse Organisatie voor Wetenschappelijk Onderzoek, and Spanish Instituto de Astrofísica de Canarias. The primary focus of the telescope hosts the Wide Field Camera (WFC), an array of four 2048 $\times$ 4100 CCDs, giving a total field of view $34' \times 34'$.

ESO 2.2 m – observatory code 809

At the La Silla observatory is a 2.2 m telescope operated by the German Max-Planck Institute, that until October 2013 was run by ESO on loan from the MPI. The telescope is a R-C on an equatorial mount. The Cassegrain focus of the telescope is equipped with the Wide Field Image (WFI) camera, a mosaic of eight 2046 $\times$ 4128 pixel CCDs, covering a total field of view of $34' \times 33'$.

The ESO LP officially finished in April 2014 with the final run at the NTT performed

Telescope	Observatory	Code	Institution	Country	Diameter [m]	Instrument	Type	Total [h]
New Technology Telescope	La Silla	809	European Southern Observatory	Chile	3.58	EFOSC	optical	430
Very Large Telescope	Paranal	309	European Southern Observatory	Chile	8.2	VISIR	infra-red	42
Ritchey-Chrétien	Table Mountain	673	Jet Propulsion Laboratory	USA	0.6	1k × 1k CCD	optical	133
Hale	Palomar	675	Caltech	USA	5	LFC	optical	108
Liverpool Telescope	La Palma	950	Liverpool John Moores University	Spain	2	CCD	optical	40
Isaac Newton Telescope	La Palma	950	Isaac Newton Group of telescopes	Spain	2.5	WFC	optical	27
ESO 2.2m	La Silla	809	Max-Planck Institute	Chile	2.2	WFI	optical	7
Faulkes Telescope South	Siding Spring	E10	LCOGTN	Australia	2	CCD	optical	4.5
Very Large Telescope	Paranal	309	European Southern Observatory	Chile	8.2	VIMOS	optical	4
Danish 1.5m	La Silla	809	European Southern Observatory	Chile	1.54	DFOSC	optical	1.25
William E. Gordon	Arecibo	251	NAIC	Puerto Rico	305	Planetary Radar	radar	20
Deep Space Station 14	Goldstone	252	JPL	USA	70	GSSR	radar	12
Robert C. Byrd	Green Bank	256	Green Bank Observatory	USA	100	receiver	radar	6

Table 2.1: Overview of the observatories participating in the ESO Large Programme (ESO LP) and supporting campaigns. The table lists the ESO LP facilities (first section, orange background), supporting optical facilities (second section, green), and radio facilities (third section, blue). *Telescope* is the name or a conventional designation used for the facility. *Observatory* is the location of the telescope. *Code* is the official MPC observatory designation[a]. *Institution* is the organisation responsible for facility operations. *Country* is where the instrument is placed. *Diameter* gives the size of the primary mirror of the telescope in meters. *Type* indicates at what wavelengths were the observations conducted. *Total* gives a lower estimate of total length of data set gathered in hours. **Acronyms used in the table:** ESO - European Southern Observatory, LCOGTN - Las Cumbres Observatory Global Telescope Network, NAIC - National Astronomy and Ionosphere Center, EFOSC - ESO Faint Object Spectrograph and Camera (version 2), VISIR - VLT Imager and Spectrometer for mid-InfraRed, CCD - charge-coupled device, LFC - Large Format Camera, WFC - Wide Field Camera, WFI - Wide Field Image, VIMOS - VIsible MultiObject Spectrograph, DFOSC - Danish Faint Object Spectrograph and Camera, GSSR - Goldstone Solar System Radar.

[a] `http://www.minorplanetcenter.net/iau/lists/ObsCodesF.html`

by author of this thesis. However, observations are still being conducted to get follow-up data sets for selected objects of interest. Recently, a notable addition has been made to the campaign by using the planetary radars at Arecibo and Goldstone observatories, as is discussed in detail in Section 5.2.2.

2.1.3 Image acquisition of NEAs

To measure the light variation of small bodies investigated in this work, series of images were taken using telescopes equipped with instruments that record optical light on charge-coupled device (CCD) chips. In short, a CCD is an array of capacitors (pixels) accumulating free electrons generated by photons striking a layer of silicon. The charge accumulated in each pixel is then transferred to a read-out region and translated into analog-to-digital units (ADUs). The number of ADUs (also called counts) is proportional to the amount of charge accumulated, which in turn depends linearly on the intensity of incident light. Therefore, the intensity of light coming from the source can be easily quantified.

There are many different architectures of CCDs applied in modern astronomical instruments (for the list of facilities used by ESO LP and in this thesis see Table 2.1) but regardless of a specific design all of them share similar characteristics and problems. Therefore, a typical observing night at an optical facility starts with the instrument cool-down and calibration. Due to electron noise at high temperatures the CCD cameras need to be cooled a few tens of degrees below the ambient temperature. However, the detector still has a non-zero initial charge, so-called bias level, that needs to be later removed from the science frames. To measure that initial charge, the CCD is read out a few times. The sensitivity of the detector is uneven across the chip, and the design and faults of optical system can cause the sensor to be unevenly illuminated. Those imperfections are dealt with by obtaining so-called flat-field calibration at an evenly illuminated screen, or twilight sky.

The images of NEAs are taken with the telescope position adjusted throughout the observation to accommodate the asteroids' motion across the sky. The exposure time of a single frame is usually set to be below 5 % of the full rotation to resolve the lightcurve features. Using long exposure times can bring forward some more imperfections of the CCD detector used. Some devices will accumulate random electron noise, that can be corrected using dark frames. The dark frames are taken with closed shutter, with the same exposure times as science images, to statistically accumulate the same noise. For some CCD architectures the thickness of optical elements can be close to the wavelength of the collected light, leading to occurrence of interference patterns in the images. The so-called fringe effect is additive, accumulating with exposure time and magnified by bright sky emissions. It is especially visible in the Bessel-R filter of the EFOSC camera used in this work (see example in Figure 2.4). The R filter is still used due to high sensitivity of the CCD in the red part of the spectrum. However, the Bessel-V filter is free from the fringe pattern, so it was applied as well.

Another factor to take into account is the asteroids' apparent motion relative to the stellar

background. In case an asteroid is bright enough the exposure time can be limited, so that the target would move no further than by the value of seeing across the sky. Then the telescope can be used with sidereal tracking, only compensating for the Earth's rotation. In some cases sidereal tracking is discouraged, when a longer exposure is required because the asteroid is too faint and moves quickly, which is not an unlikely scenario for a NEA. Then the telescope follows the asteroid's motion to keep it in one place on the detector during a single exposure and the stars in frame get slightly elongated. However, to avoid the asteroid always falling on the same area of CCD throughout a night, some observatories offer the possibility to dither the telescope position between the exposures. This is sometimes needed to correct for systematic errors that might be still present even in the pre-processed images. Finally, the observer must consider that motion of the object over a few hours of observations can be larger than the size of the detector used. To ensure the correct tracking, the asteroid positions are frequently updated throughout the observation series, using ephemeris generated using the Horizons ephemeris system. The observer has to plan and monitor the target movement to maintain the asteroid within the CCD frame, and ensure continuity of background stars during observations. That means planning for overlaps between the sets of stars visible in the image at different time. Finder charts are usually prepared ahead of an observing night to ensure identification of the target.

2.1.4 Pre-processing of CCD imaging data

The images are not ready for measurements immediately after recording. As mentioned above, the device accumulates electric noise, the sizes of some sensor elements are of the same scale as the wavelengths of the light detected causing internal interference, and the sensitivity varies across the detector. On top of that, the pixels degrade with time creating regions where the information can be unreliable, and the Sun constantly emits high-energy radiation which penetrates through the instrument causing bright spots to appear on the images.

Fortunately, all of those problems can be dealt with using well known image reduction methods. The process has been described and detailed in numerous sources (French and Binzel, 1989; Berry and Burnell, 2005), so the rest of this section will be just brief overview of the procedure outlined on a schematic in the Figure 2.3. The `IRAF` system was used for the purpose of data reduction and extraction of asteroid instrumental magnitudes (Tody, 1986, 1993; National Optical Astronomy Observatories, 1999).

Step 0 - Science frames assessment

Before the actual data reduction begins all images are examined for some obvious problems. For example, the presence and position of the observed object in the frames has to be confirmed. To locate the asteroid the imaging frames are compared with finder charts for the time the observations were performed (see illustration in Figure 2.5). If the imaging was

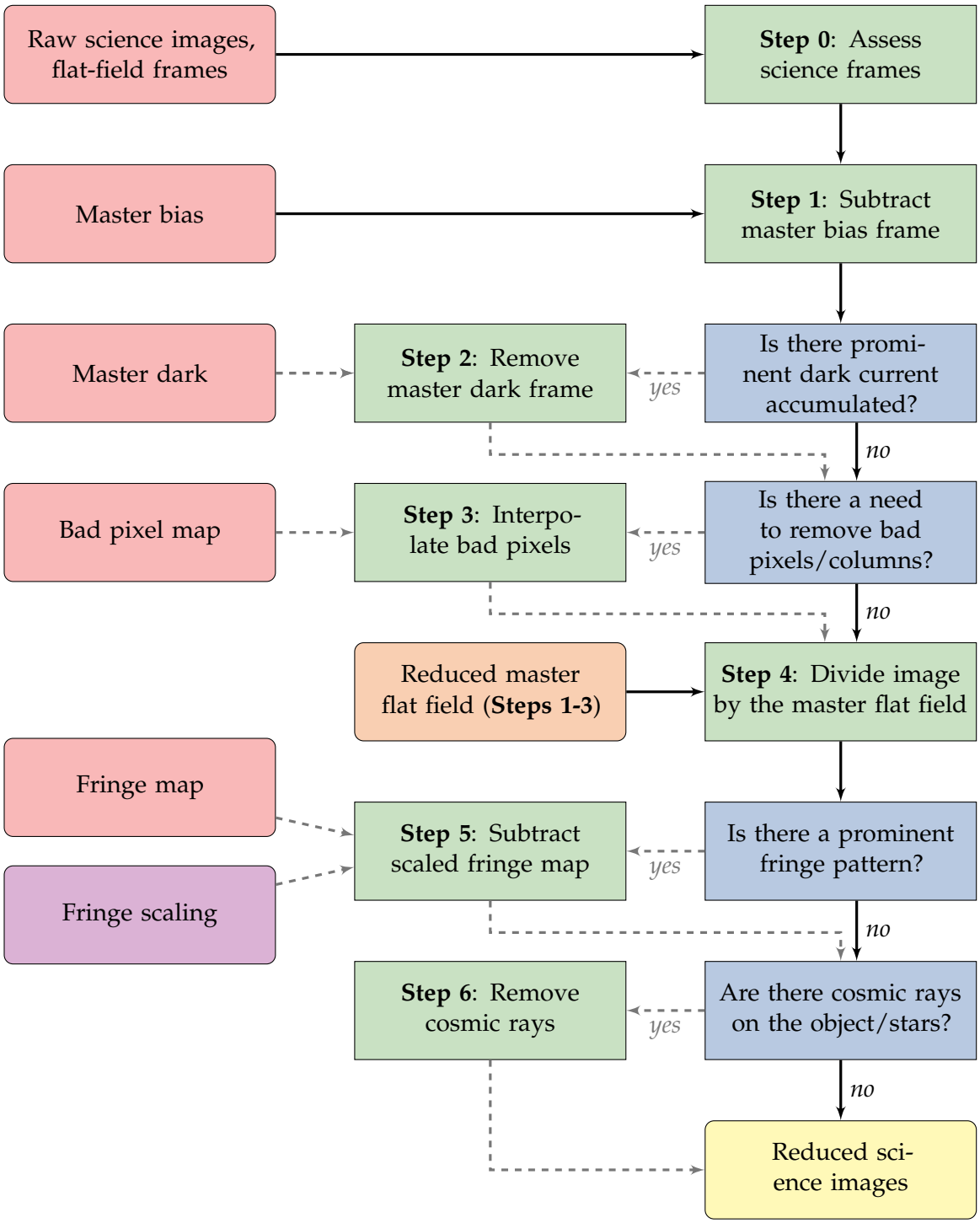

Figure 2.3: Schematic of CCD-image data reduction. Red fields mark input data, purple field marks user-defined parameters, orange field is output of one part of the process that is being used as input to the other, and yellow field contains the output. Blue fields are points at which decisions are made about how the analysis proceeds, green fields mark steps of the data reduction. The optional input and steps of the analysis are connected to the main flow with dashed lines. The process is described in Section 2.1.4.

done with an array of CCDs, the chip that contains the object is identified and the rest of the mosaic is not used in further processing. The images in which the asteroid image is clearly on top of a stellar image or overexposed frames, can be discarded at this step as well. An additional step might be trimming the science and calibration frames to crop out regions with bad pixels, that contain no useful information.

Step 1 - Bias removal

First step is removing the detector initial charge from frames. The calibration frames used for that purpose are taken with 0 s exposure time. Depending on the telescope, those are usually taken in a series at the beginning and end of the night, but sometimes also throughout the night, to monitor the detector performance. Those *bias* images are checked for any irregularities, as they should have small pixel-to-pixel variation and have a low median pixel value relative to the maximum value possible. The images are combined into a *master bias*, by taking a median value of each pixel after rejecting the most extreme values. The median value is preferred to mean as being less likely to be affected by outliers. The *master bias* frame is then subtracted from all science and calibration frames.

Step 2 - Dark current removal

Some CCD detectors accumulate charge during exposure solely due to thermal radiation of the instrument itself. This is called the dark current and needs to be accounted for. For that purpose a series of calibration images, *dark frames*, are taken with the same exposure times as the science images, but with the camera shutter closed. The *dark frames* are then combined by averaging the pixel values into a *master dark* which is subtracted from the science images. However, most large observatories, like the ESO NTT, operate effective cooling systems of their instruments. At a sufficiently low temperature, specific to each camera, the acquisition of the dark current is slow enough to be negligible, and the use of *dark frames* is no longer required.

Step 3 - Bad pixel correction

The CCD detectors degrade with time and bad pixels (either dark or saturated) start appearing in the images taken with an aged CCD. Those can be removed by using maps of bad pixels provided by an observatory. Alternatively the areas of the image where the correction is to take place can be selected manually during data reduction. The values of bad pixels in the original image are substituted by interpolating values from surrounding areas. This procedure should be performed with care and any objects or field stars measured known to initially lay on bad pixels should be treated with adequate caution. Sometimes the procedure is omitted altogether, for example when there are no obvious faults to the image.

Step 4 - Flat-field correction

One significant source of error on a CCD comes from the imperfections of the chip and the optical system that are being used. Tiny grains of dust on the optical elements, uneven sensitivity of the chip and irregular illumination of the recording area can all be dealt with using a process called flat-field correction. The calibration frames used for that purpose are dubbed *flat fields*, as they are known to be uniformly illuminated. They are usually taken at dawn or dusk, when the sky is still bright, at an area of sky with low star count. Alternatively, an evenly illuminated screen can be used. The sensor, as well as the optical system, will behave slightly differently depending on the wavelength of the light detected. This is why a different *flat field* is required to correct images taken in each filter. The exposure times of *flat fields* often vary, hence they are scaled before taking out the median and creating the *master flat*. The scaling factor depends on the average number counts, measured in the same region of each *flat field* frame. The science exposures are then divided by the *master-flat* frame scaled to the image's average background value, measured in a star-less area of the image.

Step 5 - Fringe correction (for R images)

De-fringing of the images is the next level of field correction. The distinct fringe pattern can appear in the background of images taken in the red part of the spectrum, especially when there is a high level of sky emission or the exposure time is long. The fringing is a product of light interference on the layers of the CCD chip, creating patterns similar in their nature to Newton's rings (Gullixson, 1992), with alternating lighter and dimmer areas. In this thesis, it was necessary to apply this kind of correction to the images from NTT's EFOSC taken in Bessel R filter, as shown in Figure 2.4. The fringe subtraction procedure described here is similar to the method offered by EFOSC instrument team (Snodgrass and Carry, 2013). However, the automatic scripts available through the instrument website proved to be ineffective in finding correct fringe scaling factors.

Fringing patterns are generally fixed as they are a function of the CCD detector thickness rather than the observing conditions. A *fringe map* showing the pattern, characteristic to the used filter, might be available from an instrument's website, as is case for EFOSC*. The amplitude of the fringes, however, is a function of the background sky level and varies throughout the night. The scaling factor of the fringe map is measured as a ratio of the amplitude of the fringes in the image and in the map.

For the observations reported here the amplitude of the fringes is probed using six pairs of regions in each image. Each pair corresponds to one bright and one dark region in the fringe map (see Figure 2.4a). The difference between any pair of regions should scale in the same way across the image for a single exposure. The fringe map multiplied by the scaling factor can be removed from the image.

*http://www.eso.org/sci/facilities/lasilla/instruments/efosc/inst/fringing.html

(a) Fringe map **(b)** Raw image **(c)** Correction applied

Figure 2.4: An example of a *fringe map* supplied for the EFOSC at the New Technology Telescope is in the leftmost panel (a). The coloured rectangles show the selection of bright (marked with white) and dark (marked with green) fringe-pattern regions used for scaling the fringe amplitude. Middle panel (b) is the image of (1917) Cuyo taken with a 45 s exposure time in Bessel R filter on 25th February 2012 at 3:23:16 UT (see Chapter 4). The last panel (c) shows the effect of fringe removal. The large bad-pixel region in the bottom-right corner of the image was intentionally left uncorrected, as measurements done on extrapolated values would hold little merit.

The resulting image is then smoothed. Each pixel in the image is assigned an average value from the 5 by 5 pixel region around it. The quality of fringe removal can be then assessed visually, as the smoothing would emphasise any residual fringes. In case fringes are still present, the fringe scaling factor is later manually adjusted, and the process goes through as many iterations as necessary to obtain satisfactory results.

Step 6 - Cosmic rays

Cosmic rays are emissions of high-energy particles causing rapid accumulation of charge in single CCD pixels. They need to be removed if they lay inside the apertures used for measuring instrumental magnitudes of stars and asteroids. If they lay in the region of sky background measurements, they can usually be disregarded The median sky value from few tens of pixels is taken into account in photometry and a cosmic ray normally spreads over just a few pixels. The region containing a cosmic ray is marked and interpolated from surrounding area, in a process similar to removing bad pixels. Though, while the bad pixel correction is automatic and uses predefined bad pixel maps or regions, the positions of cosmic rays are input manually on an image-by-image basis.

2.1.5 Relative photometry of asteroids

After all frames from a given night are reduced for the detector artefacts and cosmic rays, the actual photometric measurements can begin. The procedure described below was used whenever the author was performing the photometry. The `IRAF` data reduction system was

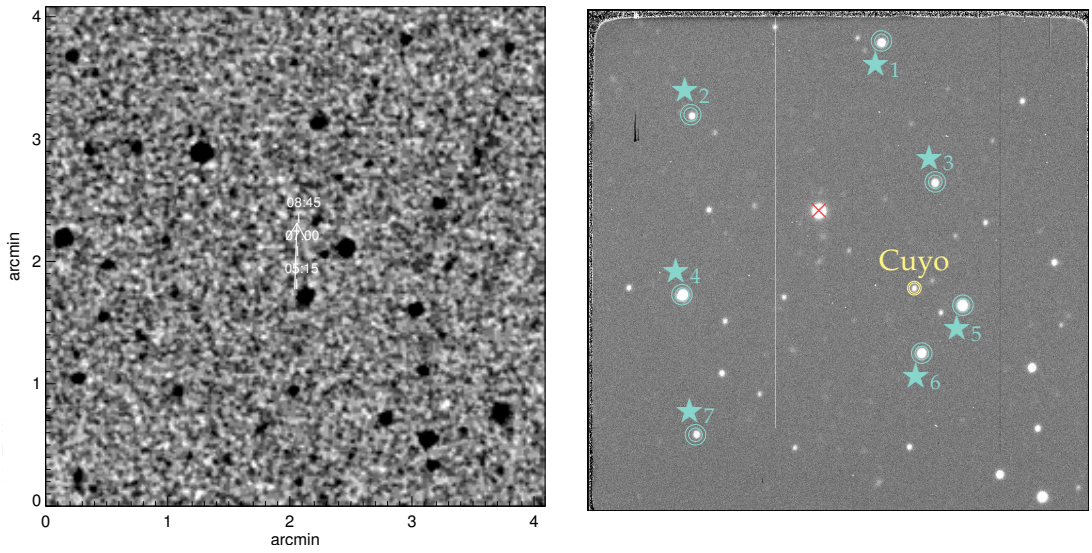

(a) Finder chart

(b) Science frame

Figure 2.5: Identification of the target and background stars. The right panel (a) is the finder chart prepared for observations of (1917) Cuyo at the NTT on the night of $4^{th}/5^{th}$ February 2013. The image has the angular size of the EFOSC chip. The asteroid positions throughout the time it was observable are marked with a white arrow, labelled with UT times at which the object would be found along the track. The left panel (b) is a reduced science frame of (1917) Cuyo taken on 5^{th} February 2013, at 08:15:06 UT with the NTT (see Chapter 4). The FWHM was measured to be 7 pixels. The asteroid is marked with yellow circles with radii of 10.5 and 14 pixels (1.5 and 2 FWHM). The stars are marked with blue circles with radii of 14 and 21 pixels (2 and 3 FWHM). The red-crossed star in the centre of the image was too bright for relative photometry.

used, along with `CL` (`IRAF` interface) (Tody, 1986, 1993). The author used custom `AWK` and `BASH` scripts to speed up and partially automate the process.

The object is at this stage identified on the frames. Once the asteroid is correctly located, it is marked on each image, the centroid is measured by an `IRAF` routine, and its coordinates are recorded. A group of bright stars present in the field is then selected as background comparison stars. Usually, the background stars are hand-picked on the first image and their positions are recorded, and then just one star is used as reference to calculate the shifts in stellar positions between the first and subsequent frames. Those shifts are then applied to the positions of the other background stars and centroids are found for all of them. It sometimes happens that the asteroid is too faint to correctly measure its centroid in the images. In that case, the position of the asteroid relative to the stars is measured on a few images and then it is calculated for the remainder of frames, based on the asteroids proper motion ephemeris.

To ensure accurate measurement of target brightness, a few reference stars are used, preferably brighter than the object itself and distributed around the chip. An example of such selection is shown in Figure 2.5b. The stars selected cannot be too bright, as each CCD has its saturation level, or a maximum ADU value. An object that is sufficiently bright can generate a charge too large for the CCD capacitors, producing a saturated image with a sharp

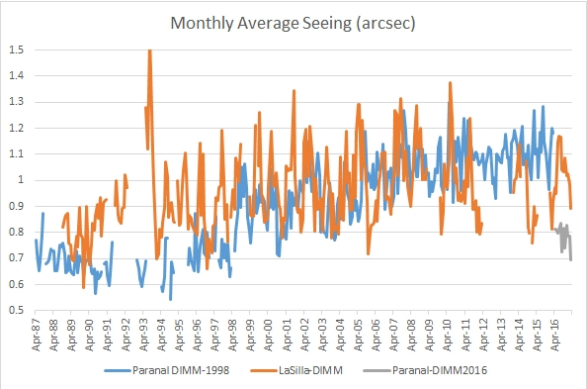

Figure 2.6: The average monthly seeing at two ESO sites in Chile. The orange line corresponds to the La Silla site (home to NTT), while the blue line marks measurements for Paranal (hosting the VLT). The conditions are given for 500 nm observations at zenith, and are measured by Differential IMage Monitors (DIMM) at each site. The image is downloaded from the ESO Astroclimatology site[a].

[a] `http://www.eso.org/gen-fac/pubs/astclim/paranal/seeing/`

cut-off and a flat top rather than a smooth profile. The photometry done on stars that are saturated or close to saturating is highly inaccurate, as this is the regime where CCDs loose their linear response to illumination and some information on their brightnesses is lost, so such stars had to be avoided.

The images of unresolved objects, or point-sources, like stars and asteroids on a CCD frame, usually span across multiple pixels in a way described by the image point-spread function (PSF). A cut across a given well-sampled star on the image reveals the profile of the PSF, similar to a Gaussian curve. One of the main characteristics of the PSF is the width of the profile at the level corresponding to half of its height, called the full width at half maximum (FWHM). When given in arc-seconds, this quantity is considered the angular resolution of the image. It is limited by the diffraction of light by the optical system and, by seeing conditions on the night of observations. The seeing conditions are determined by the fluctuations in the atmosphere and are greatly depend on the climate on site. Astronomical observatory sites are usually set up in dry, high-altitude site that benefit from low atmospheric turbulence, and therefore excellent seeing conditions, like the ESO sites at La Silla and Paranal (their average seeing is illustrated in Figure 2.6). Adaptive optics can reduce the influence of seeing on the quality of the observations, but telescopes equipped with such systems were not used in the photometric study presented here. The objective when collecting images to be used in the aperture photometry applied here is to integrate the amount light collected from a source rather than to obtain a very sharp image.

The pointing of the telescope at a certain patch of the sky is maintained throughout observation by allowing the telescope to follow the apparent motion of the sky resulting from Earth's rotation. This set-up of the telescope motion is called sidereal tracking. However, the asteroids move across the stellar background. Gathering light of the asteroid is a priority here, therefore the telescope can be set to follow its motion, in a set-up called differential tracking. The differential tracking causes the asteroids appear roughly circular in the science frames analysed in this thesis. To gather most of the light emitted by a source a circular aperture around the centroid of the object is set up, that had diameter a few times the FWHM. The FWHM is usually measured on the target. However, in case the object is too faint, and the

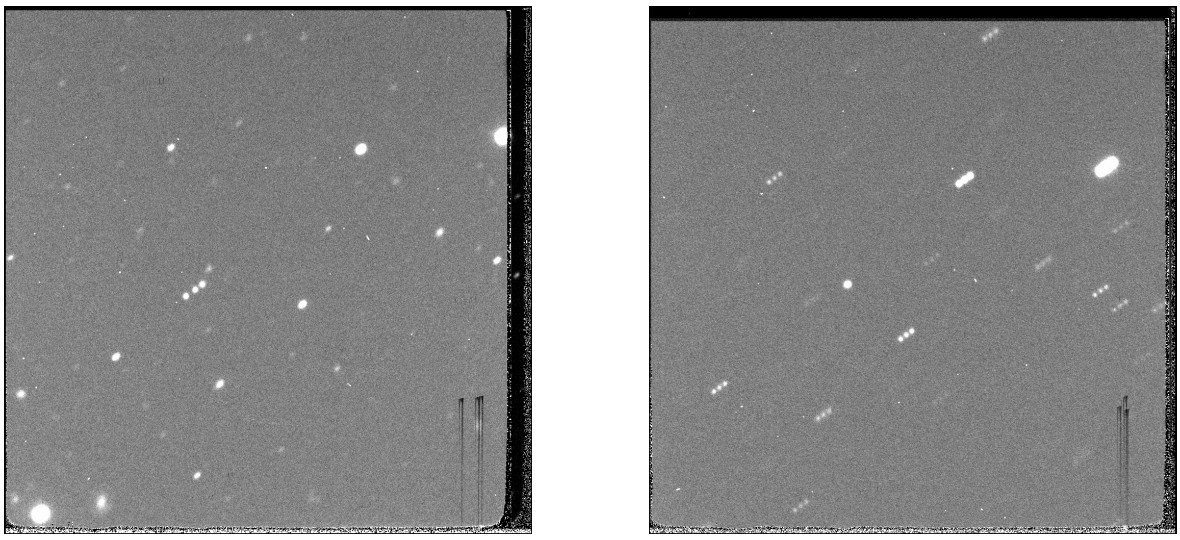

(a) Stacking on stars **(b)** Stacking on asteroid

Figure 2.7: A sum of three images of asteroid (85990) 1999 JV_6 taken on 4th February 2013 with EFOSC instrument at the NTT (see Chapter 5). The images were registered on the background stars (a), so the change of the apparent position of the object can be clearly seen. The images in the second panel (b) were stacked keeping the asteroid position fixed.

stars appear circular, the FWHM can be measured on the field stars and averaged. Separate values were normally used for each science frame. In exceptional cases of very stable seeing conditions a single FWHM can be applied throughout a night. In most cases described in this thesis, an aperture about 1.5-2 times larger than the FWHM that was used for the asteroids (see illustration in Figure 2.5b).

The asteroids move across the sky especially quickly if they are NEAs, which were the original focus of this work, observed most often when they are passing close to Earth. They are also likely to be quite faint objects requiring long exposure times. This means that following the stellar motion can smear the image of the asteroid if the exposure time is too long. The alternative is to set the telescope to follow the asteroid across the sky. This allows the observer to keep all the light of the asteroid in one place on the CCD, but it also means the stars might get trailed. If the stellar trail is not much longer than the seeing, expressed as the maximum imaging resolution in seconds of arc, taking a slightly larger circular aperture diameter than for the object, around 2-3 times the FWHM, is normally sufficient (see illustration in Figure 2.5b). In case of strong trailing, a rectangular aperture is applied, with the star trail centred within it. One side length is set to a multiple of FWHM and the other to a sum of the multiple of FWHM and length of the trail.

On deciding the exposure time the observer has to compromise between having low signal-to-noise ratio for the asteroid or allowing the stars (or object) to trail. It might arise during the analysis that the exposure time was too short to get a reliable lightcurve. In that case, to improve the signal-to-noise ratio on the object, science frames need to be stacked. The images are divided into groups and then summed in two ways, giving a set of two output images for each group. In the first way, each group of frames is registered on the

background stars, shifted, so that the stellar images would fall always in the same location and then summed (see Figure 2.7a). The instrumental magnitudes of stars are calculated using this image. In the second, the frames are registered on the asteroid and then summed (see Figure 2.7b). The photometry of the asteroid is then performed on the resulting image. A sum of exposure times for each frame is adopted as the new exposure time, and the moment halfway between the beginning of the first exposure and the end of the last in the sum is adopted as the new observation time.

The IRAF photometry routines are used to calculate instrumental magnitudes, m_{inst}, of the object and the stellar background, using Equation (2.1) regardless of the aperture shape.

$$m_{\text{inst}} = m_0 - 2.5 \log_{10} \frac{I}{t_{\text{exp}}} \tag{2.1}$$

Where

m_{inst}	the instrumental magnitude of the measured object
m_0	the instrumental 0-point, it is chosen arbitrarily, but kept constant throughout the measurements performed for a given night,
I	the total flux in ADU,
t_{exp}	the exposure time (in seconds).

The flux, I, is expressed in ADUs and is the total number of counts in the aperture excluding sky background. It is calculated by summing all pixel values within the aperture and subtracting the average sky pixel count (calculated on a small region of sky surrounding the aperture).

The instrumental magnitude measurement has its associated error which is computed by the IRAF routine using Equation (2.2)

$$m_{\text{err}} = \frac{1.0857}{I} \sqrt{\frac{I}{g} + A\sigma^2 + \frac{A^2\sigma^2}{n_{\text{sky}}}} \tag{2.2}$$

Where

m_{err}	is the instrumental magnitude error in magnitudes,
g	the camera gain in electrons per ADU,
A	area of the aperture (in pixels^2),
σ	the standard deviation of the pixel value distribution in the aperture,
n_{sky}	the number of sky pixels averaged to get the sky pixel value.

Raw instrumental magnitudes of the asteroid obtained in this manner will not yet be the final data product. The variation in the lightcurve will come not only from the intrinsic changes of brightness of the observed object, but also from fluctuations in seeing due to

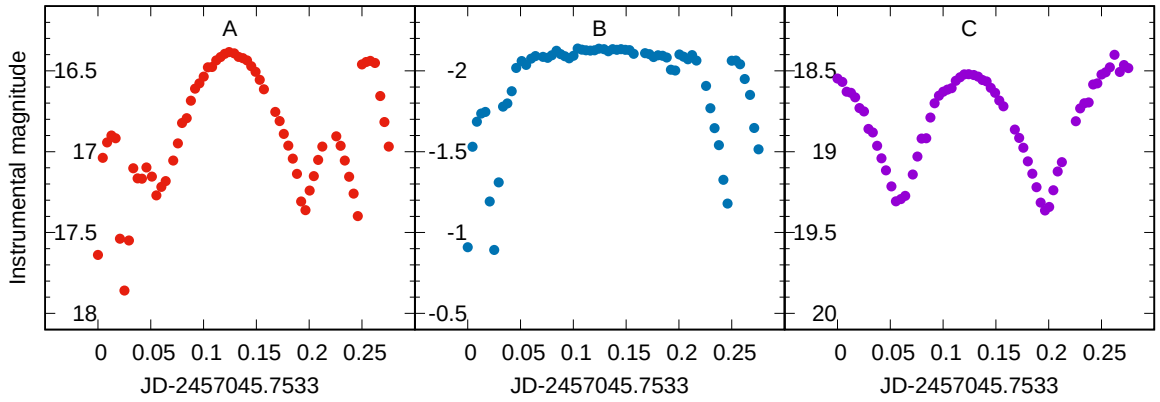

Figure 2.8: The three panels show how a relative lightcurve is constructed. The first panel (A) shows the raw instrumental magnitudes as measured for the asteroid (85990) 1999 JV_6 on 23rd January 2015 at the Table Mountain Observatory (see Chapter 5). The middle panel (B) represents the variations in averaged Δm of all the reference stars over the time, which illustrate changing observing conditions. Finally, the rightmost panel (C) depicts the final relative lightcurve, obtained by subtracting the Δm from the raw instrumental magnitudes. The instrumental magnitudes in each panel are plotted against time (in days) since the first observation of the night. The horizontal scale is the same for all three images. The units on the vertical scale are the same for all three panels.

weather conditions and the fact that the objects are observed at a changing airmass. The background stars present in the imaging frames should in principle have constant brightness throughout the night, so the measurements of changes to their instrumental magnitudes between frames can be used to correct the asteroid brightness for systematic shifts.

The first frame in a night or in a subset of frames is treated as a reference frame. For subsequent images a difference between instrumental magnitude of each background star on the current and reference frames, Δm, is calculated. The Δms for all background stars are then used to calculate a weighted average, with the inverse squares of m_{err} for each star used as weights. For all background stars the Δms should be changing in a similar way. If there are any discrepancies, due to bad columns or cosmic rays, the star in question can be either corrected or temporarily removed from the average Δm. It is also straightforward to identify any intrinsic variability of the star and the variable star can be immediately dropped from the analysis. The Δm rather than m is used, as it allows to easily combine stars of different brightnesses. Using the variation in stellar brightnesses Δm has also the advantage of enabling linking parts of a light curve when the field of view changes and a new set of background stars has to be established.

The averaged Δm of the background stars is then subtracted from the asteroid instrumental magnitude, see Figure 2.8. The corrected magnitudes obtained this way are not calibrated, they just represent the relative changes of asteroid brightness throughout the night. Absolute photometry would require obtaining photometric standards for each observational data set and that condition is not always met for the observations presented. Though, the shape effects are preserved in the relative lightcurves, making them sufficient for the shape

modelling procedures used.

2.2 Radar observations

2.2.1 Overview of asteroid radar observations

The radar observations provide a rich source of information about Solar System bodies. For over 50 years they had been used to map and monitor the surfaces of inner planets, the moons, including the Galilean satellites and our Moon, comets, both Main Belt and near-Earth asteroids, and even the rings of Saturn. The uniqueness of this technique is that the astronomer is performing an active experiment and is not restricted to being a passive observer. Before recording the light reflected off a target surface, the observer has an active role in determining the properties of the light that illuminates the object (Ostro, 1989).

In a radar experiment an electromagnetic wave with a specific frequency is transmitted in the direction of the observed body. Upon reflection the signal frequency gets shifted due to the movement of the object along the line-of-sight, and the reception of signal can get delayed due to the radio wave having to travel additional distance to different parts of an object's surface. The returning radiation is converted to voltage, sampled and recorded for further analysis. The Doppler spectrum or Doppler-delay image of the target is later obtained by means of fast Fourier transform of the recorded signal. Unlike an optical image which is a projection of a fragment of sky on the detector, the radar image is not perpendicular, but rather parallel to the line of sight (as was shown in Figure B.4). This complicates the telescope pointing as it is not only the position of the object on the plane-of-sky that needs to be tracked, but also the radial velocity, contributing to the Doppler offset of reflected radiation, and distance. For that a precise ephemeris is needed and often adjusted during the observation.

The radar observations have a wide range of applications in studies of near-Earth asteroids. The radar astrometric measurements are complimentary to the plane-of-sky measurements, done with optical telescopes. They add the radial velocity and distance components, which are measured with higher precision than the angular positions, significantly improving the accuracy of long-term orbital predictions. This improvement can lead, for example, to a detection of the subtle non-gravitational forces acting on small NEAs, like the first asteroid Yarkovsky detection on (6489) Golevka (Chesley et al., 2003, see also Section 1.3.3) or, more recently, the OSIRIS-REx sample-return mission target (101955) Bennu (Chesley et al., 2014).

By comparing the transmitted and received signal strength one can determine radar albedo of an object (Ostro, 1989). The surface roughness at the scale of the emitted signal wavelength can be estimated based on the ratio of the signal received at the same (SC) and opposite (OC) circular polarisation as the signal emitted. On each reflection from the asteroid surface the polarisation of the radio wave changes sign. If the object was completely smooth, only signal with OC polarization would be detected, so the presence of SC signal suggests

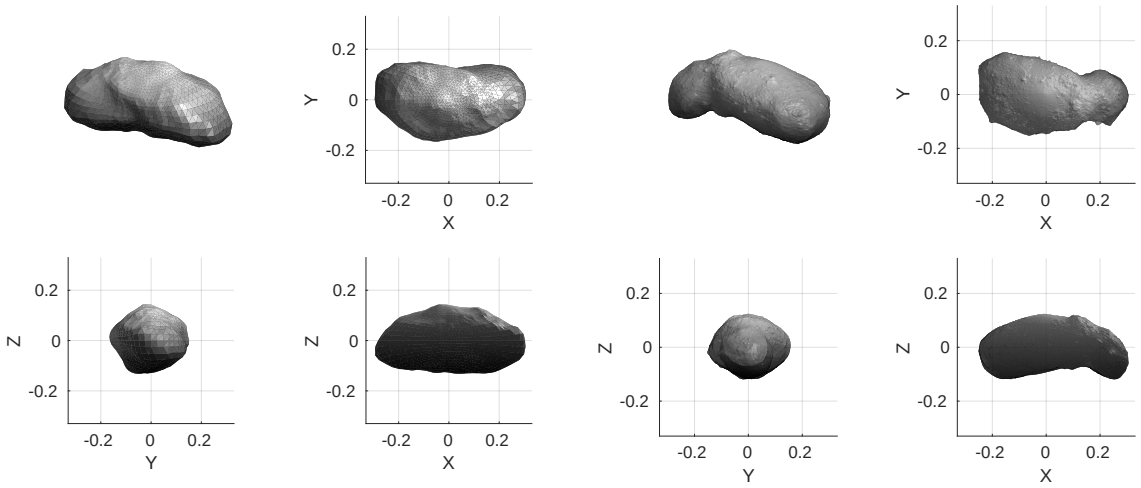

(a) Radar model **(b)** Spacecraft model

Figure 2.9: The two shape models of asteroid (25143) Itokawa. Panel (a) shows four views of the radar shape developed from delay-Doppler imaging (Ostro et al., 2004). Clockwise from top-left they are: a general overview of the shape, a view from positive end of the z-axis, a view from the negative end of y-axis, and from the positive end of the x-axis. Panel (b) shows the same projections, but for a high-resolution model developed using the spacecraft observations from Hayabusa (Demura et al., 2006; Gaskell et al., 2008). Both models were rotated to align x-axes with maximum moment of inertia assuming an uniform density. To be precise, they should be also shifted to account for the non-uniform density (Lowry et al., 2014).

some wavelength-scale (cm) features. The SC/OC ratio is considered a measure of near-surface roughness to the surface (Ostro et al., 2002) and it was found to be correlated with the taxonomic classes of asteroids (Benner et al., 2008).

By combining radar observations with the lightcurves, it was possible to establish solid spin-state and shape models for a few dozen near-Earth asteroids*. For example, the radar observations were instrumental in determining the size and shape of the asteroid (54509) YORP (2000 PH_5). Combining the radar-derived quantities with the spin-state assessed from optical lightcurves made the very first YORP effect detection possible (Lowry et al., 2007; Taylor et al., 2007, see also Section 1.4.4). The radar measurements were also used to characterise shapes as well as orbital properties of NEA binary systems like (66391) 1999 KW_4 (Ostro et al., 2006). In terms of recovering fine surface details of asteroids, radar is only surpassed by spacecraft missions. The reader is encouraged to compare the radar shape of (25143) Itokawa (Ostro et al., 2004) with the spacecraft images (Demura et al., 2006) and model (Gaskell et al., 2008), as shown in Figures 2.9 and 7.3. The radar model reproduces the general shape properties of the asteroid, and conveys some of the information on an uneven terrain, especially in vicinity of the neck region. However, it fails to reproduce the fine details of rocks and boulders visible in spacecraft images and model.

The two main facilities used to perform radar experiments on Solar System objects are

*http://echo.jpl.nasa.gov/

the Arecibo Observatory in Puerto Rico (Ostro, 1999) and Goldstone Solar System Radar in the US (Slade et al., 2011). Both were used for this work and the first one was visited by the author of this thesis. Both telescopes have their unique advantages, for example, Arecibo is more sensitive and Goldstone has the ability to track objects for longer periods of time, and were frequently proven to be complimentary (Ostro, 1989; Ostro et al., 2002; Benner et al., 2015).

The William E. Gordon telescope in Arecibo is the biggest telescope in the world equipped with a radar transmitter (Figure 2.10a). With a 305 m diameter it had only recently given up the first place as the largest single-dish radio-telescope to the Chinese FAST instrument which has a 500 m dish, but lacks the radar capabilities (Nan et al., 2011). The Arecibo telescope has a spherical primary mirror set in a natural depression of a karst sink-hole in a mountainous region of the western part of the tropical island of Puerto Rico. The Planetary Radar transmitter is an S-band antenna capable of transmitting signal of the power of up to 1 MW, although it usually operates at the level of about 800 kW. The central frequency of the transmitted signal is 2380 MHz, corresponding to wavelength of about 13 cm. The transmitter is installed in a Gregorian dome containing parabolic secondary and tertiary mirrors, suspended from a massive moving platform 137 m above the floor of the primary (see Figure 5.3). The platform is equipped with a rotating azimuth arm, which allows tracking of astronomical objects, although, because the position of the primary mirror is fixed, it offers limited elevation range.

The other radar facility is the Goldstone Solar System radar. Its fully steerable DSS-14 70 m antenna can be found in the Goldstone Deep Space Network complex in the Mojave Desert in the United States (Figure 2.10b). The DSS-14, that can be also used for communications with spacecraft missions, equipped with a 500 kW X-band transmitter, is capable of transmitting signal at 8560 MHz ($\sim$3.5 cm). For the purpose of radar experiments it can be used in either a mono-static mode, where the same instrument is used to transmit and receive signal, or it can provide the illumination for objects detected by other observatories in bi-static mode, for example by the 100 m Robert C. Byrd Green Bank Telescope (US) (Figure 2.10c). The Green Bank antenna is fully steerable and capable of receiving radio signal between 200 MHz and 116 GHz. It is located across the Northern American continent from Goldstone, in West Virginia.

2.2.2 Data processing

There are two basic types of radar observations. They are continuous-wave (*cw*) *spectra* and delay-Doppler *images*. Regardless of the observation type, the experiments are performed in a similar way and can be done in two modes. In mono-static mode of observations the telescope transmits the signal roughly for a period of time that is required for the electromagnetic wave to reach the target and come back, sometimes called the round-trip time (RTT). To prevent loss of any returning signal the transmit time might be set to be a bit shorter than

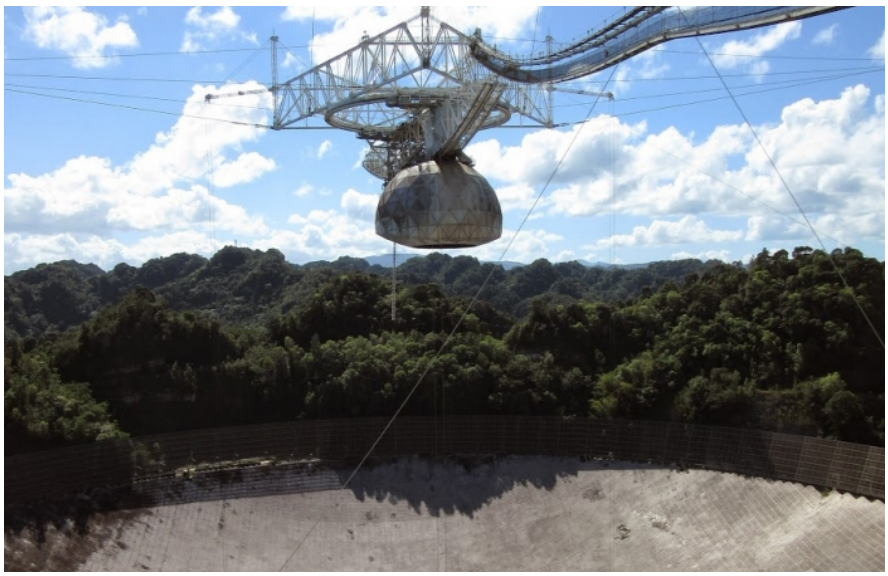

(a) Arecibo 305 m telescope rim and Gregorian dome (`http://www.naic.edu/~pradar/`).

(b) Goldstone Deep Space Complex DSS-14 70 m antenna (`http://www.gdscc.nasa.gov/`).

(c) Green Bank Telescope 100 m dish (`http://greenbankobservatory.org/telescopes/gbt-2/`).

Figure 2.10: The three radio telescopes used in this work. The Arecibo image by the author, Goldstone and Green Bank Telescope images from their respective websites.

RTT, as the switching to receive mode might take some time. Then the telescope is receiving the signal for as long as it was transmitted. The received radio echo is pre-processed by sets of analogue mixers, filters and attenuators and finally sampled and recorded in digital form.

To save time lost on the switching between transmit and receive, which is especially important for very close passes, the small bodies are sometimes observed in a bi-static mode. The major difference is that one telescope emits the radiation to illuminate the target and another one is used to record it. The transmit and receive times are then only limited by the visibility of the target from both facilities used. In case of observations of (85990) 1999 JV_6 (Chapter 5) the Goldstone antenna was used to transmit, with the Green Bank Telescope receiving.

The reduction of the radar data was done largely using the scripts available at the Arecibo Observatory computer system. Only a limited amount of interaction was required. Some basics of the reduction process will be outlined here, following closely the description provided by Magri et al. (2007) and keeping the naming conventions therein. The Goldstone observations were supplied already reduced, but the same principles hold.

Continuous-wave observations - Doppler spectra

The *cw* observations, in short, are a measurement of the Doppler offset of the frequency of the transmitted signal. The *cw* spectra of the radar echo do not include the distance information, but are useful to assess the ephemerides and give an initial indication of some of the object properties. The frequency of transmitted or received signal is adjusted for the centre of mass radial velocity using a precise Doppler ephemeris. Different parts of the object would be seen at higher frequencies than the centre of mass frequency f_0 if they are approaching the observer, or lower frequencies if they are moving away. The breath of the received echo in Doppler frequency shift is called the objects bandwidth, B. The B can be expressed as

$$B = \frac{4\pi D \sin\alpha}{\lambda P} \tag{2.3}$$

and it depends on the apparent diameter of the object, D, the wavelength of transmitted radiation, λ, the synodic rotation period of the body, P, and the angle between the body spin axis and the line of sight, or observational aspect angle, α (Ostro, 1989). As the apparent diameter of the object would change through a rotation, combining the B measurements at different rotation phases at similar observing geometry (when the aspect does not change much) provides some rough estimate of the pole-on silhouette of the object (see Figure 2.11).

The reduction of the digital *cw* observations entails performing an n-point fast Fourier transform (FFT) of the digitally sampled voltage time-series. The signal is sampled at a f_s frequency (which is the total bandwidth of the received signal, 12.5 kHz for current Arecibo observations) and there are a total of n_s samples collected over the integration time τ, where $n_s = f_s \cdot \tau$. In mono-static observations this time is limited by the transmit-receive cycle. In

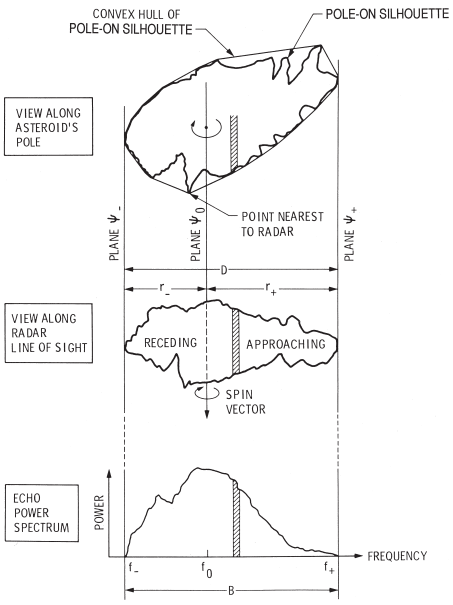

Figure 2.11: A schematic of how a Doppler echo of an irregularly shaped object is produced. The returning radiation from the centre of mass would have the same frequency as the emitted radio wave, f_0 (if the ephemeris is correct). The echo from the parts of the object approaching the observer would be shifted to higher frequencies (f_+), and from the receding to lower (f_-). As the continuous-wave observations are not decoded in delay, the power of the spectrum will be integrated across the whole area moving with the same radial velocity (see the dashed areas in different projections of the shape and the same in spectrum). The measurements of the bandwidth, B, of the received echo done across different rotation phases can be used to reconstruct the convex hull of the pole-on silhouette of the shape Ostro et al. (1988a). The image is reproduced here from Ostro (1999) (Fig. 7).

case of the bi-static observations one can select a subset of the, typically long, time-series. The frequency resolution is selected in post-processing by selecting an n that is, ideally, a divisor of n_s. The resolution of the FFTed signal is then f_s/n, which cannot be higher than $1/\tau$. The ratio of $n_s/n = N_{looks}$ is the number of independent 'looks' at the objects, what would be called individual frames in photometry. Multiple 'looks' can be summed incoherently to increase the signal-to-noise ratio of the Doppler spectrum, which increases with $\sqrt{N_{looks}}$. The final spectra are normalised, so that the mean noise of any spectrum would be 0, and the standard deviation of the noise is adopted as a unit of the power spectra.

In processing the Arecibo data, all *cw*s taken consecutively were summed. The resolution was then decreased by smoothing spectra reduced with highest possible frequency, usually using a factor of 2 or 3, to avoid repeating performing FFTs of different lengths. The smoothing was performed because the high-resolution spectra display many spikes confusing the shape modelling algorithm.

Delay-Doppler imaging

The delay-Doppler imaging is done with a coded signal being transmitted. The code provides means to recover the information of the delay of the returning radiation. The recorded time-series of voltages is then split into multiple delay 'rows' adding distance information missing in Doppler spectra. The fast Fourier transform is applied to each 'row' separately. In a way, a delay-Doppler image can be seen as a series of *cw* spectra taken at a range of distances to the radar. The interpretation of the delay-Doppler images is not as straightforward as is the case with direct imaging at optical wavelengths. The elements of the asteroid surface moving at the same radial velocity and positioned at the same distance from the radar will contribute to the same pixel even if they are physically separated on the object, see Figure 2.12. In other

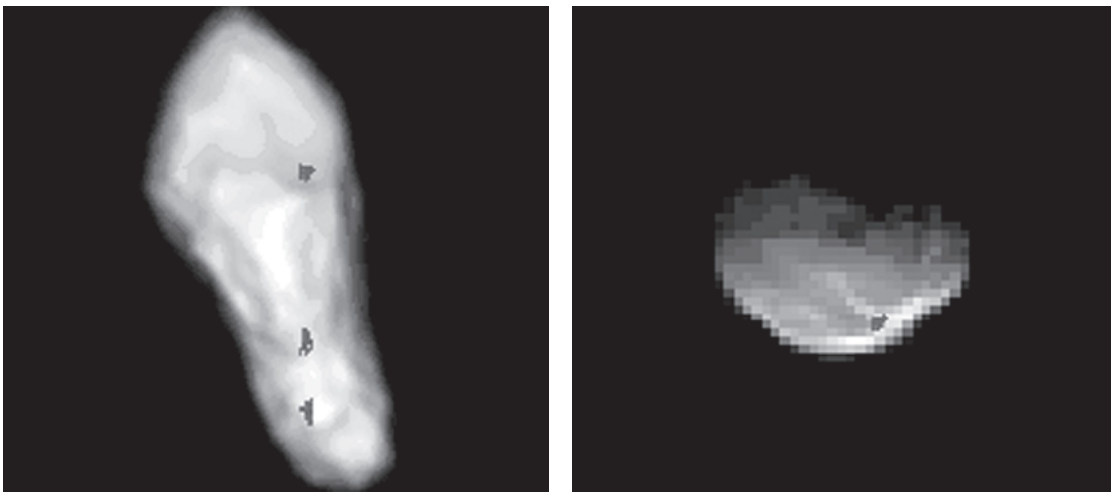

Figure 2.12: An illustration of how different surface elements are mapped onto a Doppler-delay image. The right panel is a plane-of-sky projection of the asteroid (4179) Toutatis shape model, the left panel is a modelled Doppler-delay image with delay on vertical axis and Doppler frequency shift on horizontal. The three small dark grey regions on the model lay in the same distance from the radar, and have the same radial velocity, thus are represented as one region of the echo. The image is reproduced from Ostro et al. (2002) (Figure 1).

words, it is impossible to differentiate between echoes coming from positive or negative latitudes on the object.

The code used for transmitting signals used in delay-Doppler imaging is a pseudo-random binary sequence of instructions to invert, or not, the transmitted signal sinusoid for a 'baud', b, length of time. It usually has a length, L, that is a prime number, and is set up to have low self-correlation if the lag between two copies of the code is different than 0. The code is repeated multiple times over the transmit time, τ, and each repetition is $p = b \cdot L$ seconds long.

On receive, the signal is sampled with s samples per baud. The recorded signal is then cross-correlated with the binary code, and the result is $N \cdot s$ rows that each contain a voltage time-series that corresponds to a specific delay in the code, or distance to a surface element. Each row is then subject to an n-point FFT, similar to how the Doppler spectra are treated. The maximum FFT length is limited by the total number of code repetitions, n_r, with $n_r = \tau/p$. Using n_r as the FFT length gives the highest possible frequency resolution. Usually, the images are reduced with a lower n, resulting in a lower resolution than maximum, to increase the signal-to-noise ratio, by effectively summing multiple 'looks' on a single image. The result is an image with $N \cdot s$ rows corresponding to different delays and n columns representing Doppler shifts and the power normalised so that a mean value of the noise outside the echo is 0 and the r.m.s. is 1.

After initial reduction of the delay-Doppler Arecibo images, the subsequent images were summed, to increase the number of 'looks'. In order to further improve the SNR, the images were binned in delay, an operation that is especially justified when s (the number of samples

per baud) is higher than 1 decreasing the delay resolution of the images, but bringing it closer to the actual baud length.

2.3 Preparing data for the shape modelling software input

The three types of observations described in this chapter have to be adequately formatted to be used as an input of the shape and spin-state modelling software used. The lightcurve data is the sole input for the convex lightcurve inversion, performed here using the CONVEXINV package (Kaasalainen and Torppa, 2001; Kaasalainen et al., 2001; Ďurech et al., 2010). Lightcurve and radar data can be combined to determine shape and spin-state models using the SHAPE tools (Magri et al., 2007). The details of shape modelling are discussed in Chapter 3, so this section summarises what kind of information is available to the modelling algorithm.

Formatting the CONVEXINV input file

The convex lightcurve inversion program CONVEXINV requires a file that starts with a single line containing the number of input lightcurve files in the set. Then each set is initiated by a line containing the number of data points and a 0/1 flag (0 marking relative lightcurves, 1 - calibrated). Each line consist of a light-time corrected Julian date (JD), brightness of the object in intensity units , three-element vector describing the position of Sun relative to the object (in ecliptic Cartesian coordinates), and three-element vector describing the position of Earth relative to the asteroid. The light-time corrected JD represents the time the light left the object, rather than when it was recorded on Earth, and is obtained from mid-exposure JD by removing time it takes the light to travel the Earth-asteroid distance. The brightness in intensity units is calculated from instrumental magnitude m as $10^{-(m-m_o)/2.5}$, where m_o is an arbitrary offset, chosen so that the intensity would be close to 1. An example lightcurve input file for the asteroid (1917) Cuyo is shown in the Appendix Figure D.1. A similar input file format is used in the spin-state modelling with MATLAB scripts developed at the University of Kent, that the author of this thesis expanded and improved. The only difference is an additional column, containing the error in object's brightness expressed in magnitudes (as shown in the Appendix Figure D.2).

Formatting the SHAPE input file

The SHAPE modelling software was used here to integrate the lightcurve observations with radar data. The program has an intricate system of formatting the input file. Rather than a single file containing all of the information, like the input file for CONVEXINV, it gathers various types of observations in one meta-file containing references to the actual data files. The file begins with a number indicating the total number of different data sets, followed by a meta-data description of each set. For a lightcurve set the meta-data contains the type of the observations,'lightcurve', and an identification number of the scattering law used as

there can be different formulae used for separate lightcurves. Next is a rough ephemeris information: the distance to the object, the right ascensions and declinations. Those are given for the observatory and the Sun only for a sample of dates at the time of observations, and specific viewing geometries are later interpolated for each observational point. What follows is the number of points in the lightcurve and a line containing the name of the data file, a flag ('f' if the calibration factor can be adjusted and 'c', if the lightcurve is calibrated), calibration factor which allows to adjust the level of the lightcurve and a weight that can be assigned to the set. An example of a lightcurve meta-data file for asteroid (85990) 1999 JV_6 is shown in Appendix Figure D.3. The lightcurve file itself has just three columns: uncorrected JD (mid-exposure time as registered on Earth), brightness of the object in magnitude scale and uncertainty in magnitudes.

Preparing cw *observations for* SHAPE *input*

The SHAPE input file, like in case of the lightcurves, contains meta-data about the observation. These include type of observations ('doppler'), identification number of the radar scattering law (determining how the asteroid surface will reflect the signal), ephemeris information (apparent right ascension, declination and distance of the object), the nominal frequency of the transmitted signal, the number of frequency bins, frequency resolution and the predicted centre of mass position in the spectrum. As the observational ephemeris is usually not perfect, it also contains a correction that needs to be applied to align the centre of mass frequency f_0 with the 0, corresponding to the location of centre of mass echo in the model spectrum. Next is a Doppler scaling factor, that can be used to adjust the frequencies for objects observed at a very low aspect. Then a data directory name follows and a number of input data files. In lines describing each file, a link to the data file is given, along with the standard deviation (unit of spectra power), calibration factor, number of 'looks' (see N_{looks} above), a weight that is considered in χ^2 calculations, and a flag indicating whether a mask should be applied. An example of a *cw* meta-data file for asteroid (85990) 1999 JV_6 is shown in Appendix Figure D.4.

Preparing delay-Doppler images for SHAPE *input*

The SHAPE entry in the meta data file is similar as in the case of Doppler spectra. The data set type is defined as 'delay-Doppler', followed by the identification number of scattering law used, ephemeris information (right ascension, declination and distance to the object) and transmitter frequency. The details of the delay dimension of the image include the number of rows and pixel height, number of samples per baud, stride, which is the number of samples per pixel, and code type which is always 'short' . The details of the Doppler dimension include the number of columns, the pixel width in Hz, the centre of mass column (which can have fractional part), DC column (as the signal is usually offset from the nominal transmitter frequency) and the FFT length used to reduce the original data. A delay-Doppler correction

polynomial can be added to account for the slight inaccuracy of the ephemeris prediction of the signal location. Then, there is a Doppler scaling factor, serving the same role as for *cw* spectra, data directory and number of input data files. Each file is described with a line consisting of the file name, mid-exposure time, standard deviation of the signal (which is typically 1), calibration factor, number of 'looks', centre of mass delay row number, a weight, and a flag marking whether a mask file should be used. An example of a delay-Doppler meta-data file for asteroid (85990) 1999 JV_6 is shown in Appendix Figure D.4.

For the application in this thesis scripts available at the Arecibo Observatory computer system were used to prepare the meta-files for lightcurves, Arecibo *cw* spectra and delay-Doppler images. The descriptions of data-files provided by Goldstone observatory were prepared manually, based on the information provided in the log files.

Chapter 3

Small body shape and spin-state modelling

3.1 Convex lightcurve inversion

3.1.1 Introduction

Photometric lightcurves, as discussed in Chapter 2, are an invaluable resource for modelling the physical properties of small Solar System bodies. The characteristics features of an optical lightcurves, including their shapes, amplitudes, and timing, are related to the observing geometries. The geometry information includes the distance between the observer and the target, the solar elongation (angles between Sun, observer and target), phase angle (angle between Sun, target and observer), timing of observations and location of the target on the celestial sphere. The different observing geometries provide the observer with different views of the target, changing illumination conditions and visibility of surface elements. The lightcurve inversion methods are used for recovering the spin-states, surface properties and shapes of the bodies from lightcurves taken at diverse geometries. An early analytical analysis of the lightcurve inversion theory led to a long-lasting preconception that shape and albedo effects are virtually inseparable (Russell, 1906). For a long time the lightcurve analysis methods concentrated on retrieving information about the spin-state of the objects and allowed reconstruction of only simple shape characteristic (Magnusson et al., 1989).

For example, the synodic rotation period can be obtained from even just one lightcurve by means of FFT (Harris et al., 1989). However, the time at which certain lightcurve features are observed is not only a function of the rotation period, but will change depending on the observational geometry. The epoch method makes use of timing the lightcurve features, under assumptions that they are produced by the same shape feature on an asteroid rotating with a constant sidereal period. By observing the change in the timing of the lightcurve features due to relative motion of the target and the Earth, the epoch method provides an approximate position of the rotation pole, or at the very least a sense of rotation (Magnusson et al., 1989). An elegant method of convex-profile inversion (Ostro and Connelly, 1984; Ostro et al., 1988b) requires assumptions of an uniform and geometric scattering, convex shape and almost equatorial viewing geometry. The modulation in the lightcurves under these assumptions is attributed to the changing observed cross-sectional area of a rotating target, and a unique solution can be determined. The method allows for extraction of the mean pole-on profile, meaning an average of profiles obtained by intersecting the shape with planes parallel to the equator. The convex-profile inversion provides reasonable results for regularly shaped bodies, as can be seen in Chapter 4.

There are other semi-analytical, experimental and numerical approaches to lightcurve inversion that have been reviewed in great detail before, most notably in *Asteroids II* (Magnusson et al., 1989) and *Asteroids III* (Kaasalainen et al., 2002). The current developments of asteroid shape modelling tools concentrate around combining data from different data sources, and go beyond the scope of purely lightcurve-based inversion (*Asteroids IV* Ďurech et al., 2015). The focus of a large part of this thesis is on the convex lightcurve inversion method (Kaasalainen and Torppa, 2001; Kaasalainen et al., 2001; Ďurech et al., 2010).

This method takes full advantage of the shape information contained in the optical lightcurves of asteroids taken at different times, allowing the reconstruction of reliable shape models. This method works best in recovering convex hulls. Reconstruction of non-convex shapes using there methods is also possible, however it yields degenerate solutions (Viikinkoski et al., 2015).

Albedo distribution, or differences in colour at the asteroid surface, could be a source of lightcurve variation. In principal they require either a very extensive optical set of lightcurves' or thermal observations to distinguish them from shape effects (Magnusson et al., 1989). However, for the small bodies, like NEAs considered here, the shape effects seem to prevail (Kaasalainen and Torppa, 2001). The spacecraft flyby data suggest little surface reflectivity variation is to be expected for small NEAs due to their surfaces being covered in a layer of dust-like regolith rendering the bodies uniform in colour (Sears, 2015).

The shapes reconstructed using the convex inversion lack concavities and are rarely calibrated in size. Still, they usually successfully reproduce the lightcurve features of even strongly non-convex bodies, as shown for comet 67P (Chapter 6). Modelling shape concavities purely from lightcurves gives non-unique solutions and provides hints on the locations of shape features rather than robust solutions. Another source of information about the body features is required in order to resolve this ambiguity, like occultations, direct imaging, or radar observations as discussed in Section 3.2.2 and applied to observations of asteroid (85990) 1999 JV_6 in Chapter 5.

3.1.2 Shape modelling with `CONVEXINV` and using this method to detect YORP-induced torques

Convex shapes approximate the real asteroid features, but without any surface concavities (like crevices or craters). The reconstructed shape resembles the convex hull of the real object, which is commonly described as the real shape of the asteroid being 'gift-wrapped'. The shape modelling software used for the convex lightcurve inversion in this thesis is based on the convex inversion package, `CONVEXINV`, released by Ďurech et al. (2010). The inversion problem, solved by the least-square optimisation in the `CONVEXINV` package, is cast as

$$\vec{L} = A\vec{g} \tag{3.1}$$

as is stated by Kaasalainen and Torppa (2001, Eq. 2), where $\vec{L}$ is the vector of measured brightnesses of the asteroid, and $\vec{g}$ is the vector of parameters being fitted. The matrix A describes the relation between $\vec{g}$ and $\vec{L}$. Most of the elements of vector $\vec{g}$ are related to the shape of the object. The goal of the modelling is then to minimise the χ^2 defined as a function of the model parameters with the expression

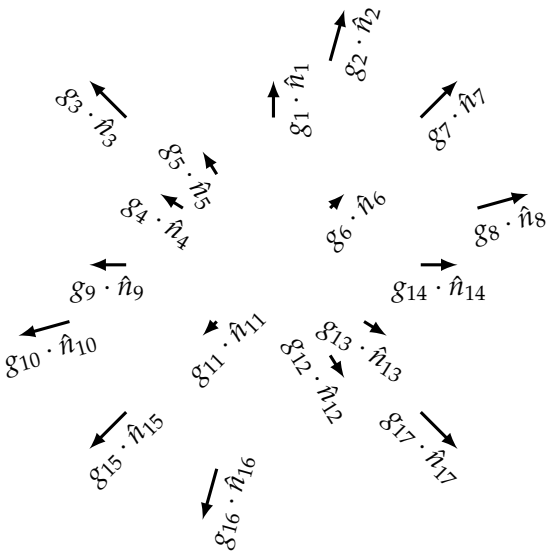

Figure 3.1: Within `CONVEXINV` procedures an asteroid model is represented with a set of vectors $g_i\hat{n}_i$, where $\hat{n}_i$ is a unit facet-normal vector, and g_i is a scale factor representing the surface area. The $\hat{n}_i$ are a collection of fixed-direction unit vectors, usually surface normals of a sphere or an ellipsoid (Kaasalainen and Torppa, 2001). The 'areas' of the facets g_i are optimised to obtain the best least-squares fit to the lightcurve data set, while keeping the surface closed by observing Equation (3.3). The surface is triangulated using the Minkowski regularisation procedure after the modelling is done, giving the shape model that is the actual output (Kaasalainen and Torppa, 2001; Kaasalainen et al., 2001; Ďurech et al., 2010).

$$\chi^2(\vec{g}) = \sum_i \left\| \frac{\vec{L}^{(i)} - A\vec{g}^{(i)}}{\bar{L}^{(i)}} \right\|^2 \tag{3.2}$$

with index i denoting a single lightcurve, and $\bar{L}^{(i)}$ the mean brightness of the lightcurve (expressed in units of intensity rather than magnitudes), following Kaasalainen and Torppa (2001, Eq. 7). In a problem defined this way neither the uncertainties of individual data points, nor the calibrated brightnesses are taken into account. This can be considered a weakness of the method, as there is no direct way of decreasing the contribution of poor quality observations from the fit. This issue was tackled in alternative lightcurve shape modelling procedures (Viikinkoski et al., 2015).

Internally within the `CONVEXINV` procedure, the shape is at first approximated as a spherical harmonic series. At a later stage of optimisation is represented with a selection of unit vectors $\hat{n}_i$. Those are pre-determined facet normals of the optimised shape, describing the initial surface (Figure 3.1). The unit surface normals are multiplied by areas g_i that satisfy two conditions. First of all that the shape is convex, ensured by keeping $g_i > 0$, and that the surface is closed, by preserving

$$\sum_i \hat{n}_i g_i = \vec{0}. \tag{3.3}$$

The problem stated in that way would always give a unique solution. However, the asteroid shapes are rarely purely convex and might display albedo variegation across the surface. Hence, minimisation of Equation (3.2) could yield a small residual in the Equation (3.3) that is fixed by using a convexity regularisation parameter implemented as a 'dark'

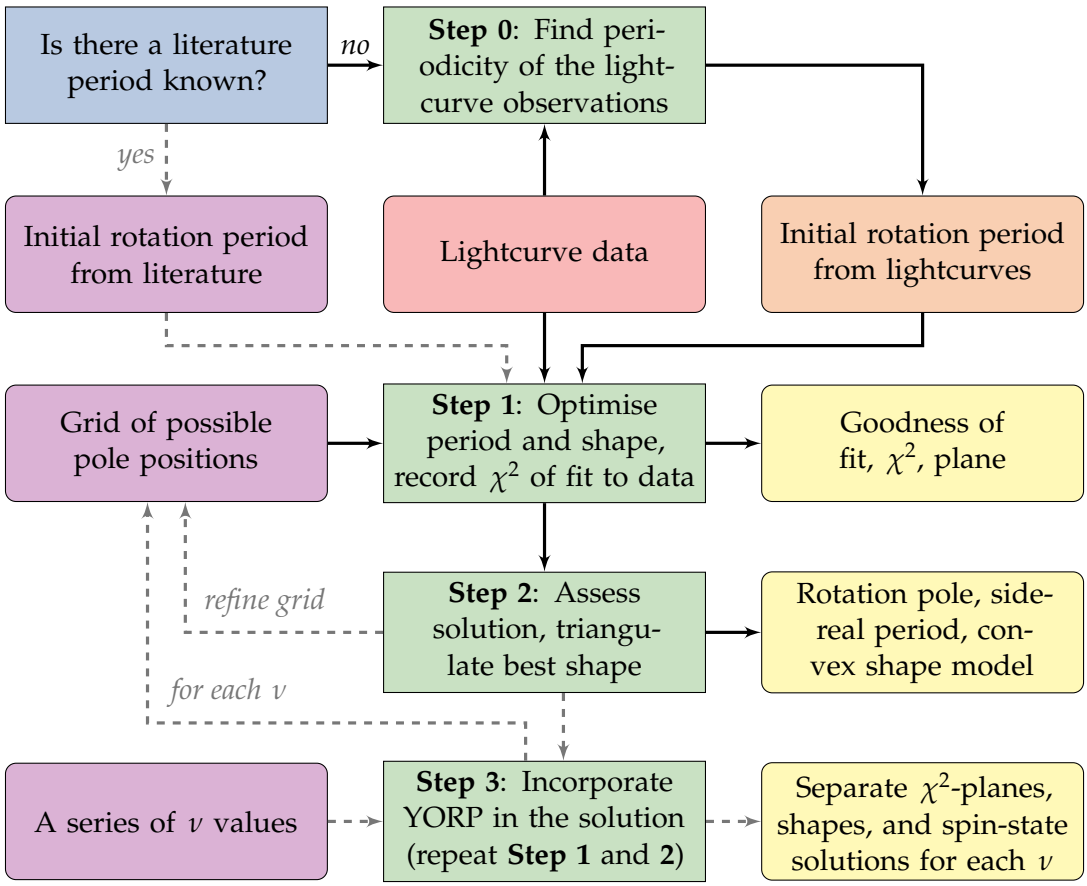

Figure 3.2: Schematic of shape modelling using convex lightcurve inversion method with `CONVEXINV`. Green fields mark steps of modelling, and the blue field is used to mark the decision to include literature period in the shape modelling procedure. The red field marks input lightcurve data, purple fields mark user-defined input parameters, the orange field highlights the lightcurve-derived period that is output of one part of the process and is being used as input to the other, and yellow fields contain the output. The arrows mark the sequence of modelling steps, with optional steps and input/output connected to the main flow with grey dashed lines. The process is described in Section 3.1.2.

facet with an area selected to bring the sum in Equation (3.3) to zero. The contribution from the 'dark' facet compensates for the lightcurve features impossible to reproduce with a convex shape. The area of the dark facet is usually very small even for strongly non-convex shapes (Kaasalainen and Torppa, 2001). To obtain a shape model that can be further used, for example in modelling spin-state or application to thermal-infra-red data, an additional step is needed. The surface of the internal representation of the shape, as shown in Figure 3.1, is triangulated using Minkowski regularisation to create a mesh that can be used as input for other procedures (see Figure 3.9).

The shape modelling procedure, that was applied in this thesis to lightcurve-only data sets, utilises the convex inversion implementation by Ďurech et al. (2010) and follows the steps outlined in the scheme in Figure 3.2 and will be discussed in the next few paragraphs.

Step 0 : Period estimation

The convex inversion software `CONVEXINV` requires an initial estimate of the spin-state solution. The synodic rotation period, acquired by fast Fourier transform from the lightcurve data (Harris et al., 1989), can be used as a first approximation. The FFT method is usually applied to a subset of available lightcurves, after applying a correction bringing all available lightcurves to a common observing geometry. Alternatively, a program included in the modelling package can be used. It implements a different approach, where at a selection of possible period values it probes 6 different pole locations and quickly optimizes an ellipsoid shape and scattering function. The quality of fit, χ^2, of the best solution for each period is recorded while the information on pole location and preliminary shape is lost. The sidereal period estimate with the lowest χ^2 goodness-of-fit can then be selected and adopted as initial period solution.

It is possible that this step could be omitted, if an earlier literature value of the period was available for a given object. If there are no earlier evaluations of the period, or the measurement is spurious, then one of the two available methods is applied to the full lightcurve data set.

Step 1 : Period and shape optimisation

The position of the rotation pole for principal-axis-rotators (majority of the NEAs) is fixed relative to the orbital plane of the body (see Figure B.2) and ecliptic plane (see Figure B.3). Thus, the position of the spin-axis described with the pole ecliptic latitude, β, and pole ecliptic longitude, λ. While it is possible for `CONVEXINV` to fit for the rotation pole along with the shape, this introduces new parameters to the model and produces additional minima to the fitting procedure. To avoid any ambiguity, in the work described here, a grid of fixed pole positions is used, with period and shape optimised at each point. Usually the points are selected on a rectangular grid with a target resolution. Normally a rough resolution on the order of $10^\circ \times 10^\circ$ is first applied to the full celestial sphere to find an initial pole orientation.

The rotation axis of the body is aligned with the z-axis of the shape, which should also be the axis of the principle moment of inertia. The `CONVEXINV` does not output any initial rotation phase offset. The starting T_0, the epoch from which the rotation phases are calculated, is by default the Julian date of the very first data set, or first point in the oldest lightcurve, rounded down to an integer. The T_0 can also be forced to be a specific value, as sometimes it can be beneficial to use a different date. Therefore the T_0 defines the x-axis of the body-fixed reference frame, as it is the time when the x-axis is in the plane of sky, see schematic in Figure B.3 and discussion in Section 3.3.1 for an explanation of the relationship between the body-centric and ecliptic coordinate systems. However, it has to be noted, that the x- and y-axes of the body are in no particular relation to the second and third principal moments of inertia of the output shape.

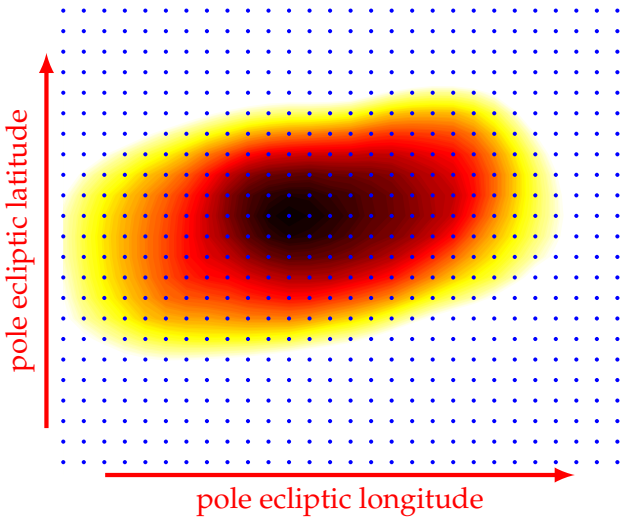

Figure 3.3: At **Step 2** of the convex modelling (Figure 3.2), the solution might be assessed using a χ^2 plane. The plane is created based on the χ^2 values obtained after optimising shape and period at different ecliptic longitudes and latitudes of the pole (marked here with blue dots). The values are interpolated between the grid points to create a smooth surface and color-coded, with the darker colors in this example representing the smaller χ^2 values.

The shape optimisation is set up on a computing cluster, so that several models can be optimised at the same time, and χ^2 of the fit is recorded for each model. After modelling is finished the χ^2 values for all tested solutions are gathered. The goodness-of-fit can be plotted as a function of the pole ecliptic coordinates, creating a χ^2-plane.

Step 2: Solution assessment

After the scan is finished the best solution is assessed. The χ^2-plane gives an estimate on the pole position from the rough scan. A more detailed scan (**Step 1**) can be then performed on a refined grid of possible pole solutions and then the χ^2-plane, depicted in Figure 3.3, can serve as means of estimating the error in pole position. An increase of χ^2 is interpreted by decrease in the quality of lightcurve fit, with all solutions within 1 % of the best χ^2 treated as equally good.

After iterating the pole scan, the best solution is identified and is then passed to the triangulation procedures to obtain the final shape model. The spin-state corresponding to the shape, including a refined sidereal rotation period, is also recorded. The resulting model can then be used in detailed spin-state analysis.

In some cases **Steps 1** and **2** are iterated using different subsets of the full lightcurve data set to ensure the best possible solution is found.

Step 3: Incorporating YORP spin-up

In the `CONVEXINV` implementation of the lightcurve inversion methods, it is assumed that a constant period can be applied to all available data. The code was modified by S. Lowry and S. Duddy at the University of Kent to allow for a period change due to the YORP effect. The lightcurves are represented within the modelling procedures as functions of rotation phase (φ), calculated from the time at which observations were gathered. Taking into account the

linear rate of change of the rotation frequency (ω) with time, the rotation phase of an asteroid can be expressed for any given time as

$$\varphi(t) = \varphi(T_0) + \omega(t - T_0) + \frac{1}{2}\nu(t - T_0)^2, \tag{3.4}$$

where:

$\varphi(t)$	observed rotation phase in radians,
$\varphi(T_0)$	initial rotation phase in radians,
ω	rotation frequency, or rate, in rad/d; $\omega \equiv \frac{2\pi}{P}$, P is period in days,
ν	the change of rotation rate in rad/d^2; $\nu \equiv \dot{\omega}$,
t	the time of observation (JD),
T_0	starting epoch of the model (JD).

The linear change of rotation rate, $\dot{\omega}$, can be attributed to the spin component of the YORP torque, as defined by Equation (1.2) (Rubincam, 2000), and will be further referred to as the YORP factor, or YORP strength, ν. The original package does not have the last term of this expression, which is equivalent to a constant-rotation-rate solution. The addition of a non-zero ν allows us to explore the possibility of systematic change to the rotation rate. It has to be stressed here that ν is not treated within the shape modelling procedure as a parameter that could be optimised, but rather as a constant value.

The inclusion of ν in rotation phase calculation allows for adding another dimension to the grid search described above. This step of the modelling process consists of assuming different values of ν and repeating **Step 1** and **2**. The shape and period are still optimised for a grid of possible pole solutions, usually located on a fragment of the celestial sphere. The optimisation is performed for each iteration, creating multiple χ^2-planes, or YORP-

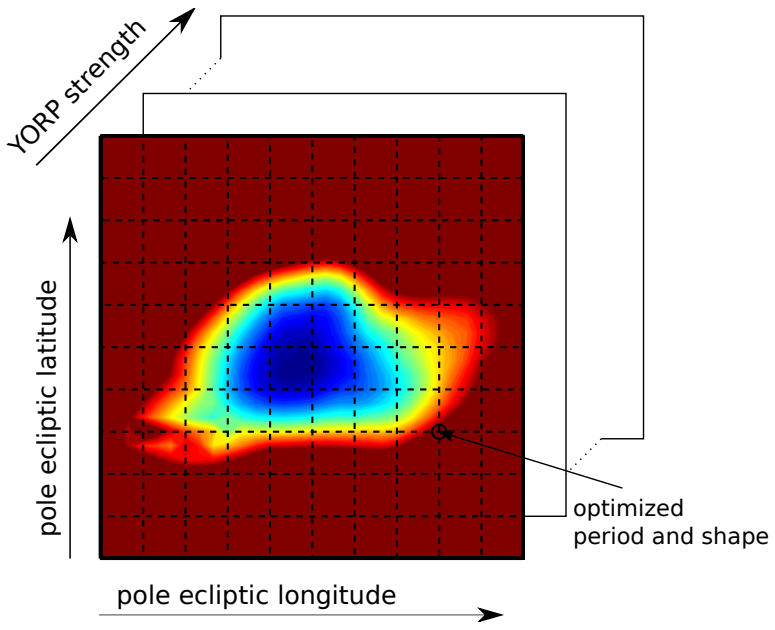

Figure 3.4: A schematic of the simultaneous shape and YORP modelling. For a discrete set of assumed YORP strengths (referred to in the main text as ν). **Steps 1** and **2** of the analysis Figure 3.2 are repeated to obtain a series of χ^2-planes. The best solution from each χ^2-plane is then recorded to identify the optimum YORP strength required to model the data.

planes, see Figure 3.4. The best solutions from such YORP-planes can then be used in further analysis and a 'global' solution can be sought. The lowest χ^2 value from each YORP-plane is then extracted and plotted as a function of ν, giving a constraint on the possible YORP torque. This grid scan including search over different YORP acceleration values is done automatically using scripts developed by the author of this thesis.

3.2 Modelling radar images

3.2.1 Introduction

There are two general types of radar observations of small Solar System bodies. As discussed in Section 2.2, they are the Doppler spectra, also called continuous-wave (*cw*) observations, and delay-Doppler imaging. Before delay-Doppler images of asteroids became available, the bandwidth and shape of the frequency power spectrum of the *cw* radar echo signal gave insight into the rotation state of the object and served to obtain information about the pole-on profile of the observed body (Ostro et al., 1988a), as well as physical properties of the surface (Ostro, 1989). Lately, *cw* spectra and delay-Doppler images are often combined with asteroid lightcurves to determine the size and shape of the observed object (Ostro et al., 2002; Benner et al., 2015).

Due to the many-to-one mapping of the asteroid surface onto the radar image, see Section 2.2, the inversion of radar data gives a non-unique solution. Unlike the convex lightcurve inversion methods discussed above, it requires a good starting point, including approximate period and an initial shape model roughly reproducing the radar echo. The process is heavily user-supervised, requiring frequent interventions. Reliable reproduction of surface features from radar echoes requires observations at a wide range of viewing geometries or information from other types of observations. For example the rotation period can be easily deduced from lightcurves and allows for decoupling the object size from the spin-state.

3.2.2 Shape modelling with SHAPE

A software package SHAPE, introduced by Magri et al. (2007), was used for the modelling. A set of scripts and procedures was written by the author allowing SHAPE to be run on the Kent computing cluster Tor. These scripts are modified versions of programs provided by C. Magri (University of Maine), M. Nolan (University of Arizona) and P. Taylor (Arecibo Observatory). The goal of the fitting is once more to optimise the χ^2 of the fit of models to the observations. However, in the CONVEXINV package this optimisation is considered for only one type of input data, the lightcurve data. In SHAPE, the data structure is more complicated, and can involve both types of radar data as well as optical data, as illustrated in Figure 3.5. Minimising the χ^2 function of the model, $\mathcal{M}$, is the ultimate goal, and can be expressed as

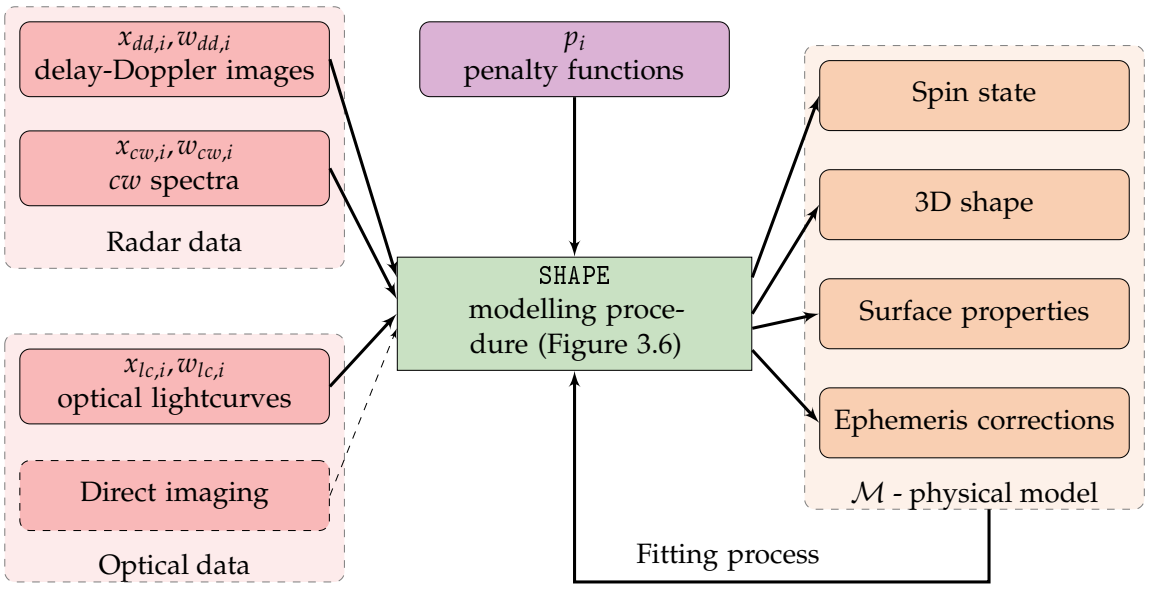

Figure 3.5: The structure of input and output of SHAPE modelling software. The boxes are annotated with symbols used in Equation (3.5). The red fields on the left denote the various types of observational data that can be input to the shape modelling procedures. In this thesis, two types of radar data were used, the delay-Doppler images, and continuous-wave spectra. Along with those, lightcurve data was included in the fit using SHAPE. The direct imaging (spacecraft or adaptive optics) data was not used, due to lack of availability of such data for any of the analysed targets. The purple field in the middle symbolises the penalty functions, which control the physical feasibility of the model, penalising unwanted traits, such as deviation of the centre-of-figure from centre-of-rotation. Those can be treated as another type of input, as they are set up subjectively by the user, rather than being fit by the procedure. The orange fields to the right list the output parameters of the shape modelling procedure. They are also, in a way, an input, as the SHAPE software requires the user to provide an initial guess of those parameters. The green field symbolises the modelling process using the SHAPE software, as illustrated in Figure 3.6.

$$\chi^2(\mathcal{M}) = \sum_j \sum_i w_{j,i} \left(y_{j,i}(\mathcal{M}) - x_{j,i} \right)^2 + \sum_i |p_i(\mathcal{M})|. \tag{3.5}$$

Here

- χ^2 the goodness-of-fit function,
- $\mathcal{M}$ asteroid model (shape and physical parameters),
- $w_{j,i}$ weight (can be assigned observation-by-observation),
- $y_{j,i}$ synthetic observation calculated from the model,
- $x_{j,i}$ observation (data point),
- p_i penalty functions (or penalties),
- j index, iterates over types of observations, $j = dd$ for delay-Doppler data, cw denotes continuous-wave data, and lc denotes lightcurve data (see Figure 3.5),

i index, iterates over all available observations of a given type, or all applicable penalty functions.

A major difference from the Equation (3.2) expression for χ^2 is that individual data points (for example a single radar image, spectrum, or a lightcurve) can be assigned weights that influence the fitting. Another new factor is a set of penalty functions, that are dependent on the model properties, rather than on the relation between model and observations. The penalties can be used for example to enforce principal axis rotation by aligning the z-axis of the body with the spin axis, keep the spin axis close to the centre of mass, or restrict the scale of non-convex features. The penalty functions are arbitrarily selected by the user, and are sometimes modified throughout the process.

The modelling procedure follows the literature examples (Magri et al., 2007, 2011) and was further developed by the author to fit the modelling requirements of (85990) 1999 JV_6. However, the steps roughly outlined in Figure 3.6 could also be applied to other objects.

Step 0: Convex inversion

Convex lightcurve inversion methods (see Section 3.1.2 and Figure 3.2) can be used to assess the initial spin-state and shape properties of the object. If the lightcurve set covers a diverse range of observing geometries and the shape model is close to convex this might provide a starting point for the non-convex `SHAPE` modelling procedure. Otherwise it gives a good first estimate of the period and provides some indication as to the region in which the rotation pole might be located. This step might be irrelevant if the lightcurve data set is very limited, or if there are initial models of the object available.

Step 1: Construct initial model to fit radar echoes

The radar observations are introduced at this stage. A representative set of continuous-wave (*cw*) spectra and delay-Doppler images is included to limit the computation time required to calculate model echoes for all the input files. The subset is selected to sample the rotational phases as well as different observing geometries. The aim of this step is to gain a basic understanding of general features of the shape, rather than to develop a detailed model.

The most important information to be retrieved from the *cw* observations is the echo bandwidth. The *cw* spectra are masked to preserve that information. In some cases there might be significant drops in the signal due to the irregular shape of the object, and those regions could be considered when setting up the masks. The masks are initially set up manually, see Figure 3.7. After a few iterations of the shape model, new masks can be generated based on the location of the edges of the model echo. The *cw* files contain the information about the echo power in a range of frequency bins. The mask is a logic filter, marking which parts of the spectrum are important (mask value set to 1), and which can be

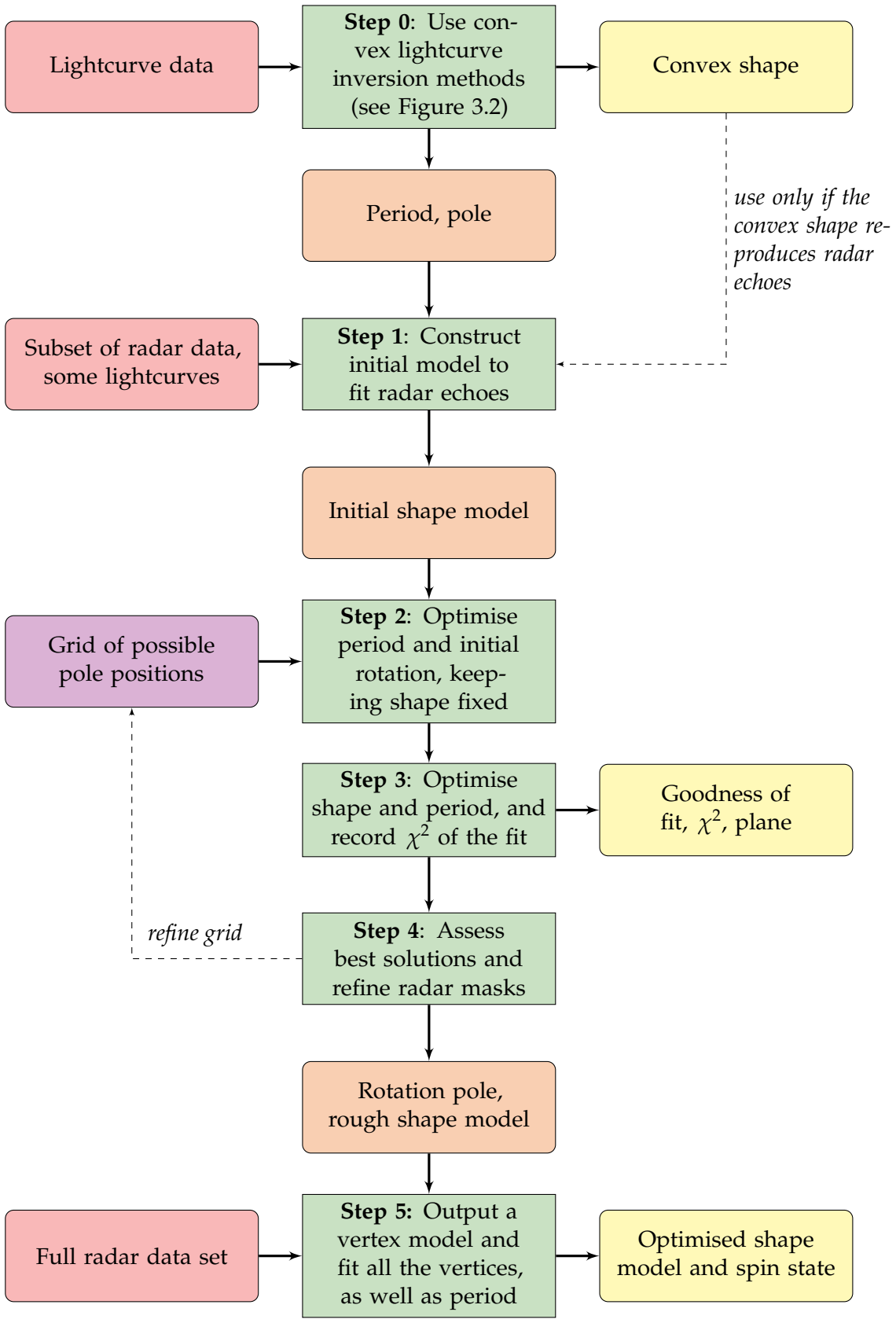

Figure 3.6: Schematic of shape modelling using radar data and SHAPE. Green fields mark steps of modelling. The red field marks input lightcurve and radar data, purple field marks user-defined input pole positions, the orange field highlights the output of one part of the process that is being used as input to the other, and yellow fields contain the output. The arrows mark the sequence of modelling steps, with optional input/output connected to the main flow with grey arrows. The process is discussed in Section 3.2.2.

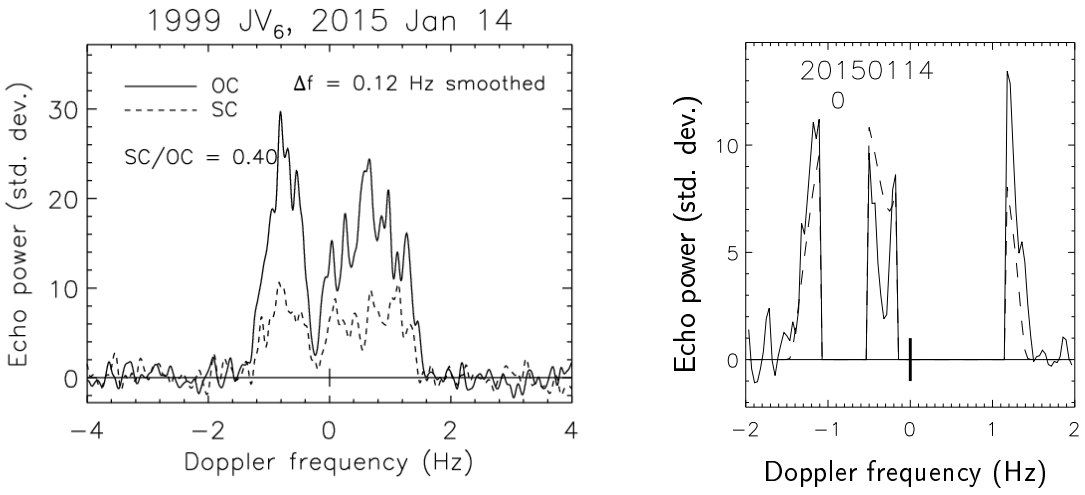

(a) SC and OC spectra (cropped)

(b) OC spectrum, masked

Figure 3.7: An example of continuous-wave spectrum, 14th January 2015 Arecibo observations of (85990) 1999 JV_6. The first panel (a) shows the spectra taken in two channels, with the opposite circular polarisation (OC, continuous line) and the same circular polarisation (SC) as the emitted radiation. The second panel shows the OC data that were used in shape modelling, masked to highlight the most important features (b).

discarded (mask set to 0). Hence, when calculating the quality of the model fit to data, χ^2, only values for the bins corresponding to a non-zero mask are considered.

The delay-Doppler images are normally cropped, to restrict the size of the input file, which can be very large if the full bandwidth and delay range are to be used. The frames are then masked, very much like the continuous-wave spectra. Again, the images are multiplied by the mask before calculating χ^2 of the model fit. The initial mask was always a rectangular window fitted manually to incorporate all of the signal. After few iterations of the shape model new masks are generated using the `SHAPE` model predictions.

Additionally, some of the lightcurves are included to provide accurate phasing information. For the sake of computation speed the lightcurves are binned in rotation phase and limited to those obtained closest to the date of the radar data acquisition.

The `SHAPE` package includes tools to manually establish simple shape models that would provide a starting point for fine-tuning with the optimisation methods. The options are a Gaussian sphere (a shape expressed with series of spherical harmonics), an ellipsoid, an ovoid (distorted ellipsoid), or a combination of these. The shapes described with those types of object can be parameterised with a few variables, and provide a quick fix. The model that is the output of `CONVEXINV` procedures could be potentially used at this stage, as it provides quite reliable information about the convex hull of the object. However, it has the disadvantage of being represented with a discrete set of vertices rather than a smooth parametric function. Fitting a model with hundreds or thousands of vertices is computationally expensive and is usually reserved for later stages of modelling. The initial model, that roughly reproduces the radar echoes, is valid only for a pre-determined spin-state, selected from the

lightcurve inversion or just arbitrarily.

Using the example of (85990) 1999 JV_6, at this stage of modelling, the shape was described with two ellipsoids. There are nine parameters to describe an ellipsoid in `SHAPE`: the size (longest axis) and two axial ratios, three rotational offsets around the axes of an arbitrary, body-fixed, reference frame, and three linear offsets along the directions of x, y and z-axes in this frame. A total of 18 parameters can thus be used to describe a two-ellipsoid model.

Step 2: Optimise period and initial rotation, keeping the shape fixed

This step and the next one are an equivalent of **Step 1** of the convex inversion procedure (Figure 3.2). A grid of possible pole positions is selected. Again, a rectangular grid might be used, with points evenly spaced in terms of absolute values of λ and β, but the `SHAPE` procedure is much slower and more computationally intensive than `CONVEXINV` would be even for a very large lightcurve data set. The grid might be set up with the points evenly spaced on the celestial sphere, lowering the number of pole positions for which the `SHAPE` needs being executed and optimising the process.

At each point of the grid of possible poles the spin-state parameters are adjusted, that is the sidereal rotation period and initial rotation phase. Similar to `CONVEXINV`, the T_0 is set by the user as the point in time from which the rotation phase is calculated, using the Equation (3.4). `SHAPE` does not require the initial rotation phase, $\varphi(T_0)$, to be 0, but rather defines the 0 rotation phase as the moment when the long axis of the body, x, crosses the plane of sky. The description of the spin-state includes three Euler angles required to align the body-fixed reference frame with the ecliptic reference frame. The first two are related to the position of rotation pole. The third, the additional rotation around the z-axis, is the phase offset, $\varphi(T_0)$, and this parameter is adjusted at this stage.

Step 3: Optimise shape and period, and record χ^2 of the fit

Once the initial spin-state is resolved, the shape can be improved. The shape parameters are now allowed to vary, along with the fine adjustments to the period and rotation phase. The software optimises each of those quantities, one at a time. The modelling stops after a certain accuracy goal is reached. Usually there is a limit of a minimum improvement of χ^2 relative to the previous iteration. However the number of iterations itself can be used as a limiting factor. Other than setting the accuracy goal and step size at which each parameter can be modified, the software is also given some additional restrictions called the penalties, see Equation (3.5). The penalty functions contribute to the final χ^2 and can serve a range of purposes, for example ensuring the principal axis rotation, or keeping the centre of rotation in the centre of mass.

Step 4: Solution assessment

After each model is optimised, the goodness-of-fit χ^2 is recorded. Once again, this is plotted as a function of ecliptic coordinates of the pole and is used to determine the best solution as well as pole uncertainty. The best models are then selected, and compared visually to the observational data.

The SHAPE package provides tools to do that. The modelling software can be used to 'write' out a selected model. This procedure calculates the model radar echoes and light-curves in the same way as is done during the modelling, but allows the user to save them. The output can be displayed graphically to be examined. Additionally, the information about the expected echo location can be utilised to determine masking of the experimental data, with the masks computed to be within a few pixels of the synthetic data. Hence, the masks used on *cw* spectra and delay-Doppler images are improved at this step.

If required, **Steps 2**, **3**, and **4** can be iterated using a finer grid of poles and an adjusted representation of the shape as a starting point. The whole process sometimes also needs to be repeated as the penalty functions are adjusted to better direct the modelling procedure.

Step 5: Output a vertex model and fit all the vertices, as well as rotation period

Once the simplified model reaches a satisfactory level the fine adjustments can be made to retrieve the information about the asteroid surface features. In order to do that the optimised model obtained at **Step 4** is represented as a set of vertices gathered into triangular facets. Individual vertices can then be adjusted with SHAPE. The resolution at which the surface is triangulated can be adjusted to reflect the target resolution of the model.

Each vertex is described with a total of seven parameters, as illustrated in in Figure 3.8. The first three parameters are components of a vector describing the position of the base vertex displacement in the body-fixed coordinate system, $\vec{v_b}$. The next three are components of a unit vector showing the direction of the vertex deviation, $\vec{v_d}$. Both vectors are held fixed throughout the fitting process. The position of a given vertex is a sum of the vertex base position and the vertex deviation. The directions of the vertex deviations are set at the time of the shape conversion and can be chosen to be normal to the actual surface, pointing radially away from the centre of mass, or perpendicular to the surface of a best-fit ellipsoid. The seventh parameter is the deviation magnitude, d, the only parameter that can be fitted by SHAPE. It can be either positive or negative, see Figure 3.8.

This representation of the vertices within SHAPE forces some limits to how much a model can be changed. As shown in Figure 3.8, it means that the position of a vertex can be only manipulated by sliding it along the direction of the vertex deviation. As a result it is possible to add small features like mountains or craters to the surface. However, it would be quite difficult for the procedure to reproduce a neck of a highly bifurcated shape, like (8567) 1996 HW_1 (Magri et al., 2011), if the initial model was not bi-lobed already.

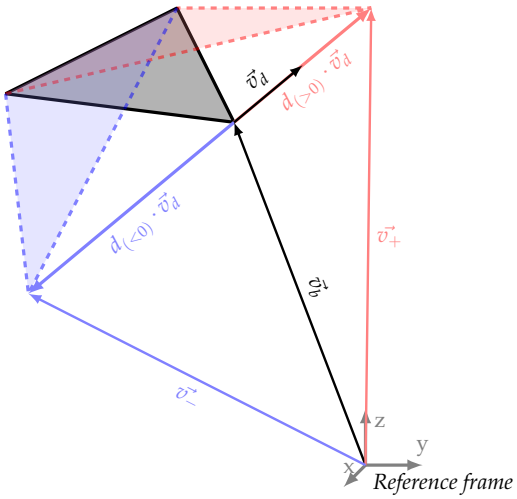

Figure 3.8: The schematic shows a vertex of a triangular facet as represented in SHAPE. The location of a given vertex in the body-centric reference frame is given by a vector, which is a sum of base displacement $\vec{v}_b$ and deviation vector. The deviation is expressed by a unit vector $\vec{v}_d$ multiplied by magnitude d. The vectors are set up in a way at the beginning of the modelling process such that the $\vec{v}_d$ is a unit vector and $d = 0$. The magnitude of the deviation d is one of the free parameters in SHAPE. The different colours show, in exaggeration, what happens to a face when the value of d is changed, with black showing the initial conditions ($d = 0$, vertex located at $\vec{v}_b$), red – a positive value of d (vertex at $\vec{v}_+$), and blue – negative (vertex at $\vec{v}_-$).

Some new penalties increasing the χ^2 value for a model with unwanted properties, see Equation (3.5), are useful at this stage. For example, they can be used to control the amount of global and local non-convexity of the shape. The final result is a spin state of the object and a shape model that can be used in further spin-state analysis routines.

3.3 Spin-state modelling using pre-existing models

There are several possible approaches to the spin-state analysis. In a 'global' approach the YORP-induced spin-rate change can be incorporated as one of the parameters when developing shape and spin-state model of a target. This was discussed in context of the convex lightcurve inversion in Section 3.1.2, but is also possible for radar shape reconstruction (this possibility was not explored in this work). However, it might be the case that a shape model already exists for the observed target, or a model was developed from a subset of data at an earlier stage of the analysis. New lightcurve observations can then be used not to improve the shape model, but for assessment of a period change instead (Mottola et al., 2014, for example). Currently, as of 20$^{\text{th}}$ February 2018, the Database of Lightcurve Inversion Models (Ďurech et al., 2010) contains 1707 models of 944 asteroids (including just 19 NEAs, which is a fraction of a percent of the population). The radar shape models are available only for a couple dozen asteroids so far*.

Two approaches are feasible when a shape model already exists. In one, the lightcurves can be combined with an existing shape model and pole position to test a range of possible sidereal rotation periods and YORP acceleration values, limiting the fit to just two parameters. In the other, the shape models are used to generate artificial lightcurves for each available lightcurve data set. Offsets are then measured between rotation phases of the

*https://echo.jpl.nasa.gov/asteroids/shapes/shapes.html

observed and modelled lightcurves. The YORP effect produces a quadratic trend in time in those phase offsets. Lightcurve observations at more than three epochs are required to detect this trend. Both approaches are discussed in this section. To begin this kind of analysis, tools are required that would generate the artificial lightcurves from any shape model.

3.3.1 Generating artificial lightcurves

The shapes are usually represented as sets of vertices gathered into triangular facets, see Figure 3.9. Whereas artificial lightcurves can in principle be generated from either `CONVEXINV` or `SHAPE`, the individual steps of the process can have multiple applications, as discussed in Chapter 6. The `MATLAB` tools available at Kent were improved and expanded by the author to speed-up the computation as well as include the self-shadowing of surface elements, thus enabling the use of non-convex shape models.

The shape model is read from a text file into two arrays in the `MATLAB` routine. The array **V** contains Cartesian coordinates of each vertex in the body-fixed coordinate system reference frame. The array **F** contains triplets of numbers, the indices of vertices required to form triangular facets.

For example, as shown in Figure 3.10, a facet is described by a row in array **F** containing three indices 1, 2 and 3. The three vectors, $\vec{v}_1$, $\vec{v}_2$ and $\vec{v}_3$, marking the positions of the vertices V_1, V_2, and V_3 relative to the body centre are retrieved by reading out rows numbered 1, 2

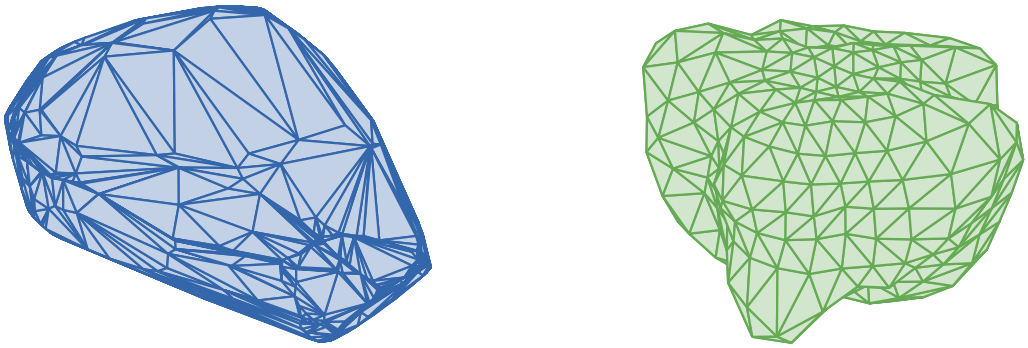

(a) Convex shape of (3103) Eger **(b)** Non-convex shape of (54509) YORP

Figure 3.9: The two panels show triangular meshes of the shape models derived for two NEAs, for which the YORP effect was detected. Panel (a) shows a convex lightcurve-inversion model of asteroid (3103) Eger (Ďurech et al., 2012). Panel (b) shows a radar-derived non-convex shape of asterod (54509) YORP (Lowry et al., 2007; Taylor et al., 2007). Both shapes are represented by two arrays, one listing positions of individual vertices, the other listing the triages of points making up triangular facets.

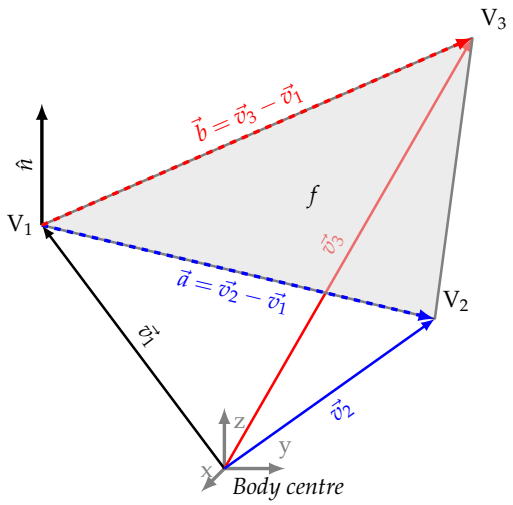

Figure 3.10: The routines used to generate lightcurves take shape models made up with triangular facets as their input. The models are stored as text files including two arrays. The first array stores the Cartesian coordinates of all the shape vertices, V_i. The second array holds sets of indices pointing to vertices. In the example shown here the vertices V_1, V_2, and V_3 make up the triangular face that has area f and unit surface normal $\hat{n}$. The positions of vertices V_2 and V_3 relative to V_1 are marked by vectors $\vec{a}$ and $\vec{b}$.

and 3 from the **V** table. The area of the face, f, is given as

$$f = \frac{1}{2}\left\|\vec{a} \times \vec{b}\right\|, \tag{3.6}$$

where

$\vec{a}$ is the position of vertex V_2 relative to V_1 , $\vec{a} = \vec{v_2} - \vec{v_1}$,
$\vec{b}$ is the position of vertex V_3 relative to V_1 , $\vec{b} = \vec{v_3} - \vec{v_1}$.

The facet unit normal, $\hat{n}$, is then defined as

$$\hat{n} = \frac{1}{2f}\left(\vec{a} \times \vec{b}\right) \tag{3.7}$$

The indices for each facet are ordered so that the facet normal would always point to the outside of the modelled surface. For the purpose of calculating self-shadowing effects, the vectors $\vec{a}$ and $\vec{b}$ as well as dot products $\vec{a} \cdot \vec{a}$, $\vec{b} \cdot \vec{b}$, and $\vec{a} \cdot \vec{b}$ are calculated and stored for each facet of a non-convex shape.

To calculate the illumination of each facet, the information about observing geometry is required. The input lightcurve file contains ephemeris information about the positions of Sun, $\vec{d}_\odot$, and Earth, $\vec{d}_\oplus$, relative to the asteroid in the ecliptic reference frame for each data point. Working under the assumption that the geometry does not change significantly for the time it takes to record a single lightcurve, the positions of Sun and Earth from the ephemeris are averaged, and then normalised to unit vectors

$$\hat{d} = \vec{d}/\|\vec{d}\|. \tag{3.8}$$

The direction vectors are then transformed from the ecliptic coordinate system to the body-fixed frame, as illustrated in Appendix Figure B.3, using rotation matrices

$$\hat{d}' = \begin{pmatrix} \cos\phi_0 & \sin\phi_0 & 0 \\ -\sin\phi_0 & \cos\phi_0 & 0 \\ 0 & 0 & 1 \end{pmatrix} \begin{pmatrix} \cos\beta' & 0 & -\sin\beta' \\ 0 & 1 & 0 \\ \sin\beta' & 0 & \cos\beta' \end{pmatrix} \begin{pmatrix} \cos\lambda & \sin\lambda & 0 \\ -\sin\lambda & \cos\lambda & 0 \\ 0 & 0 & 1 \end{pmatrix} \hat{d}, \quad (3.9)$$

where

- $\hat{d}'$ is the unit vector pointing either at Earth ($\hat{d}'_\oplus$), or the Sun ($\hat{d}'_\odot$), in the body-fixed reference frame at phase 0 for the given lightcurve,
- ϕ_0 is the initial rotation of the model (relevant if the definition of T_0 requires the axis of minimal inertia rather than the x-axis of the body to be in plane-of-sky for phase 0),
- β' is calculated from the ecliptic latitude of the rotation pole, β, as $\beta' = 90° - \beta$,
- λ is the ecliptic longitude of the rotation pole,
- $\hat{d}$ is the unit vector pointing either at Earth ($\hat{d}_\oplus$), or the Sun ($\hat{d}_\odot$), in the ecliptic coordinate system.

In some cases (like when the SPICE kernels are used, see Chapter 6), the position vectors $\vec{d}$ can be given in equatorial coordinate system (see Figure B.1 for the relation between the two systems). For example, the spin-state of comet 67P was defined with equatorial coordinates of the pole (δ and α). In this case, to perform the rotations of observer and illumination from the equatorial to body-centric coordinates, instead of Equation (3.9), one should use

$$\hat{d}' = \begin{pmatrix} \cos\phi_0 & \sin\phi_0 & 0 \\ -\sin\phi_0 & \cos\phi_0 & 0 \\ 0 & 0 & 1 \end{pmatrix} \begin{pmatrix} 1 & 0 & 0 \\ 0 & \cos\delta' & \sin\delta' \\ 0 & -\sin\delta' & \cos\delta' \end{pmatrix} \begin{pmatrix} \cos\alpha' & \sin\alpha' & 0 \\ -\sin\alpha' & \cos\alpha' & 0 \\ 0 & 0 & 1 \end{pmatrix} \hat{d} \quad (3.10)$$

where

- δ' is calculated from the declination of the rotation pole, δ, as $\delta' = 90° - \delta$
- α' is calculated from the right ascension of the rotation pole, α, as $\alpha' = 90° + \alpha$
- $\hat{d}$ is the unit vector pointing either at Earth ($\hat{d}_\oplus$), or the Sun ($\hat{d}_\odot$).

The rotation phase, φ, for each data point is calculated using the Equation (3.4). The positions of Sun, $\hat{d}''_\odot$, and Earth, $\hat{d}''_\oplus$, relative to the asteroid at any rotation phase, $\hat{d}''$, are then given as

$$\hat{d}'' = \begin{pmatrix} \cos\varphi & \sin\varphi & 0 \\ -\sin\varphi & \cos\varphi & 0 \\ 0 & 0 & 1 \end{pmatrix} \hat{d}' \tag{3.11}$$

For each facet the illumination and visibility are then calculated. First, the dot product of the position of the Sun and facet normal, indicating whether or not a facet is illuminated

$$\mu_\odot = \hat{n} \cdot \hat{d}''_\odot \tag{3.12}$$

As both vectors are unit vectors, $\mu_\odot$ is the cosine of the solar zenith angle. Similarly $\mu_\oplus$ is the dot product between the facet normal and the direction towards the Earth, or cosine of the viewing angle, which gives an indication of the level of visibility of the facet from Earth,

$$\mu_\oplus = \hat{n} \cdot \hat{d}''_\oplus \tag{3.13}$$

In MATLAB the computations can be done rather quickly using array operations. Fixing the reference frame to the body and rotating the positions of the Sun and Earth relative to the asteroid rather than using ecliptic coordinates and rotating positions of hundreds of vertices makes the computation much more efficient.

The next step is to calculate each facet's contribution to the overall brightness. First of all, the facet has to be illuminated and visible from Earth, so if either of $\mu_\odot$ or $\mu_\oplus$ comes out negative, the value of 0 is assigned. If the shape is non-convex, some further computations are required to take into account possible shadowing effects, which include both the elements of the surface casting shadows on certain areas and parts of the surface being obstructed from viewing from Earth. The details of this computations are explained at the end of this section.

The model brightness, m, is then calculated by summing the contributions from each facet and converting it to magnitude scale

$$m = -2.5 \log_{10} \sum S(\mu_\odot, \mu_\oplus) f \tag{3.14}$$

Where S is a surface reflectance function of the Sun and Earth direction cosines and depends on the assumed scattering model. Here, following (Ďurech et al., 2010), mostly Lambertian and Lommel-Seelinger laws are used. Using the Lambertian scattering, the reflectance is calculated as

$$S_L = \mu_\odot \mu_\oplus \tag{3.15}$$

or, using the Lommel-Seelinger as

$$S_{LS} = \frac{\mu_\odot \mu_\oplus}{\mu_\odot + \mu_\oplus} \tag{3.16}$$

Sometimes, the two scattering laws are combined using a weighting factor, c, producing Lambertian-Lommel-Seelinger scattering in the form

$$S_{LLS} = cS_L + S_{LS} \tag{3.17}$$

Any more complex reflectance function can be used as well, but these three proved sufficient for the requirements of the modelling performed in this thesis. Also, as relative lightcurves are used, the factors used to account for the distance to Sun and Earth while computing a model lightcurve, are omitted.

For each observational lightcurve the artificial lightcurve is generated for two sets of rotation phases. One is for the rotation phases at which the object was actually observed, as calculated from the observation epochs using the model spin-state (see Equation (3.4)). The other set is computed for 100 rotation phases selected between 0 and 1 rotation phase every 1 % of rotation. Combining those two sets produced an impression of a smooth light-curve. The level of the artificial lightcurve is adjusted for display purposes, so that it oscillates around 0. The correction to the magnitude of the input lightcurve are also made, so that the observational points lay as close as possible to the artificial curve.

Self-shadowing computation using ray-tracing

Some additional computations are required for the non-convex shapes. The major difference between the convex and non-convex surface is that in the latter case some parts of the object might be obstructed from view or shadowed by another surface element. The simple 'ray-tracing' procedure applied here relies on checking whether a 'ray' (a vector of an arbitrary magnitude pointing towards the Earth or the Sun) intersects with any of the shape's triangular facets. If this condition is fulfilled the facet is considered obstructed (from view or illumination) and therefore does not contribute to the lightcurve. An algorithm described by Sunday (2012) is closely followed in computation of the intersections between 'rays' and facets.

First of all, a matrix of possible 'shadow casters' for each facet is prepared. The convention used is that facet j can cast a shadow on, or obstruct from view, facet i, if its centre, $V_{C,j}$, is above the horizon of facet i and the centre of facet i, $V_{C,i}$, is below the horizon of facet j, as illustrated in Figure 3.11. Facet j will be then listed as a possible 'shadow caster' for facet i.

To check if a facet is above another facets horizon, first an 'origin' is selected for each facet, the vertex with index from the first column in array **F**. Then the relative positions of

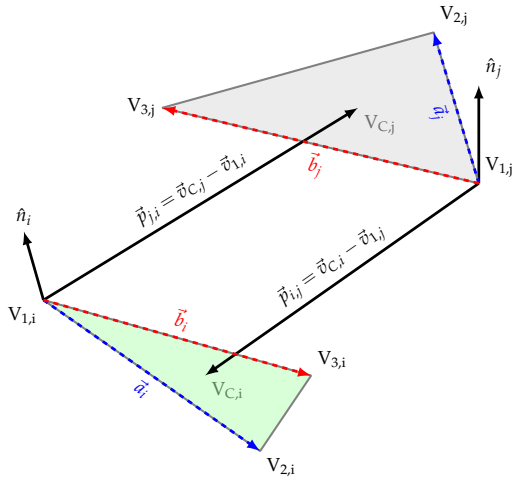

Figure 3.11: A schematic of the various quantities calculated for each pair of facets, useful in determining the self-shadowing geometry. The facet i has vertices $V_{1,i}$, $V_{2,i}$, and $V_{3,i}$. The vector $\vec{v}_{C,i}$, not pictured, is the position of the centre of this facet, $V_{C,i}$, relative to the asteroid centre. The edges $\vec{a}_i$ and $\vec{b}_i$ are the respective positions of vertices $V_{2,i}$ and $V_{3,i}$ relative to $V_{1,i}$. Finally, the $\vec{p}_{i,j}$ is the position of the centre of facet i relative to the 'origin' vertex, $V_{1,j}$, of facet j.

centres of all facets relative to the 'origins' of all other facets are calculated, being

$$\vec{p}_{i,j} = \vec{v}_{C,i} - \vec{v}_{1,j}, \tag{3.18}$$

where

- $\vec{p}_{i,j}$ is the position of the centre of facet i relative to one of the vertices of facet j,
- $\vec{v}_{C,i}$ is the position of the centre of facet i in the body-fixed frame, $\vec{v}_{C,i} = (\vec{v}_{1,i} + \vec{v}_{2,i} + \vec{v}_{3,i})$,
- $\vec{v}_{1,j}$ is the position of vertex 1 of facet j in the body-fixed frame, so-called 'origin'.

The vector $\vec{p}_{i,j}$ is then projected on the surface normal of facet i, $\hat{n}_i$. The scalar $D_{\mathrm{i,j}}$ represents the distance, between the centre of facet j and the plane containing facet i, calculated along $\hat{n}_i$,

$$D_{\mathrm{i,j}} = \hat{n}_i \cdot \vec{p}_{j,i}. \tag{3.19}$$

If $D_{\mathrm{i,j}}$ is greater than 0 then the centre of facet j is above the horizon of facet i. If, at the same time $D_{\mathrm{j,i}}$ is smaller than 0, then facet j qualifies as a possible 'shadow caster' for facet i. For the purpose of future calculations the `MATLAB` procedure computes and stores the $D_{\mathrm{i,j}}$ and $\vec{p}_{i,j}$ for each pair of facets.

For a specific observing geometry and rotation phase the illumination and visibility of facet i is checked (see Equations (3.12) and (3.13)). If both are positive, then the list of 'shadow casters' is then examined. The same computation is relevant for both the Earth and the Sun, so $\hat{d}''$ can be substituted by either $\hat{d}''_{\oplus}$ or $\hat{d}''_{\odot}$.

First, we consider the possible 'shadow caster' j can obstruct the view of either Sun or Earth only if it itself is illuminated or visible (see Equations (3.12) and (3.13)). Second, we

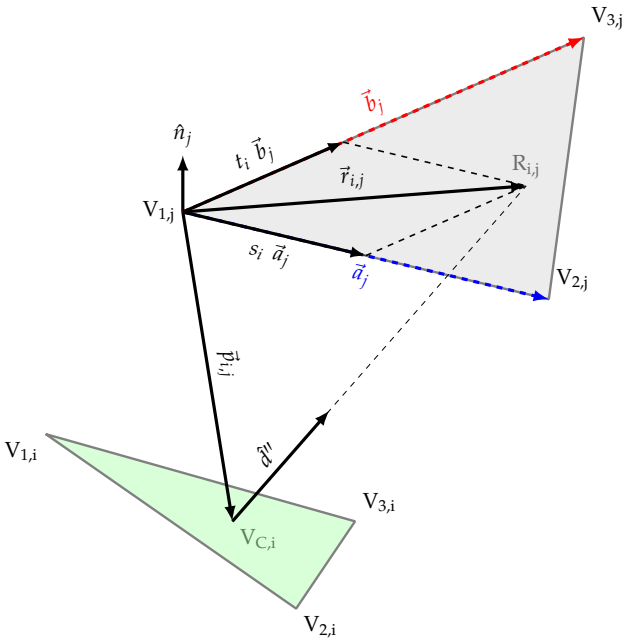

Figure 3.12: A schematic of the ray-tracing procedure used to determine whether the ray cast from centre of facet i in the direction of celestial body, $\hat{d}''$ would hit a possible 'shadow caster', facet j. If this happens, then facet j shadows, or obstructs from view, facet i. For explanation of the designations used see the main text and Figure 3.11.

check if the facet j lies in the line-of-sight of facet i. To do that a ray is traced from the centre $V_{C\,(i)}$ along the vector $\hat{d}''$, as shown in in Figure 3.12.

The ray will intersect the plane containing facet j at the interception point $\mathrm{R_{i,j}}$, which will have position $\vec{r}_{i,j}$ relative to the 'origin' of vertex j, $\mathrm{V_{1,j}}$.

$$\vec{r}_{i,j} = \vec{p}_{i,j} - \frac{\hat{n}_j \cdot \vec{p}_{i,j}}{\hat{n}_j \cdot \hat{d}''}\hat{d}'' \tag{3.20}$$

where

$\hat{n}_j \cdot \vec{p}_{i,j}$ can be substituted with $\mathrm{D_{j,i}}$, which is pre-computed for each pair of facets,
$\hat{n}_j \cdot \hat{d}''$ can be substituted with either $\mu_\odot$ or $\mu_\oplus$ depending if the shadowing of obstruction from view is calculated,

leaving a relatively simple expression

$$\vec{r}_{i,j} = \vec{p}_{i,j} - \frac{D_{\mathrm{j,i}}}{\mu}\hat{d}''. \tag{3.21}$$

The $\vec{r}_{i,j}$ vector can be expressed in j-facet-coordinate-system as

$$\vec{r}_{i,j} = s_{i,j}\,\vec{a}_j + t_{i,j}\,\vec{b}_j \tag{3.22}$$

where

$s_{i,j}$ is the non-orthogonal projection of vector $\vec{r}_{i,j}$ onto the edge $\vec{a}_j$ of facet j,
$t_{i,j}$ is the non-orthogonal projection of vector $\vec{r}_{i,j}$ onto the edge $\vec{b}_j$ of facet j.

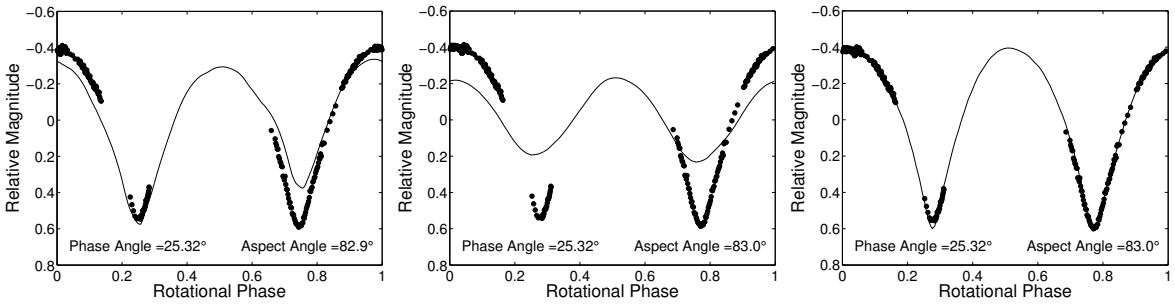

(a) Convex model – no shadows

(b) Non-convex model – no shadows

(c) Non-convex model – with shadows

Figure 3.13: Lightcurve of asteroid (8567) 1996 HW_1 taken on 8th September 2008 at Kharkiv (see Table 2 in Magri et al., 2011). The lightcurve in panel (a) was reproduced using a lightcurve-inversion convex shape model with pole position $\lambda = 282°$, $\beta = -39°$. The lightcurves in panels (b) and (c) were generated using non-convex radar-derived model with $\lambda = 281°$, $\beta = -31°$. Both models have sidereal rotation period $P = 8.76243$ h and were derived by Magri et al. (2011). All three panels show relative lightcurves of the target plotted against rotation phase. The dots mark observations and solid lines the synthetic lightcurves. The lightcurve in panel (b) was generated from the non-convex model, but using the same procedure as for convex shapes, that is ignoring obstructions and self-shadowing. The lightcurve on panel (c) shows the quality of the shadowing procedure described in the text, when applied to the highly bifurcated shape model of asteroid (8567) 1996 HW_1. As can be seen in this example, taking into account self-shadowing is essential for the model correctly reproduce lightcurve features (compare panels b and c). While the convex model does a good job (a), the quality of fit is higher for the non-convex one (c).

If both the $s_{i,j}$ and $t_{i,j}$ are positive and their sum, $s_{i,j} + t_{i,j}$ is smaller than 1 then the intersection point $R_{i,j}$ lies within facet j and the view to the relevant body (Sun or Earth) is obstructed. As the facet edges $\vec{a}_j$ and $\vec{b}_j$ define a non-orthogonal coordinate system, the computation of $s_{i,j}$ requires more than a simple dot product of $\vec{r}_{i,j}$ with $\vec{a}_j$, more precisely

$$s_{i,j} = \frac{\left(\vec{r}_{i,j} \cdot \vec{b}_j\right)\left(\vec{a}_j \cdot \vec{b}_j\right) - \left(\vec{r}_{i,j} \cdot \vec{a}_j\right)\left(\vec{b}_j \cdot \vec{b}_j\right)}{\left(\vec{a}_j \cdot \vec{b}_j\right)^2 - \left(\vec{a}_j \cdot \vec{a}_j\right)\left(\vec{b}_j \cdot \vec{b}_j\right)}. \tag{3.23}$$

Similarly, to obtain $t_{i,j}$, a following expression is utilised

$$t_{i,j} = \frac{\left(\vec{r}_{i,j} \cdot \vec{a}_j\right)\left(\vec{a}_j \cdot \vec{b}_j\right) - \left(\vec{r}_{i,j} \cdot \vec{b}_j\right)\left(\vec{a}_j \cdot \vec{a}_j\right)}{\left(\vec{a}_j \cdot \vec{b}_j\right)^2 - \left(\vec{a}_j \cdot \vec{a}_j\right)\left(\vec{b}_j \cdot \vec{b}_j\right)}. \tag{3.24}$$

Many of the terms in Equations (3.21), (3.23) and (3.24) are independent of the observing geometry. This allows for storing their pre-computed values on disk, and reducing the number of operations required to generate a single lightcurve, making the ray-tracing procedure efficient.

Finally, the results can be incorporated in calculating the amount of light received from

each facet. If the facet j is found to be shadowing, or obstructing from view, the centre of facet i, then the relevant cosines, $\mu_\odot$ or $\mu_\oplus$, are set to 0 and then the lightcurve is computed in the same way as for the convex case using Equation (3.14). This seems like a crude approximation, but it was sufficient to successfully reproduce the lightcurves of the object with a known non-convex shape used to test it, asteroid (8567) 1996 HW_1, see Figure 3.13 (Magri et al., 2011), as well as the asteroid (85990) 1999 JV_6 discussed in Chapter 5.

3.3.2 Two-parameter period and YORP fits to confirm spin-rate change

Once the artificial lightcurves are generated, the results can be used to analyse the spin-state of the object and search for a YORP-induced period-change signature. One approach is to try out different combinations of possible sidereal period values (P) and YORP spin-up factors (ν). A rectangular grid is prepared in the space of P and ν, initially around the original spin-state solution with a coarse resolution, and later, with a finer accuracy, around the most likely solution. For each pair of parameters, new rotation phases are calculated for every observational relative-magnitude data point. In the legacy procedure that was initially in use at Kent, the artificial lightcurve would then be calculated for each new rotation phase. However, because of the extra steps needed to evaluate self-shadowing, the generation of lightcurves for non-convex bodies is computationally expensive. To speed up the computation we can use the fact that as different pairs of P and ν are applied to calculate the rotation phases for observational points, the shape of the lightcurve remains the same. Thus, the pre-generated artificial lightcurves can be used and interpolated as needed for the rotational phases that were not previously covered.

The newly phased observational points are then adjusted to lie as close as possible to the artificial lightcurves. Then, the quality of fit is assessed with a χ^2 value calculated for each lightcurve as

$$\chi^2 = \sum \left(\frac{m_c - m_o}{\delta m} \right)^2 \tag{3.25}$$

Where

- m_c is brightness of the asteroid in magnitude scale as calculated using the shape model, normalised to oscillate around 0,
- m_o is the observed instrumental brightness of the asteroid (with a correction added, so that the whole lightcurve would lay as close as possible to the model lightcurve),
- δm is the uncertainty of the measurement.

This is different from the `CONVEXINV` output, which is calculated in the intensity space and does not consider the measurement uncertainties. It is also different from the `SHAPE` output value, which takes into account the radar data. A sum of χ^2 for all the lightcurves for a given set of P and ν is then recorded and can be plotted creating a P/YORP-plane. This

can be used to assess the need to introduce a ν to explain the exact timing of the asteroid lightcurves.

3.3.3 Phase offset measurements as a tool to measure period change

A different approach is to measure the phase offsets of the observed lightcurves required to put them in phase with the artificial lightcurves. In order to do that, the initial rotational phase for each point is calculated according to the model spin-state using Equation (3.4). Then the points are 'slid' across the artificial lightcurve by adding different phase offsets to the original ones and the χ^2 of the fit is recorded at each step. The best solution is selected, the optimal phase offset required to obtain the best fit is recorded, and the measurement uncertainty is calculated. This process is repeated for each lightcurve in the data set.

The phase offsets are plotted against the time elapsed since T_0. As can be deduced from Equation (3.4) a quadratic trend in the phase offset measurements could suggest a period change. This change can be quantified by fitting a parabola to the measurements

$$\Delta\varphi(t) = \Delta\varphi(T_0) + \Delta\omega(t - T_0) + \frac{1}{2}\nu(t - T_0)^2, \tag{3.26}$$

where:

$\Delta\varphi(t)$	observed rotation phase offset in radians,
$\Delta\varphi(T_0)$	error in initial rotation phase determination (in radians),
$\Delta\omega$	error in determination of the rotation rate in rad/d^{-1}.

The equation describes the difference between the observations and constant-period model. Note that this is equivalent to calculating a difference between Equation (3.4) with a non-zero ν, and Equation (3.4) but assuming a constant period ($\nu = 0$). The measurement is not the rotation phase of each data point itself, but the global difference between the lightcurve phase expected from a constant-period solution and the observed rotation phase across each lightcurve. Hence we obtain a single value of a phase offset per lightcurve.

Measuring the phase offsets is done, once again, using pre-computed artificial lightcurve. So, at this stage it does not matter if the input shape was convex or not. This technique has been successfully used to confirm YORP-induced rotation rate change as discussed in the case of (54509) YORP in Section 1.4.4 (Lowry et al., 2007; Taylor et al., 2007, see also Figure 1.9b),

3.4 Application of spin-state analysis to asteroids and comets

The shape and spin-state modelling tools discussed here were used to determine whether a YORP-induced period change could be observed for NEAs (1917) Cuyo and (85990) 1999 JV$_6$,

targets of the ESO LP. The asteroid (1917) Cuyo was investigated using convex-profile inversion before this thesis work commenced. Hence a pole-on silhouette of the target, and period were known. However, the detailed pole solution and robust 3D shape model are developed for the first time. The object was investigated using the 'global' approach, as well as the two-parameter period-and-YORP fit. The limits on possible YORP values are derived, however a constant-period solution is currently preferred (Chapter 4).

Considering the shape and spin-state of the asteroid (85990) 1999 JV_6, only the period was known before the target became subject of this work. The contact-binary nature was first revealed with radar observations performed by the author, and a spin-state solution was developed. The 'global' approach was applied to the lightcurve data to determine limits on possible YORP detection, resulting in a non-detection. Then the radar-derived shape model was used to validate the constant-period solution using the phase offset measurement method (Chapter 5).

The spin-state analysis tools described here have a wider application. The information required to compute an artificial lightcurve can be used for example to display illumination of the surface of a small body and can serve to calculate quantities like average daily insolation of a surface element. Another interesting application was found for the phase offset measurements. They were used to prove that the rotation rate of the comet 67P/Churyumov-Gerasimenko, as seen via its optical lightcurves, cannot be explained with a single period or a gradual period change. The model developed during the earlier perihelion passage (Lowry et al., 2007) reproduced the shape of lightcurves obtained on approach of the Rosetta spacecraft to the comet 67P/Churyumov-Gerasimenko. However, the phase measurements done with the period corresponding to that initial model showed significant scatter for the recent observations. A second, much shorter, period was needed to fit the spacecraft lightcurves (Mottola et al., 2014). This result along with other cometary applications of the lightcurve-inversion and spin-state analysis tools are discussed in Chapter 6.

Chapter 4

Physical modelling of (1917) Cuyo using ground-based optical observations

4.1 Introduction

The asteroid (1917) Cuyo, initial designation 1968 AA, was discovered on 1st January 1968 at the Argentinian observatory El Leoncito by C.U. Cesco and A. G. Samuel (Schmadel, 2007). The object is a NEA with a semi-major axis of 2.15 AU and eccentricity of 0.51. It belongs dynamically to the Amor group of NEAs which members have their orbits entirely outside the orbit of Earth and inside the orbit of Mars. At a low ΔV, 8.6 km s^{-1} , (1917) Cuyo could be a potential target for future spacecraft missions. The ΔV is the velocity impulse required to put a spacecraft into a transfer orbit from low Earth orbit to rendezvous with the target (Shoemaker and Helin, 1978). The object has been selected for this work because of the extensive lightcurve data set available, spanning the period from 1989 to 2013. The availability of data combined with its near-Earth orbit, size, and estimated period made it a likely target for a YORP-induced period change detection.

The asteroid had been first subject to an observing campaign during its approach in 1989 when it passed as close as 0.1 AU from Earth. It was detected with the planetary radar at the Arecibo Observatory in September 1989 and with Goldstone radar in October 1989 (Ostro and Wisniewski, 1992). The radar observations were linked to optical photometric lightcurves taken with the 2.3 m Steward Observatory telescope at Kitt Peak, which allowed an estimate of the rotation period of $P = 2.693$ h (Wisniewski et al., 1997). The early convex-profile lightcurve inversion modelling revealed a 'quasi-triangular' pole-on outline of the shape (Ostro and Wisniewski, 1992, see Figure 4.1). The elongation of the asteroid's mean cross section was estimated to be 1.14, measured as a ratio the maximum to minimum breadth of the profile (Ostro et al., 1988b). The radar observations collected were only strong

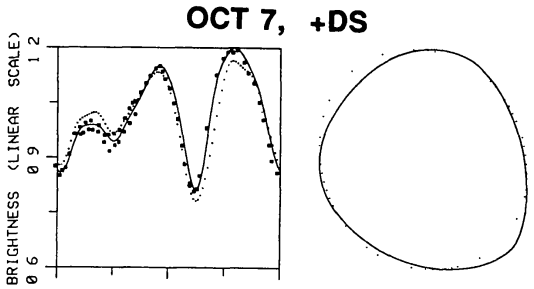

(a) south-pole-on model

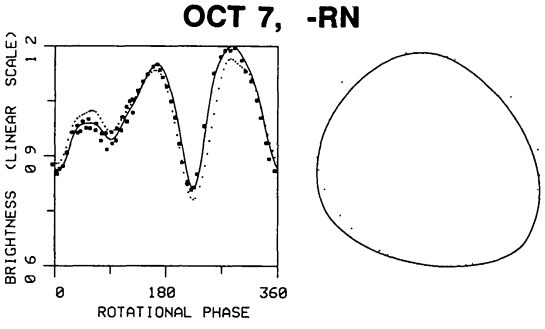

(b) north-pole-on model

Figure 4.1: A fragment of Figure 1 from Ostro and Wisniewski (1992). The upper row (a) corresponds to solution assuming we are looking at the asteroid's south pole (the spin vector pointing away form the observer) and lower row (b), north (the spin-vector pointing towards the observer). Both rows consist of two panels. The left panel shows a lightcurve obtained on 7th October 1989 (dots), a Fourier series fit (solid line), and a Fourier series constrained by the profile fit (dotted line). The right panel is a convex mean cross-section profile for a given pole solution (Ostro et al., 1988b). Regardless of the pole solution the profiles have a similar 'triangular' appearance, with a measure of the 'distance' of the profile from a circle, or non-circularity of 4. The maximum-to-minimum breadth ratio of the profiles is 1.13.

enough to confirm the small elongation of the asteroid and conclude the observing geometry for the photometry was close to equatorial. Size calculated from the radar echo bandwidths, combined with the synodic rotational period estimate, revealed quite a large NEA with a maximum breadth of approximately 3.9 km.

Later lightcurve studies refined the initial synodic rotational period estimates to (2.6905 ± 0.0007) h, by applying fast Fourier transform (FFT) in analysing the periodicity of the lightcurves (Velichko et al., 1989; Hoffmann et al., 1993; Harris, 1998; Erikson et al., 2000; Manzini and Behrend, 2013). A spectroscopic study from 0.8 µm to 2.5 µm shows that the object is an Sr type in Bus-DeMeo taxonomy, with a spectrum close to that of an ordinary chondrite meteorite rich in iron (Popescu et al., 2011). The asteroid (1917) Cuyo has also been a target for near-IR spectral observations with the Spitzer space telescope (Thomas et al., 2014). The object was observed 6 times on 24^{th} of June 2011, over a period of time covering a little more than 3 hours, and an additional spectrum was acquired on 14^{th} August 2011. The rotationally resolved spectra from Spitzer revealed no significant variation of the asteroids surface. Lastly, the Monte-Carlo methods were used to calculate the $H = 15.00 \pm 0.12$ and $G_{12} = -0.487 \pm 0.095$ from Pan-STARRS 1 observations (Vereš et al., 2015). The absolute magnitude, H, is the brightness of the asteroid as it would be measured at a distance of 1 AU at phase angle 0°, and it can give an indication about the objects size. The photometric parameter, G_{12}, is used to predict asteroid brightness at various phase angles using the two-parameters phase function (Muinonen et al., 2010).

The aim of this study was to develop the physical model of the asteroid Cuyo and search for possible signature of a YORP-induced spin-state change. The extensive observing campaign was performed primarily as a part of the ESO Large Programme and is described in Section 4.2. The wide range of observing geometries provided ground to produce a reliable shape model for the object, as described in Section 4.3. The accompanying spin-state analysis performed, and two approaches taken to seek YORP spin-up for this object are described in Sections 4.3.1 and 4.3.2.

4.2 Optical lightcurve data

4.2.1 The ESO LP observing campaign

The lightcurve observations of (1917) Cuyo with the YORP programme were carried out at changing observational geometries, necessary to precisely determine the position of the rotation pole and constrain the shape, see Figure 4.2. The primary source for the lightcurve observations was the NTT where the object was observed on 12 nights between April 2010 and April 2013, making up a total of 11 lightcurves (marked by black filled circles in the figure). Additional data were obtained from the ESO 2.2 m telescope (Chile) - 4 lightcurves, JPLs Table Mountain Observatory's 0.6 m (USA) - 6 lightcurves, and JPLs Palomar 5 m (USA) - 1 lightcurve. The YORP programme data from outside ESO LP is marked by open black

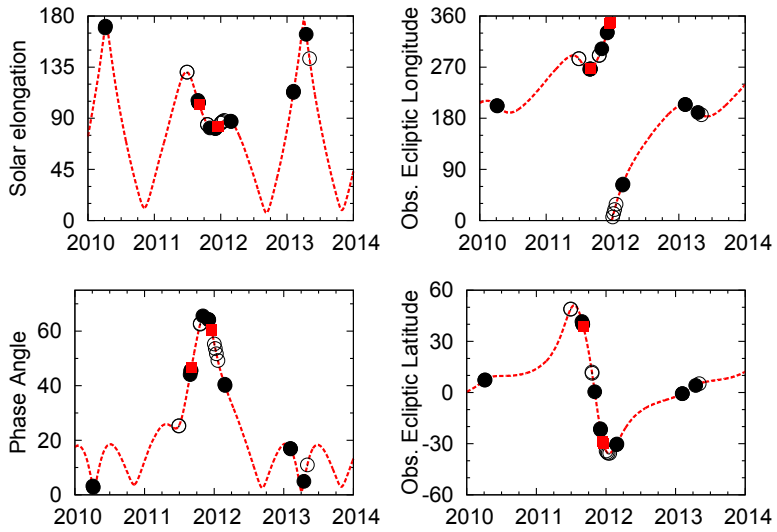

Figure 4.2: Asteroid (1917) Cuyo observing geometries during the YORP programme. The graphs display different quantities as a function of time (in years). The *solar elongation* is the angle between the positions of the Sun and the target asteroid as observed from Earth. The *phase angle* is the angle between the positions of Earth and Sun as observed from the target. The *observed ecliptic longitude* and *latitude* are the positions of the object in the ecliptic coordinate system, as observed from Earth. Optical lightcurve data from NTT are marked with closed black circles. Additional lightcurve data from 2010-2013 period is marked with open black circles. Red squares represent VISIR infra-red observations. The red dashed line is the objects observational ephemeris.

circles. There were additional lightcurve segments from Faulkes Telescope South 2 m (Australia), and data has been reduced but is not included in this thesis due to low signal-to-noise ratio of the lightcurves.

The asteroid (1917) Cuyo has been observed during 7 different observing runs at the NTT telescope in ESO's La Silla Observatory, Chile. Two Bessel filters were used for the NTT campaign, V and R. Detailed characteristics and transmission curves for those filters can be found on the EFOSC instrument website (ESO, 2016). All the NTT images had to be reduced using the standard steps described earlier (see Section 2.1.4), that is bias subtraction and flat-fielding using sky flats taken at either dusk or dawn. Additionally the images taken with R filter (lightcurves 9, 10, 13, 16, 19, 20, 21, 26 and 27, Table 4.1) had to undergo the fringe removal procedure. Relative photometry was performed according to the procedure outlined in Section 2.1.5.

The data reduction procedures are very similar regardless of the instrument. There are, however, some small differences. The ESO 2.2 m telescope at La Silla is equipped with a WFI instrument where data is simultaneously collected on 8 CCD chips, making a mosaic image. Before performing any reduction, the chip collecting the object images was identified and any data reduction was performed only on that chip. There was no special treatment required for the TMO and Palomar images other than bias subtraction and flat-fielding.

All of the reduction of the YORP programme data has been performed by the author of

ID	Date (UT)	R_h [AU]	Δ [AU]	α [$^\circ$]	Observing facility	Reference
1	05/09/1989 08/09/1989	1.19	0.32	48.23	Mt. Lemmon	Wisniewski et al. (1997)
2	07/10/1989 08/10/1989	1.08	0.14	54.10	Kitt Peak	"
3	06/10/1989	1.08	0.15	53.95	Kharkov	Velichko et al. (1989)
4	11/10/1989 12/10/1989	1.07	0.14	56.03	ESO 1 m	Hoffmann et al. (1993)
5	31/05/1995 01/06/1995	2.48	1.57	13.23	ESO Danish	Erikson et al. (2000)
6	02/08/2008	1.21	0.57	56.27	FOAM13	Beherend & Manzini[a]
7	05/08/2008	1.20	0.55	57.43		
8	07/08/2008	1.19	0.54	58.20		
9	04/04/2010	3.23	2.24	3.03	NTT	This work
10	06/04/2010	3.23	2.24	2.65		
11	28/06/2011	1.81	0.98	25.19	TMO	"
12	29/06/2011	1.81	0.97	25.31		
13	28/08/2011	1.39	0.73	44.25	NTT	"
14	31/08/2011	1.38	0.72	45.09	TMO	"
15	01/09/2011	1.37	0.72	45.48		
16	01/09/2011	1.37	0.72	45.80	NTT	"
17	19/10/2011	1.12	0.61	62.43	TMO	"
18	20/10/2011	1.12	0.61	62.70		
19	03/11/2011	1.08	0.59	65.65	NTT	"
20	02/12/2011	1.08	0.62	64.45	NTT	"
21	03/12/2011	1.08	0.62	64.24		
22	02/01/2012	1.19	0.75	55.45	ESO 2.2 m	"
23	07/01/2012	1.22	0.78	53.82		
24	13/01/2012	1.25	0.82	51.88		
25	21/01/2012	1.30	0.88	49.38		
26	24/02/2012	1.52	1.21	40.43	NTT	"
27	26/02/2012	1.54	1.23	40.01		
28	05/02/2013 06/02/2013	3.12	2.59	16.91	NTT	"
29	15/04/2013	3.21	2.23	5.17	NTT	"
30	03/05/2013	3.22	2.37	11.16	Palomar	"

Table 4.1: Lightcurve data sets used in this study. For each lightcurve, labelled with an *ID*, the *Date* of the beginning of the night is given as well as the heliocentric (R_h) and geocentric (Δ) distances measured in AU, and the solar phase angle (α). In some cases (lightcurves 1, 2, 4, 5, and 28) a single lightcurve has been composed of segments gathered over a few nights. Where applicable, a reference to the already published work is given.

[a] `http://obswww.unige.ch/~behrend/page_cou.html`

ID	frames	exposure [s]	total [h]	filter	observers
ESO 3.6 m New Technology Telescope + EFOSC2, La Silla (Chile)					
9	85	40	2	R	A. Fitzsimmons (QUB)
10	139	40	3	R	
13	104	25	0.8	R	
16	175	25	1.2	R	
19	180	15	2.5	R	
20	20	20		R	S. Duddy
20	62	15	2.5	R	
20	90	20		R	
21	55	20	3	R	
21	107	25		R	
26	140	45	1.8	R	C. Snodgrass (OU)
27	135	45	1.7	R	
28	22	180	1.1	V	S. Duddy / A. Rożek
28	58	180	2.9	V	
29	90	80	2	V	S. Lowry
JPL 0.6 m Table Mountain Observatory (USA)					
11	36	200	3	R	P. Weissman (JPL)
12	30	300	2	R	
14	32	240	3	R	
15	33	240	3	R	
17	21	240	2.25	R	
18	27	240	2.75	R	
ESO 2.2 m + WFI, La Silla (Chile)					
22	61	20	4	V	C. Snodgrass / S. Lowry
23	39	20	1	V	
24	39	20	1	V	
25	50	20	1	V	
Palomar 5.1 m + LFC (USA)					
30	20	240	3	Rb	P. Weissman

Table 4.2: The YORP programme data gathered for (1917) Cuyo. First column is the chronological *ID*, the same as in Table 4.1, followed by the number of *frames*, *exposure* time per frame in seconds, a *total* time-span of the lightcurve in hours, imaging *filter* used, and the *observers*. The sets are grouped according to the observing facility and then sorted chronologically. Where the affiliation of the observer is not with the University of Kent, it is given in parentheses.

this thesis with the exception of the April 2010 NTT run (lightcurves 9 and 10 in Table 4.1) that had been fulfilled by S. Duddy at Kent.

4.2.2 Previously published data

The general summary of all available lightcurve data for (1917) Cuyo included in this work is gathered in Table 4.1. A total of 30 lightcurves had been used, 8 of which are previously published data. The data sets from Mt. Lemmon and Kitt Peak, dating back from 1989 had been kindly provided by T. Michałowski, the co-author of Wisniewski et al. (1997). Four separate lightcurves segments were obtained by the authors and 'folded' forming two lightcurves, meaning that the two nights 5th and 8th September at Mt. Lemmon form one lightcurve (see Figure 4.3a), and the two nights of 7th and 8th October at Kitt Peak result in another one (see Figure 4.4a). Creating a composite of a pair of relative lightcurves requires that they would both have the same level, or can be represented with the same function of rotation phase. The authors applied the FFT method and fitting a Fourier series to the lightcurve data from the first lightcurve of a pair (Harris et al., 1989). Fitting the second lightcurve with the same Fourier series required a vertical offset of $0.06\,^{\mathrm{mag}}$ for September and $-0.005\,^{\mathrm{mag}}$ for the October lightcurves, as reported by (Wisniewski et al., 1997, Table I).

A more precise estimate of this vertical shift can be obtained by using a shape model, and this approach was used when folding the lightcurves to be used in the analysis presented here. As a shape model reproducing the newer data was already available (see Section 4.3.1), it was used to generate artificial lightcurves corresponding to both nights. Then the vertical offsets that put the observations closest to the artificial lightcurve was calculated. The results are magnitude offsets between mean values of each lightcurve and the model. The vertical offsets used to create the composites using this method are $0.073\,^{\mathrm{mag}}$ for the September 1989 lightcurve (see Figure 4.3b) and $-0.025\,^{\mathrm{mag}}$ for the October 1989 lightcurve (see Figure 4.4b).

The other observations from 1989, from Kharkov and ESO 1 m, are available from the Asteroid Photometric Catalogue (APC) (APC) (Piironen et al., 2001). The Kharkov data was only taken on one night, 6th October 1989 (Velichko et al., 1989), creating one lightcurve. The observations at ESO, spanning 4 nights, had been folded by the author to produce two lightcurves presented in Hoffmann et al. (1993, in Figure 1 and Figure 2, reproduced here in Figure 4.5 and Figure 4.6 respectively).

Retrieving this data had been challenging. Only three lightcurve segments related to Hoffmann et al. (1993) were available on-line and could be downloaded from the APC. The first one, labelled as 29th September, only contains three points, so it is too short to be considered useful as well as does not seem to match any of the sets depicted in Figures 4.5 and 4.6a. The second segment has 40 points and corresponds to the data plotted with crosses in Figure 4.5. This segment however does not match the amplitude and shape of other lightcurves from that epoch. The lightcurve has been labelled as spurious and later rejected when even the models that reproduced all of the other lightcurve data sets failed to reproduce this one. The last segment from APC, taken on 11th October, contains 21 points. The fragment is represented as circles in Figures 4.6a and 4.6b.

As there is exact timing information only about the circles in Figure 4.6, forming quite

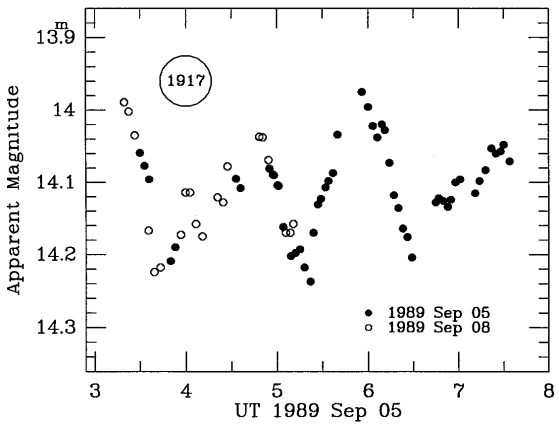

(a) Original folded lightcurve

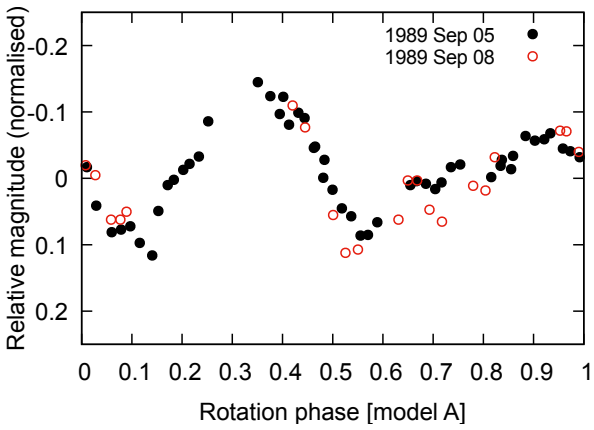

(b) Composite prepared by author

Figure 4.3: The graph in left panel was published with following caption: 'Composite lightcurve of 1917 Cuyo in September 1989' (see Wisniewski et al., 1997, Figure 56, panel a). The data was received from the co-authors as two segments corresponding to the different dates. The left panel (a) shows the lightcurve as originally published with apparent magnitudes plotted against the UT time of the first night and the data from second night moved vertically according to the Fourier series fit and with times adjusted to demonstrate the fit quality. The right panel (b) shows the lightcurve composite obtained using the convex model A to calculate the rotational phase (expressed as a fraction of full rotation) and the vertical shift between segments, additionally, magnitudes in the right panel were normalised by removing the mean value for the first night.

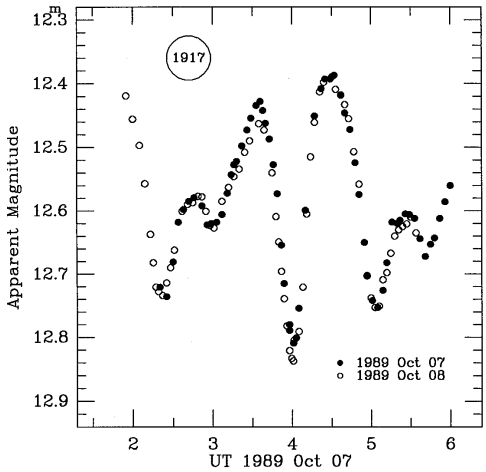

(a) Original folded lightcurve

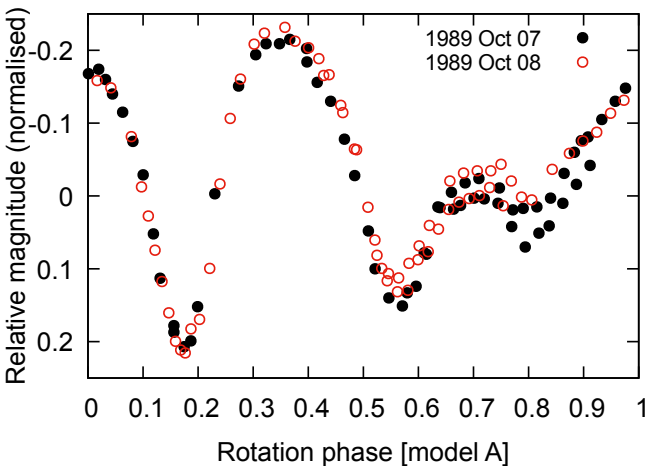

(b) Composite prepared by author

Figure 4.4: The graph in left panel was published with following caption: 'Composite lightcurve of 1917 Cuyo in October 1989' (see Wisniewski et al., 1997, Figure 56, panel b). The data was received from the co-authors as two segments corresponding to the different dates. The left panel (a) shows the lightcurve as originally published with apparent magnitudes plotted against the UT time of the first night and the data from second night moved vertically according to the Fourier series fit and with times adjusted to demonstrate the fit quality. The right panel (b) shows the lightcurve composite obtained using the convex model A to calculate the rotational phase (expressed as a fraction of full rotation) and the vertical shift between segments, additionally, magnitudes in the right panel were normalised by removing the mean value for the first night.

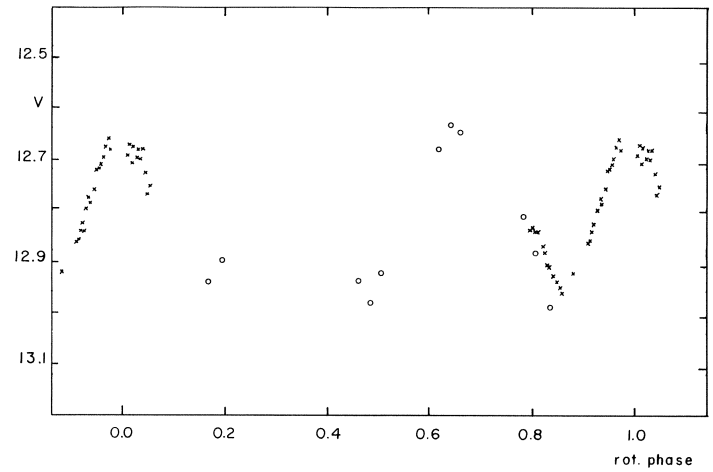

Figure 4.5: The Figure 1 from Hoffmann et al. (1993). The original caption was 'Composite lightcurve of 1917 Cuyo between 1989 September 30 (circles) and October 2 (crosses).' The data represented with crosses could be retrieved from APC. However, this lightcurve is not included in the analysis, as the lightcurve features and amplitude could not be reproduced even by the models that match all other data.

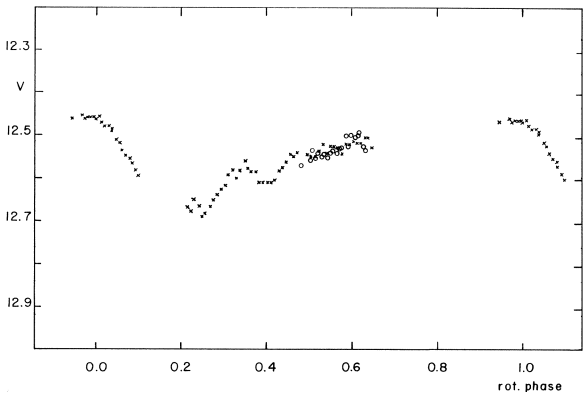

(a) Original folded lightcurve

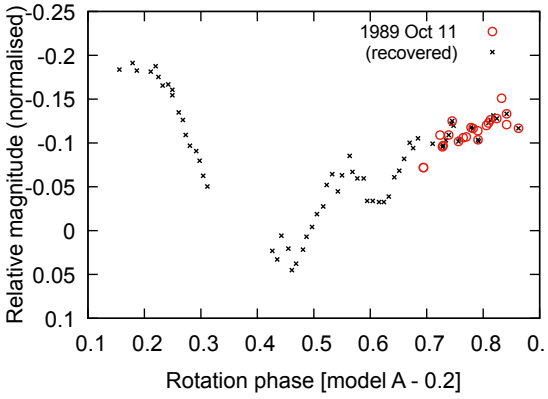

(b) Composite prepared by author

Figure 4.6: The Figure 2 from Hoffmann et al. (1993). The original caption was 'Composite lightcurve of 1917 Cuyo of 1989 October 11 (circles) and 12 (crosses).' Only the data represented with circles was available for download from APC. The points represented with crosses were retrieved using digital image analysis software and information in the original publication.

a short sequence without many features, an attempt was made to retrieve the information from the longer segment, from 12th October, pictured with crosses. The author phased the observations from two consecutive days using a period of 2.7 h and plotted the magnitudes of the asteroid against the rotation phase. There is no information included on when the observations on 12th October exactly begun and what is the chronological sequence of points depicted as crosses in Figure 4.6a. Under assumption that the data marked with crosses was taken on the same night as the circles the Julian dates of the observations can be recreated. Given the error in the period used by Hoffmann et al. (1993) will lead to an error in the rotation phase of up to 0.03 of the full rotation (10°) over the 24 h interval between observations on 11th and 12th October.

Points in the Figure 4.6a had been digitized using Engauge Digitizer software (Mitchell et al., 2002, Version 5.2). The values of rotation phase were recorded, for both the circles and crosses, with a resolution of 0.0012 rotation and an estimated error of 0.002, and corresponding magnitudes with resolution of 0.0012 ^{mag} and error of ∼0.002. The relation

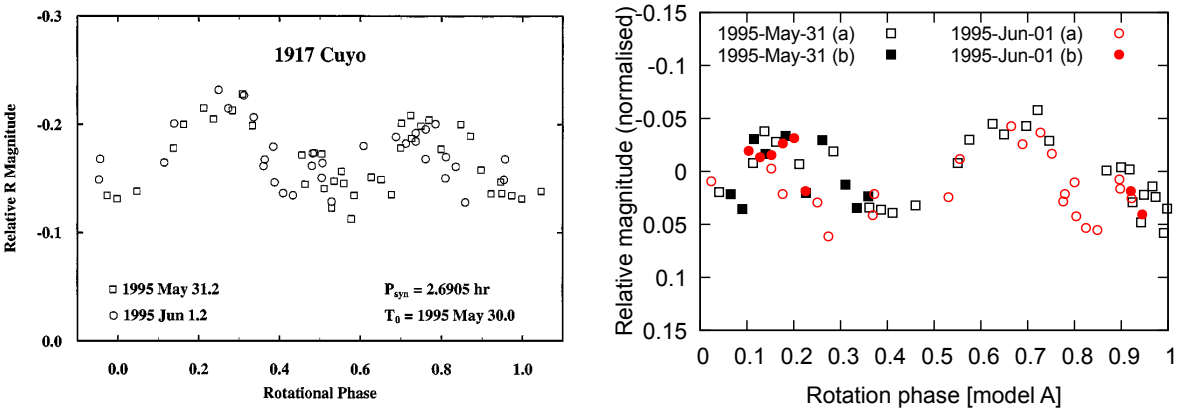

(a) Original folded lightcurve

(b) Composite prepared by author

Figure 4.7: The original caption of the graph in the left panel is 'Composite lightcurve for 1917 Cuyo during the 1995 apparition' (see Erikson et al., 2000, Fig. 2). The left panel (a) shows the lightcurve as originally published with relative R magnitudes plotted against the rotational phase obtained from the Fourier series fit. The right panel (b) shows the lightcurve composite obtained using the convex model A to calculate the rotational phase (expressed as a fraction of full rotation) and the vertical shift between segments, additionally, magnitudes in the right panel were normalised by removing the mean value for the first night.

between Julian dates of the observations downloaded from the APC and the rotation phase on Figure 4.6a had been found by comparing the shapes of plots of both representations of the same data. The actual time, T - measured in days, of observations was set against the rotation phase, ϕ - measured between 0 and 1 as a fraction of full rotation, and the following linear relation was fitted

$$T = T_0 + P \cdot \phi, \tag{4.1}$$

where T_0 is the time when $\phi \equiv 0$ and P is the period (in days). The conclusion was that a $T_0 = 2\,447\,810.616\,552\,55$ and a $P = 0.1127\,\mathrm{d} (\equiv 2.7048\,\mathrm{h})$ is required to obtain the actual JDs from the plotted rotation phases for the circle-data in Figure 4.6a (this value is different from the $0.1125\,\mathrm{d} (\equiv 2.7\,\mathrm{h})$ used by the author, but still gives values within the error of measurement). The relation had been used to produce synthetic times for the crosses (see Figure 4.6b). The author of this thesis acknowledges that adopting this approach might introduce errors in period-change determination. However, there is other data available from this epoch that provided grounds for a reliable measurement and shows good agreement with the recovered lightcurve. The two approaches to the shape modelling adopted here give consistent results. The first one does not take into account the archival data when determining shape (described in Section 4.3.1), and the other, more global approach, includes the archive observations (presented in Section 4.3.2).

The data from 1995 observations at the ESO Danish 1.5 m telescope were provided by the author (see Erikson et al., 2000, Fig. 2). The published folded lightcurve is labelled as made up of two segments, with squares representing '1995 May 31.2' and circles for '1995

Jun 1.2' (see Figure 4.7a). However, the data provided by the author was divided into four segments (two for each night, see Figure 4.7b). Model A was once again used to generate artificial lightcurves for the dates when the lightcurves were collected and calculate the vertical offsets between mean values of all segments. Using the first data set (labelled '1995-May-31 (a)' in Figure 4.7b) as a reference the required offsets for the other segments are $0.002^{\,\mathrm{mag}}$ (for '1995-May-31 (b)'), $-0.014^{\,\mathrm{mag}}$ (for '1995-Jun-01 (a)'), and $0.004^{\,\mathrm{mag}}$ (for '1995-Jun-01 (b)').

We had access to the 2008 data set from FOAM13 via private communication, the lightcurve plot can be viewed on-line (Manzini and Behrend, 2013). The lightcurve monitoring campaign within the ESO LP between April 2010 and May 2013 had been detailed in Table 4.2. Finally, it has to be noted that there are recent lightcurve observations performed by Warner (2014b, 2015a), that can be accessed via the MPCs Asteroid Lightcurve Catalogue (Warner et al., 2009), which were published after the bulk of this analysis presented here was done. Those lightcurves have much higher noise than other data used in this analysis and the shape and location of lightcurve features could not be reproduced with any of the models presented here. As this issue would require an investigation that goes beyond the scope of this work, they were not included in this thesis.

4.3 Shape modelling with visual lightcurve data

4.3.1 Shape modelling with 2008-2013 lightcurve data

The YORP effect is a very subtle change of rotation period, so in order to be detectable it requires precise monitoring of rotation rates over sufficiently long periods of time. For (1917) Cuyo the data set spans 24 years of lightcurve observations. The ESO LP campaign spans only 3 years. Expanding this to 5 years, by including the 2008 data set (Manzini and Behrend, 2013), gives a baseline of 1736 days. The YORP torque would have to be stronger than about $1 \times 10^{-7}\,\mathrm{rad/d^2}$ for the shift in rotation phase to be larger than 10°. In most cases of the direct YORP detections, the torques are of the order of $1 \times 10^{-8}\,\mathrm{rad/d^2}$ (see Table 1.2). Equation (3.4) can be used to calculate a possible phase offset in this period using a typical YORP strength of $1 \times 10^{-8}\,\mathrm{rad/d^2}$. The result is an offset of 0.8°, which would be difficult to reliably measure. Moreover, the asteroid was observed in near infrared with the VISIR instrument within the ESO LP. The infra-red data, a preliminary shape model, and the ATPM (Rozitis and Green, 2011, ATPM) were used to estimate the YORP acceleration strength to be $\nu = (1.568 \pm 0.486) \times 10^{-10}\,\mathrm{rad/d^2}$ (Rożek et al., 2017). This kind of YORP-induced acceleration would create an even smaller phase offset, of only about 0.014° (48.7″), so it should be safe to assume a constant-period model for the 2008-2013 subset of lightcurves.

The initial step in the shape modelling is to obtain an estimate of the synodic rotation period at the beginning of the time interval covered by the lightcurves (see Figure 3.2 for an

outline of the process). The period is then refined and updated at various stages of the shape and spin-state modelling, but a good starting point is essential. Normally FFT methods (Harris et al., 1989) would be used to seek an initial approximation on the period, but as a literature estimate for the synodic period of 2.6905 h (Wisniewski et al., 1997) was available, it has been used as a starting point.

The shape modelling followed Steps 1 and 2 of the convex lightcurve inversion procedure (see Figure 3.2). The whole celestial sphere was initially divided into a $5^\circ \times 5^\circ$ grid, in ecliptic longitude λ and latitude β. At each point on the grid a convex shape model and sidereal rotation period were optimised (see Section 3.1.2 for details) while keeping the pole position fixed. Goodness of fit χ^2 values, for fitting the model to the 2008-2013 lightcurves, were recorded for each model. After this initial scan was finished the search for the pole position was then narrowed down to a region of the celestial sphere with the lowest χ^2 and a refined $1^\circ \times 1^\circ$ scan was performed with results presented in Figure 4.8.

The scan produced two very similar models with poles separated by 15° in ecliptic latitude. The two solutions A and B, detailed in Table 4.3, give a very good fit to the rotational lightcurves from the 2008-2013 period, within 1 % of the lowest χ^2. Both models have a similar, slightly flattened shape and a 'quasi-triangular' outline, when viewed from the pole-on

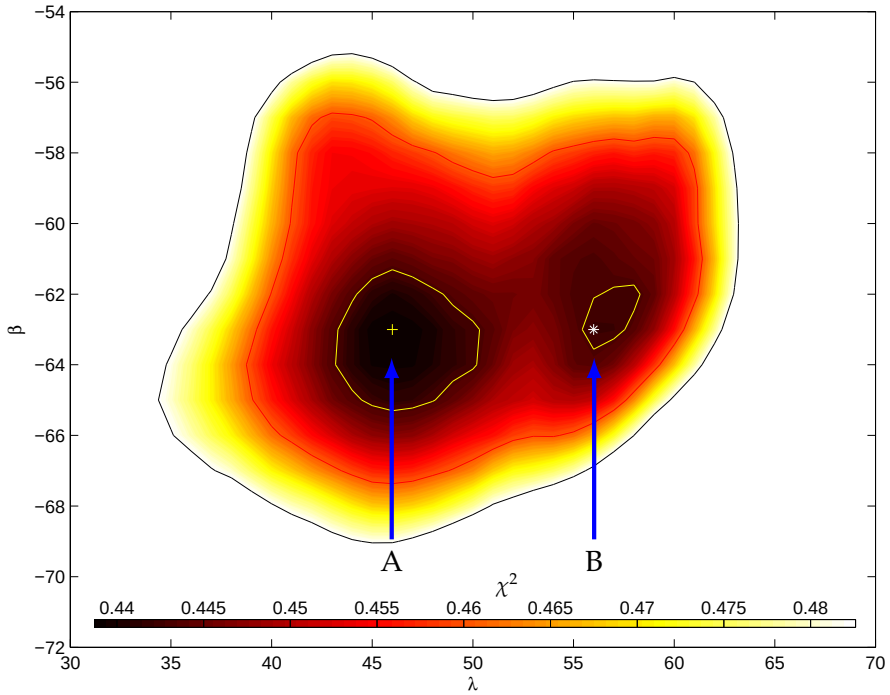

Figure 4.8: For a $1^\circ \times 1^\circ$ grid of possible pole positions - in ecliptic longitude λ and latitude β - shape model and sidereal rotation period were optimized. Goodness-of-fit χ^2 values for each model are colour-coded on a fragment of the celestial sphere here, $\lambda \in (30^\circ, 70^\circ)$, with darker colors marking the lower χ^2 values. The yellow contour line indicates a 1% increase relative to the minimum χ^2 value obtained (marked with a '+'), the black contour line is a 10% increase. Two best pole solutions, A and B, were chosen with the smallest χ^2 within each yellow contour.

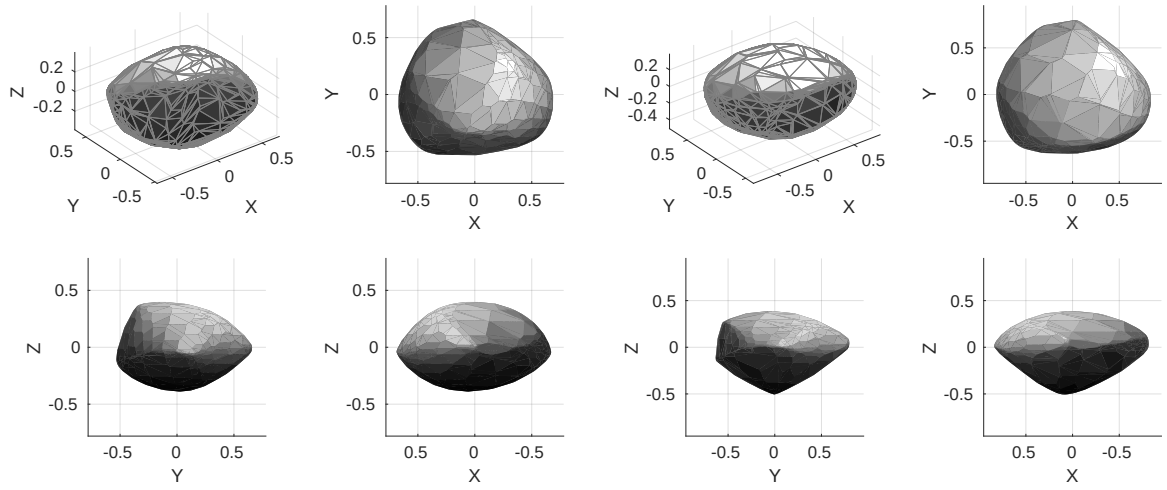

(a) Model A **(b)** Model B

Figure 4.9: The two similar shape models above were derived from pole solutions A (Figure 4.9a) and B (Figure 4.9b), which also reproduce the archived LC shapes (from 1989 and 1995). Clockwise, from upper left corner each set of figures represents a general view of the shape, and views along the axes corresponding to principal moments of inertia, from shortest (Z), throught intermediate (Y) to the longest (X). There is no relation between the longest axis of inertia and the x-axis of the body, as used in shape modelling and spin-state analysis.

direction as shown in Figure 4.9. The profile of the asteroid is consistent with the mean cross-sections obtained from early convex-profile lightcurve inversion performed for (1917) Cuyo, compare with Figure 4.1 (Ostro and Wisniewski, 1992, Figure 1). Neither of the shapes can be discarded straight away as seeming non-physical, they both have spin-axes aligned with the maximum moment of inertia, and are not excessively flattened. In fact, the diamond-like shape B resembles the shape of asteroid (2867) Steins, as imaged by the Rosetta spacecraft during its flyby in 2008 (Keller et al., 2010).

Having well-established shape models for the object enabled an attempt to measure the YORP factor for both of them. The two models were used to generate artificial lightcurves for the 1989 and 1995 data. The values of T_0 and P_0 tabulated in Table 4.3 were used to compute rotation phases for the archive lightcurves, see Figures A.1 and A.2. It is worth noting that both models produce a slight phase offset for the 1989 data indicating a possible period change. For the purpose of YORP measurement it is preferable to have the starting point of the model (the epoch, or moment in time when the rotation phase is 0) set at either end of the observing data set. As the models have been generated using only the most recent data, their T_0 are set in 2008. The first step to the YORP modelling was then to determine a new T_1, that would be a date close to the first observations performed in 1989. The first three lightcurves were used for that purpose and synthetic lightcurves were compared with the observations. A range of possible starting dates, T_1, were tested with a step of 0.5° of rotation. The best-fit values for the three lightcurves were then averaged and a new T_1 was recorded (Table 4.3).

Using the new starting point for each model, a grid of possible YORP factors, ν, and initial sidereal rotation periods, P_1, were scanned. The artificial lightcurves were generated using the fixed pole orientation and shape, the model sidereal period P_0 and the newly determined T_1. The asteroid brightness was calculated for all available observations and for 100 points evenly spaced in rotation phase across the full rotation. The lightcurves were then interpolated to achieve a continuous representation. At each point of the grid the observations were phased with the new period and YORP acceleration. The χ^2 of the fit of artificial lightcurves to all the observations at each point were recorded. To illustrate the best-fit for each model we plot the 1σ and 1 % error ellipses in period and YORP space, Figure 4.10. The 1σ error ellipse corresponds to an increase of χ^2 of 2.3 above the minimum,

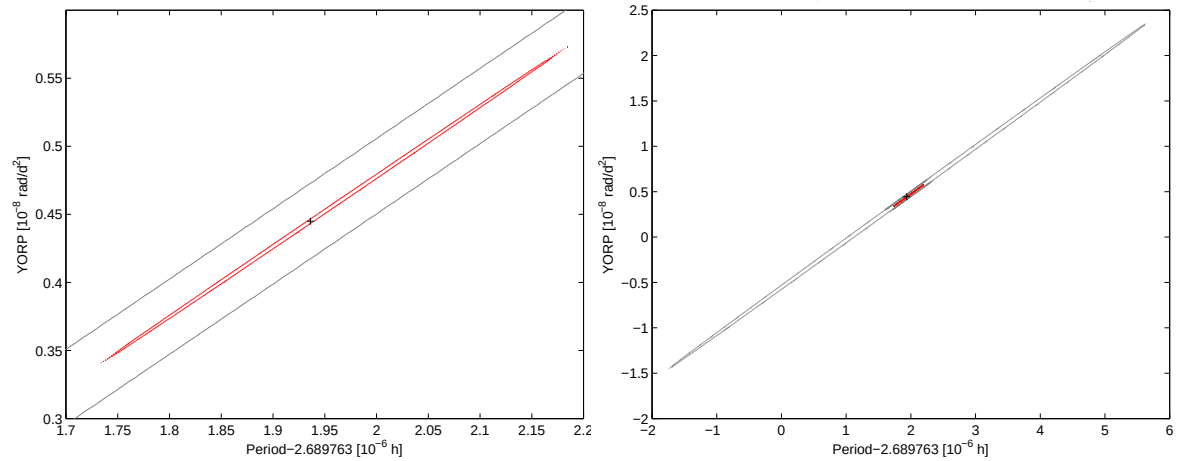

(a) Model A **(b)** Model A

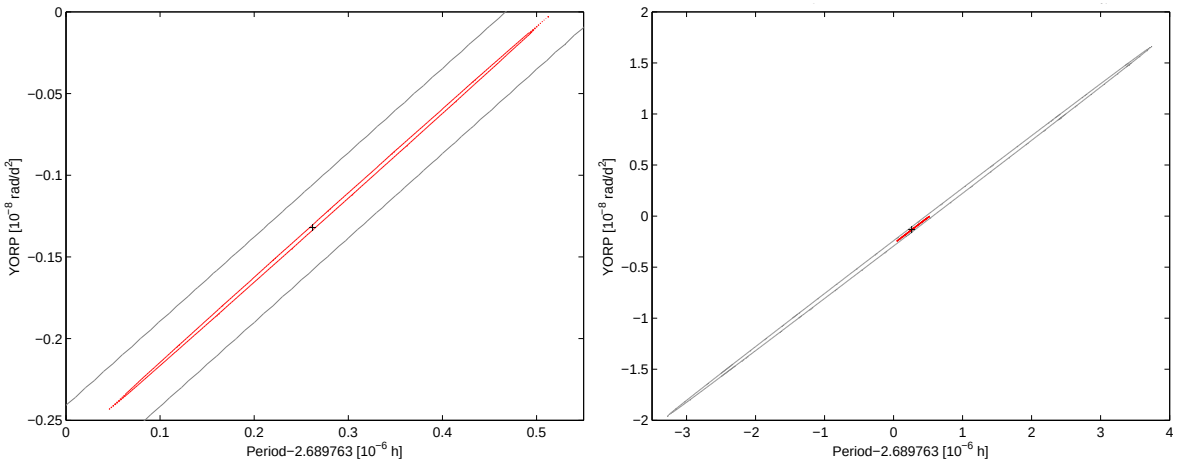

(c) Model B **(d)** Model B

Figure 4.10: Panels on the left focus on the red contours representing the 1σ error ellipses for YORP strength (rotation-rate change) versus initial synodic rotation period two-parameter fit for models A (Figure 4.10a) and B (Figure 4.10c). Panel on the right represent a zoomed-out view, with the blue-outlined error ellipse marking a 1 % increase in χ^2 value, which the author considers more realistic representation of the measurement error for the YORP/period scan, panels correspond to models A (Figure 4.10b) and B (Figure 4.10d). Black crosses mark the best-fit solution. It is clear that the 1 %-ellipses encompass a constant-period solution for both models.

Model	A	B	C
Data range	2008 to 2013	2008 to 2013	1989 to 2013
λ	$(46 \pm 5)°$	$(56 \pm 5)°$	46°
β	$(-63 \pm 5)°$	$(-63 \pm 5)°$	−62°
T_0 [JD]	2 454 680.0	2 454 680.0	2 456 416.0
P_0 [h]	2.689 763 0	2.689 763 4	2.689 764 2
T_1 [JD]	2 447 774.0309	2 447 774.0312	—
P_1 [h]	$2.689\,764\,9(\pm 3.3 \times 10^{-6})$	$2.689\,763\,7(\pm 3.5 \times 10^{-6})$	—
ν [rad/d^2]	$(0.4 \pm 1.7) \times 10^{-8}$	$(-0.1 \pm 1.8) \times 10^{-8}$	$0^{+1.5 \times 10^{-8}}_{-0.7 \times 10^{-8}}$

Table 4.3: Summary of model parameters for the three convex-inversion models of (1917) Cuyo. Models A and B were developed from the 2008-2013 data, model C is the best-fit solution for the modelling than involved all available data. The table lists: the ecliptic coordinates of the rotation pole, longitude (λ) and latitude (β), T_0 – the model epoch according to `CONVEXINV` output (set at the beginning of the 2008 data for models A and B, and at the end of 2013 for model C), P_0 – the period for a constant-period solution as output by the `CONVEXINV`, T_1 – the new epoch of the model (calculated to fit the first lightcurves in the 1989 data), P_1 – the best-fit period solution, and ν– the best-fit YORP spin-up factor. The uncertainties of P_1 and ν are estimated based on 1 % increase of minimum χ^2 value.

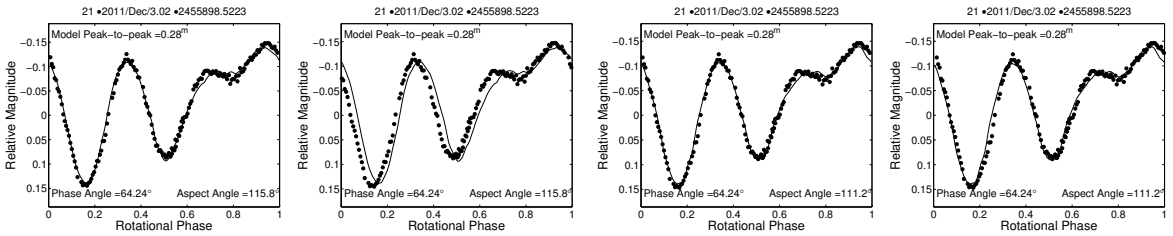

(a) With YORP **(b)** Without YORP **(c)** With YORP **(d)** Without YORP

Figure 4.11: Examples of lightcurve fits for both models and $T_1 + 22$ years (lightcurve 21, NTT Run K, Table 4.1). The artificial lightcurves from left to right were generated with: model A with T_1, measured YORP factor $\nu = 4 \times 10^{-9}$ rad/d^2 and starting period P_1 (a), model A with T_1 and constant period P_1 (b), model B with T_1, measured $\nu = -1 \times 10^{-9}$ rad/d^2 and initial period P_1 (c), and model B with T_1 and a constant P_1 (d).

as the fit is considered a 2-parameter fit (Wall, 1996). However, the χ^2 values are quite large, given the noise in some data sets. Additionally, the data set is not treated as a whole, but each artificial lightcurve level is separately adjusted to best fit the data for each P and ν pair. Therefore one should be careful when treating fitting for period and ν as a two-parameter fit. The author considers the 1 % increase of χ^2 value above minimum to be a more realistic measure of uncertainty of the result.

The exact values of best-fit period and YORP factor are reported in Table 4.3, including uncertainties of period, P_1, and ν estimated from the 1 %-ellipse. It could be concluded that a slight YORP-induced slow-down is observed for both shapes A and B. However, careful inspection of lightcurve fits for model B shows a very minuscule improvement of the fit after including the YORP spin-up factor. An example of such fit is presented in Figure 4.11. Two sets of panels, for models A and B, show the fit of an artificial lightcurve to the data gathered

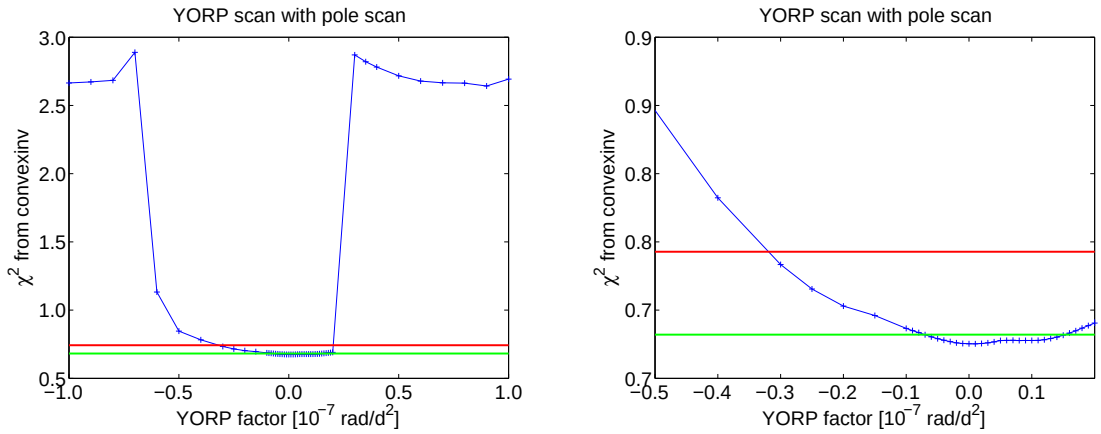

Figure 4.12: Minimum χ^2 value from each plane versus YORP factor plot has a 'top-hat' shape with a wide flat bottom (a). The green line marks the best-fit χ^2 minimum +1%, red +10%. A zoomed view of the 'top-hat' (b) shows that there is a wide range of possible solutions including spin-up, spin-down, or no period change.

during December 2011 NTT run (lightcurve labelled 21 in Table 4.1). In each case two fits are shown. The first one shows the model propagated from T_1 with period, P_1, changing due to a YORP factor ν. The second panel shows the same model, also propagated from T_1, but this time the period, P_1, is treated as constant. The full set of artificial lightcurves generated with the T_1, P_1 and ν values for both models can be found in the Appendix Figures A.3 and A.4.

4.3.2 Global shape modelling including archive data

Another approach to dealing with the long time-span of the observations was to use all available lightcurves for modelling (1917) Cuyo at once. In order to account for the possibility of changing sidereal period, the YORP-induced acceleration of the rotation rate had to be included in the modelling procedure, as discussed in subsection 3.1.2.

A fragment of celestial sphere was selected around the region containing the likely pole position, as concluded from the previous section. For the full data set an initial period and shape optimization was performed on a grid of possible pole positions. The T_0 was fixed to be 2 456 416.0, which is a date in 2013, close to the last observation. The last few years of observations provide a denser data set, so the selection of the T_0 at this end should provide the modelling procedure with solid starting conditions when propagating the model backwards to the archive data sets. At each grid-point χ^2 values of the fit of artificial lightcurves to the data were recorded creating a χ^2-plane. The χ^2-planes were created for a range of YORP factor values between -1×10^{-7} and 1×10^{-7} rad/d^2 as shown in Figure 3.4.

The best-fit models from each χ^2-plane were then extracted and examined. The smallest χ^2 value from each YORP plane has been plotted against the YORP factor corresponding to that plane to identify the best solution and assess the possibility of a YORP detection. The

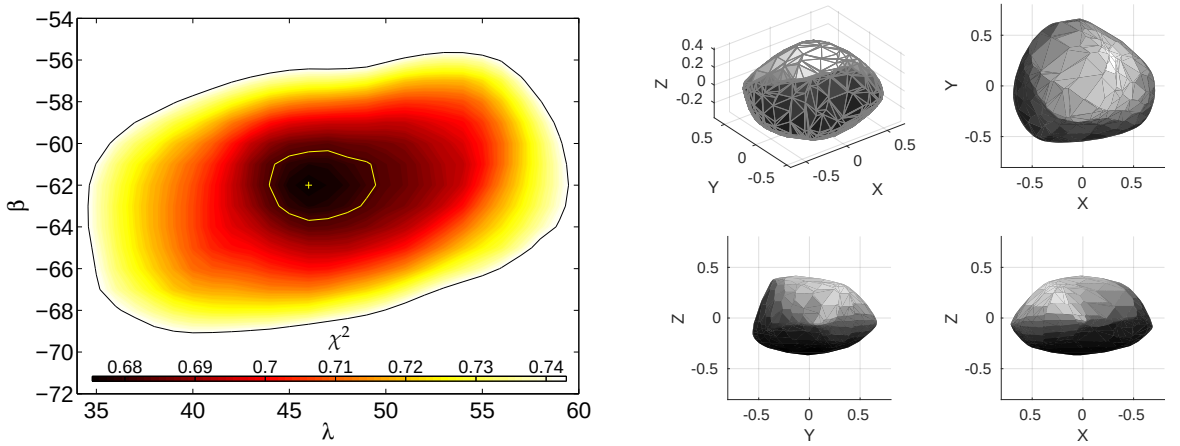

(a) χ^2 plane obtained with $\nu = 0$ **(b)** Model C projections

Figure 4.13: The results of the pole scan with full data set and the ν value set to 0 are shown in the left with the χ^2 values colour-coded. In the χ^2 plot the best solution is marked with a yellow cross, the yellow line marks 1 % increase of χ^2 value above the minimum, and the black contour marks 10 % increase (compare to Figure 4.8). The best-fit model, model C, is shown in the left on four panels (for descriptions of the panels see Figure 4.9). The shape strongly resembles the best-fit model from just the most recent data, model A (see Figure 4.9a). The spin-state parameters for this model are also close to model A (see Table 4.3).

shape of the resulting plot resembles an inverted top-hat, see Figure 4.12. While the best-fit solution is at $\nu = 1 \times 10^{-9}\,\mathrm{rad/d^2}$ the 0-YORP solution has 0.01 % worse χ^2, so it is the latter that is adopted here as model C, see Table 4.3. The broad minimum of the χ^2 plot envelops all possible scenarios, including no-YORP (constant period), as well as positive and negative rotation rate change solutions. All of those lay within 1 % above the minimum χ^2 value. The three cases are indistinguishable, with all three cases providing models that can perfectly reproduce shapes of lightcurves from all the epochs. The lightcurve fits of model C to all available data can be found in the appendix Figure A.5. For both the spin-up and slow-down scenarios one example of lightcurve fit is shown in Figure 4.14. Even though in all the plots the model has been propagated with a starting point, T_0, set in 2013 and all of them have different starting period values and YORP factors, they all match the lightcurve taken in 1989.

4.3.3 Summary and discussion of the spin-state analysis

Lightcurve observations of the asteroid (1917) Cuyo spanned almost 24 years. In such a long time a YORP-induced change of rotation period, on the order of magnitude typical to the detections to date, should be clearly visible. For example, a $\nu = 1 \times 10^{-8}\,\mathrm{rad/d^2}$ (a typical value of YORP-induced rotation acceleration for the detections made to date, see Table 1.2) would produce a phase offset between the artificial lightcurves and the data of about 44°. Two different approaches were applied to assess the spin-state of this object. At this stage any YORP-induced change of the rotation rate can be neither confirmed nor totally ruled out. The two models that had been developed from only the most recent data both indicate a

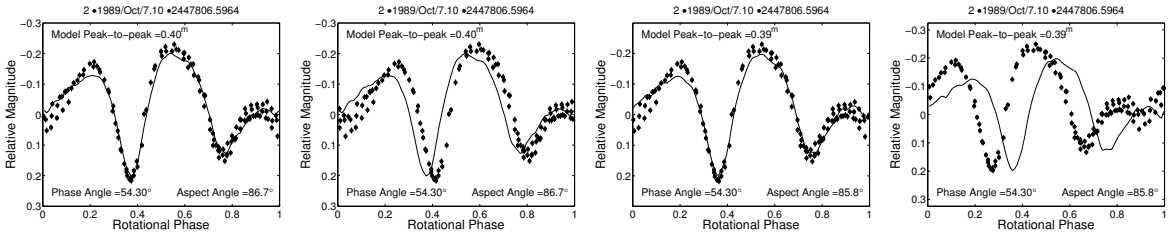

(a) Model C- **(b)** C- , no YORP **(c)** Model C+ **(d)** C+ , no YORP

Figure 4.14: Lightcurve fits to best-fit models from selected YORP planes. All models have been generated with $T_0 = 2456416.0$ in Julian days (year 2013, at the end of the last lightcurve set). The example lightcurve was taken at $T_0 - 22$ years (lightcurve 2, (Wisniewski et al., 1997), Table 4.1). Both models have been developed using the same lightcurve set as model **C** (Table 4.3). The model **C-**, in the two panels to the left (a and b), is representing a YORP-slow-down, with $\nu = -70 \times 10^{-10}\,\mathrm{rad/d^2}$, and rotation pole $\lambda = 46°$, $\beta = -62°$. The model **C+**, in the panels to the right (c and d), is an example of a model showing a YORP-spin-up, with $\nu = 150 \times 10^{-10}\,\mathrm{rad/d^2}$, and rotation pole $\lambda = 48°$, $\beta = -63°$.

slight slow-down of the rotation rate. The models utilising all available lightcurve data from across the 24 years of observations can be developed for a constant period solution just as well as for a spin-up or slow-down.

One possible source of a large uncertainty in the period and spin-up measurements can be linked to the quality of the archive data sets. The observations can be essentially divided into two epochs, the earliest observations from 1989 together with the ESO Danish telescope lightcurves from 1995, and the most recent observations from 2008-2013. In terms of looking for a quadratic trend in phase offsets, as was found for Itokawa (Lowry et al., 2014, Figure 1), the YORP fitting can be compared to trying to decide whether a parabola or a straight line fits two points better. What is required to resolve the ambiguity is another series of observations of the object in a somewhat more distant future, for example during the next radar opportunity in 2030 when the target would pass about 0.0896 AU from Earth allowing for high-resolution imaging (which, while at a distant date, will remain a part of the author's scientific plans).

4.4 Conclusions

The analysis of lightcurve data for (1917) Cuyo allowed a determination of a few robust convex shape models. Two possible models were developed using an extensive visual lightcurve data set from 2008-2013, both indicating a slight spin-state change when linked to the archived data set, but with uncertainties encompassing the constant-period solution. On the other hand, the recent observations can be successfully combined with archived data from 1989 and 1995, at the level of shape-modelling to create models that reproduce lightcurves for all possible scenarios, that is spin-up, slow-down, and constant period. Currently, a YORP-induced rotation-rate change over the entire time-frame of our data cannot be confirmed, however the range of possible ν values was constrained. To measure any possible

YORP value an additional data point would be required to determine the quadratic trend in the phase offset change with time, or an independent shape and pole orientation estimate, perhaps by radar. The three shape models that were obtained give consistent lightcurve fits and ν measurements. The shapes are also in agreement with earlier lightcurve estimates (Ostro and Wisniewski, 1992).

The results of this work were applied in further physical characterisation of the asteroid. The ESO LP data includes near-infra-red observations from VISIR at ESO VLT. Those observations were combined with the shape models, and the ATPM model (Rozitis and Green, 2011, 2012, 2013) was used to establish some physical properties of (1917) Cuyo. Thermophysical modelling with the ATPM provides valuable constraints on physical properties required to make a theoretical prediction of the strength of the YORP and Yarkovsky effects that can be compared with the observed values. Assuming that $H = 14.7 \pm 0.3$ and $G = 0.23 \pm 0.10$. The geometric albedo was estimated to be $P_v = 0.25 \pm 0.07$. The maximum equatorial diameter $D_{eq} = (4.33 \pm 0.05)$ km compares well with the radar-derived $D_{eq} = 4.6^{+0.6}_{-0.4}$ km, Ostro and Wisniewski (1992)). The thermal inertia value is quite small, $\Gamma = (50 \pm 10)\,\mathrm{J\,m^{-2}\,s^{-1/2}\,K^{-1}}$, which, together with quite high roughness fraction of 0.72 ± 0.17, indicates a surface covered in fine regolith. The thermal inertia mainly affects the Yarkovsky effect, a non-gravitational force affecting orbital motion of asteroids. The surface roughness changes the beaming of thermal radiation and significantly alters predicted strengths of YORP and Yarkovsky. This combination of parameters enabled a YORP strength prediction of $\nu = (1.568 \pm 0.486) \times 10^{-10}\,\mathrm{rad/d^2}$. This value lies within the uncertainties of values measured for all three asteroid shapes.

Chapter 5

Combined planetary radar and lightcurve observations of asteroid (85990) 1999 JV_6

5.1 Introduction

The asteroid (85990) 1999 JV_6 is an object of the Apollo group discovered on 13th May 1999 by MIT Lincoln Laboratory's Near-Earth Asteroid Research program (Stokes et al., 2000), classified as a Potentially Hazardous Asteroids due to its absolute magnitude and close approaches to Earth. It has been identified as the spectral type Xk (Binzel et al., 2001) in the SMASS taxonomy (Bus, 1999; Bus and Binzel, 2002). The spectral class contains asteroids with rather broad spectral features marking a transition between classes X and K. The Xk-type spectral properties are attributed to the presence of orthopyroxene, an iron-bearing mineral from the pyroxene family (Fornasier et al., 2011). The X-complex to which this class belongs is the third most numerous among the near-Earth population (Binzel et al., 2004).

The thermal-infra-red observations from the ExploreNEOs (Trilling et al., 2010, near-infra-red survey with the Spitzer Space Telescope) had been used to estimate the object's diameter to be 498^{+134}_{-88} m (Mueller et al., 2011). The optical observations from January 2014 demonstrated a large amplitude of the lightcurve, $0.87^{\,\mathrm{mag}}$ (Warner, 2014a). The observations also allowed an initial estimate of the synodic rotation period of (6.538 ± 0.001) h using Fourier transform of the lightcurves. The object was followed up in January 2015 when the lightcurve amplitude was slightly larger, $0.93^{\,\mathrm{mag}}$, and the synodic rotation period was determined to be (6.543 ± 0.002) h (Warner, 2015b). Both data sets are available via the Minor Planet Centre (Warner et al., 2009) and were included in the analysis.

The object was previously observed through our YORP programme in 2007 and 2008 with the 2.5 m INT in La Palma (Spain). It was then monitored photometrically as one of the ESO LP targets at the NTT in 2013. The specific orbital configuration of the object offered an opportunity to observe it with ground-based radars. Two consecutive proposals were submitted and A. Rożek was successful in securing over 20 hours of time at the Arecibo Planetary Radar over two observing runs in January 2015 and January 2016. The object was also followed by the Goldstone Solar System Radar (GSSR) team in January 2016, and additional lightcurve data were collected within the YORP programme at TMO in 2015, and at INT in 2016.

A comprehensive description of the observing campaign is contained in Section 5.2. The radar and lightcurve data were combined and analysed in order to obtain a realistic shape model of (85990) 1999 JV_6. This has been a complex and multi-stage process. Initial modelling was done as part of the first radar observing run and training at the Arecibo telescope in January 2015, see Section 5.3. The shape model was later improved and updated by adding data from the 2016 observations, covered in Section 5.4. The results of spin-state analysis, that uses all available lightcurves and the best radar-derived model, are detailed in Section 5.5.

5.2 Observing campaign

5.2.1 Optical lightcurve data

The visual lightcurve data for (85990) 1999 JV_6 span ten years. The orbit of this near-Earth asteroid is inclined only about 5°, and has a semi-major axis of 1.008 AU. It takes just over 4 days longer than the Earth to complete a full orbit around the Sun. From an observers point of view, it means that it can be seen quite regularly, always returning at a similar time of year, appearing in a very constrained location in the sky. But it also means that the observational geometry does not vary much. The graphs in Figure 5.1 illustrate the distance from Earth, ecliptic latitude and longitude, and phase angle at which the target was observed, and a summary of all available lightcurves is in Table 5.1. Those conditions make the lightcurve-inversion methods quite difficult to use in this case, as they rely on changing observational geometries to assess the shape properties. That is one of the reasons why supporting lightcurve observations with radar was crucial in the case of (85990) 1999 JV_6.

Isaac Newton Telescope (INT) – 2007, 2008, 2016

The asteroid (85990) 1999 JV_6 was observed optically by the YORP programme collaboration (discussed in 2.1.2) before the ESO Large Programme started. It was monitored primarily at the 2.5 m Isaac Newton Telescope in La Palma (Spain) on four different nights in 2007, three in 2008, and another four in 2016, giving a total of 10 usable lightcurves. One lightcurve, collected on 16 February 2016 had been dropped from the analysis due to poor observing conditions on that night (thick clouds overcasting the sky). The INT sets from 2007 and 2008 had been provided for the analysis, already reduced, by A. Fitzsimmons at the Queens University, Belfast. The data reduction of the newest lightcurves, from 2016 INT run, was

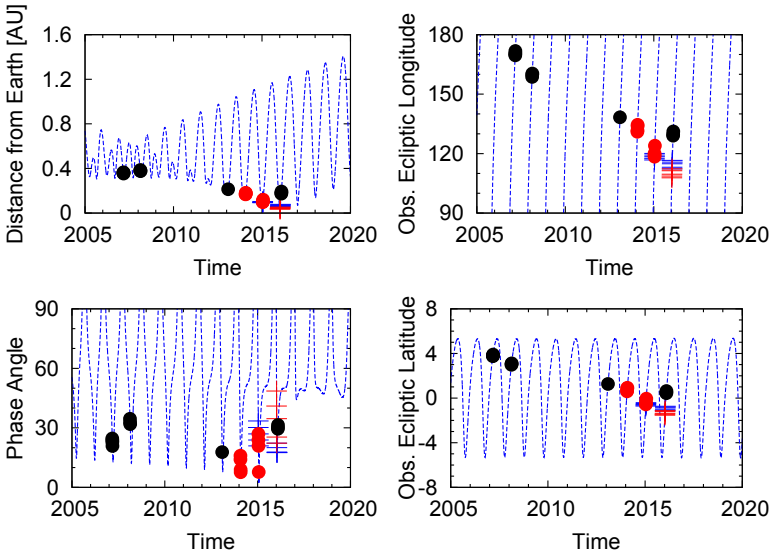

Figure 5.1: Asteroid (85990) 1999 JV_6 observing geometries during the ESO LP and associated projects. The black closed circles mark data gathered within the YORP programme. The red circles mark the two data sets acquired from MPC (Warner, 2014a, 2015b). The blue crosses mark Arecibo Planetary Radar observations while Goldstone Solar System Radar data are the red crosses. The blue dashed line is the objects observational ephemeris.

ID	Date (UT)	R_h [AU]	Δ [AU]	α [$^\circ$]	Observing facility	Reference
1	02/03/2007	1.31	0.36	24.16	INT	this work
2	03/03/2007	1.31	0.36	23.21		
3	04/03/2007	1.31	0.36	22.25		
4	06/03/2007	1.32	0.35	20.39		
5	15/02/2008	1.28	0.38	34.09	INT	"
6	17/02/2008	1.29	0.38	32.25		
7	18/02/2008	1.29	0.37	31.35		
8	04/02/2013	1.19	0.21	16.82	NTT	"
9	04/02/2013	1.19	0.21	16.61		
10	28/01/2014	1.14	0.17	16.56	Palmer Divide	Warner (2014a)
11	28/01/2014	1.14	0.17	16.26		
12	29/01/2014	1.15	0.17	14.63		
13	29/01/2014	1.15	0.17	14.32		
14	01/02/2014	1.16	0.18	9.29		
15	02/02/2014	1.16	0.18	8.01		
16	02/02/2014	1.16	0.18	7.80		
17	16/01/2015	1.07	0.10	27.83	Palmer Divide	Warner (2015b)
18	16/01/2015	1.07	0.10	27.37		
19	17/01/2015	1.07	0.10	24.73		
20	17/01/2015	1.07	0.10	24.29		
21	18/01/2015	1.08	0.10	21.69		
22	18/01/2015	1.08	0.10	21.29		
23	23/01/2015	1.10	0.12	8.30	Table Mountain	this work
24	03/02/2016	1.14	0.18	29.79	INT	"
25	04/02/2016	1.14	0.18	30.43		
26	06/02/2016	1.15	0.20	31.71		

Table 5.1: A chronological list of lightcurve data sets for (85990) 1999 JV_6 used in this study. For each lightcurve an *ID* is listed, that is used though the chapter for identification, then the *Date* (Universal Time) of the beginning of the night is given as well as the heliocentric (R_h) and geocentric (Δ) distances measured in AU, the solar phase angle (α), and the *Observing facility* used to obtain the lightcurve. Where applicable a *Reference* to the already published work is given. Each line represents a single lightcurve (sometimes a few segments were observed on a night).

handled by T. Zegmott at Kent.

New Technology Telescope (NTT) – 2013

The asteroid was observed optically at two further facilities. A few lightcurve data sets were obtained at ESO's 3.6 m NTT telescope in La Silla (Chile) in 2013. The object was detected on three nights, between 4^{th} to 6^{th} of February 2013. Strong winds imposed pointing restrictions

ID	frames	exposure [s]	total [h]	filter	observers
2.5 m Isaac Newton Telescope + WFC, La Palma (Spain)					
1	55	36	6.3	r	A. Fitzsimmons (QUB)
2	54	35	6.0	r	
3	54	34	5.4	r	
4	67	32	6.4	r	
5	31	51	2.7	r	A. Fitzsimmons (QUB)
6	49	46-92	3.2	r	
7	143	43-86	5.1	r	
24	107	150	5.9	V	S. Lowry / T. Zegmott
25	110	150	6.8	V	
26	102	150	5.4	V	
ESO 3.6 m New Technology Telescope + EFOSC, La Silla (Chile)					
8	88	50	2.4	V	S. Duddy/A. Rożek
9	72	50	2.0	V	
JPL 0.6 m Table Mountain Observatory + 1k $\times$ 1k CCD (USA)					
23	63	300	7.0	R	P. Weissman / M. Hicks/ W. Smythe (JPL)

Table 5.2: The YORP programme lightcurve data gathered for (85990) 1999 JV_6. First column is the chronological *ID*, the same as in Table 5.1, followed by the number of *frames*, *exposure* time per frame in seconds, a *total* time-span of the lightcurve in hours (the rotation period is ≈ 6.5h), imaging *filter* used, and the *observers*. The sets are grouped according to the observing facility and then sorted chronologically. Where the affiliation of the observer is not with the University of Kent, it is given in parentheses.

at the telescope and forced a break in the observing, which resulted in obtaining two separate lightcurve segments on 4th February. Two additional partial lightcurves were collected on 5th and 6th, but due to their length and quality they are not included in the analysis. The data were reduced using the standard procedures outlined in Section 2.1.4. Additionally, frames had to be summed to improve the signal-to-noise ratio of the resulting lightcurve.

The images are grouped into sets of 3. The pixel values of the product image are obtained by adding the values of corresponding pixels in the summed frames. This way the small fluctuations between frames are smoothed-out, in a similar way as they would be with a longer exposure. However, as the object moves across the sky, the exposure times of single frames are adjusted to prevent the asteroid and stars from trailing. A circular aperture can be used for photometry on the co-added image, when simply using a longer exposure time would cause either the target or stellar background to trail in a single frame. Relevant keywords are updated, most importantly the exposure times are added and the new mid-exposure time is calculated being midway between the start of the exposure of the first frame and the end of the last frame. Each set of three produces two output images. One image is obtained by co-adding the original frames shifted so that the background stars match up and produce a point-source-like image, so it can be used for photometry of stars. The asteroid is a series of points in this image, so it is ignored. The other image is obtained by

co-adding frames shifted to keep the target asteroid in the same place, allowing the stars to trail. Photometry is then done on the asteroid, which light is focused in one region of the frame. The results are used in calculating relative lightcurves, see Section 2.1.5 for more details on this process and an example Figure 2.7.

Table Mountain Observatory (TMO) – 2015

Last of the YORP programme data used in this work come from JPL's Table Mountain Observatory 0.6 m telescope (USA). The data reduction process in this case was performed in just two basic steps of bias removal and flat-fielding. A single lightcurve covering just over one full rotation was obtained.

Details of the YORP programme lightcurves of (85990) 1999 JV_6 are gathered in Table 5.2. The analysis presented here also includes previously published photometry from outside the ESO Large Programme collaboration, obtained at the Palmer Divide Observatory (Warner, 2014a, 2015b). The processed lightcurves were retrieved from Minor Planet Centre (Warner et al., 2009).

5.2.2 Planetary radar (85990) 1999 JV_6 campaign

Lightcurve inversion methods are powerful tools for recovering shape models for small Solar System bodies, but offer limited capabilities. The lightcurve features can be successfully reproduced even for complex lightcurve shapes, albeit what can be reliably modelled is usually a convex hull of the real object (Kaasalainen and Torppa, 2001). That means the resulting shape resembles that of the actual asteroid or comet wrapped in packing paper, therefore it might lack surface features important for modelling the YORP and Yarkovsky effects (Rozitis and Green, 2013). Including details of the surface produces degeneration of the shape model that can be resolved by combining optical lightcurves with other types of ground-based observations such as stellar occultations or radar. In a few rare cases spacecraft fly-bys provided detailed information on shapes and surface properties for small bodies. Examples include asteroid (25143) Itokawa visited by Hayabusa (Demura et al., 2006), asteroid (2867) Steins (Keller et al., 2010), and comet 67P/Churyumov-Gerasimenko (Preusker et al., 2015), both visited by Rosetta. Currently no missions are planned to visit (85990) 1999 JV_6.

The radar observations of Solar System bodies are performed mainly at Arecibo (Puerto Rico) and Goldstone (USA) facilities. The radar images can be highly detailed, providing information about even the small surface features, like boulders and craters, down to the level of 7.5 m. Large concavities can be easily modelled with radar, an important advantage when in fact many asteroids are reported to have bi-lobed shapes in a configuration that is called asteroid 'contact binaries' (Benner et al., 2015). Amongst the near-Earth asteroids, the profound examples are (25143) Itokawa for which an elongated shape was deduced from radar images (Ostro et al., 2004), contact binary nature inferred from spacecraft imagery

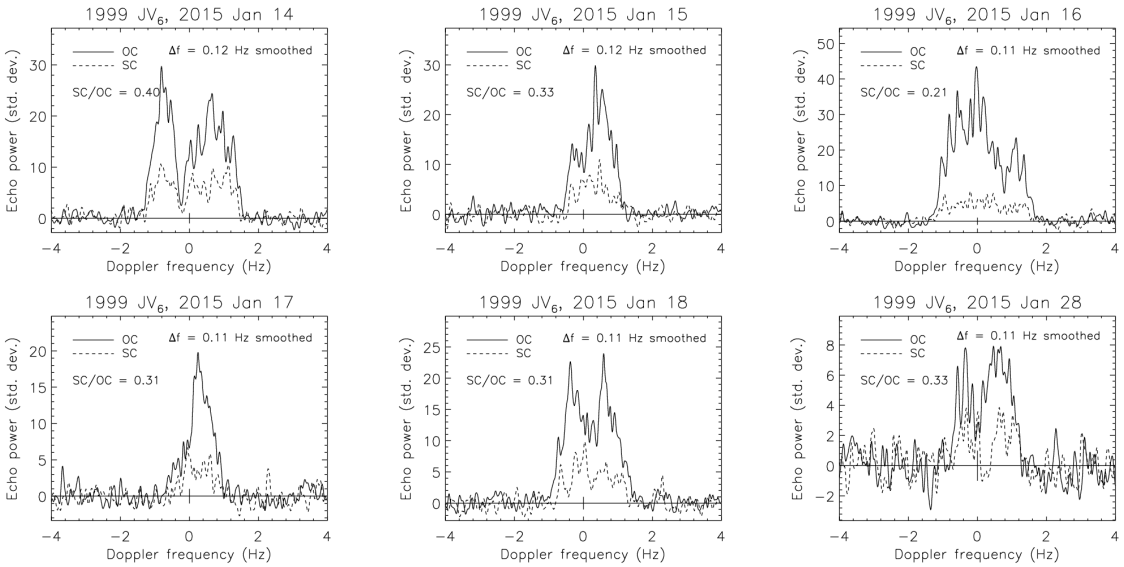

Figure 5.2: January 2015 Arecibo continuous-wave observations of (85990) 1999 JV_6 (see Table 5.3a for more details). The signal is recorded in two channels, with the same circular polarisation as the transmitted radiation (SC) marked with a dashed line in pictures, and the opposite circular polarisation (OC), marked with continuous. The spectra show high SC/OC ratio, which might suggest a rough surface. The bifurcation of the object can also be seen, especially in the first spectrum, taken on 14^{th}.

(Demura et al., 2006), and different natures of two lobes inferred from YORP measurement (Lowry et al., 2014), and (8567) 1996 HW_1 with two distinct ellipsoidal lobes (Magri et al., 2011). Even when high-resolution imaging with radar is not possible, combining radar and lightcurve observations can improve shape determination, or, at the very least, help constrain the pole (Ostro et al., 2002). Moreover, using a pre-determined radar shape model to derive artificial lightcurves greatly simplifies the spin-state analysis performed in the YORP programme.

Arecibo (2015)

Having access to an extensive lightcurve data set and in order to obtain a comprehensive physical model, A. Rożek led a proposal to observe (85990) 1999 JV_6 with Arecibo Planetary Radar in January 2015, with M. Nolan from Arecibo and S. Lowry as co-investigators. In the proposal, 6 days of observation between January 13^{th} and January 18^{th} 2015 were requested, while the object was best visible at Arecibo. Expected resolution of the images was at least 30 m per pixel and the time required, about 2.5 h/d, was sufficient to cover a full range of the rotation phases over the duration of the run.

The proposal 'Observations of a near-Earth asteroid (85990) 1999 JV_6 with Arecibo Planetary Radar' was assigned number R2959 and was subsequently awarded five nights between 14^{th} and 18^{th} January 2015, and granted a few additional hours on 28^{th} of January. The continuous-wave spectra were taken on each night (see Section 2.2.2), as well as imaging (see

UT Date *yyyy-mm-dd*	MJD	Eph	RTT [s]	P_{tx} [kW]	Baud [µs]	Spb	Code	Start-Stop *hhmmss-hhmmss*	Runs
2015-01-14	57036	138	92	809	cw		none	060253-061840	5
				789	4	1	8191	062400-063436	4
		140		734	0.1	2	65535	064205-071117	9
				819	0.5	1	8191	071648-074225	8
2015-01-15	57037	140	94	774	cw		none	055103-060510	5
				762	0.2	4	65535	061257-065021	12
				789	0.5	1	8191	065607-071324	6
				754	0.2	4	65535	071632-074010	8
2015-01-16	57038	140	96	727	0.2	4	65535	052654-062116	16
				707	cw		none	062556-064021	5
			97	716	0.2	4	65535	064850-073222	14
2015-01-17	57039	140	99	716	0.2	4	65535	052419-070422	30
				711	cw		none	070826-072318	5
2015-01-18	57040	140	102	741	0.2	4	65535	045701-065248	32
				730	cw		none	065622-071820	7
2015-01-28	57050	140	139	756	cw		none	042118-045123	7
				795	0.5	1	8191	045644-055456	13

(a) January 2015

UT Date *yyyy-mm-dd*	MJD	Eph	RTT [s]	P_{tx} [kW]	Baud [µs]	Spb	Code	Start-Stop *hhmmss-hhmmss*	Runs
2016-01-14	57401	178	56	639	cw		none	030535-031730	4
				702	0.1	2	65535	032353-040213	19
				612	0.05	1	65535	040710-043214	14
2016-01-15	57402	180	60	642	cw		none	024516-030009	5
				640	0.05	1	65535	030420-031523	6
			61	599	0.1	2	65535	032959-044409	34
2016-01-17	57404	180	70	680	cw		none	022000-023047	4
				670	0.1	2	65535	023518-033047	24
				660	cw		none	033258-034107	4
			71	641	0.1	2	65535	034429-044442	26
2016-01-18	57405	180	76	604	0.1	2	65535	021809-033245	30
				618	cw		none	033900-034744	4
				594	0.1	2	65535	035118-044306	21
2016-01-19	57406	180	81	628	cw		none	021010-021929	4
				640	0.1	2	65535	022834-044128	48

(b) January 2016

Table 5.3: Radar observations of asteroid (85990) 1999 JV_6 at Arecibo in January 2015 (a) and in January 2016 (b). *UT Date* is the universal-time date on which the observation began. *MJD* is the corresponding modified Julian date. *Eph* is the ephemeris solution number used, as listed by the on-site orbit determination system. *RTT* is the round-trip light time to the target. P_{tx} is the transmitter power. *Baud* is the delay resolution of the pseudo-random code used for imaging; baud does not apply to *cw* data. *Spb* is the number of complex samples per baud giving an effective delay resolution of baud/spb; *cw* data are typically sampled at a rate of 12.5 kHz. *Code* is the length (in bauds) of the pseudo-random code used. The timespan of the received data is listed by the UT *start* and *stop* times. *Runs* is the number of completed transmit-receive cycles. Details of radar observations can be found in Section 2.2.

Section 2.2.2), mainly with 0.2 µs baud length code, see detailed list of radar experiments executed in Table 5.3a. During the run, the object made an approach to the Earth to approximately 0.092 AU and was slowly receding. All observations were conducted by A. Rożek supported by the Planetary Radar team at Arecibo.

The asteroid appeared to have a complex shape already in the continuous-wave (*cw*) spectra, see Figure 5.2. Clear bifurcation can be noted, especially in the 14th and 16th January spectra, suggesting the object might have two different-sized lobes. Using the *cw*s, some early surface characterisation was done. The ratio of the same (SC) to opposite circular polarisation to the transmitted signal (OC), SC/OC, for this object is ≈ 0.3, which is a typical value for a near-Earth asteroid, with the mean value being 0.34 ± 0.25 (Benner et al., 2008). There is only a limited sample of Xk-class asteroids for which this ratio is measured, so it is difficult to compare it with its taxonomic class. Generally the SC/OC ratio is considered a measure of the surface roughness, as the presence of signal in SC means multiple reflections of the transmitted radiation had occurred. The high SC/OC ratio for (85990) 1999 JV_6 suggests there are surface features at the scale of the radar wavelength (13 cm for Arecibo). Doppler-delay imaging confirm the bi-lobed nature of the object. The initial simplified shape model shows that object can be represented with two different-sized ellipsoids glued together, as is discussed later (Section 5.3.3).

Goldstone (2016)

The object was observable again, during an even closer approach to Earth of around 0.053 AU in January 2016. The Goldstone Solar System Radar (GSSR) targeted the asteroid between 8th and 13th January 2016 obtaining two more *cw* spectra and high-resolution Doppler-delay images. The closest approach during the Goldstone run was to about 0.035 AU. The range resolution obtained was down to 0.125 µs (18.75 m) for observations for which Goldstone was used for both transmitting and receiving, and 0.05 µs (7.5 m) in bi-static observations between Goldstone, transmitting, and Green Bank, receiving the radio signal. The data had been provided for analysis in this work by the GSSR teams at Goldstone and Green Bank observatories (courtesy of L. Benner and colleagues).

Arecibo (2016)

A second proposal was submitted by A. Rożek for follow-up observations of (85990) 1999 JV_6 with Arecibo to improve the initial model. It was designated R3036 and was scheduled for six nights of 13th-18th January 2016. The observations were performed by P. Taylor and L. Ford at Arecibo with A. Rożek supervising the observations remotely. Only five nights were used due to transmitter malfunction on 15th January. The summary of Arecibo 2016 observations is presented in Table 5.3b. It has to be noted that not all of available radar observations are useful for the purpose of shape modelling. Whenever observations are taken at a very similar geometry, but with different resolutions, it is better to concentrate on

UT Date *yyyy-mm-dd*	MJD	Eph	RTT [s]	P_{tx} [kW]	Baud [µs]	Code	Start-Stop *hhmmss-hhmmss*	Runs	Mode
2016-01-08	57395	178	35	413	cw	none	063038-063705	6	monostatic
		180		373	0.125	127	070838-094927	138	monostatic
2016-01-09	57396	182	37	371	0.125	127	060252-061208	8	monostatic
				426	0.05	2000	061354-070000		bistatic chirped
2016-01-10	57397	184	40	395	0.125	127	043043-044204	9	monostatic
				420	0.125	127	045046-050706		bistatic
				402	0.125	127	051142-072438	100	monostatic
2016-01-12	57399	186	47	417	cw	none	061050-061802	5	monostatic
				388	0.25	127	062230-064858	17	monostatic
			48	406	0.125	127	065400-083000		bistatic
				391	0.25	127	083258-112528	108	monostatic
2016-01-13	57400	186	51	376	0.25	127	043240-043835	4	monostatic
				399	0.125	127	044300-045800		bistatic
			52	407	0.25	127	050100-084230		bistatic
				392	0.25	127	084716-103009	57	monostatic

Table 5.4: Radar observations of asteroid (85990) 1999 JV_6 at Goldstone and Green Bank. *UT Date* is the universal-time date on which the observation began. *MJD* is the corresponding modified Julian date. *Eph* is the ephemeris solution number used. *RTT* is the round-trip light time to the target. P_{tx} is the transmitter power. *Baud* is the delay resolution of the pseudo-random code used for imaging; baud does not apply to cw data. *Code* is the length (in bauds) of the pseudo-random code used. The timespan of the received data is listed by the UT start and stop times. Runs is the number of completed transmit-receive cycles. Mode indicates whether the signal transmitted from Goldstone has been received at Goldstone (monostatic), or at Green Bank (bistatic). Details of radar observations can be found in Section 2.2.

the higher-resolution images, as the low-resolution observations do not improve the model. Moreover, using more images considerably slows down the computations. Therefore, the analysis concentrates on the continuous-wave spectra (see Figure A.6) and highest-resolution imaging (see Figure A.7).

5.2.3 Arecibo observing run in January 2015

The observations with Arecibo Planetary Radar were performed as a part of A. Rożek's training visit at the Arecibo Observatory that took place between 7th January and 12th February 2015. During her visit at Arecibo A. Rożek participated in radar observations of NEAs, including the (85990) 1999 JV_6, and the moons of Jupiter. The visit included training on data reduction and development of an initial model of (85990) 1999 JV_6.

The observations at Arecibo are executed from a control room in a building situated close to the rim of the 305 m telescope. The transmitter, constantly monitored by a telescope technician, is located in the Gregorian dome that can be reached by cable-car for maintenance, see Figure 5.3. The transmitter has a maximum output power of 1 MW, and is supplied by an on-site diesel generator. The signal focused in the receiver, also situated in the dome, is then transferred with fibre optics back to the control room.

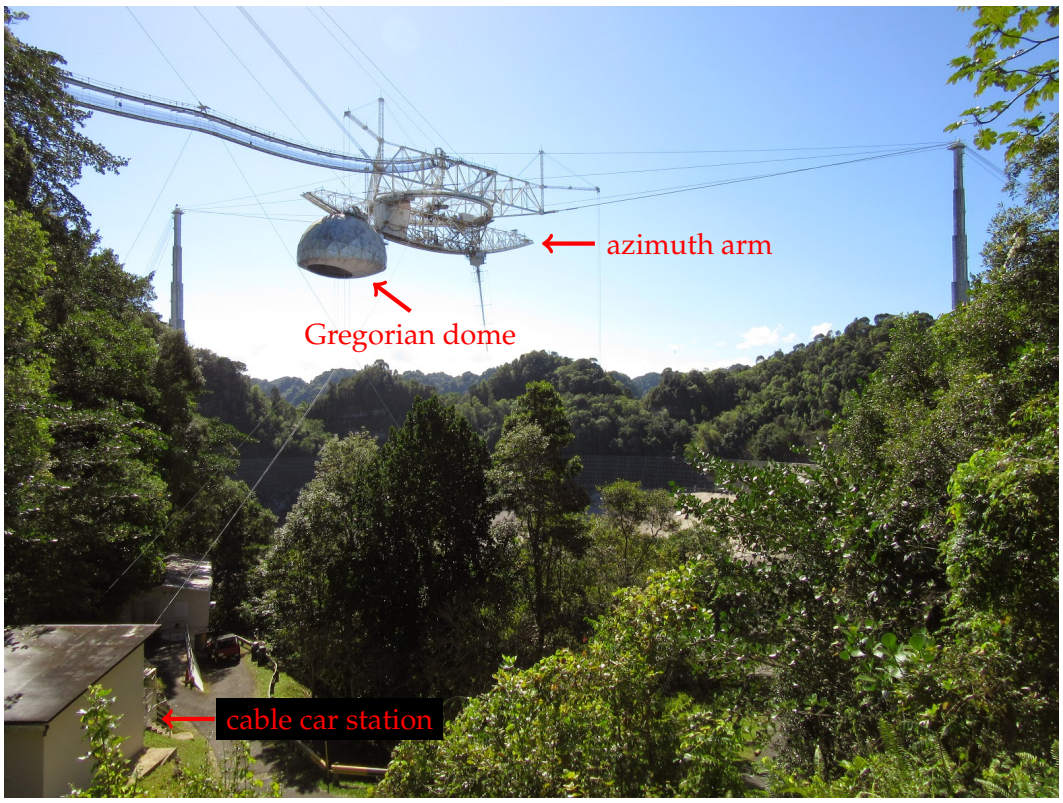

Figure 5.3: The Gregorian dome of Arecibo telescope hangs about 137 m above the 305 m primary mirror. It is attached to a rotating azimuth arm suspended from a triangular platform. The dome hosts secondary and tertiary mirrors, as well as a wide range of instruments, including the S-band radar transmitter and receiver, which can be accessed after a short trip with the cable car or a walk up a narrow bridge. As the telescopes primary mirror is not movable, the Gregorian dome can be slid along the azimuth arm to control the elevation at which objects are observed and the whole arm can be turned to adjust azimuth. The photograph was taken from the perspective of the control room by A. Rożek during her observations in January 2015.

The astronomers main place of work is the console that allows telescope pointing, and set-up of the observations (Figure 5.4). The telescope tracking is done automatically based on ephemeris generated with JPL On-Site Orbit Determination software (OSOD) installed on Arecibo computers. The system can be updated with radar astrometry to allow precise delay and Doppler predictions during the observations. The new measurements are later revised and incorporated into ephemerides available on-line through the JPL Horizons ephemeris system. The observer then requests observations in a specific mode by using one of the pre-programmed templates. The templates contain the baud length, code length, and specification of the system receiving and recording signal. They need to be adjusted for a specific target by providing ephemeris information. The transmit and receive time are then automatically selected by the software, and the user selects how many runs (full transmit and receive cycles) are to be performed. The quality of the incoming data is controlled throughout the night by processing the data after each transmit-receive cycle.

Usually, astronomical observations are a passive process, in which the light of a selected

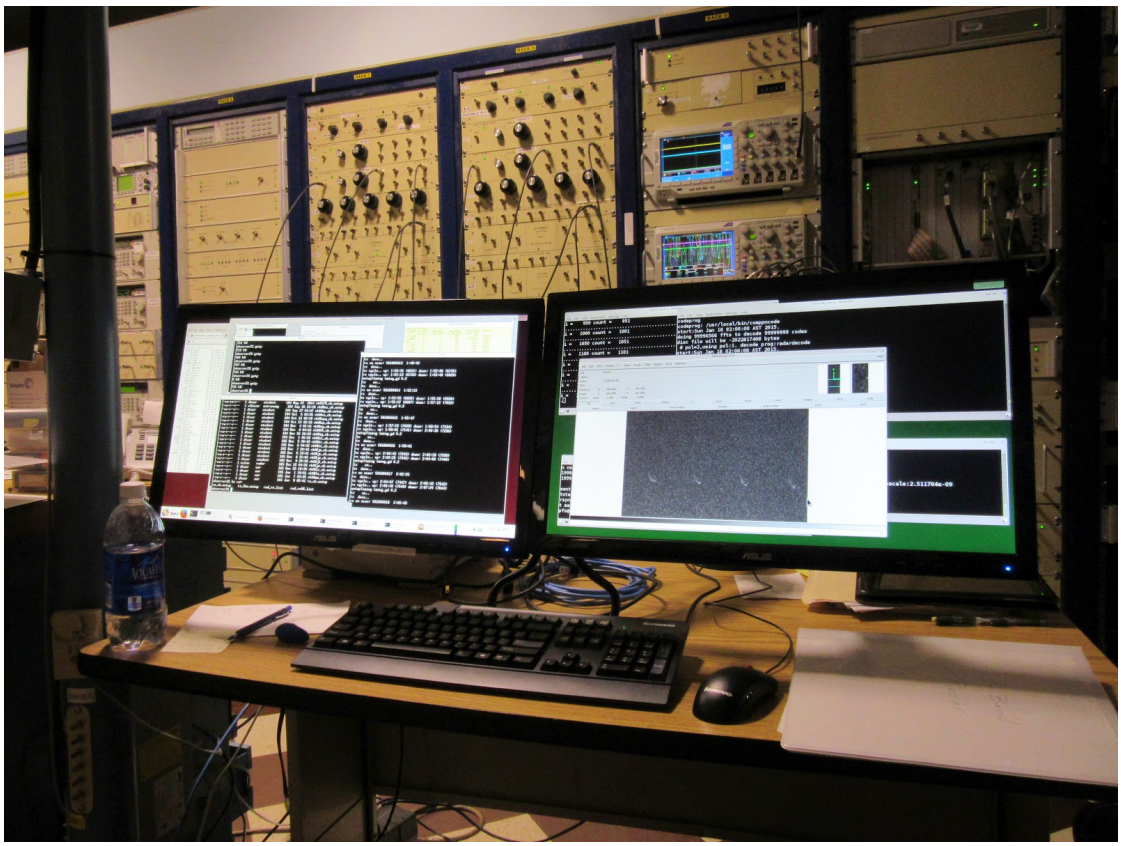

Figure 5.4: Arecibo control board and observer station. The wiring on the board, visible in the background, is set up with BNC cables every evening and adjusted throughout the observing according to the observation mode. The console shown in foreground gives the astronomer control over telescope steering and data gathering. Picture taken by A. Rożek during her observations in January 2015.

wavelength coming from the target is collected by a telescope and recorded with a relevant detector. The radar observations of Solar System bodies are an active experiment. The signal is being transmitted for the time of about the round-trip time, which is the time it takes the radio signal to reach the object, get reflected from the surface, and come back. After that the transmitter power is redirected to the cooling system and the receiving can begin. What happens next, how the signal is recorded and reduced, depends on the mode of observations. The observer can select from a few modes, with the main two types being continuous-wave spectra that record the Doppler offset of the transmitted signal, and imaging that contains the additional distance information. The details of the set-up depend on number of factors with size, rotation rate, and distance to the object being the major ones, as they limit the reflected signal power, bandwidth, and frequency and ranging resolution, as discussed in Section 2.2.2.

For new radar detections usually just the *cw* observations as well as very crude ranging are made. The latter is imaging with a very coarse range resolution, and usually reduced with low frequency resolution as well, done in order to locate the asteroid and refine its orbit before more detailed observations. In case of (85990) 1999 JV_6 the observations started with

cw and ranging, to get an accurate estimate on the signal strength and to make correction of the ephemerides in OSOD. Then, the observations focused on high-resolution imaging, mainly using code with baud-length of 0.2 µs.

In the control room, the receiving system has to be prepared for recording the signal delivered from the telescope receiver via optical fibres. This requires the astronomer to wire up specific components of the control board using BNC connector cables (Figure 5.4). Depending on the type of observations, there is a few different types of filters, to filter down unwanted part of the spectrum, and attenuators amplifying the signal, that have to be wired up, as well as oscilloscopes to check the signal strength. Ultimately the pre-processed signal is fed to the appropriate receiving system that samples and records it in a digital form. The wiring is done on an experiment-to-experiment basis and can change during a single observing night. The time for re-wiring the telescope set-up while the telescope is in operation should be kept down to a necessary minimum. Sometimes the time it takes to slew to the object is used for that purpose, but in extreme cases the re-wiring of receiver is done on-the-go, i.e. while the telescope is transmitting. Details on the data reduction can be found in Section 2.2.2.

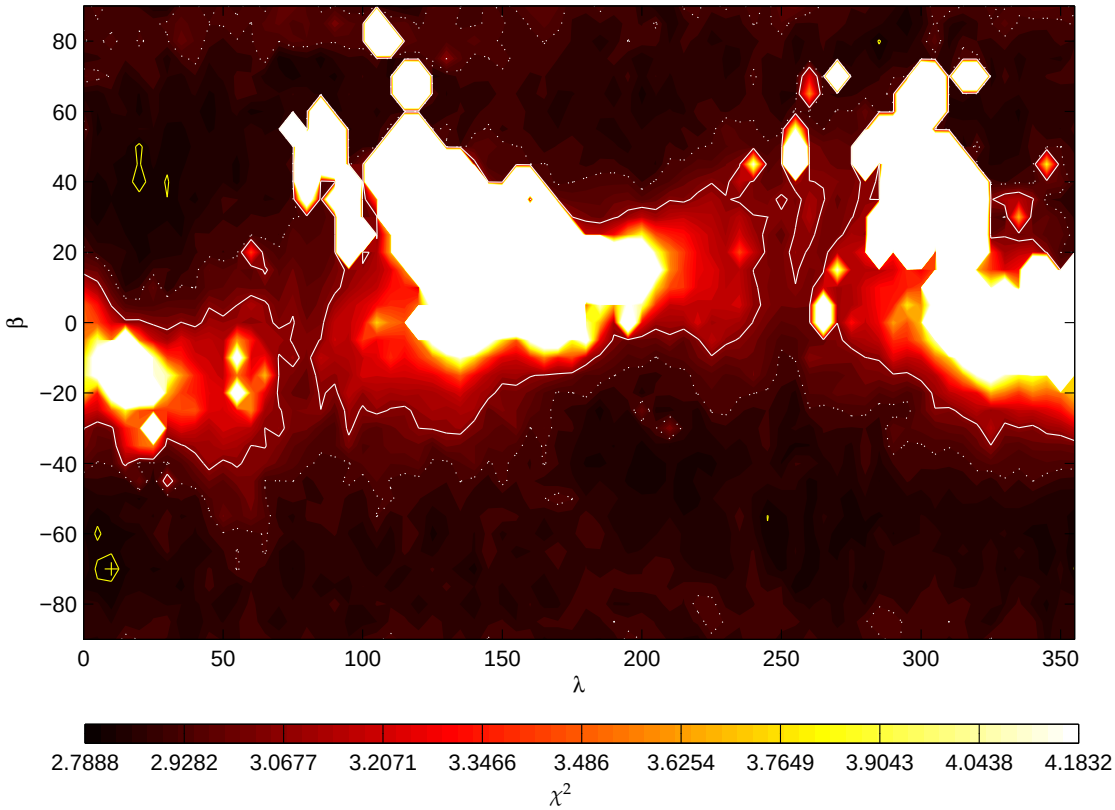

Figure 5.5: Results of the initial convex inversion pole scan for asteroid (85990) 1999 JV_6 on a $5° \times 5°$ grid. The axes are ecliptic coordinates of the asteroids pole in degrees, longitude – λ, and latitude – β. The colour changes from black at the minimum χ^2 with 1% increments of the minimum (the darker the colour, the smaller the χ^2), with the white region representing all the solutions with χ^2 more than 50% above the minimum. Additionally, the model with smallest χ^2 is marked with a '+' sign and contours corresponding to 1% (yellow), 5% (white dotted) and 10% (white solid) increase above the minimum χ^2 are plotted.

5.3 Shape modelling after the January 2015 campaign

5.3.1 Pole scan with lightcurve data

In order to obtain a good starting point for the radar modelling done during the 2015 Arecibo visit, an early lightcurve-inversion pole scan was performed, using the methods discussed in Section 3.1.2. Only 14 of the lightcurves listed in Table 5.1 were used, namely the 7 INT lightcurves from 2007 and 2008 as well as the 7 lightcurves published in Minor Planet Bulletin (Warner, 2014a). The scan was performed on a rectangular grid of ecliptic coordinates of the pole with a $10° \times 10°$ resolution on the entire celestial sphere. The initial period estimate from literature (Warner, 2014a) was used and the T_0 was allowed to be determined automatically by the software, which put it at the beginning of the first data set used.

The pole scan can be summed up as inconclusive, as there are many very similar solutions lying across the celestial sphere, see Figure 5.5. The solutions within 10 % of the best solution cover the entire southern hemisphere of the sky and most of the northern hemisphere. The pole seems to be located away from the orbital plane of the object (inclined at 5° to the ecliptic), with the best model obtained at $\lambda = 10°$, $\beta = -70°$. The convex model corresponding to the best solution is elongated, slightly flattened, and has both large planar areas covered sparsely with vertices as well as sharp corners where the vertices are quite

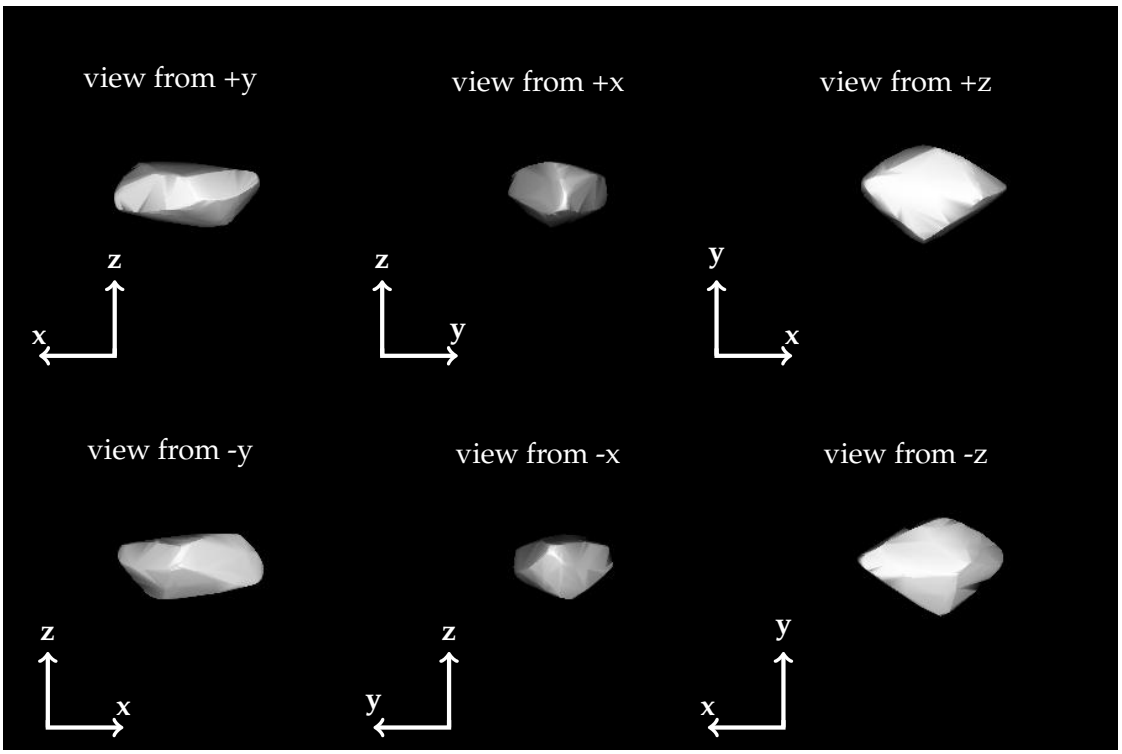

Figure 5.6: The convex shape model of (85990) 1999 JV_6, developed from a limited lightcurve set in January 2015. The model corresponds to the best solution from scan depicted in Figure 5.5. The rotation pole is located at $\lambda = 10°$, $\beta = -70°$. The six panels represent views of the shape model along the x, y and z axes of the body reference frame, with z being the rotation axis.

densely packed, see Figure 5.6.

5.3.2 Initial non-convex model

The radar shape modelling was performed using the SHAPE modelling software (Magri et al., 2007). As discussed in Section 3.2.2, the process requires an initial guess on the shape model as a starting point for the process. For the first attempt at modelling the radar data the best-fit CONVEXINV model was used. Due to the nature of the convex-inversion method the model is a convex hull of the actual shape represented with a triangular mesh. The assumption was made that the SHAPE software should be able to modify the vertices of input shape so that it would include the obvious concavities seen in the radar images (Figure A.7). This method did not bring expected results, producing an amorphous blob rather than the expected bi-lobed shape, see Figure 5.7.

The problem with using a CONVEXINV model as a base for SHAPE modelling in this specific case could stem from the way the faceted model is represented within SHAPE, see Figure 3.8. The position of each vertex can be modified only along the direction of vertex deviation vector, limiting in a way the capabilities of SHAPE. There is room for improvement of the shape detail, but the overall characteristics of the shape remains close to the initial model. Hence,

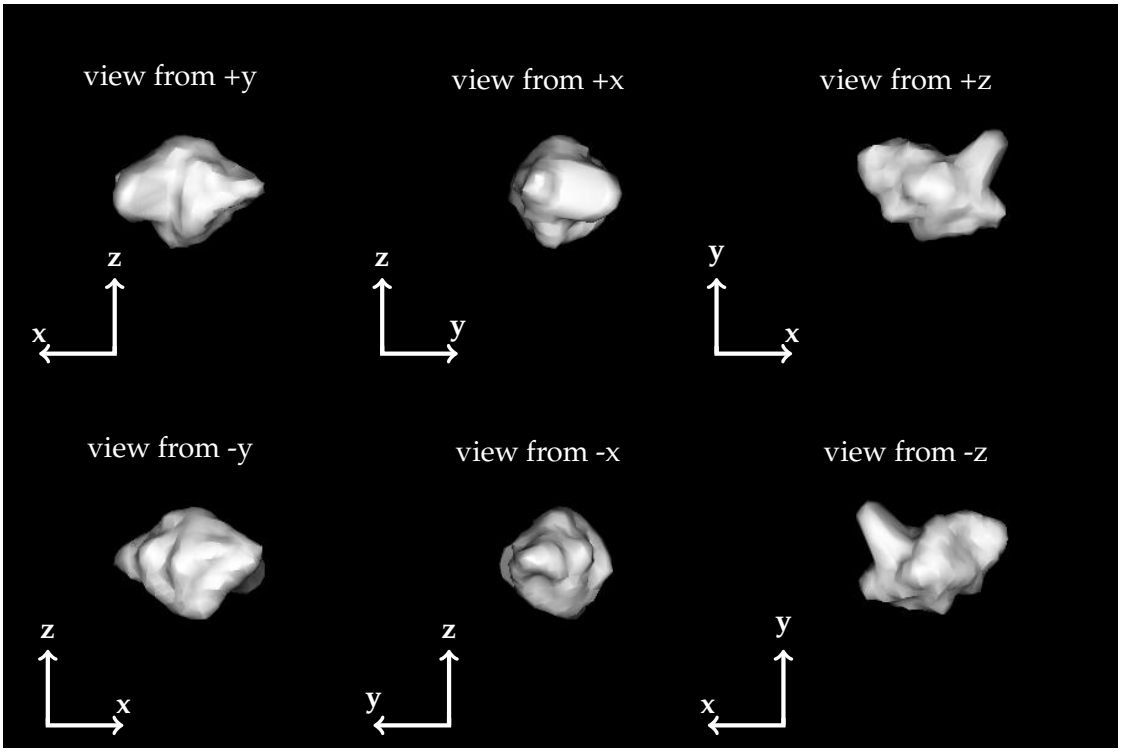

Figure 5.7: The convex shape developed from lightcurve-inversion methods, as shown in Figure 5.6, was used as a starting point of the radar SHAPE modelling. The non-convex shape solution, shown here, fails to reproduce the radar echoes and displays interesting artefacts. The six panels represent views of the shape model along the x, y and z axes of the body reference frame, with z being the rotation axis.

a model that had large planar surfaces and no vertices where the neck region should be located, failed to reproduce the bifurcation of the shape. Indeed, as can be seen in Figure 5.7, the shape obtained as a result of the process is a rather bizarre amoeboid.

Another explanation for the unexpected result of the shape modelling process might be improper use of the various penalties that can be implemented in SHAPE. The penalty functions control for example the amount of non-convexity on the local and global scales, or the deviation of the centre of rotation from centre-of-mass. The SHAPE software computes the quality of the model not only by comparing it to observations but adds an extra term to the computed goodness-of-fit χ^2 value depending on the specific penalties set, see Equation (3.5). The local convexity weight might have been set too small to prevent the vertex displacements from changing too much and creating an amorphous shape.

5.3.3 Two-ellipsoid model

In this case, a better way to find initial conditions for the SHAPE modelling software was to manually set up the initial shape that would reproduce the radar echoes. For this purpose available best-quality observations, with the baud length of 0.2 µs, from the January 2015 campaign were selected, see Table 5.3a. Since the object echoes resembled those of other contact binary asteroids, like (8567) 1996 HW_1 (Magri et al., 2011) or (25143) Itokawa

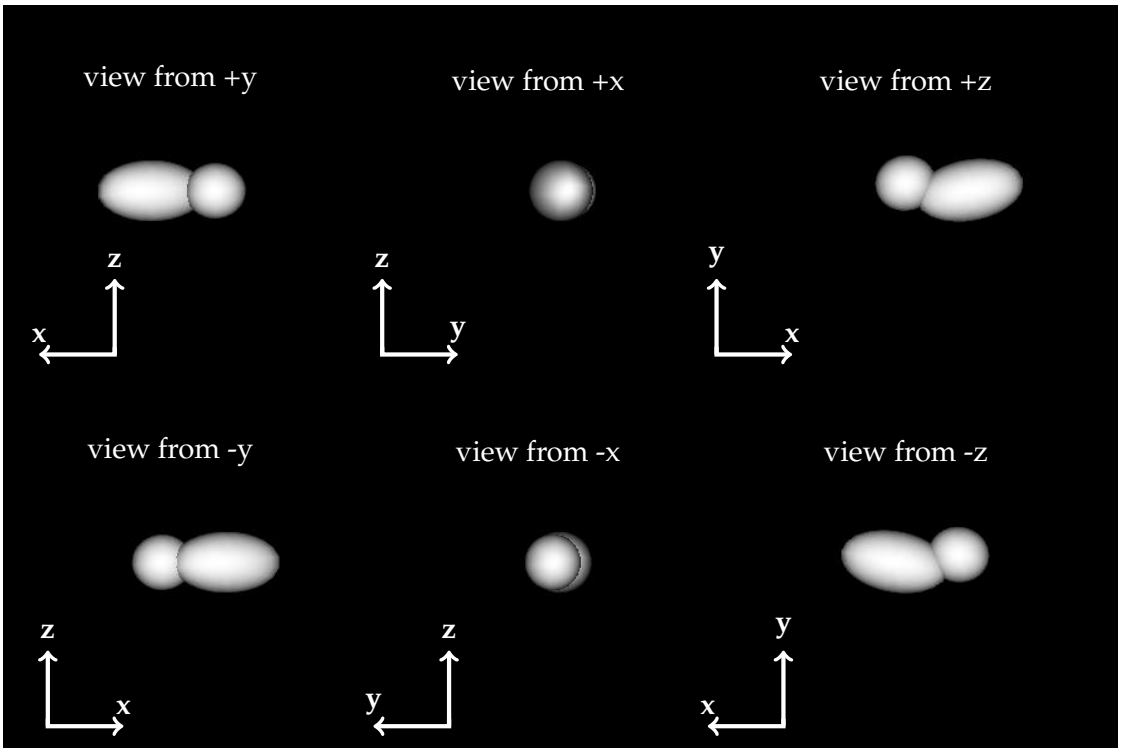

Figure 5.8: The two-ellipsoid shape model of (85990) 1999 JV_6. The model pole corresponds to the best solution from scan depicted in Figure 5.5 and is located at $\lambda = 10°$, $\beta = -70°$. The six panels represent views of the shape model along the x, y and z axes of the body reference frame, with z being the rotation axis.

(Ostro et al., 2004), a two-ellipsoid model was adopted.

The parameters that have to be set up for a two-ellipsoid model are dimensions of ellipsoids, angular and spatial offsets of both components, and initial rotation of the whole model. For an assumed pole position and rotation period, the parameters had been manually adjusted. Then the SHAPE software was used to output the synthetic radar echoes for a given set of parameters to be inspected visually. Further manual adjustments were made until the fit to the radar echoes was satisfying. Then model details were refined using SHAPE. This process has been repeated for a few different possible rotation pole positions to get a good picture of the overall model properties. Finally, the model with the pole located at $\lambda = 10°$ and $\beta = -70°$ (best-fit convex inversion pole location) was selected as the focus of further study, see Figure 5.8.

5.3.4 Refined radar model

The two-ellipsoid shape was then transformed to a faceted model. The surfaces of the two ellipsoids were sampled with a resolution of $\approx 12°$ and described with a set of 532 vertices arranged into 1059 triangular facets. The SHAPE software was used to find the optimal values of vertex displacements and sidereal rotation period. The resulting model (Figure 5.9) reproduced the radar echoes quite well, but its reliability was limited. The position of the rotation pole was not very well constrained to begin with and, for the sake of the shape

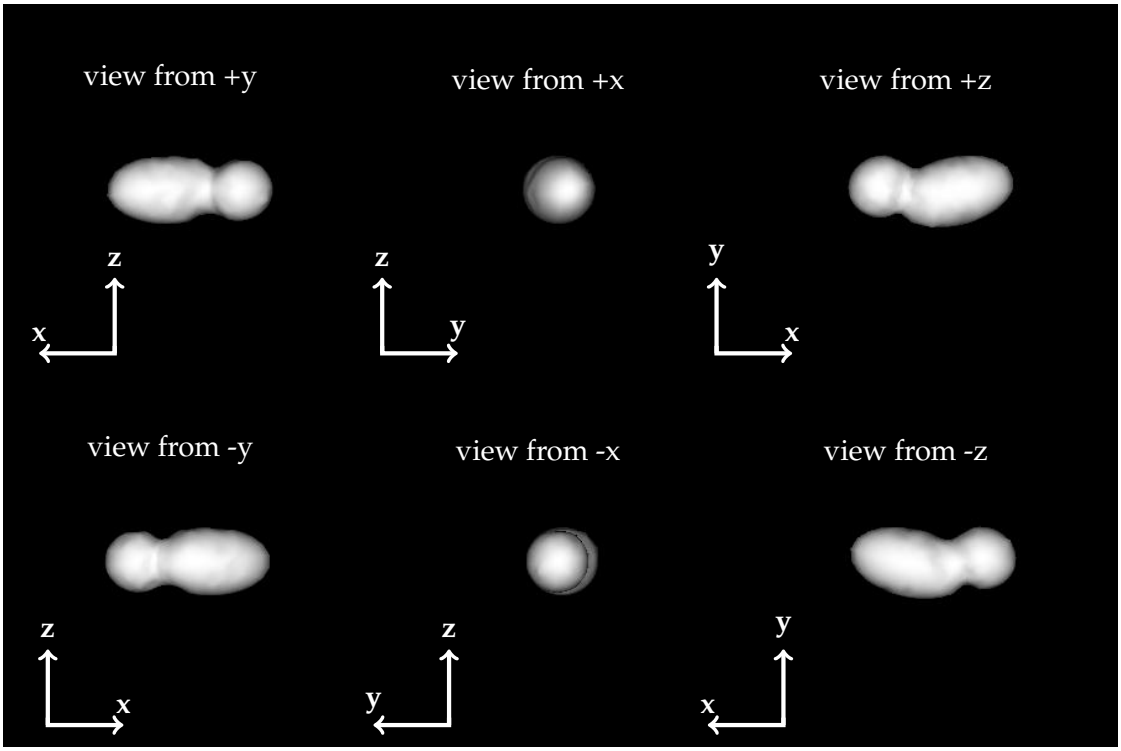

Figure 5.9: The vertex model developed from the two-ellipsoid shape model of (85990) 1999 JV_6 depicted in Figure 5.8. The six panels represent views of the shape model along the x, y and z axes of the body reference frame, with z being the rotation axis.

modelling exercise, was chosen almost arbitrarily from a wide range of possible solutions. More detailed study of the object was possible after the asteroid was observed during the even closer approach to Earth in January 2016. The additional observing geometries, and higher resolution radar observations helped to improve the model.

5.4 Shape modelling after the January 2016 campaign

5.4.1 Pole scan with expanded lightcurve data

Having an expanded lightcurve observations set, after the 2015 and 2016 radar observing campaigns, a new convex pole scan was attempted. However, not all available lightcurves were included in the scan, some pre-selection was made based on completeness and signal-to-noise ratio. The first and last lightcurves from 2007 were used (lightcurves 1 and 3 in Table 5.1), and the 2008 set was limited to the only full lightcurve, the last one (number 7), which gives a total of 22 lightcurves included in the scan. The T_0 for this scan was selected automatically to be the beginning of the first lightcurve (in March 2007). The initial period was set to be 6.53679 h, an approximation from earlier scans. A grid of $5° \times 5°$ fixed pole positions covering the entire celestial sphere was used to perform shape and period fitting. At each point of the grid the quality of the fit, χ^2, of the model to all the lightcurves included in the modelling, were recorded.

The process was repeated for a range of YORP spin-up factors, ν, in order to obtain a first estimate on whether the effect is acting on this asteroid or not. In other words, multiple pole scans were performed, keeping the ν factor fixed for each scan, creating plots of χ^2 against fragment of celestial sphere, or YORP-planes (Figure 3.4). The minimum χ^2 value from each of the YORP-planes was plotted against the values of ν in Figure 5.10. The best fit to the

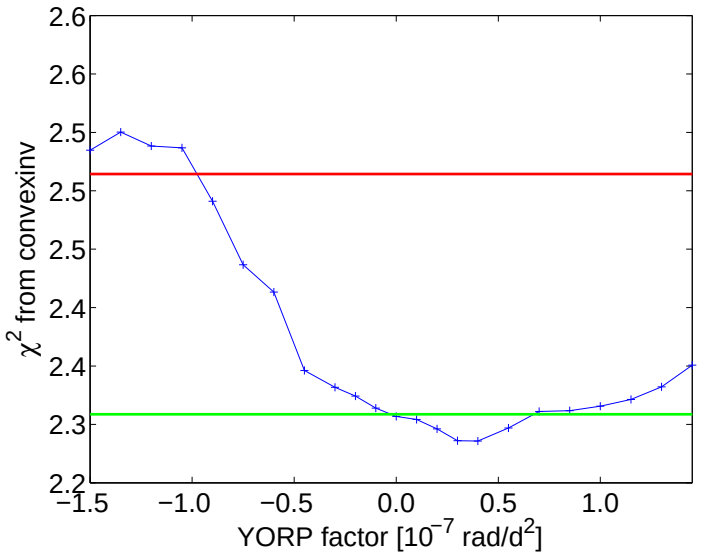

Figure 5.10: Results of combined convex shape and YORP scan for (85990) 1999 JV_6. For a set of YORP factors, ν, a grid of possible pole positions was scanned with shape and period optimised at each point. The quality of the fit, χ^2, was recorded and a smallest value of χ^2 from each scan is plotted here against the values of ν. The green line marks the best-fit χ^2 minimum +1%, red +10%. A YORP-induced spin-up of 4×10^{-8} rad/d^2 gives the best fit to observational data, but the constant period solution cannot be discarded.

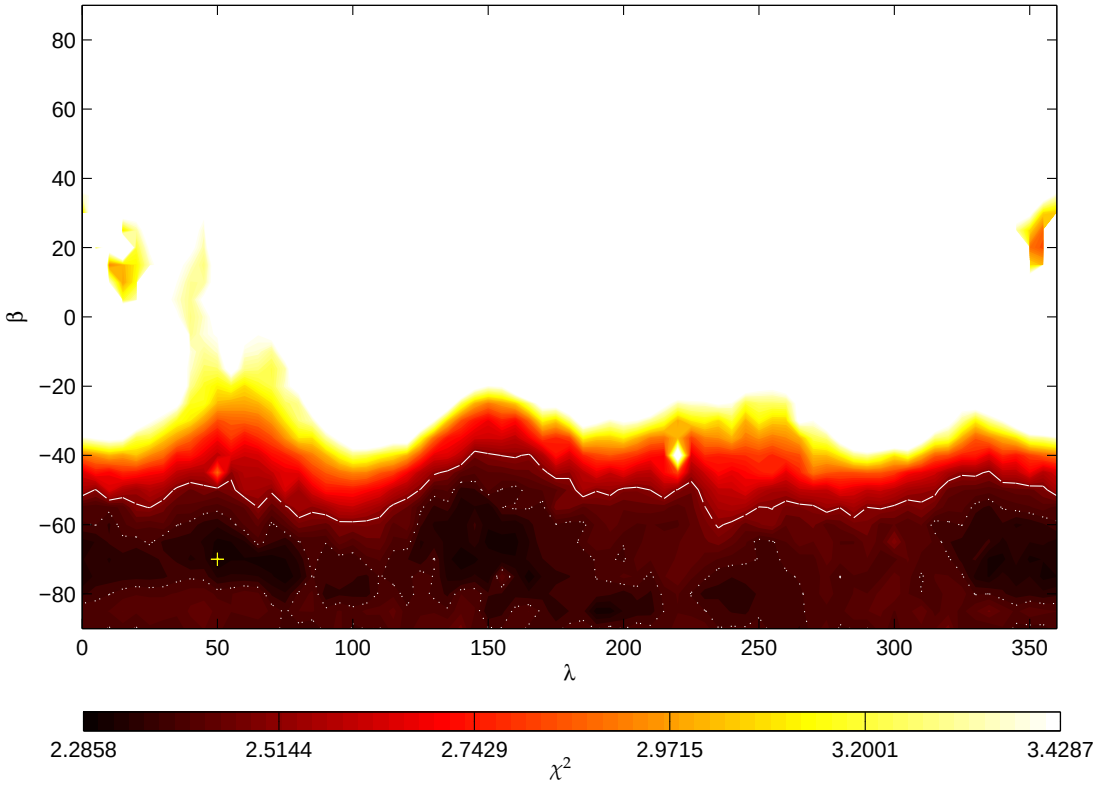

Figure 5.11: Final results of the convex lightcurve-inversion pole scan for asteroid (85990) 1999 JV_6 on a $5° \times 5°$ grid, which used lightcurve data up to and including the new lightcurve data from 2016. The axes are ecliptic coordinates of the asteroids pole in degrees, longitude – λ, and latitude – β. The colour changes from black at the minimum χ^2 with 1% increments of the minimum (the darker the colour, the smaller the χ^2), with the white region representing all the solutions with χ^2 more than 50% above the minimum. Additionally, the model with smallest χ^2 is marked with a '+' sign and contours corresponding to 5% (white dotted) and 10% (white solid) increase above the minimum χ^2 are plotted.

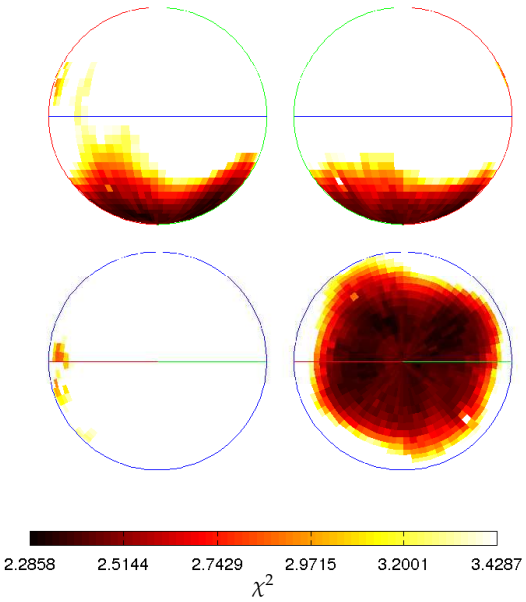

Figure 5.12: Results of the convex inversion pole scan for asteroid (85990) 1999 JV_6. This is same as Figure 5.11, but the results are projected on the surface of the celestial sphere described in ecliptic coordinates of the asteroids pole. The blue line marks the equator with latitude $\beta = 0$. The red line marks the longitude $\lambda = 0$ and the green line $\lambda = 180$. From top-right clockwise, the coordinates of the central point in each projection are $(\lambda = 90°, \beta = 0°)$, $(\lambda = 270°, \beta = 0°)$, $(\beta = 90°)$, and $(\beta = -90°)$. The colour changes from black at the minimum χ^2, with 1% increments of the minimum, and the white region representing all the solutions with χ^2 more than 50% above the minimum. Projecting the pole scan results this way rather than as a rectangular projection of the celestial sphere is a much better way of illustrating the constraint on the pole position, especially for ecliptic longitude.

lightcurve set for (85990) 1999 JV_6 is obtained for a shape model developed assuming a slight YORP-induced spin-up with $\nu = 4 \times 10^{-8}\,\mathrm{rad/d^2}$, and the YORP torque could be as strong as $\nu = 7 \times 10^{-8}\,\mathrm{rad/d^2}$. However, the constant period solution, with $\nu = 0$, still reproduces the lightcurves very well, with the χ^2 different by less than 1% from the best-fit model.

The pole search under assumption of a constant period, $\nu = 0$, puts a better constraint on the rotational pole position than the initial scan performed in 2015. The pole can be restricted to negative ecliptic latitudes (Figures 5.11 and 5.12). The proximity of the location of the rotation pole to the southern pole of the celestial sphere and the range of observing geometries available (Figure 5.1) make estimating the longitude of the pole, using only the lightcurve-inversion methods, unreliable for this object.

5.4.2 Pole scan with two-ellipsoid model

Using the radar data, a new pole scan was performed, with one of the two-ellipsoid models developed after the January 2015 run used as a starting point. To speed-up the computation at this stage, only a sample of radar data were used. The radar subset was selected to cover the full range of rotation phases and be representative of the two years of the observing campaign. An illustration of the selection process can be found on Figure 5.13.

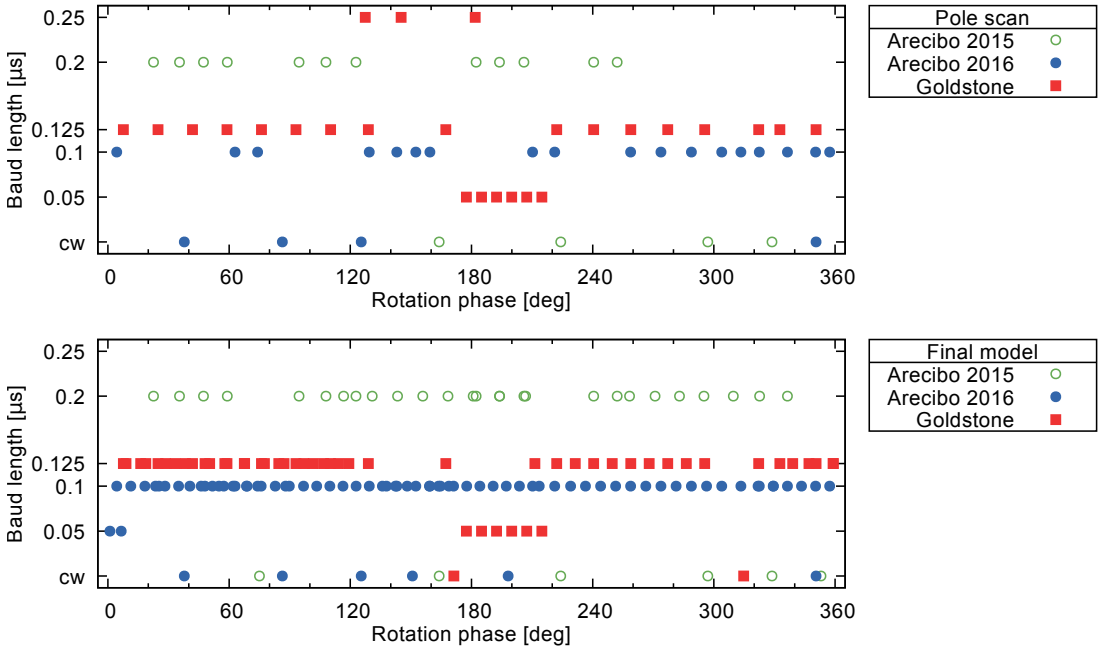

Figure 5.13: Rotation phase coverage of radar data used in the pole scan (upper panel) and in the final shape modelling (lower panel) of (85990) 1999 JV_6. The rotation phase was calculated using the best-fit vertex model with $\lambda = 132°$, $\beta = -88°$. Circles represent the two Arecibo runs, with green open circles marking data gathered in 2015, and blue filled – 2016. The red squares mark Goldstone data (both mono-static and bi-static with Green Bank). The horizontal axis on both plots is the rotation phase in degrees and the vertical axis is the baud length for imaging frames. The *cw* observations are marked as well.

A total of 8 continuous-wave spectra from Arecibo were used, 4 from each year. The *cw* spectra were masked to show only the bandwidth of the recorded signal and any drops due to bi-lobed shape of the asteroid. Any signal outside the masked region was multiplied by 0, see Figure A.6. This masking speeds up the computation and is especially important at a later stage, when SHAPE might unnecessarily try to fit all the spikes often present in *cw*s and create a hedgehog-like structure, comparable to what is shown in Figure 5.7.

Rotational phase coverage and delay resolution were the main criteria applied when selecting the Doppler-delay frames for the scan. Preference was given to data sets where a series of consecutive images was taken, rather than single observations. The analysis focused on the 0.1 µs and 0.2 µs-baud imaging from Arecibo and 0.125 µs from Goldstone, as well as the highest resolution (with baud of 0.05 µs). Due to some intermediate issues with data reduction of higher-resolution data sets, a few low-resolution, baud length 0.25 µs, frames from Goldstone were used. Those issues were later resolved and the rotation phases covered initially by the 0.25 µs were covered by 0.125 µs imaging from Goldstone in later fits (compare both panels of Figure 5.13).

The radar imaging frames can be quite large compared to the number of pixels that contain the actual echo. Unconstrained calculations of the χ^2 would take into account all image pixels, effectively making SHAPE attempt to fit the background nose. Therefore the images are initially vignetted, to contain as little background as possible. Having synthetic radar images from the earlier modelling based on an initial model were used to set up more accurate masks. For any image the mask would cover the area of the image where the radar signal is expected to be plus an extra 5 pixels (Magri et al., 2011, value selected following). Pixel values outside the mask were multiplied by 0, so they would not provide any input to the χ^2 sum.

The lightcurve data were included, though limited to those obtained closest to the radar runs. Lightcurves 19, 20 and 21 (Warner, 2015b), 23 (from TMO, 2015), and 24 and 25 (from INT, 2016) were selected. The Table 5.1 lists the numerical IDs of all the lightcurves. Once more, to speed up the computation, the lightcurves were binned with a resolution of 15° in rotation phase.

Running the SHAPE modelling procedure is computationally demanding even with a limited data set and a simplified model. Therefore a pole scan as detailed as for the lightcurve inversion is not necessarily recommended, and the parameter space needed to be restricted. Taking into account the earlier results the rotation pole could be constrained to high negative latitudes. Hence, the spin-state modelling with radar data has been performed on a selection of pole positions which were divided into two batches, as shown in Figure 5.14.

In the first batch, a coarse pole scan was performed using pole positions approximately evenly distributed on a celestial sphere, with a resolution of 10°. The distribution is achieved by selecting points lying on circles on the celestial sphere parallel to the ecliptic (circles of constant latitude, β), separated by 10°. A point with ecliptic longitude $\lambda = 0°$ is always

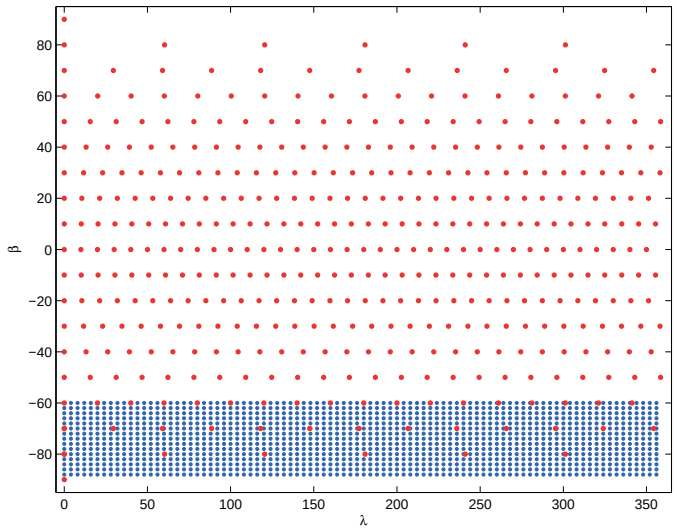

Figure 5.14: The set up of the (85990) 1999 JV_6 pole scan with `SHAPE` using two-ellipsoid model and the radar data. The pole directions for which the model was optimised were marked. The scan was divided in two batches. The red dots show the coarse whole-sky scan with points evenly distributed with a 10° separation. The blue dots show the detailed 2° × 4° scan on a fragment of celestial sphere below $\beta = -60°$.

selected and the distance between subsequent points along each circle is such that it is approximately 10°, when it is calculated along each circle as the product of $\cos\beta$ and difference in λ.

The second batch was restricted to a rectangular grid with a 4° separation in λ and 2° in β. This grid was set up on a fragment of celestial sphere most likely to contain the pole solution. The region enclosed pole positions with λ from 0 ° to 356 ° and β from −88 ° to −60 °.

The pole scan was then executed in two steps. In the first step the size-related parameters of the two ellipsoid components were held fixed. The quantities optimised for each possible pole were the rotation rate, the initial rotation phase, and the angular offsets of the two ellipsoids, which could be tilted in any direction. After that a second round of modelling was performed on each model, this time adjusting the sizes of both ellipsoids along three axes, as well as all the angular variables. The result of the pole scan was more conclusive than when using the lightcurves alone. The χ^2 plot, Figure 5.15, shows that the ecliptic latitude of the rotation pole of (85990) 1999 JV_6 is lower than $\beta = -80°$. As seen in the spherical projection in Figure 5.16, the proximity to pole of the celestial sphere makes the longitude of the pole quite difficult to determine, albeit less relevant for the solution.

The best solution from the two-ellipsoid radar scan is located at $\lambda = 144°$, $\beta = -84°$. Some basic assessment of the asteroid properties can be done based on a set of 100 models with the smallest χ^2, which all lie within 3% of the best-solution χ^2 value. As can be seen in Figures 5.15 and 5.16 the uncertainty region is roughly circular around the pole $\lambda = 0°$, $\beta = -90°$, with a radius $\approx 10°$. The smaller lobe is close to spherical and has diameters 345 ± 9, 281 ± 8 and 291 ± 9 m, and the larger is more elongated, with 580 ± 10, 322 ± 5 and 332 ± 7 m. The refined period $(6.536\,787 \pm 0.000\,006)$ h.

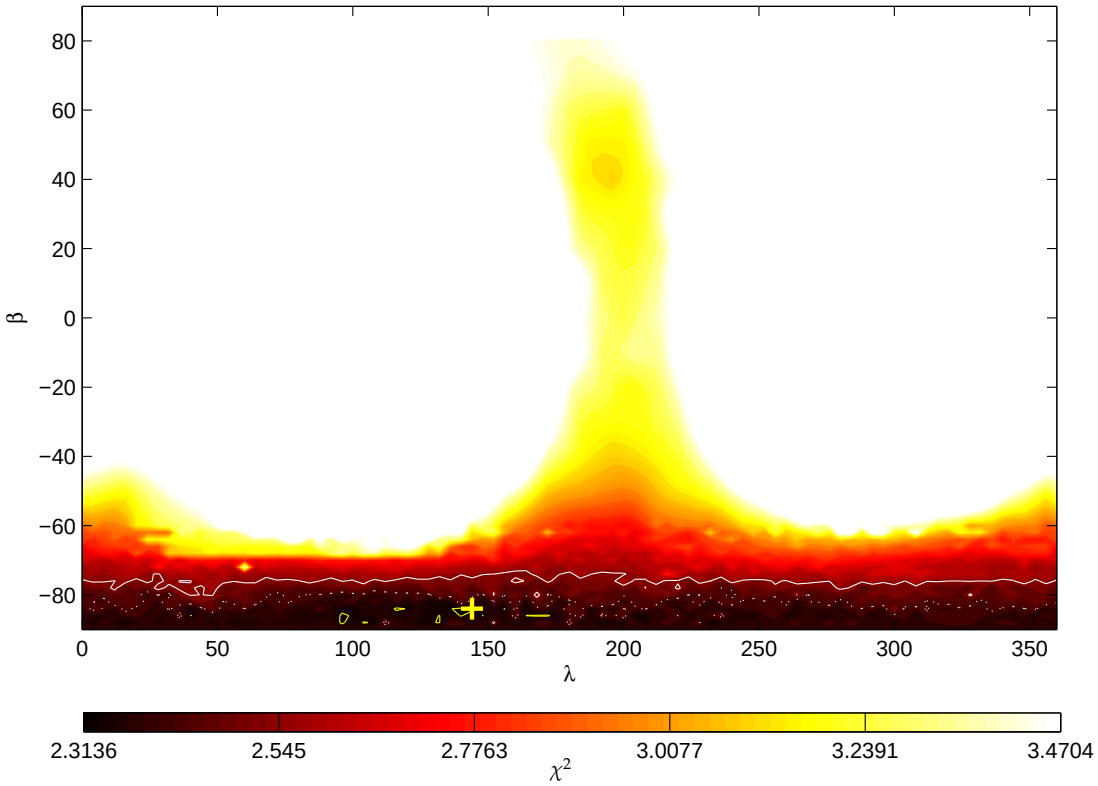

Figure 5.15: Results of the pole scan for asteroid (85990) 1999 JV_6 on a sample of possible pole positions. The scan was performed using a two-ellipsoid model, and a selection of lightcurve and radar data. The axes are ecliptic coordinates of the asteroids pole in degrees, longitude – λ, and latitude – β. The colour changes from black at the minimum χ^2 with 1% increments of the minimum (the darker the colour, the smaller the χ^2), with the white region representing all the solutions with χ^2 more than 50% above the minimum. Additionally, the model with smallest χ^2 is marked with a '+' sign and contours corresponding to 1% (yellow), 5% (white dotted) and 10% (white solid) increase above the minimum χ^2 are plotted.

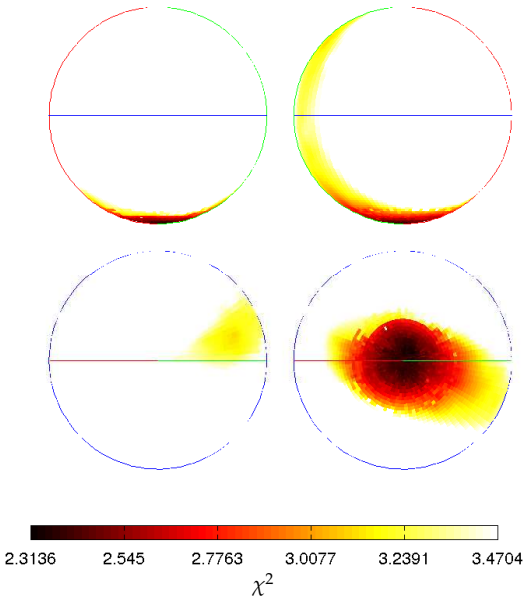

Figure 5.16: Results of the two-ellipsoid pole scan for asteroid (85990) 1999 JV_6. This is same as Figure 5.15, but the results are projected on the surface of the celestial sphere described in ecliptic coordinates of the asteroids pole. The blue line marks the equator with latitude $\beta = 0$. The red line marks the longitude $\lambda = 0$ and the green line $\lambda = 180$. From top-right clockwise, the coordinates of the central point in each projection are ($\lambda = 90°, \beta = 0°$), ($\lambda = 270°, \beta = 0°$), ($\beta = 90°$), and ($\beta = -90°$). The colour changes from black at the minimum χ^2, with 1% increments of the minimum, and the white region representing all the solutions with χ^2 more than 50% above the minimum.

5.4.3 Refined radar model

In the two-ellipsoid pole scan there are a few solutions within 1 % of the minimum χ^2, and those within 10 % of the minimum essentially cover the southern pole of the celestial sphere up to latitude −74°. Given the uncertainty on the pole position, especially in determining the pole longitude, a few models were selected for further development, rather than just the best-fit model. As illustrated in Figure 5.19, a sample of 16 models were selected for further development, with a focus on the radar models with goodness-of-fit within 1 % of the best solution.

Each of the models was realised with around 1000 vertices, arranged into approximately 500 facets for each model, with an average length on a facet edge being 40 m. Vertex realisation of the models had been optimised using an extended radar data set and the same lightcurves as were used in the pole scan. The observation set now included all *cw* observations available, see Figure A.6 and Table A.1, all frames with 0.2 µs, 0.1 µs, and 0.05 µs baud length from Arecibo, and 0.125 µs and 0.05 µs from Goldstone. The sampling of rotation phases for the radar data used is shown in Figure 5.13. Each of the models was optimised in two stages, allowing first the size and then the deviation of each vertex to vary, along with the sidereal rotation period and initial rotation phase at both stages (this is similar to adjusting the T_0 in `CONVEXINV`).

The final quality of the fit of the new model to the extended data set is correlated with

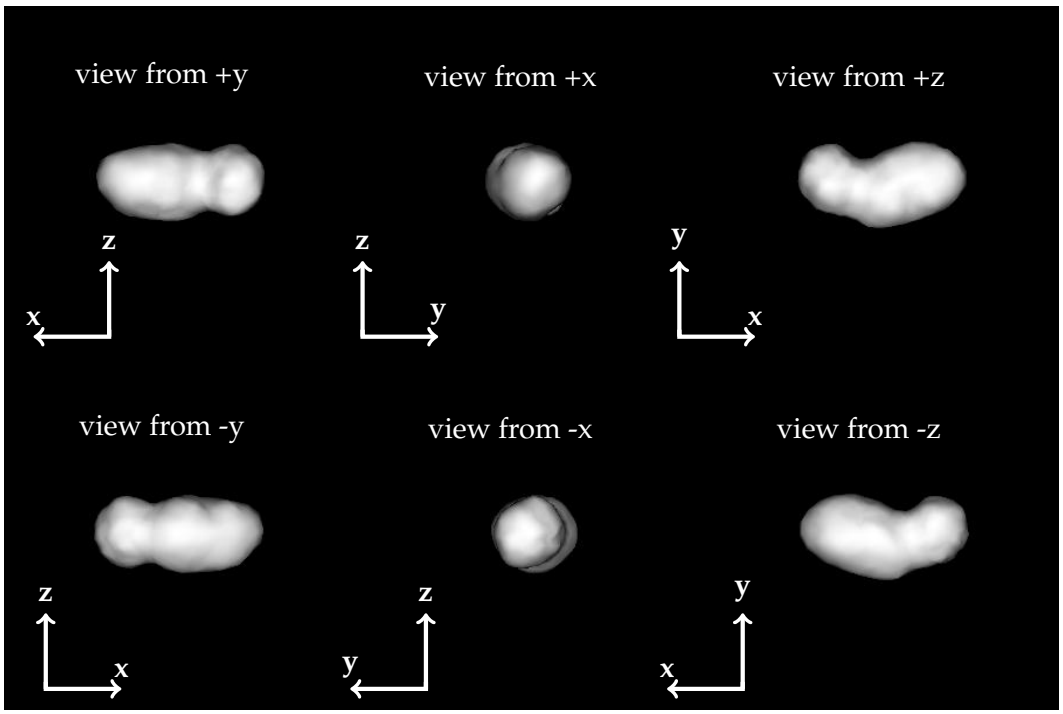

Figure 5.17: The model corresponds to a solution with a χ^2 within 1 % of the best solution from the scan depicted in Figures 5.15 and 5.16. This is the model that best reproduced the full lightcurve data set, with the rotation pole located at $\lambda = 96°$, $\beta = -88°$. The six panels represent views of the shape model along principal axes of inertia.

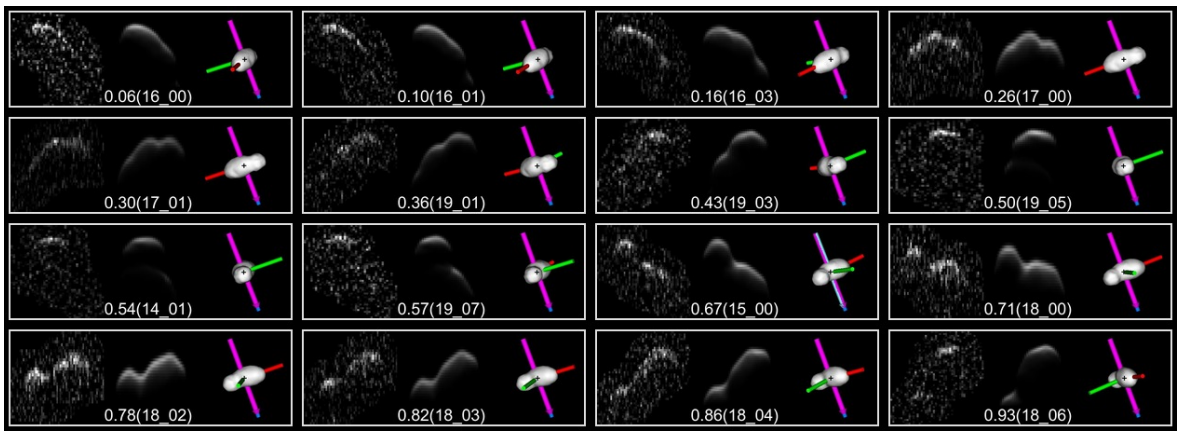

(a) Arecibo 2015

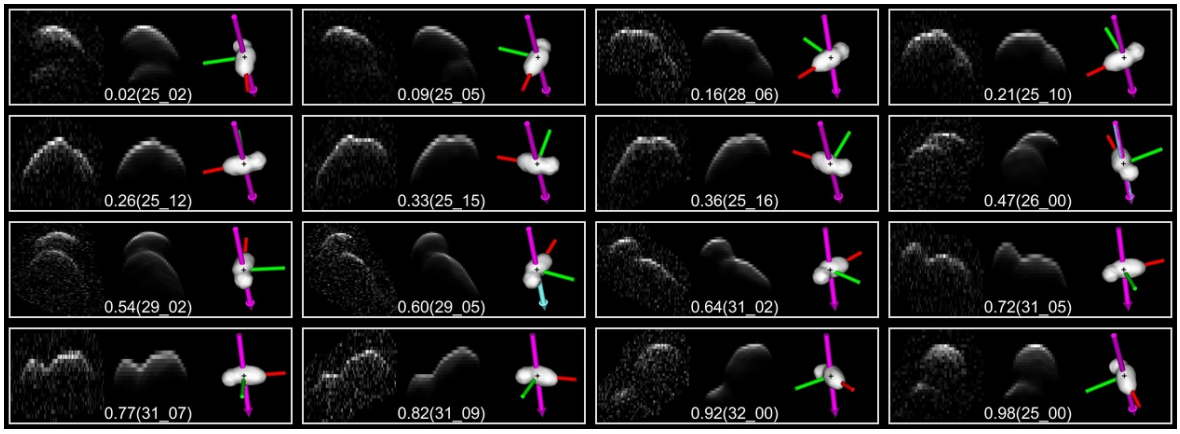

(b) Goldstone

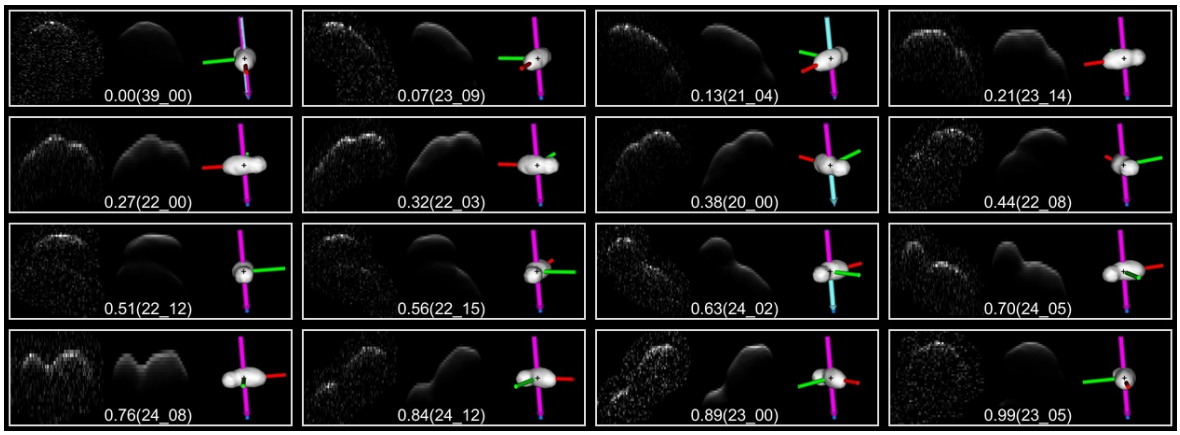

(c) Arecibo 2016

Figure 5.18: Example of the quality of fit of the final shape model with $\lambda = 96°$ and $\beta = -88°$ of asteroid (85990) 1999 JV_6 to the radar data. The three subfigures represent different observing runs: Arecibo 2015 (a), Goldstone (b), Arecibo 2016 (c). The subsets of 16 images were selected to cover a full rotation for each run and are subscribed with the rotation phase (as a fraction of the full rotation) as well as set and frame number in the `SHAPE` observations file (in brackets). Each set of three panels represents one Doppler-delay image and is made of the actual observation (left panel), echo simulated from the model (middle panel), and plane-of-sky projection of the model (right panel). On the observation and simulation images the delay increases downwards and the frequency (Doppler) to the right. The plane-of-sky image is orientated with north to the top and east to the left. The principal axes of inertia are marked with coloured rods (red, green and blue), and the rotation vector (z-axis of fixed body coordinate system) is marked with a purple arrow. Note the rotation axis and z-axis of the body overlap with the axis of maximum inertia.

Set	Frame	Obs.	UT Date *yyyy-mm-dd*	UT Time *hh:mm:ss*	Baud [μs]	Pix. height [μs]	Pix. width [Hz]	Looks	Phase
16	00	A1	2015-01-16	05:35:46	0.200	0.100	0.067	24	0.06
16	01	A1	2015-01-16	05:49:48	0.200	0.100	0.067	24	0.10
16	03	A1	2015-01-16	06:15:40	0.200	0.100	0.067	24	0.16
17	00	A1	2015-01-16	06:54:26	0.200	0.100	0.067	24	0.26
17	01	A1	2015-01-16	07:08:59	0.200	0.100	0.067	30	0.30
19	01	A1	2015-01-18	05:23:57	0.200	0.100	0.074	28	0.36
19	03	A1	2015-01-18	05:51:18	0.200	0.100	0.074	28	0.43
19	05	A1	2015-01-18	06:18:35	0.200	0.100	0.074	28	0.50
14	01	A1	2015-01-15	06:31:06	0.200	0.100	0.068	24	0.54
19	07	A1	2015-01-18	06:46:54	0.200	0.100	0.074	28	0.57
15	00	A1	2015-01-15	07:22:01	0.200	0.100	0.068	24	0.67
18	00	A1	2015-01-17	05:31:40	0.200	0.100	0.065	24	0.71
18	02	A1	2015-01-17	05:58:37	0.200	0.100	0.065	24	0.78
18	03	A1	2015-01-17	06:11:49	0.200	0.100	0.065	24	0.82
18	04	A1	2015-01-17	06:27:44	0.200	0.100	0.065	24	0.86
18	06	A1	2015-01-17	06:56:56	0.200	0.100	0.065	30	0.93

(a) Arecibo 2015

Set	Frame	Obs.	UT Date *yyyy-mm-dd*	UT Time *hh:mm:ss*	Baud [μs]	Pix. height [μs]	Pix. width [Hz]	Looks	Phase
25	02	G	2016-01-08	07:31:45	0.125	0.125	0.158	40	0.02
25	05	G	2016-01-08	07:59:50	0.125	0.125	0.158	40	0.09
28	06	G	2016-01-10	06:20:56	0.125	0.125	0.158	47	0.16
25	10	G	2016-01-08	08:46:38	0.125	0.125	0.158	40	0.21
25	12	G	2016-01-08	09:05:21	0.125	0.125	0.158	40	0.26
25	15	G	2016-01-08	09:34:02	0.125	0.125	0.158	45	0.33
25	16	G	2016-01-08	09:44:32	0.125	0.125	0.158	45	0.36
26	00	G	2016-01-09	06:07:31	0.125	0.125	0.158	40	0.47
29	02	G	2016-01-09	06:34:59	0.050	0.050	0.144	70	0.54
29	05	G	2016-01-09	06:59:29	0.050	0.050	0.144	70	0.60
31	02	G	2016-01-12	07:20:03	0.125	0.125	0.160	96	0.64
31	05	G	2016-01-12	07:50:03	0.125	0.125	0.160	96	0.72
31	07	G	2016-01-12	08:10:03	0.125	0.125	0.160	96	0.77
31	09	G	2016-01-12	08:30:03	0.125	0.125	0.160	96	0.82
32	00	G	2016-01-13	04:48:26	0.125	0.125	0.160	96	0.92
25	00	G	2016-01-08	07:13:03	0.125	0.125	0.158	40	0.98

(b) Goldstone

Table 5.5: Details of the example radar imaging frames shown in Figure 5.18. The three sub-tables represent different observing runs: Arecibo 2015 (a), Goldstone (b), Arecibo 2016 (c). *Set* column lists the number of set as it appears in the `SHAPE` observations file. *Frame* column contains the frame number in the `SHAPE` file. The set and frame numbers are given as they are unique labels and are convenient for identification of images in the figures. *Obs.* is a designation of the observing run, *A1* for Arecibo 2015, *A2* for Arecibo 2016, and *G* for Goldstone. *UT Date* is the UT date at which the observation was taken. *UT Time* is the mid-receive time. *Baud* is the signal code baud length in μs. *Pix. height* is the pixel size in the delay domain in μs. *Pix. width* is the pixel size in the frequency (Doppler) domain in Hz. *Looks* is the total number of independent measurements (looks) in each frame. *Phase* is the rotation phase, assuming the spin-state of the refined radar model with $\lambda = 96°$ and $\beta = -88°$, as a fraction of full rotation. The frames for each run are listed in order of increasing rotation phase.

Set	Frame	Obs.	UT Date *yyyy-mm-dd*	UT Time *hh:mm:ss*	Baud [µs]	Pix. height [µs]	Pix. width [Hz]	Looks	Phase
39	00	A2	2016-01-15	03:06:49	0.050	0.050	0.038	6	0.00
23	09	A2	2016-01-18	03:29:39	0.100	0.100	0.044	9	0.07
21	04	A2	2016-01-15	03:56:06	0.100	0.100	0.038	6	0.13
23	14	A2	2016-01-18	04:24:48	0.100	0.100	0.044	9	0.21
22	00	A2	2016-01-17	02:38:12	0.100	0.100	0.032	6	0.27
22	03	A2	2016-01-17	02:59:29	0.100	0.100	0.032	6	0.32
20	00	A2	2016-01-14	03:26:09	0.100	0.100	0.042	6	0.38
22	08	A2	2016-01-17	03:46:12	0.100	0.100	0.032	4	0.44
22	12	A2	2016-01-17	04:13:24	0.100	0.100	0.032	6	0.51
22	15	A2	2016-01-17	04:34:43	0.100	0.100	0.032	6	0.56
24	02	A2	2016-01-19	02:48:46	0.100	0.100	0.041	9	0.63
24	05	A2	2016-01-19	03:13:03	0.100	0.100	0.041	9	0.70
24	08	A2	2016-01-19	03:37:33	0.100	0.100	0.041	9	0.76
24	12	A2	2016-01-19	04:10:21	0.100	0.100	0.041	9	0.84
23	00	A2	2016-01-18	02:21:15	0.100	0.100	0.044	9	0.89
23	05	A2	2016-01-18	02:59:15	0.100	0.100	0.044	9	0.99

(c) Arecibo 2016

Table 5.5: Continued from Page 123.

how well the two-ellipsoid model fit the original data set, which is to be expected. An example of a final vertex model is shown in Figure 5.17. The model that gives the best fit to all of lightcurve data is shown. For the same model a sample of radar images from each radar run was selected to illustrate full rotation of the asteroid and is shown in Figure 5.18, details of the imaging frames used in this illustration are gathered in Table 5.5. For a figure showing the full imaging data set used in the modelling please refer to Figure A.7 with images listed in Table A.2

5.5 Spin-state analysis

The 16 candidate shape models, that had their faceted shapes optimised, were used for phase offset measurements for the full lightcurve data set described in Table 5.1. The T_0 used in spin-state analysis should be, ideally, set at either end of the observing interval. Within the shape modelling, it was forced to be after the date of the last observation with INT, so this point was used to propagate the model.

First of all, the quality of the fit χ^2 of the model to the full lightcurve data set was checked, see Figure 5.19. The best fit is obtained for a model with $\lambda = 132°$ and $\beta = -88°$. The selected shape models reproduce the full lightcurve data set quite accurately, with a few % difference in χ^2 between them. The Figure 5.19 illustrates the location of the rotation pole positions of the models investigated and the differences between χ^2 of lightcurve fits for them, over-plotted on the χ^2 plot obtained from the two-ellipsoid pole scan (a fragment of Figure 5.15).

Then, for each model the phase offsets between the data and artificial lightcurves were measured. The nominal rotation phase of each observed data point was calculated using the selected T_0 and period P. An artificial lightcurve was then calculated for those phases as well as a 100 equally spaced points in the phase angle space. Then the artificial lightcurve was interpolated, using linear interpolation, to create a continuous representation of the curve. The observed points were then slid along the artificial lightcurve, by adding a phase offset with a step of 0.5° of rotation. At each point, the quality of the fit of the artificial lightcurve to the data was calculated and the offset giving the best fit was recorded.

The phase offsets for each of the lightcurves, given in degrees, were then plotted as a function of time. The number of days elapsed since T_0 is used here, but sometimes the number of years since T_0 can be given. An example of such plot is shown here, in Figure 5.20, for the model that best reproduced the lightcurves, but additional plots for the remaining 12 models can be found in Figure A.8. The expected result for a constant period solution is the measurements laying in a straight line, either representing a systematic phase offset if the T_0 is set incorrectly, or tilted to indicate an inaccuracy in period measurements. In case that

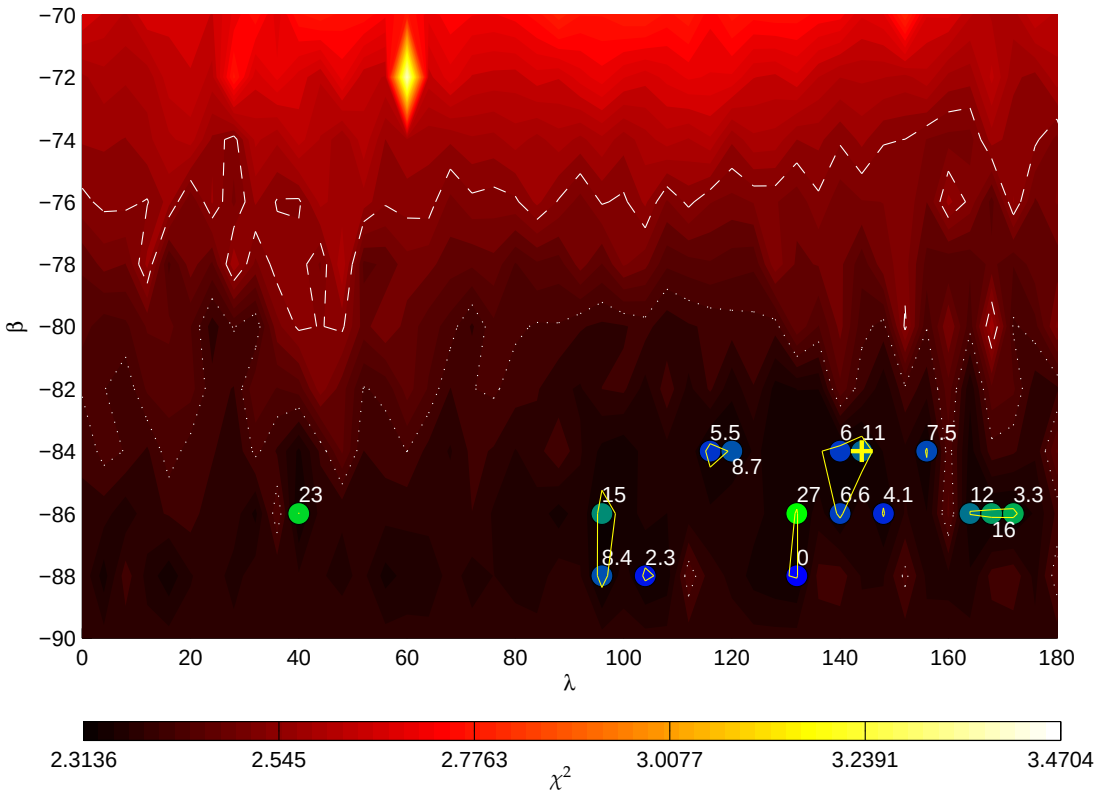

Figure 5.19: A few of the best two-ellipsoid models of (85990) 1999 JV_6 were selected for further development. The coloured dots mark positions of the rotation pole for each model. Colour changes from best fit marked with blue, to worst fit marked with green, with text labels showing the increase of χ^2 goodness-of-fit of the model to all available lightcurves above the minimum value in %. The background is a fragment of scan illustrated by Figure 5.15. It can be noted that however the solution with $\lambda = 136°$, $\beta = -88°$ produced the best overall fit to the combined data, it was the $\lambda = 96°$, $\beta = -88°$ that produced the best lightcurve fit.

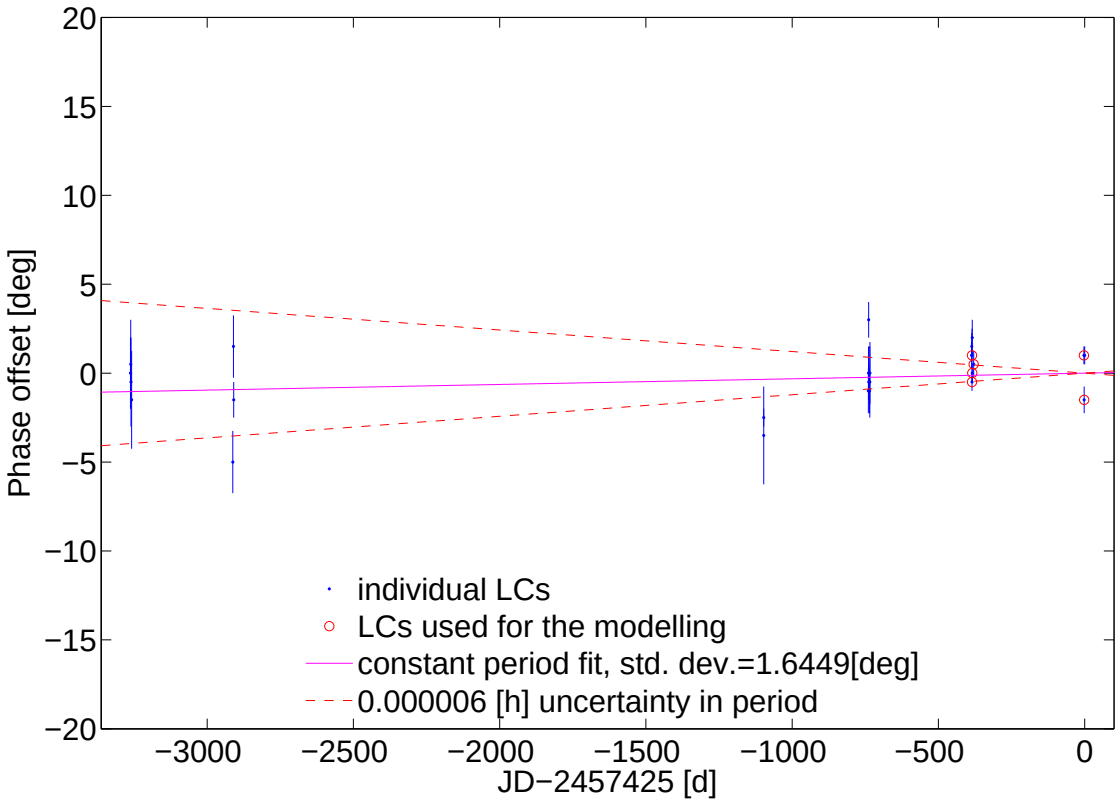

Figure 5.20: Phase offset measurements for (85990) 1999 JV_6 model that best reproduces the lightcurves, with $\lambda = 132°$, $\beta = -88°$, period $P = 6.536782$ h, and starting point $T_0 = 2\,457\,425.2133$ (February 2016). The blue points represent individual lightcurves with error in the phase offset measurement marked with the vertical bars. The lightcurves utilised in SHAPE modelling are circled in red. Purple solid line marks best-fit, assuming a constant-period solution (the σ of the fit is given in the legend). The red dashed lines mark possible spread in phase offsets due to uncertainty in the measured period alone.

YORP would be acting, the phase offsets would demonstrate a quadratic trend, as seen for example for (25143) Itokawa (Lowry et al., 2014), or (54509) YORP (Fig. 2 Taylor et al., 2007, reproduced here in Figure 1.9b).

The constant period solution seems to reproduce all of the (85990) 1999 JV_6 data very well. A small spread can be observed in the phase offset measurements, see Figures 5.20 and A.8, but the trend corresponding to a constant period solution can be fitted to the observations with $\sigma \approx 2°$, and individual offsets lay within the error in period determination for most models. The points from 2013 NTT run seem not to follow those trends, but these are short lightcurve segments and the phase offset measurement error might be underestimated. The lightcurve fits corresponding to the model with $\lambda = 96°$ and $\beta = -88°$ are shown in Figure 5.21.

5.6 Conclusions

The asteroid (85990) 1999 JV_6 is a bi-lobed body, a likely representative of a class of asteroid called contact-binaries, which are estimated to make up to 35 % of NEA's population (Jacobson et al., 2016). The characterisation of asteroid (85990) 1999 JV_6 was made possible thanks to combining the extensive lightcurve data set with precise radar measurements. The lightcurves have a large amplitude of variation, often close to 1 ^{mag}. The shape of the lightcurves is characteristic of an elongated body, they have two sharp minima and arched maxima. The lightcurve analysis constrains the rotation pole to be located at a low ecliptic latitude.

The radar observations were collected at Arecibo and Goldstone observatories in January 2015 and January 2016. The radar experiment revealed a bi-lobed body with surface characteristic typical for a near-Earth asteroid. A robust shape model was obtained with a rotation pole very close to the southern pole of the celestial sphere in ecliptic coordinates. The base for developing the model was a shape constructed with two ellipsoids. One of the lobes was slightly more spherical and had the largest semi-major axis about 40 % shorter than the larger lobe. The larger lobe is elongated and has the smaller lobe attached at an angle. A vertex model was developed with an effective resolution of about 40 m.

The analysis including radar data confirmed the findings from the lightcurve study and allowed to further constrain the location of rotation pole. The radar-derived shape of (85990) 1999 JV_6 is similar to other known contact-binary asteroids, like (8567) 1996 HW_1 (Magri et al., 2011) which had a clear neck region. The two lobes of (85990) 1999 JV_6 are not quite as distinct. One way to confirm the contact-binary status, would be to investigate the interior structure. This was done for example in case of asteroid (25143) Itokawa (Lowry et al., 2014). In case of Itokawa, it was impossible to match the theoretical predictions of YORP strength without shifting the centre of mass away from the geometric centre of the figure. The shift was explained with different densities assigned to the lobes. In case of (85990) 1999 JV_6 the model was developed assuming a principal axis rotation and forcing the centre-of-mass position in the geometric centre using modelling penalties. A linear offset of the centre of mass might be probed in the future to check whether there is a scope for investigation of density inhomogeneity.

While the YORP spin-up was not detected for this asteroid, it can be noted here that the radar astrometry performed at Arecibo in January 2016 led to a detection of non-gravitational force changing the orbit of (85990) 1999 JV_6. The discovery was announced in an electronic circular by Giorgini et al. (2016). The asteroid had a well known orbit, with 945 optical astrometric measurements available as well as 4 radar astrometric measurements from January 2015 at Arecibo, and four in early January 2016 from Goldstone. The new measurements were taken on 14^{th}, 17^{th} and 19^{th} January did not follow a ballistic trajectory. The new measurements are reportedly offset by $(-5.6 \pm 1.0) \times 10^{-6}$, $(-8.4 \pm 0.5) \times 10^{-6}$ and $(-11.4 \pm 0.5) \times 10^{-6}$ seconds from the ephemeris round-trip time. Some non-gravitational force is required to explain the detected offsets. A new orbital solution was thus published, incorporating all existing

astrometry and including a transverse acceleration $(-1.6 \pm 0.2) \times 10^{-12}\,\mathrm{m/s^2}$ necessary to describe the orbital motion of (85990) 1999 JV_6. A possible explanation of the observed orbital dynamics of this asteroid might be the influence of Yarkovsky effect, see Section 1.3.

The YORP programme collaborator, B. Rozitis form the Open University, Milton Keynes modelled thermal observations for this object using the shape model and spin-state developed here. Working under the assumption that the acceleration detected in the orbital motion could be explained by the Yarkovsky effect, allowed him to estimate the mass of (85990) 1999 JV_6. Depending on the thermal inertia, the density of this object might be between $500\,\mathrm{kg/m^3}$ to $850\,\mathrm{kg/m^3}$. The low bulk density might suggest that the object could be an extinct comet. Indeed, the target's geometric albedo measured by the ExploreNEOs campaign $p_v = 0.076^{+0.058}_{-0.035}$ could put it in the low-albedo regime typical for comets and P-type asteroids (Mueller et al., 2011; **?**). However, due to the considerable error-bar on the albedo measurement, the target might still belong to the metallic M-type which is unlikely to be linked to cometary population.

Some further work is required for this asteroid. The radar scattering law needs to be refined to better reproduce the fine details of imaging and continuous-wave spectra. Influence of surface roughness on the lightcurves could also be investigated (the high SC/OC ratio suggests a rough surface, see Figure 5.2). New radar observations of (85990) 1999 JV_6 were performed at Arecibo and Goldstone in January 2017. They are lower resolution than the observations used here, and consisted with the current model. More photometric observations are required to confirm or fully reject the possibility of YORP effect acting on this asteroid.

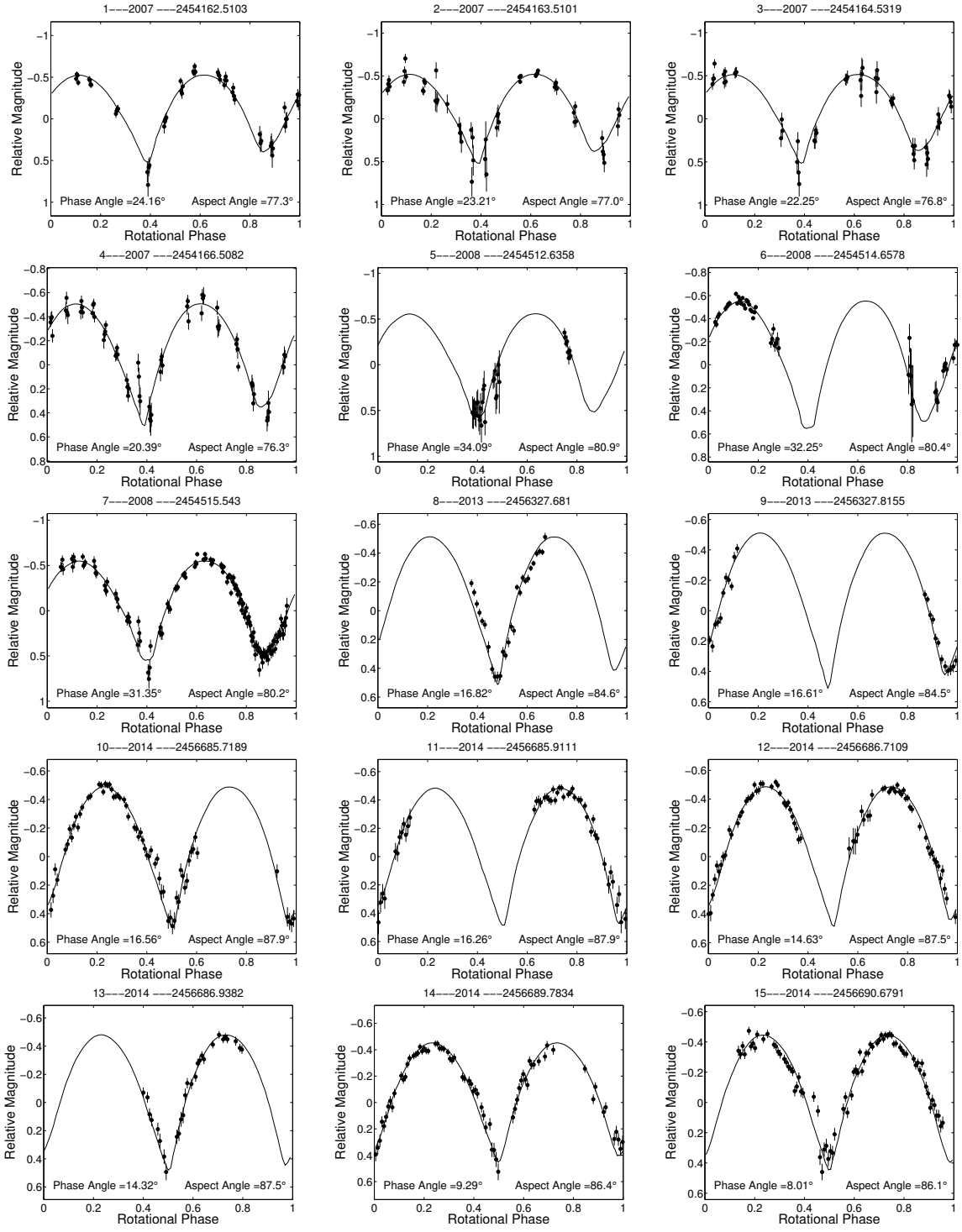

Figure 5.21: Lightcurve fits of shape model of (85990) 1999 JV_6 to all available lightcurves. The model was generated with $\lambda = 132°$, $\beta = -88°$, $P = 6.536782\,\mathrm{h}$, $T_0 = 2457425.2133$.

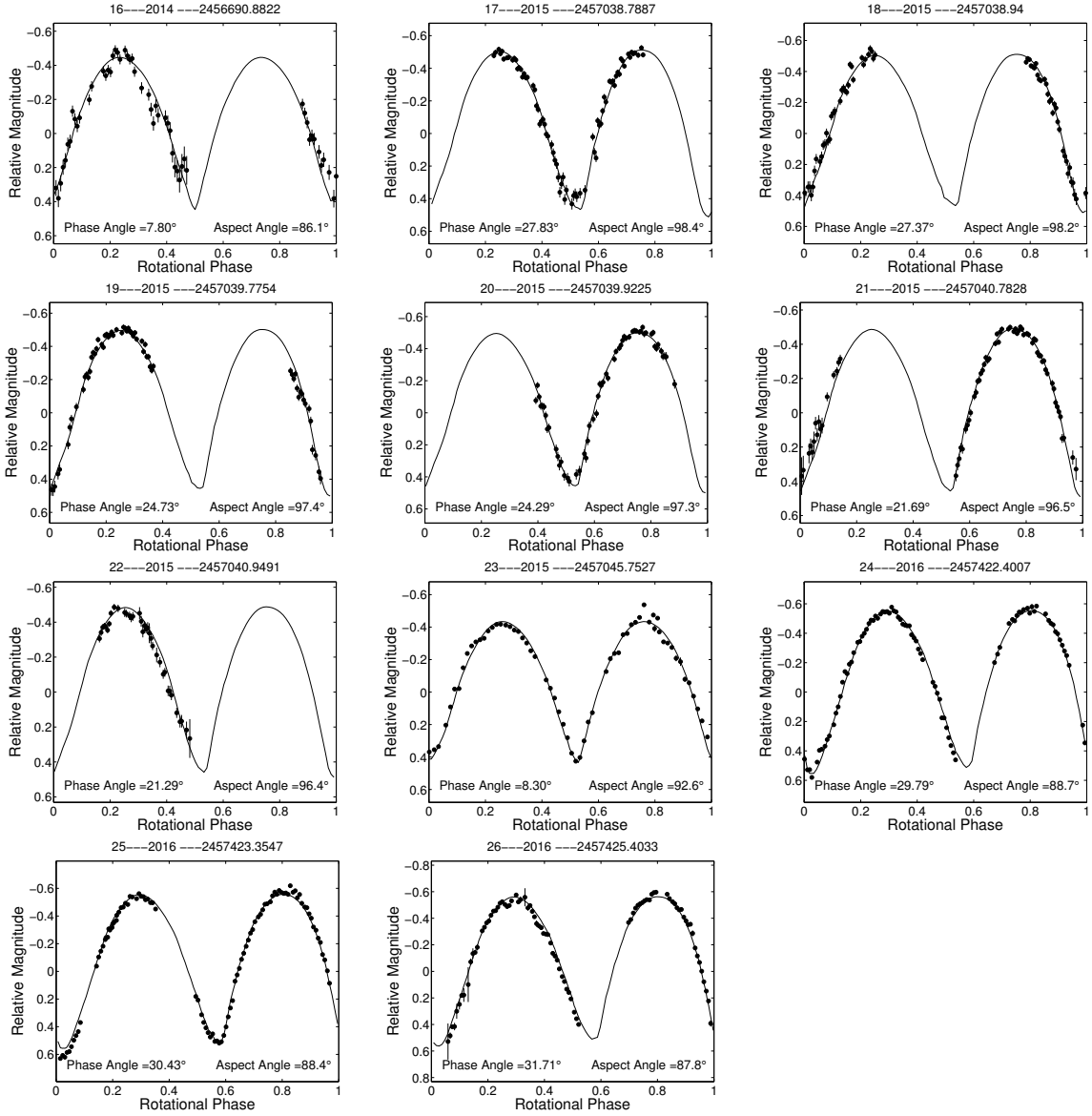

Figure 5.21: Continued from page 129

Chapter 6

Analysis of Rosetta OSIRIS and ground-based data of comet 67P

6.1 The Rosetta mission to the Jupiter family comet 67P

Comets can be studied using similar techniques, as were applied to NEAs in Chapters 4 and 5. In a few rare cases the comets come within the planetary radar range and can be modelled using delay-Doppler images (Harmon et al., 2011, for example). With sufficient data, lightcurve-inversion methods can be used to develop shape model of any small Solar System body, including a cometary nucleus, as was done for 67P/Churyumov-Gerasimenko. The Jupiter family comet 67P was recently visited by the Rosetta spacecraft, equipped with a suite of instruments including the Optical, Spectroscopic, and Infrared Remote Imaging System (OSIRIS). The instrument imaged the nucleus and its environment in detail, and was used for lightcurve study before the comet could be resolved. The framework described in Chapter 3 was used to model the data acquired by OSIRIS in early stages of the Rosetta mission.

The analysis of the lightcurves OSIRIS acquired on approach to 67P was performed using convex-lightcurve-inversion method and phase offset measurements. It built on results of earlier ground-based observational campaign and brought a robust detection of the sidereal rotation period decrease by about 20 minutes (Mottola et al., 2014, incl. A. Rożek). The tools developed for artificial lightcurve computation, described in Section 3.3.1, were used for assessment of mean daily insolation of the nucleus surface, leading to determination of dust production rates (Guilbert-Lepoutre et al., 2014, incl. A. Rożek). The calculations of illumination and visibility of surface elements were also incorporated in a geometric method for identification of source-regions of cometary jets (Lara et al., 2015; Lin et al., 2015, 2016, incl. A. Rożek). And finally, the artificial lightcurves were produced for the complex spacecraft shape model (Snodgrass et al., 2016, incl. A. Rożek).

Selected results are presented in this chapter. Following a brief Rosetta mission overview in this section, the detection of spin period change is discussed in Section 6.2, and the determination of jet-source regions in Section 6.3.

6.1.1 The 'comet chaser' mission overview

The European Space Agency (ESA)'s Rosetta spacecraft mission was first endeavour by a man-made object to orbit and land on a comet. It was launched on 2nd March 2004, after an initial launch delay prompted a change of mission target, comet 46P/Wirtanen, to comet 67P/Churyumov-Gerasimenko (67P). The target was selected from amongst the Jupiter family comets, characterised by short orbital periods and strong dynamical influence from Jupiter (see Figure 1.1). The mission benefited from multiple gravity assists and survived over 2.5 years of hibernation to rendezvous with the target on 6th August 2014. The spacecraft carried eleven instruments on-board, designed to provide an in-depth physical characterization of the comet nucleus and activity. It deployed a small lander Philae onto the surface of 67P on 12th November 2014. The lander bounced off the cometary surface a few times, before landing in a position inconvenient for prolonged operation, where it carried

Figure 6.1: The Rosetta mission poster shows the orbital probe, the lander Philae and the target comet 67P/Churyumov-Gerasimenko. The peculiar duck-like shape of the nucleus came as a big surprise (Sierks et al., 2015). The lander Philae reached the comet nucleus in November 2014 and bounced off it a few times before landing sideways under a cliff (Biele et al., 2015). The image of the comet was taken with the navigation camera on Rosetta (ESA/Rosetta/NavCam), and the collage was downloaded from the ESA website[b].

[b] http://sci.esa.int/rosetta/55799-rosetta-at-comet-67p-landscape/

out most of its planned science experiments (Biele et al., 2015). The mission ended on 30$^{\text{th}}$ September 2016 with the probe delivering final data from as close as 20 meters from the surface before crashing into the nucleus.

Comets are considered the primordial bodies of the Solar System. The giant planets, as they were formed and migrated through the Solar System, perturbed gravitationally the material around them that failed to form planets (Walsh et al., 2011). The cometary material, that was delivered this way to the outer reaches of the Solar System, likely reflects the composition of the early proto-planetary disk (Meech et al., 2016). Some scenarios for Earth formation predict that comets, as they collided with a young Earth, brought water or components of life to the surface (Altwegg et al., 2015). The Rosetta mission was designed to investigate that possibility by looking into the composition and constitution of the comet. It was also the first mission to follow a comet along for an extended period of time rather than a short fly-by. It would provide insight into the activity on perihelion approach usually limited by the cometary nuclei being mostly obscured by coma at that stage.

The mission brought multiple breakthrough scientific results, many of them regarding chemical composition of the comet. The ratio of deuterium to hydrogen in the emitted gases was shown to be the highest for any comet measured to date (Altwegg et al., 2015), significantly different to the Earth's oceans. This has shown that Jupiter family comets have a varied composition and thus origin, which makes this family of comets less likely to be the main source of water on Earth. New numerical simulations suggest that the presence of water in the inner Solar System can be explained with the material pushed towards Earth from Jupiter's surroundings when it accreted gas (Raymond and Izidoro, 2017). Amongst some other chemical compounds, glycine was found in the 67P coma. The presence of this basic amino-acid combined with other organic molecules and phosphorus encouraged theories of life ingredients originating from comets (Altwegg et al., 2016).

6.1.2 The orbiter OSIRIS camera system

The physical appearance of the comet 67P/Churyumov-Gerasimenko was mainly investigated using the Optical, Spectroscopic, and Infrared Remote Imaging System (OSIRIS). The instrument incorporated two devices, the Narrow Angle Camera (NAC) and the Wide Angle Camera (WAC). Each Camera encapsulated a 2048×2048 pixels CCD detectors, yet was equipped with a slightly different optical systems. The NAC was equipped with a telescope with $2.2° \times 2.2°$ field of view, while the WAC's was $11.3° \times 12.1°$. The main goal of the instrument was to characterise the shape, spin-state, and surface details of the comet nucleus, and also monitor the near-nucleus environment. The NAC was achieving those goals by providing high-resolution imagery, for example close-ups of the cliffs and surface formations, while the WAC was used when the size of the field-of-view was a priority, for example to monitor the near-nucleus activity (Keller et al., 2007).

The OSIRIS cameras proved to be a rich source of information on the comet's nature. Early images revealed a peculiar bi-lobed shape with a varied morphology (Sierks et al., 2015). The surface of the cometary nucleus showed great diversity with wide dust-covered planes, sharp ridges, cliffs, cracks, and numerous boulders (Thomas et al., 2015). The comet was changing and evolving as it was followed by Rosetta, with collapsing cliffs (Pajola et al., 2017), boulders shifting across the surface and widening cracks (El-Maarry et al., 2017). Surface ice forming by condensation by night and sublimating under sunshine was found to be the source of short-term activity bursts (De Sanctis et al., 2015). Perfectly round sink-hole-like features were linked to the dust and gas jets (Vincent et al., 2015) and were a target of the final descend imaging sequence. And the layered structure of cliffs was a base for suggesting that the comet is made of two independently formed lobes (Massironi et al., 2015).

6.2 Determination of rotation period decrease for 67P

Precise spin-state determination was crucial for planning the orbit insertion manoeuvre prior to Rosetta's arrival at the comet. The collection of ground-based lightcurve data begun before the mission was launched, and continued around the time of the comet's previous perihelion approach (Lamy et al., 2006; Tubiana et al., 2008, 2011; Lowry et al., 2012, list details of the 2003-2007 observing campaign). Two models were functioning in mission planning before the early OSIRIS data became available, a spherical harmonics non-convex model (Lamy et al., 2006), and a convex lightcurve-inversion model (Lowry et al., 2012).

The FFT of those early lightcurves also contained a signature of two possible rotation periods, $(12.762\,36 \pm 0.000\,06)$ h and $(12.409\,71 \pm 0.000\,05)$ h. However, the shorter period solution was rejected as some of the lightcurves appeared out-of phase when fitted with this period, and the longer period was adopted. The best convex lightcurve-inversion model, shown in Figure 6.2, indicated the rotation pole should be at the ecliptic longitude $\lambda = (78 \pm 10)^\circ$ and latitude $\beta = (58 \pm 10)^\circ$. The sidereal rotation period was refined to $(12.761\,37 \pm 0.000\,06)$ h (Lowry et al., 2012).

The spacecraft rotational lightcurves of the nucleus were collected by OSIRIS cameras on the approach to the comet, between 23$^{\text{rd}}$ March, before the nucleus could be resolved, and 20$^{\text{th}}$ June 2014, just a few weeks before the rendezvous (Mottola et al., 2014). The lightcurves were reduced to a standard observing geometry at 1 AU. A composite of the spacecraft lightcurves was made by using FFT method to phase them (Harris et al., 1989). The Fourier series fit required a synodic rotation period about 20 minutes shorter than previously measured, around 12.4 h, see Figure 6.3. The tools discussed in Section 3.3 were used to confirm the spin-rate change, and develop new robust shape and spin-state model.

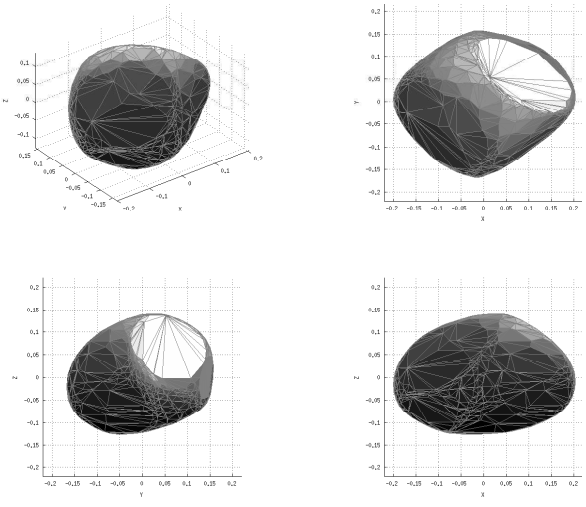

Figure 6.2: The starting point of the spin state analysis was the convex model and spin-state solution developed from Earth-based observations (Lowry et al., 2012). The sidereal rotation period was determined to be $(12.761\,37 \pm 0.000\,06)$ h, with pole ecliptic coordinates $\lambda = (78 \pm 10)^\circ$, $\beta = (58 \pm 10)^\circ$. Clockwise from the upper left corner the images show a general overview of the shape, projection along the z-axis, projection along the y-axis, and projection along the x-axis of the body.

6.2.1 Modelling OSIRIS lightcurves using the convex shape model of Lowry et al. (2012)

The first issue to resolve was whether the cometary rotation period has actually changed between the 2009 perihelion visit and spacecraft approach. That is to examine the possibility that a shorter period could reproduce ground-based data, as reported earlier by Lowry et al. (2012). The first step to confirm the rotational speed-up was to verify if there was scope to fit all of the lightcurve data with a single period using the existing shape. That would mean either fitting the original data set with a shorter rotation period, or the newer data with longer spin period.

The spin-state analysis requires generating artificial lightcurves with a known shape solutions at geometries corresponding to the spacecraft observations. The asteroid ephemerides used in generating lightcurves for NEAs usually come from the Horizons ephemeris system. However, the service provides only position vectors for small bodies relative to major bodies. Due to high positional accuracy required for observations done on such short distance from the comet it was practical to use ephemeris from SPICE kernels (Spacecraft ephemeris, Planet, satellite, comet, or asteroid ephemeris, Instrument description, C-matrix, Events) (Acton, 1996). The positions available through the kernels are updated regularly with live mission data.

Some adjustments to the spin-state analysis software were required to use ephemeris from SPICE kernels. The position of the spacecraft relative to the comet was given in km and represented in the J2000 equatorial coordinate system based on the International Celestial Reference Frame (ICRF). This is different to the ecliptic coordinate system normally used to represent the position vectors in Horizons. Both systems are illustrated in Figure B.1. They use the same reference frame, ICRF, and have the x-axes pointing towards the same point, the point of vernal equinox, designated Υ. However, the reference plane for the ecliptic system is the Earth's orbital plane and the z-axis overlaps with the Earth's orbital momentum. The coordinates in this system are ecliptic longitude, λ, and ecliptic latitude, β, both expressed in degrees. This system is traditionally used for Solar System objects. For the equatorial coordinate system the reference plane is Earth's equator so the z-axis of the system is parallel

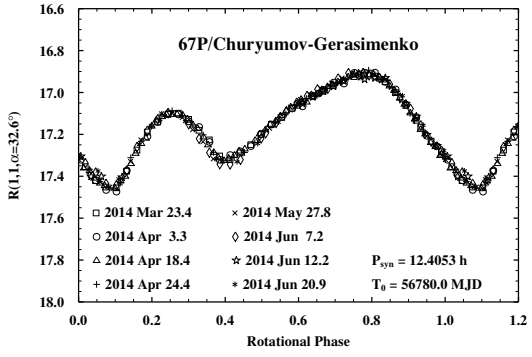

Figure 6.3: Figure reproduced from Mottola et al. (2014, Fig. 1). The composite lightcurve was obtained by performing the FFT on the lightcurves (Harris et al., 1989). The lightcurves were then reproduced using the Fourier series and their mean brightness levels were shifted to overlap. The horizontal axis is the rotation expressed in the units of full rotation, with the 1-1.2 range reproducing the 0-0.2 of rotation phases. The vertical axis is calibrated to reflect the first lightcurve in the series.

to Earth's spin axis. The longitude angle is called right ascension α and can be sometimes expressed in hours, minutes, and seconds of arc. The latitudinal angle is called declination, δ, and is given in degrees.

In order to transform a vector from the ecliptic to equatorial coordinate system a rotation matrix is needed:

$$R_{\varepsilon_\oplus} = \begin{pmatrix} 1 & 0 & 0 \\ 0 & \cos\varepsilon_\oplus & \sin\varepsilon_\oplus \\ 0 & -\sin\varepsilon_\oplus & \cos\varepsilon_\oplus \end{pmatrix} \tag{6.1}$$

Where $\varepsilon_\oplus = 23°26'21.448''$ is the obliquity of Earth's rotation axis for J2000 epoch (the angle between the orbital and equatorial planes of the Earth). It can be used to transform vectors from the equatorial to ecliptic coordinate system before transforming them to the body-centric coordinate system (see Figure B.3 and transformations discussed in Section 3.3). After performing this extra step, the lightcurves were calculated using the procedures described in an earlier chapter (see Chapter 3). Artificial lightcurves for the archive observations (2003-2007) were calculated using the position vectors from Horizons.

The shape of the spacecraft lightcurves was correctly reproduced by the available convex-inversion model and pole developed by Lowry et al. (2012). However, the period and T_0 did not seem to be valid for the newest data. An offset of few tens of degrees could be clearly seen between the rotation phases of artificial lightcurves and observations. Phase offset measurements were used to assess whether the rotation rate could be adjusted to accommodate all the lightcurves.

For all measurements, a $T_0 = 2452709$ was adopted, corresponding to the earliest lightcurve observations available with the original sidereal period from convex lightcurve-inversion. Then, to ensure that the misalignment of lightcurves is not due to of period uncertainty, a series of sidereal period values was selected in two ranges, close to both 'long' and 'old' period. For each potential sidereal period solution phase offsets were calculated and a straight line was fitted to the points representing phase offset against time elapsed since the first observation. The line had the equation similar to Equation (3.26), but without the YORP term

$$\Delta\phi = \Delta\omega(T - T_0) + \phi_0, \tag{6.2}$$

where

- $\Delta\phi$ is the offset of rotation phase (in °)
- $\Delta\omega$ is the error in synodic spin rate (in $° \, d^{-1}$), which would be related to the error in period determination, as here $\omega = \frac{360°}{P}$,
- T the epoch of the lightcurve (Julian date of the first point),
- T_0 the epoch of the model,
- ϕ_0 the initial phase offset.

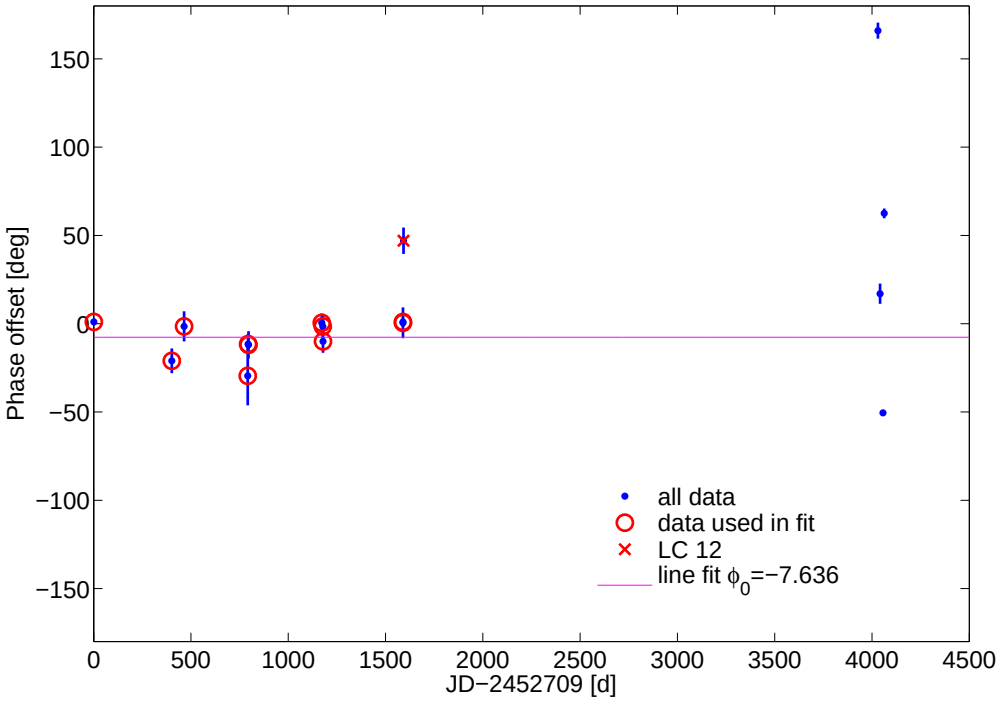

(a) $P = 12.7614\,\mathrm{h}$, $\phi_0 = -7.6°$, $\sigma_\phi = 10.3°$

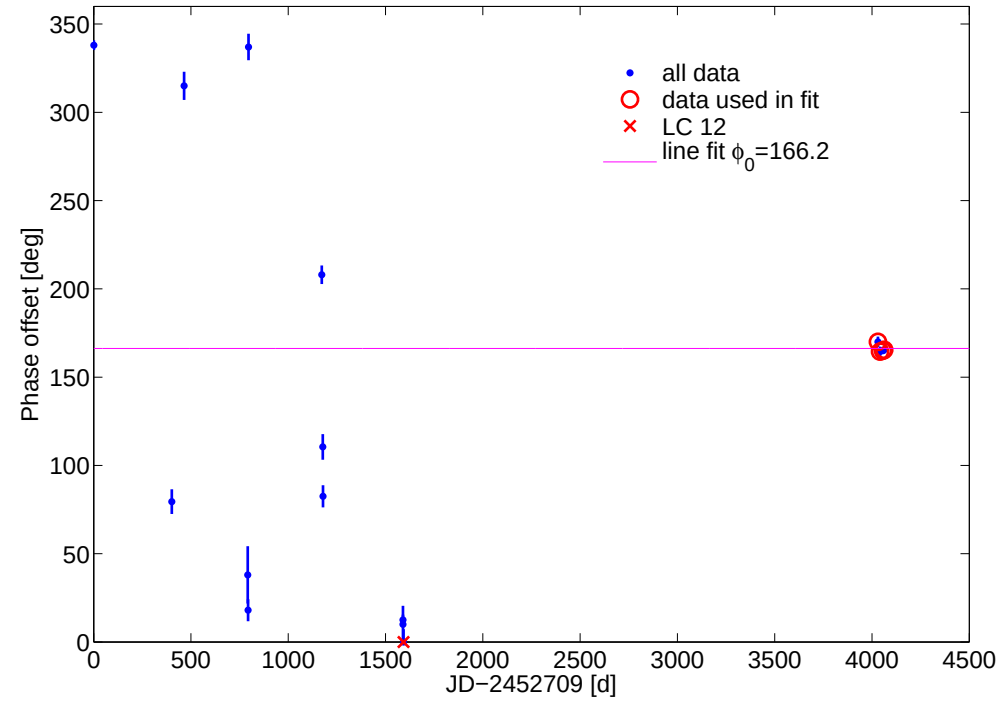

(b) $P = 12.4047\,\mathrm{h}$, $\phi_0 = 166.2°$, $\sigma_\phi = 2.5°$

Figure 6.4: The two panels in this figure represent the phase offset measurements made using the best convex shape and rotation pole model from Lowry et al. (2012). The upper panel (a) shows the phase offset measurements for a period close to the spin-state reported by Lowry et al. (2012), $P = 12.7614\,\mathrm{h}$. The lower panel (b) shows the measurements done with a period close to the spacecraft period solution, $P = 12.4047\,\mathrm{h}$. The blue dots mark individual lightcurves and are plotted with phase offset measurement uncertainties. The red circles mark lightcurves used for constant-period fits, the red 'x' marks the only lightcurve that couldn't be reproduced with the shape model (it is essentially a lightcurve fragment with no clear maximum). The purple line marks a constant-offset fit to a subset of data, corresponding to a constant-period solution. Fitting a constant period to all the data has proven impossible.

The phase offset measurements lying near a straight line would mean that the whole data set could be fit with a single rotation period. If the line was at an angle to the x-axis, then there was an error in the rotation period determination. A line parallel to the x-axis would mean that the period is correct, but there is an error in determining the T_0, in other words a constant offset ϕ_0 has to be applied to all the artificial lightcurves in order to match the observed data. The conclusion of these measurements was that there are two separate spin-rate solutions, as shown in Figure 6.4.

The phase offsets of the archival lightcurve observations lay approximately around a straight line when fitted with a sidereal period $P = 12.7614\,\mathrm{h}$. The line corresponds to a constant rotation phase offset $\phi_0 = -7.6°$, with the early observations scattered around it with a deviation of $\sigma_\phi = 10.3°$. But, with this period, the newer lightcurves are scattered across over half of a rotation. The spacecraft lightcurves can, in turn, be very well reproduced with a sidereal period $P = 12.4047\,\mathrm{h}$, requiring a $\phi_0 = 166.2°$. The mean noise of the phase offsets of the most recent lightcurves is $\sigma_\phi = 2.5°$, but the measurements made for the archive data set are scattered across the full rotation.

6.2.2 Re-evaluation of the convex-inversion model of the nucleus using ground-based and spacecraft lightcurves

Using the lightcurve phase offset measurements it was determined that the rotation period change occurred after the ground-based lightcurves were obtained and before Rosetta's encounter. Another issue remained namely how to recover the full geometry information. In other words how to combine the old and new data, to improve the pole and shape solution. Attempts to combine all the data into a single-period solution resulted in an non-physical solution with a shape rotating about the axis of minimum inertia (Mottola et al., 2014).

The convex-inversion modelling procedure was therefore altered to accommodate the (impulsive) period change between the two data sets. The whole celestial sphere was scanned, with a $2° \times 2°$ resolution of pole positions. At each point the shape was optimised. A period close to the 'old' rotation period was optimised for the ground-based data. For spacecraft data the period was held fixed at the best-fit value from the period search using phase offsets.

The χ^2 plane displays two regions with local minima, see Figure 6.5. Two best pole solutions are marked there with white dots. However, both regions have quite irregular shapes, so the more central locations, marked with crosses, were selected for further analysis. The convex shapes corresponding to the best solutions are shown in Figure 6.6. Details of the spin-states are gathered in Table 6.2.

The two solutions are about 180° apart in ecliptic longitude, an ambiguity that is a result of the limited observing geometry (Kaasalainen and Lamberg, 2006). For a target that has been observed with the viewing and illumination direction staying in the same plane two

Model	A (min)	A (pub)	B (min)	B (pub)	Spacecraft
λ	64°	$(65 \pm 15)°$	272°	$(275 \pm 15)°$	79.3°
β	64°	$(59 \pm 15)°$	54°	$(50 \pm 15)°$	42.0°
P_1 [h]	12.761 29	12.761 29(5)	12.761 29	12.761 29(5)	12.7617
P_2 [h]	12.4047	12.4043(7)	12.4047	12.4043(7)	12.4043

Table 6.2: Summary of spin-state and shape models of comet 67P/Churyumov-Gerasimenko. The spin-state solutions marked A (min) and B (min) are the best-fit solutions developed using the convex-inversion method, as marked in Figure 6.5. Those spin-states correspond to convex shape model shown in Figure 6.6 and artificial lightcurves plotted in Figure 6.7. Those solutions are slightly different to the values located more centrally in the uncertainty regions in Figure 6.5, adopted for publication, listed in columns A (pub) and B (pub). The details for the spacecraft model correspond to an early low-resolution model Capanna et al. (SHAP1 2014); Jorda et al. (SHAP1 2016) that was used to project 67P lightcurves, see Figures 6.6 and 6.7. The parameters listed for all spin-state solutions are given λ and β are ecliptic longitude and latitude of the pole, P_1 is the period before the previous perihelion passage (valid for 2003-2007 data), and P_2 is the 2014 period. A 'final' period and pole position are not given here as the pole was shown to be precessing and the period changed throughout Rosetta monitoring of the comet (Preusker et al., 2015; Jorda et al., 2016).

pole positions shifted by 180° in ecliptic longitude are indistinguishable, with corresponding shapes 'mirrored' across the z axis. The first solution, A, gave slightly better fit of the lightcurves, see Figure 6.7, and was also close to the solution preferred earlier (Lowry et al., 2012). Rotation pole obtained by OSIRIS team was $\alpha = (69.3 \pm 0.1)°$ and $\delta = 64.1°$ in equatorial coordinates (Sierks et al., 2015). This corresponds to $\lambda = 78.1°$ and $\beta = 41.5°$ in ecliptic coordinates. Given the uncertainty of the measurement, the lightcurve-inversion pole is consistent with the spacecraft result.

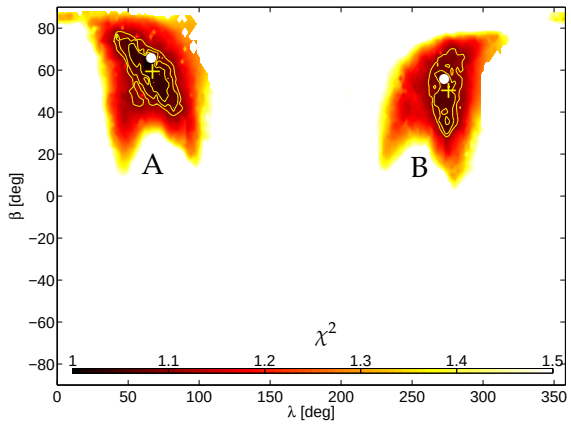

Figure 6.5: The coloured plot shows normalised χ^2 distribution for the lightcurve-inversion pole search for nucleus of 67P/Churyumov-Gerasimenko. The whole celestial sphere was scanned with a $1° \times 1°$ grid of possible poles. The ecliptic longitudes, λ, are along the horizontal axis, and the ecliptic latitudes, β, are along the vertical axis. The contour lines show the +5%, +7.5%, and +10% levels from the minimum χ^2. The darker colours mark smaller values of χ^2, and two regions, A and B with highest probability of containing the pole can be clearly seen.

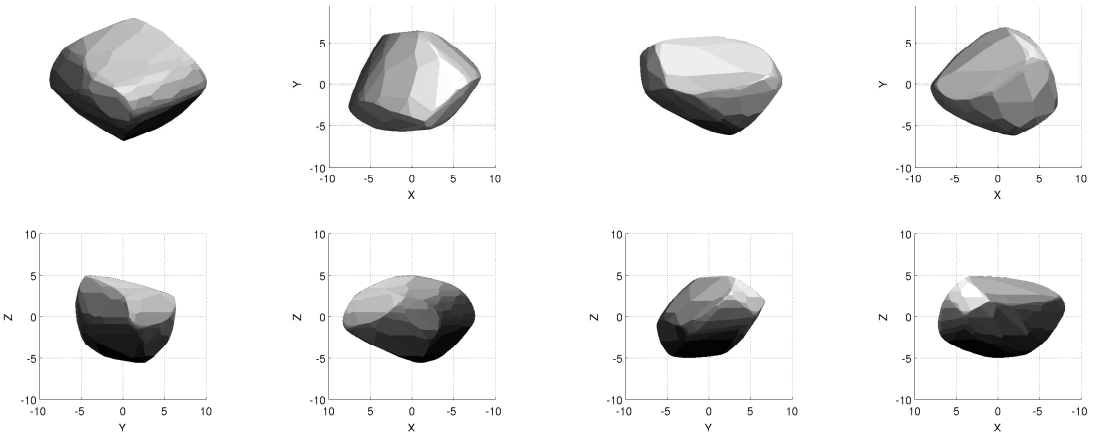

(a) Model A

(b) Model B

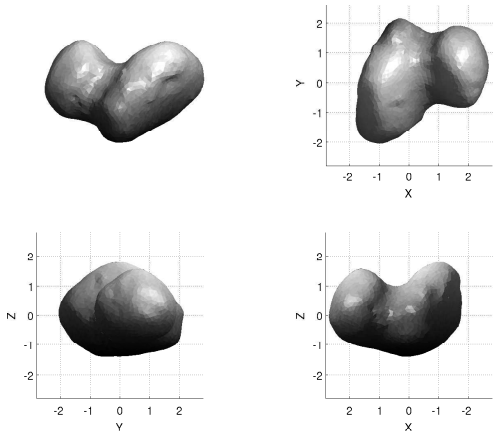

(c) Spacecraft model

Figure 6.6: The shape models in panels (a) and (b) correspond to the pole solutions A and B, as listed in Table 6.2. The model in panel (c) is an early low-resolution spacecraft model developed from OSIRIS imaging data Capanna et al. (SHAP1 2014); Jorda et al. (SHAP1 2016). Clockwise, from upper left corner each set of figures represents a general view of the shape, a view from positive z, positive y, and positive x directions. The models were rotated to have the x-axis match the axis of smallest moment of inertia. There is a clear mismatch between the convex-inversion and spacecraft shapes.

6.2.3 Discussion of spin-state change

The robust measurement of the period change along with the new spin-states were published by Mottola et al. (2014, incl. A. Rożek), and gained wide range of applications. The article was cited 50 times (as of 9th October 2017) by authors of publications in seminal journals like Nature, Science, MNRAS or A&A. The new spin-state was fundamental for spacecraft modelling of the cometary nucleus (for example Sierks et al., 2015; Preusker et al., 2015; Jorda et al., 2016), and instrumental in understanding comet's activity (for example Lara et al., 2015; Lin et al., 2016; Snodgrass et al., 2016). This was the fifth time a measurement of the spin-rate change was made at a periodic comet (Mottola et al., 2014; Kokotanekova et al., 2017). The rotation rate changes are most likely linked to cometary activity and non-gravitational torques due to out-gassing the comets are experiencing when approaching their perihelia (Keller et al., 2015b; Bertaux, 2015). The rotation period was closely monitored throughout the mission. The OSIRIS camera has seen it initially increase from the value reported here, reach a maximum in May 2015 before dropping to 12.305 h just before perihelion (Jorda et al., 2016). The precise monitoring also revealed the comet to be in an excited state rather than the initially assumed principal axis rotation (Preusker et al., 2015; Jorda et al., 2016).

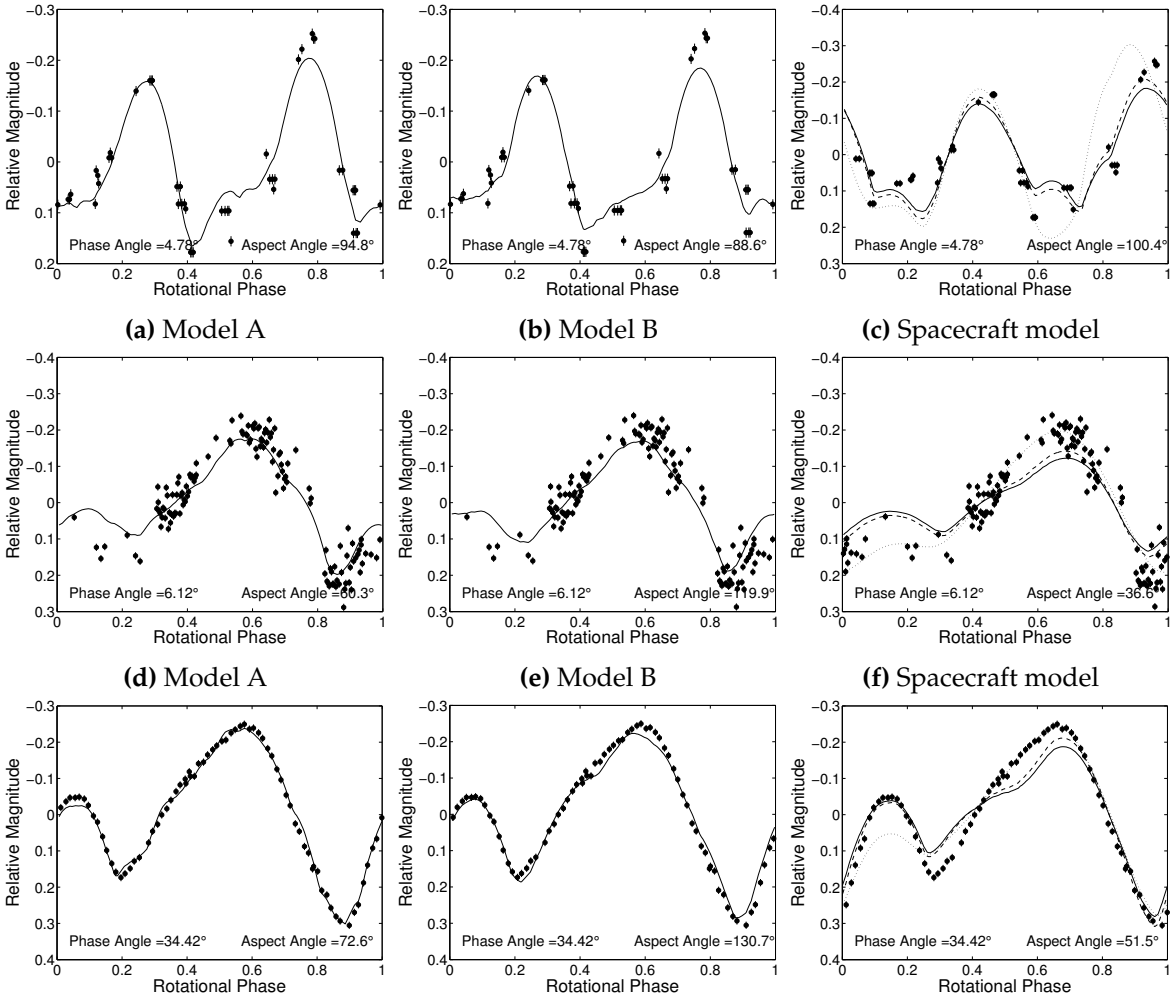

(a) Model A **(b)** Model B **(c)** Spacecraft model

(d) Model A **(e)** Model B **(f)** Spacecraft model

(g) Model A **(h)** Model B **(i)** Spacecraft model

Figure 6.7: The graphs show artificial lightcurve fits of three shape models to example lightcurve data. The lightcurve shown in panels (a-c) was collected on 11th March 2003 with the Hubble Space Telescope (Lamy et al., 2006). The lightcurve in panels (d-f) is a composite of lightcurves collected on 17th and 20th June 2007 with NTT and VLT (Tubiana et al., 2008; Lowry et al., 2012). The lightcurve in panels (g-i) was collected with the OSIRIS NAC. The model used to generate the lightcurves in panels (a), (d), and (g) was model A, and in panels (b), (e) and (h), model B see Figure 6.6. The spacecraft model was used to generate the artificial lightcurves in panels (c), (f), and (i). Details of spin-states for the models are listed in Table 6.2. From visual assessment there is little difference in the quality of the lightcurve fits between the two convex models A and B (see Figure 6.6 and table 6.2). However, model A gives slightly lower χ^2 of the fit. The pole position of this model agrees with the best convex lightcurve-inversion model (Lowry et al., 2012) and was later confirmed by spacecraft observations (Sierks et al., 2015). The spacecraft model used to generate the lightcurve is a 5120 facet model from 18th June 2014 Capanna et al. (SHAP1 2014); Jorda et al. (SHAP1 2016). The Lommel-Seelinger scattering law was used to reproduce lightcurves with convex models. The match of the artificial lightcurves to the data using spacecraft models was not as good, so different scattering functions are plotted with different line types continuous for Lommel-Seelinger, dotted – Lambertian, and dashed – linear combination (see Section 3.3.1).

At the time when the lightcurve analysis was performed, a preliminary non-convex shape model was available, developed from low-resolution images (SHAP1, version from 18th June 2014 Capanna et al., 2014; Jorda et al., 2016) using the 'Multi-resolution PhotoClinometry by Deformation' method (Capanna et al., 2013). The shape model is presented in Figure 6.6c and spin-state details listed in Table 6.2. This shape was used to generate lightcurves as illustrated in Figure 6.7. The shape of the comet nucleus from convex lightcurve inversion does not reflect the 'duck-like' bi-lobed shape of the comet. However, the convex model reproduces the lightcurves very well, both for the ground-based, as for the spacecraft observations (see Figure 6.7). Artificial lightcurves generated with the spacecraft model, on the other hand, failed to match the amplitude of the real lightcurves. Some further development is required to link the lightcurve features with the peculiar shape.

6.3 Early mapping of the nucleus surface source-regions of observed jet structures

Tracking and understanding cometary activity was one of the major science goals of the Rosetta mission. The primary signs of such activity are the presence of dust coma and tails. Previous spacecraft missions, as well as ground based observations, revealed surface material to be lifted in the form of jet-like structures (A'Hearn et al., 1986, for example). Identifying the sources of jets aids efforts to better understand their formation process and composition.

In order to investigate the source regions the positions of the jets need to be known. The focus of this chapter is the image sequence taken between 25th and 26th June 2014, by the OSIRIS WAC camera. The images were taken in the optical Vis610 filter over the span of the comet's full rotation. Selected images are displayed in Figure 6.8. The jet-like features are quite faint and difficult to locate visually. In order to enhance the jet location in the images, individual frames were filtered by co-authors using radial re-normalisation (A'Hearn et al., 1986) and Laplace filtering (Boehnhardt and Birkle, 1994) techniques. The images were then centred on the comet nucleus. Finally, the jet-like structures were identified and their angular positions measured counter-clock-wise relative to the y-axis of the image (the axis pointing up) (Lara et al., 2015).

6.3.1 Angular tolerance method of jet-source region assessment

The positions of jets identified on the OSIRIS images were used to locate the regions on the comet surface from which they originated. The method used to identify jet sources presented here is based on geometric tracing using angular tolerance limits. There are a few assumptions made. The first one is that all material would be lifted from the surface either perpendicular to the surface or at an angle close to 90°. Another is that the surface elements

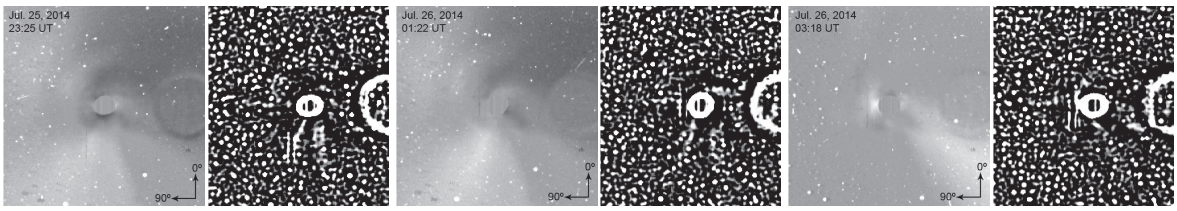

(a) 25th June 2014, 23:25 **(b)** 26th June 2014, 1:22 **(c)** 26th June 2014, 3:18

Figure 6.8: Selected panels of Figure 2 from Lara et al. (2015). Each pair of panels represents a different OSIRIS WAC image, as labelled in the captions, with a field-of-view of approximately 73 km × 73 km. In each pair, the left panel shows the radially renormalised image (A'Hearn et al., 1986), and the right panel, the Laplace-filtered image (Boehnhardt and Birkle, 1994). The arrows on the radially renormalised images indicate how the image coordinate system is defined. The jet position angles were measured counter-clock-wise from the direction 'up', the image y-axis. A correction, obtained from the SPICE kernels, was necessary to obtain the jet position angles relative to celestial north, as listed in Table 6.3.

UT Date *YYYY-MM-DD*	Time *hh.mm.ss.sss*	Jet 1 °	Jet 2 °	A °	B °	C °	D °
2014-07-25	20.50.54.291	38	38	19	29	32	77
2014-07-25	23.25.54.130	44	10	25	17	30	58
2014-07-26	00.04.39.142	44	7	29	19	30	9
2014-07-26	00.43.25.150	41	7	32	21	30	345
2014-07-26	01.22.10.125	41	7	36	24	31	341
2014-07-26	02.00.54.167	46	11	40	28	32	343
2014-07-26	02.39.40.112	52	6	43	32	32	348
2014-07-26	03.18.25.118	53	2	45	36	33	354
2014-07-26	03.57.10.132	61	2	46	40	34	2
2014-07-26	04.35.54.145	25	25	46	43	35	11
2014-07-26	05.14.39.151	25	25	44	46	35	21
2014-07-26	05.53.25.128	0	0	41	47	35	31

Table 6.3: The table collects locations of jets in the OSIRIS images series taken between 25th and 26th July 2014. First two columns correspond to the image exposure *UT Date* and *Time*. The *Jet 1* and *Jet 2* correspond to the jet position angles, measured anticlockwise relative to celestial north. The columns labelled *A*, *B*, *C*, and *D* list the position angles of synthetic jets generated from the possible source regions, as identified in Lara et al. (2015, Figure 7), see also Figure 6.11. The geometric jet tracing method with angle tolerances gives quite good agreement with the observations. This table can be compared to the observations log (Lara et al., 2015, Table 1). Note that the authors analysis focus was on the 25th-26th July series, but the final frame was not provided.

that produce jets would be illuminated, imposing a minimum elevation of the Sun above the facet horizon. Also related to the position of the Sun was that stronger illumination would mean greater contribution to jet activity. The last one is that jets visible at different times would come from a similar region of the surface, that is the surface activity is localised.

Before proceeding with the analysis images were rotated to align the 'up' direction, or y-axis, of the image with celestial north. The rotational offset can be retrieved from the SPICE kernels, and it had to be added to measured jet position angles. The final position angles for the jets identified in the discussed image series are gathered in Table 6.3. The position of the jets between frames were not linked, meaning the Jet 1 and Jet 2 designations in Table 6.3 do not always refer to the same two jets. Position of the Sun relative to the nucleus, $\hat{d}_{\odot}$, was retrieved using the Horizons ephemeris system, and translated into the body-centric coordinate frame using Equation (3.10). The information about the spin-state of the model was used to calculate the position of celestial north (the z-axis of the equatorial coordinate system) in body-centric coordinates using the same transformation. Finally, the position of spacecraft relative to the asteroid, $\hat{d}_{OSIRIS}$, was retrieved from the SPICE kernels to establish the OSIRIS line of sight. The $\hat{d}_{OSIRIS}$ is similar to the $\hat{d_{\oplus}}$ vector pointing at Earth, used in calculations of artificial lightcurves Section 3.3.1. The body-centric coordinate system and positions of surface elements used here come from one of the early low-resolution shape models of the comet nucleus, with approximately 5000 facets (Capanna et al., 2014;

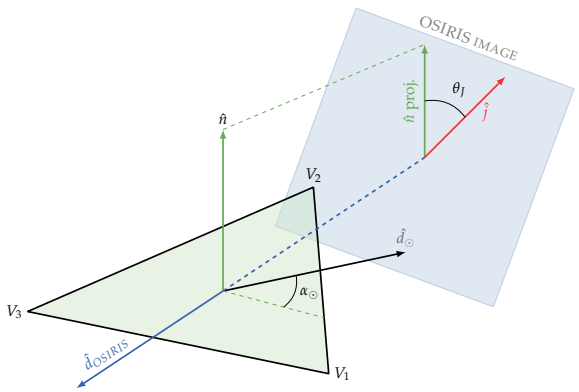

Figure 6.9: A schematic of the geometric calculations required to estimate whether a surface element can be considered as possible jet-source region. The surface element is represented here with a triangular facet, green, with vertices V_1, V_2, V_3 and facet normal unit vector $\hat{n}$. The unit vector $\hat{d}_{OSIRIS}$ points towards the OSIRIS camera. The blue square represents the plane of sky, or OSIRIS image. The facet normal projection on the image is labelled '$\hat{n}$ proj.'. The position of the jet as projected onto the image captured by OSIRIS camera is marked with vector $\hat{j}$. The angle between the facet normal projection and jet position is labelled θ_J. The unit vector $\hat{d}_\odot$ is directed at the position of the Sun with and $\alpha_\odot$ being the elevation of the Sun above facet horizon.

Jorda et al., 2016, see also Table 6.2 and Figure 6.6).

For each image in the series a set of facets was identified as possible jet sources using a simple geometric procedure, as illustrated in Figure 6.9. First, for each facet the illumination conditions were calculated. The angle $\alpha_\odot$, is the elevation of the Sun above facet horizon, calculated between the facet plane and $\hat{d}_\odot$. This angle was automatically set to 0°, if the facet was found to be in shadow. Next, the normals of illuminated facets, $\hat{n}$, were projected onto the plane-of-sky as seen from Rosetta, or plane of the specific OSIRIS image. The plane-of-sky is a plane perpendicular to the camera's line of sight, $\hat{d}_{OSIRIS}$. The vector marking the position of the jet as projected on to the image, $\hat{j}$, is constructed by drawing a vector tilted to the celestial north at the jet-position angle. The angle between the projected facet normal and the position of the jet, θ_J, was measured. In other words, the θ_J is the angle between plane containing line of sight ($\hat{d}_{OSIRIS}$) and facet normal ($\hat{n}$), and the plane containing the line of sight and the jet. The images delivered by OSIRIS camera are two-dimensional, so any single image gives only an indication of a plane in which the jet can lie.

For each image of the series the facets within certain tolerance limits for both $\alpha_\odot$ (facets with values above the minimum) and θ_J (facet with values below the maximum) were selected. The number of times a facet was identified as a possible jet - source were recorded and presented in the form of a heat-map, marking how many times a given facet was identified as the jet source region. Different tolerances were tested for both angles, as shown in the Figure 6.10. Putting too conservative a limit on the θ_J resulted in poorly defined jet-source regions, quite a liberal limit of 15° was selected. For any given value of θ_J the angular tolerance in α seemed to influence mostly the shape of the region, with larger values creating a multitude of disjoint regions. As the intention was to create continuous 'patches' on the surface we selected a small value for this angle. The results of analysis presented by in

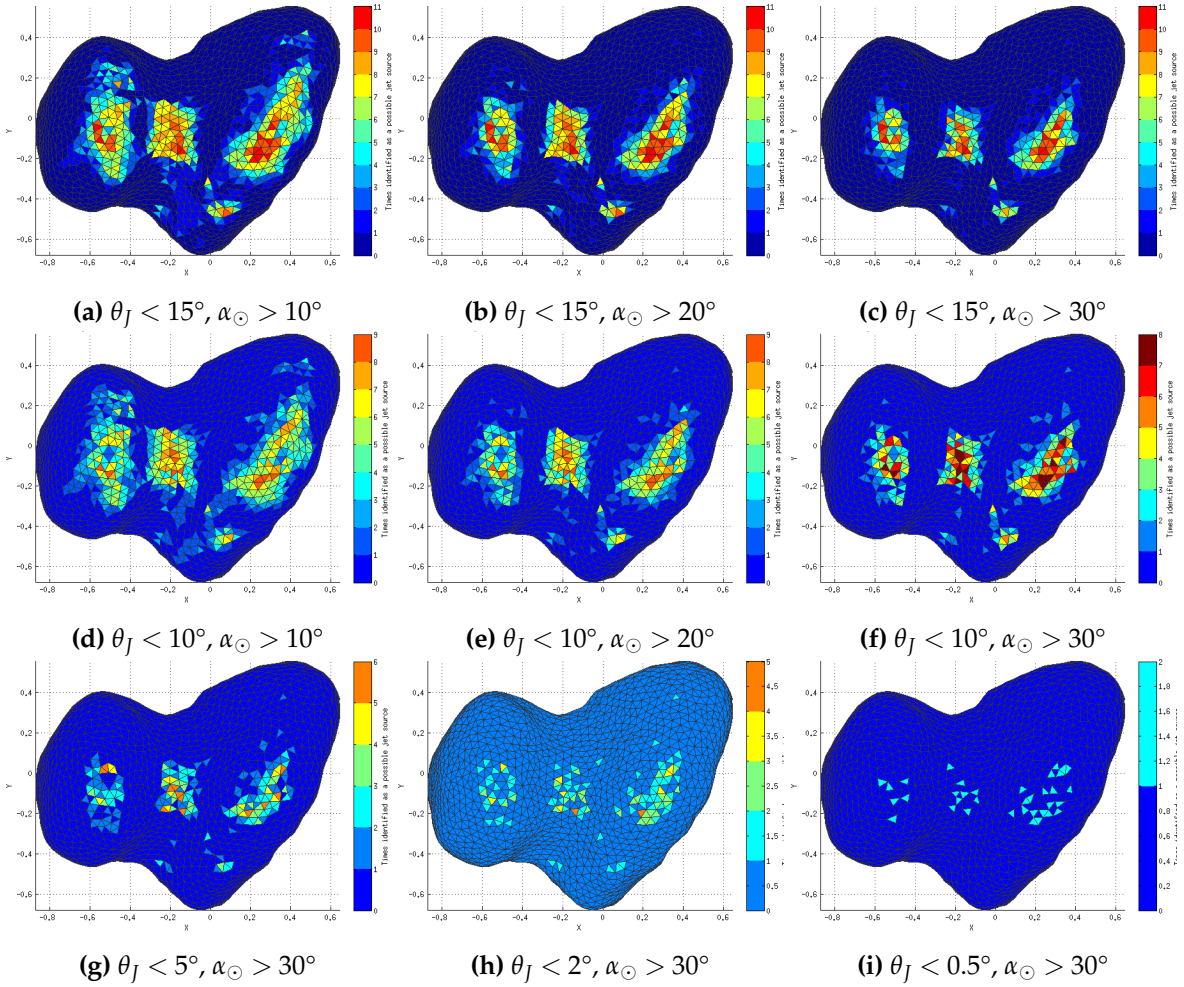

(a) $\theta_J < 15°$, $\alpha_\odot > 10°$ **(b)** $\theta_J < 15°$, $\alpha_\odot > 20°$ **(c)** $\theta_J < 15°$, $\alpha_\odot > 30°$

(d) $\theta_J < 10°$, $\alpha_\odot > 10°$ **(e)** $\theta_J < 10°$, $\alpha_\odot > 20°$ **(f)** $\theta_J < 10°$, $\alpha_\odot > 30°$

(g) $\theta_J < 5°$, $\alpha_\odot > 30°$ **(h)** $\theta_J < 2°$, $\alpha_\odot > 30°$ **(i)** $\theta_J < 0.5°$, $\alpha_\odot > 30°$

Figure 6.10: The results of the jet source identification are presented here as 'heatmaps' overlaid on the surface of comet. The 3D shape model of the comet nucleus is seen projected from the north pole (positive end of the z-axis of the body). On each individual panel the different colours correspond to how many times the facets were identified as possible jet sources (with legend always to the right). Options with different minimum solar elevation ($\alpha_\odot$ - angle between facet horizon and the position of Sun), and maximum tolerance of projected jet zenith angle (θ_J - the angle between the jet and the facet normal as projected onto the OSIRIS's plane-of-sky). The combination presented in panel (a), of $\alpha_\odot > 10°$ and $\theta_J < 15°$ was used for the final source-region determination.

Lara et al. (2015) assumed 15° for θ_J and 10° for $\alpha_\odot$. Figures 5 and 6 in Lara et al. (2015) are different projections of panel (a) of Figure 6.10.

6.3.2 Comparison of the jets projected from the identified source regions with OSIRIS images

Based on the distribution of times single facets were identified as possible jet-sources, four regions were identified, see map of the nucleus in panel (b) of Figure 6.11. The regions, that were determined with the geometric method to be possibly active, correspond to actually active and strongly insolated regions on the comet nucleus. Region A, marked with red,

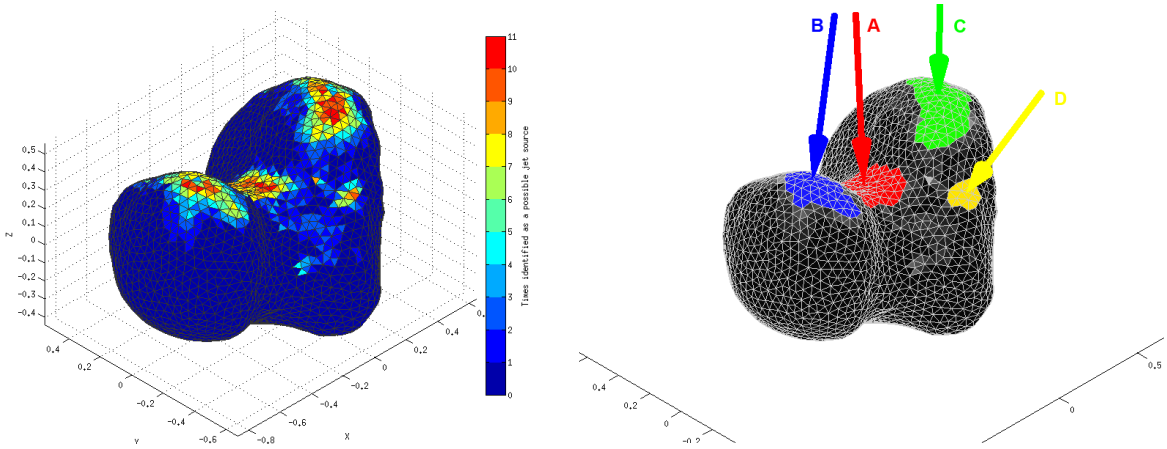

(a) Heat-map with $\theta_J < 15°$, $\alpha_\odot > 10°$ **(b)** Identified jet-source regions

Figure 6.11: The results of the jet source identification using the geometric method with angular tolerances. The panel on the left (a) is another projection of panel (a) in Figure 6.10 representing the number of times a facet was identified as a possible jet-source in a 12-frame series. The image on the right (b) shows the result of post-processing of the heat-map Continuous regions with concentrations of facets with high identification scores are selected and labelled A (red), B (blue), C (green), and D (yellow). The panel (b) is also reproduced in Lara et al. (2015, Fig. 7).

corresponds mostly to the comet's 'neck' region Hapi with a slight overlap with Hathor and Anuket regions. This area of the comet has been observed to be the major source of jet activity (Sierks et al., 2015). Region B is located on the small lobe, it's coloured blue in the figures and corresponding to the Ma'at and Serqet regions. Further two regions are found on the larger lobe, the green-coloured region C (Ash and Aten), and yellow coloured region D in the Aten area of the nucleus. The image in panel (b) of Figure 6.11 combines the view of the selected regions with a projection of an average of facet normals (indicated with colour-coded arrows), that can be viewed as an average jet direction from this region. It can be observed, that regions A, B, and C share similar directions of the possible jet activity, while region D facet normals are oriented in a considerably different way.

Selected results of a visual test of the geometric jet-source identification method for the OSIRIS images are collected in panels of Figure 6.12. The figures shown correspond to the same times as image examples in Figure 6.8. The panels show projections of jets that could be produced in the marked regions as well as illustration of the measured jet positions in the OSIRIS images. For each example, four synthetic jets were generated. Each jet corresponds to one of the regions A, B, C, or D. The directions of jets are calculated as a sum of facet normals weighted by the cosine of solar zenith angle (insolation) for each source-region facet. The images are oriented to reflect OSIRIS viewing geometry and rotated, so that the north would be up. The jets are compared with the measured position angles of the jets in OSIRIS images. In most cases there has been two position angles measured. The synthetic jets produced by regions A, B and C usually correspond to one of them, while region D seems to be the source of the other. Three images from the series of 12 are shown here. The detailed information about the measured location of the jets and projection of synthetic jets

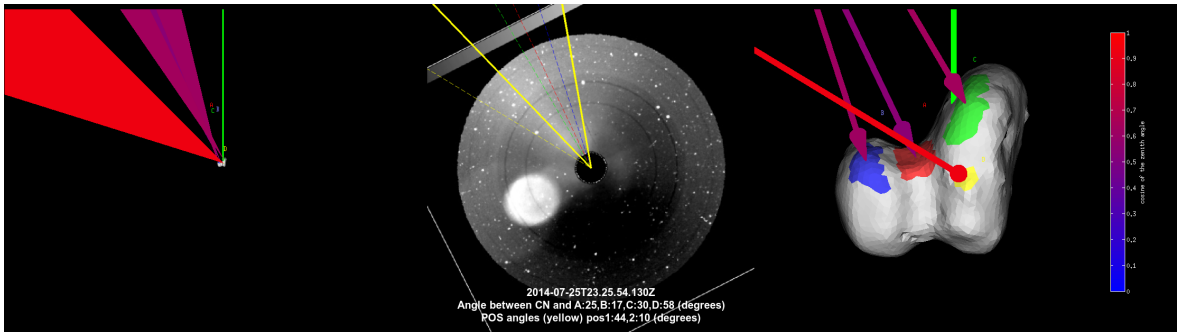

(a) 25th June 2014, 23:25

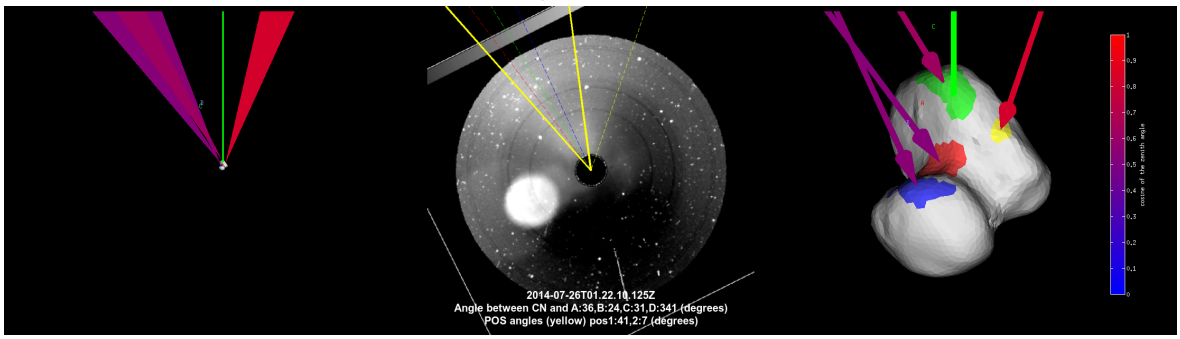

(b) 26th June 2014, 1:22

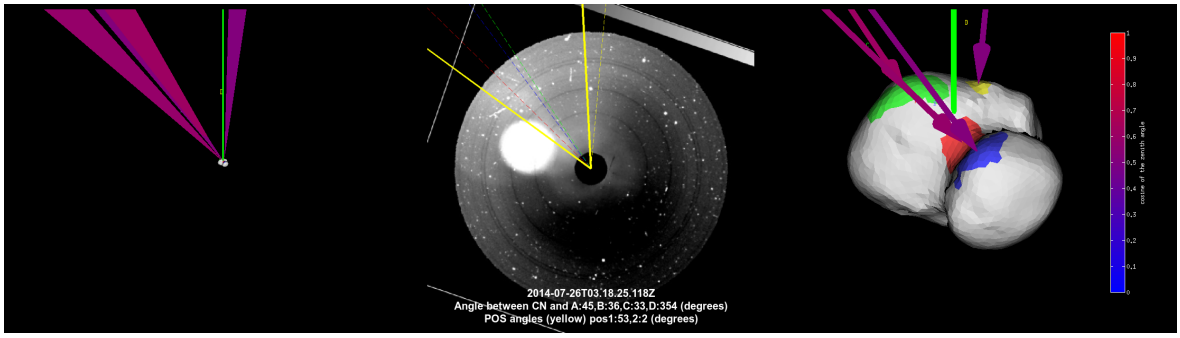

(c) 26th June 2014, 3:18

Figure 6.12: Selected jet projections, similar to panels of Figure 8 from Lara et al. (2015). Each panel (a,b,c) is made up of 3 parts. The rightmost panel shows the nucleus shape model overlaid with the active regions (the colours of the patches are consistent with panel (b) of Figure 6.11). The shape model is oriented to reflect the OSIRIS viewing geometry when the image was taken. The green line is aligned with celestial north. The directions of the coloured arrows pointed at the source regions are calculated as sum of the facet normals in a given region weighted by the cosine of solar zenith angle. The colours of the arrows correspond to the average cosine of the solar zenith angle across the source region, with red corresponding to 1 (most insulated regions) and blue to 0 (no illumination). The leftmost panel is the same projection, only at different scale, to reflect the structure of the synthetic jets. The middle panel is the processed OSIRIS frame with the measured jet position overlaid (solid yellow lines) and the projected positions of the jets protruding from the identified source regions (colour-coded dashed lines). The label contain information on the time stamp, as well as the angular positions of measured and synthetic jets (in degrees, measures counter-clockwise from celestial north). The images are oriented to be consistent with the shape-model projections, so the north is up.

onto the OSIRIS plane-of-sky is gathered in Table 6.3.

6.4 Conclusions on cometary applications of the lightcurve analysis tools

The author's involvement in the analysis of Rosetta's OSIRIS instrument data enabled further development and expansion of the software tools used primarily to analyse spin-state evolution of NEAs. The application of the lightcurve-analysis tools to the data gathered for the comet 67P/Churyumov-Gerasimenko resulted in co-authorship of 6 refereed papers. The tools were adopted to serve a range of purposes:

- to compute a map of rotationally-averaged insolation for a specific position of the comet in its orbit. This was achieved by calculating illumination, $\mu_\odot$ (defined by Equation (3.12)), of comet's surface elements for a series of evenly-spaced rotation phases. The assessment of mean daily insolation proved to be useful for determination of dust production rates (Guilbert-Lepoutre et al., 2014, incl. A. Rożek, cited 10 times).

- to confirm the spin-rate change and develop spin-state and shape of the nucleus, as discussed in Section 6.2 (Mottola et al., 2014, incl. A. Rożek, cited 50 times). The spin-pole location of the comet 67P/Churyumov-Gerasimenko nucleus by Mottola et al. (2014) has been in agreement with earlier ground-based observations as well as with the later spacecraft estimates (Sierks et al., 2015; Preusker et al., 2015; Jorda et al., 2016). Detection of the period change and determination of the new rotation period from approach photometry was crucial at the early stage of mission (Ashman et al., 2016). It could be confirmed by means of phase offset measurement, that is usually applicable in search of the YORP-induced period change (Lowry et al., 2014).

- to identify surface source regions of cometary jets at 67P, using a geometric tracing method with angular tolerance limits, as discussed in Section 6.3 (Lara et al., 2015, incl. A. Rożek, cited 24 times), and also applied in (Lin et al., 2015, 2016, cited 23 and 14 times respectively). The identification of jet-source regions gave results consistent both with other independent methods, as well as with the observed evidence (Lara et al., 2015).

- to calibrate the target brightness from sparse photometry of the comet. Investigation of comet activity from pre-landing ground-based observing campaign included absolute photometry of the nucleus. The mean brightness of, usually short, lightcurve segments was corrected for the rotation phase by computing artificial lightcurves using spacecraft model and spin-state (Snodgrass et al., 2016, incl. A. Rożek, cited 15 times).

Chapter 7

Final remarks and future work

7.1 Final remarks on spin-state and shape modelling results

The goal of this work was the investigation of how the YORP effect influences the physical evolution of small Solar System bodies. The research was part of the ESO LP, a programme dedicated to improving the YORP-related theory. By measuring YORP torques on the programme targets, it provides ground truth for YORP modelling efforts. The shape and rotational characteristic of asteroids (1917) Cuyo (Chapter 4) and (85990) 1999 JV_6 (Chapter 5) are used for thermophysical modelling and will help advance the theoretical work on the dynamic evolution of rubble-pile asteroids.

The asteroids were also targets of VLT/VISIR thermal-infra-red observations. The objects were observed at a range of near-infra-red wavelengths for the purpose of a detailed thermophysical analysis that was performed by the ESO LP collaborator, Ben Rozitis, using the Advanced Thermophysical Model (Rozitis and Green, 2011, 2012, 2013, ATPM). Thermophysical modelling with the ATPM provides valuable constraints on physical properties, which, along with the shape model, are required to make a theoretical prediction of the strength of the YORP and Yarkovsky effects. Among those parameters are size, thermal inertia, and surface roughness. The size of the asteroid derived from thermal measurements is a diameter of a sphere with the same volume and the strength of both YORP and Yarkovsky is inversely proportional to the object's size. The thermal inertia mainly affects the Yarkovsky effect, a non-gravitational force affecting the orbital motion of asteroids, and gives information about the material covering asteroid surfaces. The surface roughness influences the beaming of thermal radiation and can be set against the radar-derived measure of roughness at centimetre scales.

The robust spin-states and shapes of both asteroids, developed in this work, were used in thermophysical analysis to develop physical properties of both targets. The graph in Figure 7.1 illustrates the two NEAs discussed here, in the context of size and spin distribution of asteroids. The objects probe the region of the parameter space where YORP detections have been reported before, marked in the graph with purple squares. Therefore, in principle, they were expected to reveal signatures of YORP-induced spin-rate change. However, the reported non-detections are in line with the more detailed predictions of YORP strength using thermophysical analysis (B. Rozitis, private communication), given the shape characteristics, and as both targets seem to be highly YORP-evolved systems with obliquities close to the critical value where the YORP effect on rotation rate shuts down.

Both asteroids discussed are retrograde rotators with very low latitudes of rotation pole, and high obliquities, 173.5° for (85990) 1999 JV_6 and 133.7° for (1917) Cuyo. The two newly determined pole positions are in line with the distribution of known spin-states in Figure 7.2. Two distributions are plotted here, one is of pole ecliptic latitude, expressed by $\sin\beta$, illustrating the sense of rotation relative to the ecliptic, shown in Figure 7.2a. The other is of the spin-axis obliquity, expressed by $\sin(90° - \varepsilon)$, illustrating the sense of rotation of the asteroid relative to its own orbit, plotted in Figure 7.2b. Expressing the angles this way makes it easier to interpret the horizontal axes in Figure 7.2a. In both histograms the negative val-

ues means retrograde rotation, with $\beta < 0°$ or $\varepsilon > 90°$. The positive values correspond to prograde rotation, meaning that $\beta > 0°$ or $\varepsilon < 90°$. Both histograms for main-belt asteroids (blue bars) show a roughly symmetric bimodal distribution, with a ratio of retrograde to prograde rotators of 80:56, when considering $\sin(\beta)$, and 79:57, when looking at $\sin(90° - \varepsilon)$. For the NEAs' distribution there is a stronger excess of retrograde rotators, with the ratio 27:11 in $\sin(\beta)$, and 28:10 in $\sin(90° - \varepsilon)$. The abundance of retrograde rotators in the near-Earth environment is consistent with the model of migration of NEAs from asteroid belt (Vokrouhlický et al., 2015a). The prograde rotators can be caught in so-called spin-orbit resonances, which slow down the orbital evolution (Vokrouhlický et al., 2006b). For retrograde rotation, the diurnal and seasonal components of Yarkovsky effect add up, leading to a more effective shrinking of asteroid orbits. The locations of main 'escape paths' for asteroids to leave the main belt and join near-Earth population require a decrease in small bodies' semi-major axes (Granvik et al., 2017), hence producing the abundance of retrograde rotators.

The shapes of both asteroids suggest they are evolved systems. Asteroid (1917) Cuyo has a diamond-like shape, characteristic for a quickly rotating rubble pile (Sánchez and Scheeres, 2016). The rotation rate close to the spin fission limit, high obliquity, high orbit inclination

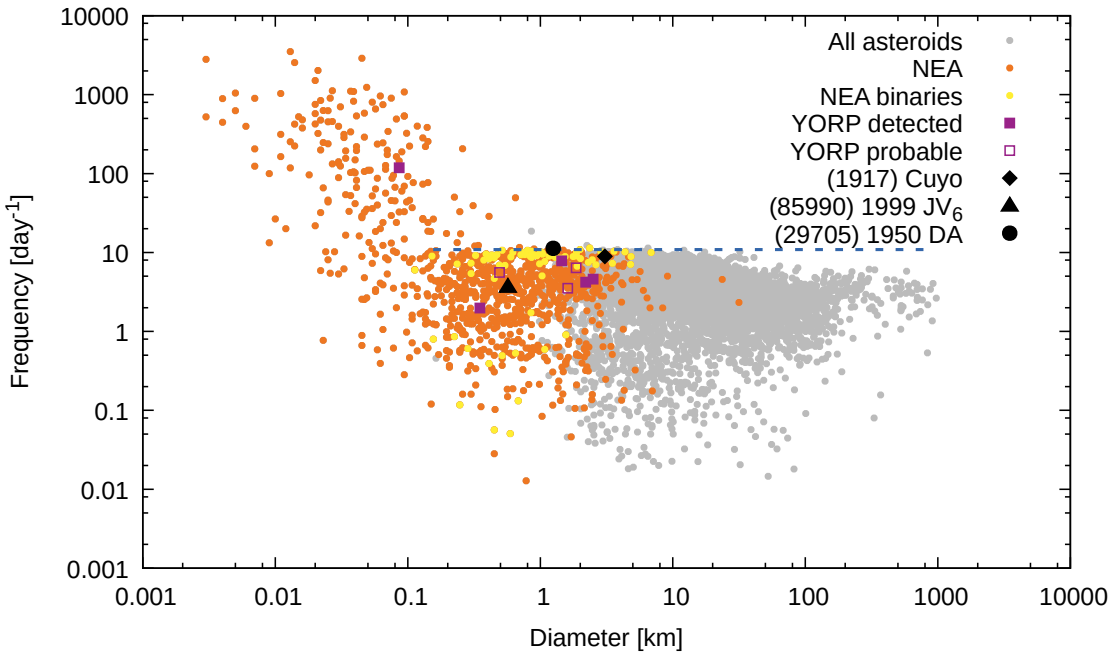

Figure 7.1: The Figure 1.2 in Chapter 1 updated to include results of the spin-state analysis and size measurements for the two NEAs discussed in this work. Putting them in context with the study of thermal recoil effects. The asteroids are marked with grey circles with the NEAs highlighted in orange, and binary asteroid population in yellow. The literature reports of YORP effect spin-up are marked with purple squares, with filled symbols marking confirmed measurements, and open symbols used for tentative detections or upper limits, see Table 1.2. Targets of interest are marked with black symbols, asteroid (1917) Cuyo, with a diamond, asteroid (85990) 1999 JV$_6$ with a triangle, and asteroid (29705) 1950 DA with a filled circle.

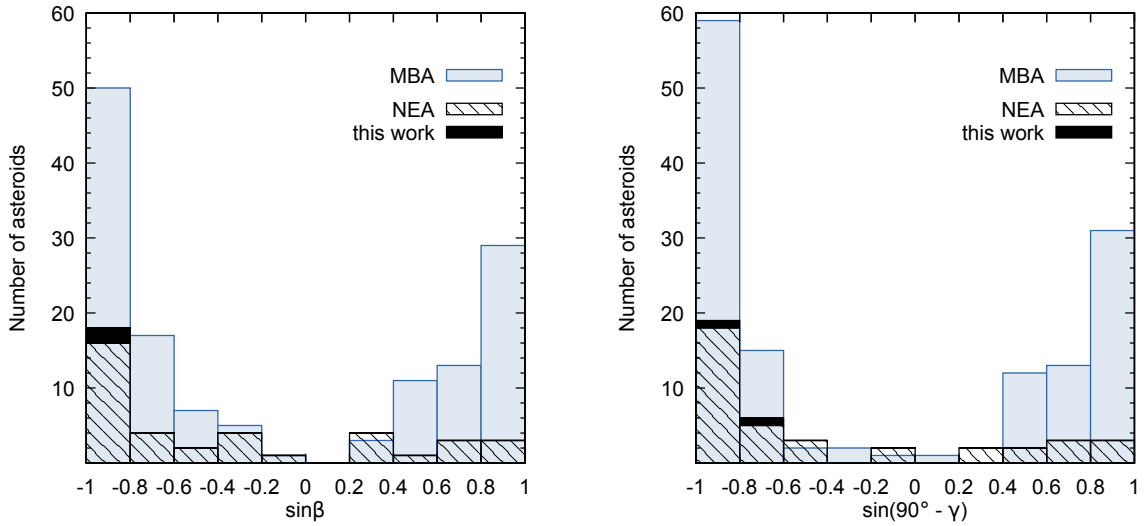

(a) β – pole ecliptic latitude **(b)** ε – spin-axis obliquity

Figure 7.2: Distribution of spin-axis orientations of 136 small main-belt asteroids (MBA - blue bars), 38 near-Earth asteroids (NEA - black patterned bard), and 2 targets investigated here (solid black). Panel (a) shows the distribution of the sine of ecliptic latitude ($\sin(\beta)$). Panel (b) illustrates the distribution of sine of spin-axis obliquities (or, more precisely $\sin(90° - \varepsilon)$). The spin-state information used in this plot was downloaded from LCDB (summary published 13th August 2017, Warner et al. (2009)). Only small main-belt asteroids are plotted here, and the 30 km cut-off was determined using sizes taken from the LCDB. The spin-states are only given for the bodies for which the most recent rotation pole is unambiguous (no more than one pole listed). The osculating orbital elements used to calculate the obliquities were taken from the NASA Solar System Dynamics site[b] (accessed 25th September 2017). *This figure is similar to Figure 9 in Vokrouhlický et al. (2015a). However, the plot in that figure included de-biased MBA spin-states fom Hanuš et al. (2013).*

[b] `https://ssd.jpl.nasa.gov/?sb_elem`

(≈24°), combined with eccentricity and semi-major axis close to the ν_6 secular resonance with Saturn (see Figure 1.1) might suggest that it recently migrated from the asteroid belt. The lack of measurable spin-up by the YORP effect in case of this object might be a result of the YORP self-limiting properties (Cotto-Figueroa et al., 2015). The reorientation of surface material on the surface can reduce the body asymmetry leading to the decrease of the YORP magnitude. The high spin rate makes this object a target of interest for the study of cohesive forces preventing asteroids from breaking up (B. Rozitis, private communication). The target is slightly larger and faster than the asteroid (29705) 1950 DA for which the effect was studied before (Rozitis et al., 2014, see also spin-rates and sizes of both objects in Figure 7.1).

The shape of asteroid (85990) 1999 JV_6 resembles that of other contact binary asteroids, like asteroid (25143) Itokawa, as shown in Figure 7.3. Itokawa has a rotation period almost twice as long as (85990) 1999 JV_6 (see list of current YORP detections in Table 1.2). The detection of YORP-induced spin-up was initially considered to be in strong disagreement with the slow-down expected from modelling the effect using the spacecraft model. However,

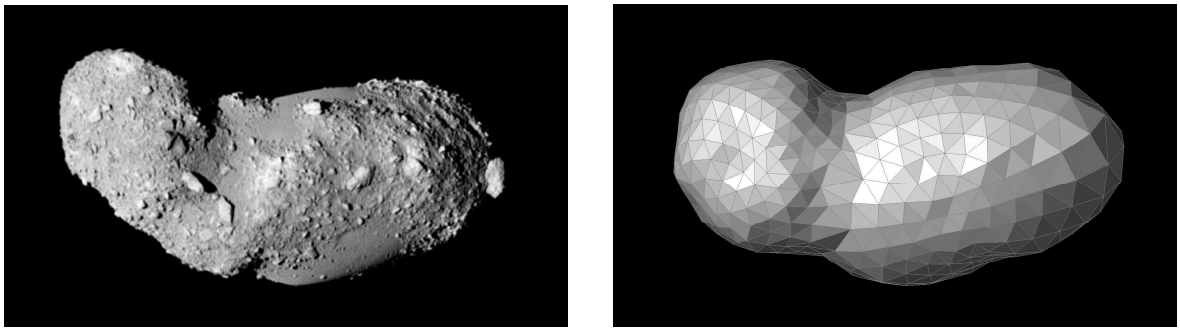

(a) Spacecraft image of (25143) Itokawa **(b)** Radar model of (85990) 1999 JV_6

Figure 7.3: The two panels compare the two NEAs, a 350 m-diameter (25143) Itokawa (a) and 570 m (85990) 1999 JV_6 (b). The asteroids have similar bi-lobed shapes, however there is a difference in projection in the presented images. Asteroid (25143) Itokawa was imaged from the body-centric negative end of y axis by Hayabusa spacecraft (Demura et al., 2006). The asteroid (85990) 1999 JV_6 is projected as seen from positive z-axis, the final radar shape model was used to create the synthetic image (see Chapter 5).

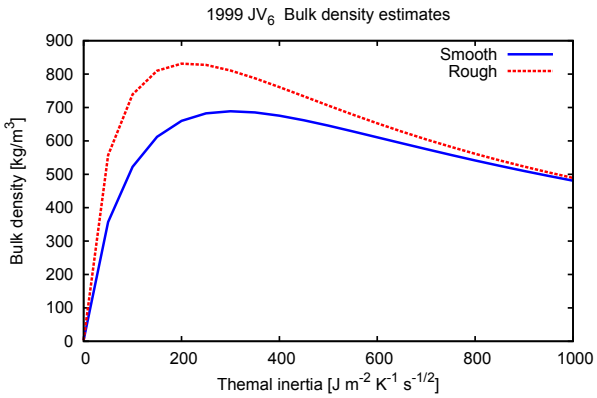

Figure 7.4: The results of thermophysical analysis performed for (85990) 1999 JV_6 by B. Rozitis using infra-red observations and modelled with the ATPM (Rozitis and Green, 2011, 2012, 2013). The plot shows bulk density estimates as a function of possible thermal inertia values. The red and blue lines mark extreme values of surface roughness. The figure was provided by B. Rozitis for presentation at the Binaries in the Solar System 4 conference in Prague, June 2016, and shows preliminary results.

the theoretical calculations of YORP were reconciled with observations by accounting for uneven density distribution (Lowry et al., 2014). In the case of (85990) 1999 JV_6 there is no detectable rotation rate change. However, the radar shape model shows even more bifurcation than asteroid (25143) Itokawa. Thus the object might still be a contact binary and a target for dynamical study of possible contact-binary formation mechanism through re-collision of a rotational-fission formed asteroid binary (Jacobson and Scheeres, 2011).

Asteroid (85990) 1999 JV_6 is a noteworthy target for future studies also due to the detection of a non-gravitational acceleration, also referred to as 'NGA' detection. If the semi-major axis drift detected could be attributed to the Yarkovsky effect, then the model requires that the object has quite low density. The early results of ATPM thermophysical analysis performed by the ESO LP collaborator, B. Rozitis, are shown in Figure 7.4. The bulk density estimates are plotted against the possible thermal inertia values, assuming Yarkovsky drift.

Different values of surface roughness are plotted, with red colour marking completely rough surface, and blue denoted a completely smooth surface. The ATPM allows for simulation of the small-scale surface roughness by adding crater-like features to triangular facets of the model. The method allows for controlling the 'roughness-fraction' expressed by the ratio of triangular facets with the roughness detail, to those without. Even considering the results of radar measurements suggesting a rough surface, the expected density range is below $0.9\,\mathrm{g\,cm^{-3}}$. This value is low even for an Xk class object, in fact closer to the comet range (Carry, 2012). Considering the abundance of X-complex targets amongst the objects arriving in the near-Earth population from the JFC family (Binzel et al., 2015), it might be possible that the object is in fact an extinct comet. An in-depth dynamical study of the orbital evolution of (85990) 1999 JV_6 would be required to confirm its origin.

The shape and spin-state modelling software package, available at Kent, was expanded to include self-shadowing effects, and perform effective phase-offset measurements. The tools were later adopted to be applied to the analysis of Rosetta data and ground-based observations of comet 67P/Churyumov-Gerasimenko. The modelling of early OSIRIS imaging described in Chapter 6 was seminal to the comet study, an important result being the determination of rotation pole and measurement of the period increase relative to the value known from the previous perihelion passage (Mottola et al., 2014).

The pre-encounter spin-state modelling of comet 67P/Churyumov-Gerasimenko was widely used in the study of the comet nucleus. The work has numerous applications, that include the result being used in

- mission and instrument operations planning (Krüger et al., 2015; Ashman et al., 2016),
- study of the comet's changing rotation rate and precession, and linking its dynamical evolution to active processes on the surface (Keller et al., 2015b; Bertaux, 2015; Jorda et al., 2016; Gutiérrez et al., 2016; Lhotka et al., 2016),
- developing the 3D shape model, and investigation morphology and surface properties from OSIRIS imaging, other on-board instruments' data, and associated ground-based campaigns (Ciarniello et al., 2015; Preusker et al., 2015; Keller et al., 2015a; Pajola et al., 2015; Mousis et al., 2015; Sierks et al., 2015; Jutzi and Asphaug, 2015; Pajola et al., 2016b; Brugger et al., 2016; Pajola et al., 2016a; Giacomini et al., 2016; Fornasier et al., 2016; Keller et al., 2017),
- modelling the formation and internal structure of the comet (Luspay-Kuti et al., 2015; Mousis et al., 2015; Sierks et al., 2015; Jutzi and Asphaug, 2015; Davidsson et al., 2016; Hirabayashi et al., 2016; Pajola et al., 2017),
- interpretation of observations, both spacecraft and ground-based, and modelling of the cometary jets, coma, and surface activity (Tubiana et al., 2015; Bieler et al., 2015; Lara et al., 2015; Nilsson et al., 2015; Bertaux, 2015; Mousis et al., 2015; De Sanctis et al., 2015; Hässig et al., 2015; Sierks et al., 2015; Moreno et al., 2016; Snodgrass et al.,

2016; Marshall et al., 2017; Liao et al., 2016; Gicquel et al., 2016; Fougere et al., 2016; Fornasier et al., 2016; Hässig et al., 2017; Opitom et al., 2017; Keller et al., 2017; Schmitt et al., 2017; Pajola et al., 2017),

- giving a context to study spin and orbital dynamics of other comets, including extrasolar comets (Santos-Sanz et al., 2015; Veras et al., 2015; Davidsson et al., 2016; Marboeuf et al., 2016; Kokotanekova et al., 2017; Barbieri and Bertini, 2017).

7.2 Future work to refine spin-state solutions and advance YORP modelling efforts

At the time of writing this thesis, the 67P/Churyumov-Gerasimenko data analysis has already gained impact. The list of published work encompasses ground-based study of cometary activity (Guilbert-Lepoutre et al., 2014; Snodgrass et al., 2016, incl. A. Rożek), study of the rotation period change (Mottola et al., 2014, incl. A. Rożek), and analysis of jet-activity from OSIRIS images (Lara et al., 2015; Lin et al., 2015; Snodgrass et al., 2016; Lin et al., 2015, incl. A. Rożek). The results for individual asteroid targets are in preparation for publication and were presented at conference meetings (a comprehensive list is presented in Publications). However, there is scope for further study and some of the ideas for future work involve the exploitation of the ESO LP, the details of spin-state analysis of small bodies of the Solar System, as well as development of the YORP effect theories.

The data-base of the ESO LP programme is rich in likely YORP-detection candidate targets observed over long periods of time. Recently, the VISIR instrument was recommissioned at the VLT, and the programme was awarded more time to observe NEAs. There are a few independent sources of information about the objects available, which means those are good material for further shape and physical modelling. Detection of a yet-unseen YORP-induced slow-down of an asteroid's rotation, that might result from the extensive ESO LP, would be a major breakthrough in study of the non-gravitational effect.

Moreover, there are a few ESO LP targets among the radar-detected targets (P. Taylor and L. A. M. Benner, private communication). Combining ESO LP optical and thermal photometry with the radar data could result in a few new robust physical models of NEAs in the near future. Amongst those is the asteroid (2102) Tantalus that has been extensively observed with optical facilities, and was a recent target of ESO LP near infra-red observations as well as Arecibo and Goldstone radar campaigns. There is also scope to include other radar-detected asteroids in planning the future ESO LP and associated programme's targets.

Majority of the spin-state modelling performed here was done assuming Lambertian or Lommel-Seelinger scattering, and the linear combination of the two (see Equations (3.15) to (3.17)). This approach has been accepted in the planetary community as a valid approximation for investigation of lightcurve shape models of most targets. The shape modelling methods that were used here were tried and tested on hundreds of targets gathered in the

DAMIT database (Ďurech et al., 2010). The spin-state analysis was tested with the known YORP detections before applying them to new objects. However, the Lambertian-Lommel-Seelinger scattering law has a caveat of ignoring small-scale shadowing effects that can be very important for rough surfaces (Wilkman and Muinonen, 2014). This issue is an avenue worth exploring, as it might explain some issues with phase offset computation that the author encountered during her investigation of asteroid (8567) 1996 HW_1 (Rożek et al., 2014). The analysis of this object was not included in this thesis, as the details of those spurious phase offset measurements require further work.

With regards to the development of spin-state modelling tools, a point to make is that most of the computation performed in this thesis utilised single processor algebra. Even when the multiple models were processed during pole-scans at the same time, each `CONVEXINV` of `SHAPE` run was still a single-CPU job. Some parallelisation of the lightcurve phase offsets measurement was achieved using `parfor` loops from `Matlab`'s Parallel Computing Toolbox. However, there is scope for improvement, especially in the field of speeding up computation of rotational lightcurves of highly convex bodies. Currently the shadowing procedure requires a pre-computed lookup table listing all possible shadow-casters for each facet, which is memory-heavy. The whole procedure of computing the lightcurve could probably be made quicker using graphics processing unit (GPU). This type of processing units can be found usually in graphics cards. They are designed to perform simple operations that need to be executed multiple times efficiently. Their main application is still graphics processing, but also in the quickly growing field of machine learning and training of neural networks. Use of processors specifically designed for graphics computations could make lightcurve studies more efficient, and also enable the use of complicated scattering functions.

An interesting fact emerged during the spin-state modelling of comet 67P/Churyumov-Gerasimenko was that the convex lightcurve-inversion model reproduced the lightcurves much better than the subsequent spacecraft models. On one hand this is to be expected, as the lightcurve inversion model is calibrated for the visible and illuminated cross-section of the object at any given time. On the other hand, it is surprising as the spacecraft models contain much more information about the surface details of the target. One solution to the problem could be to include albedo maps of the surface in the lightcurve modelling (Mottola et al., 2014). Such albedo maps were for example produced from VIRTIS photometric data (Ciarniello et al., 2015).

The recent developments in the YORP torque modelling suggest a new way the small-scale thermal conductivity can act on boulders and rocks on asteroid surfaces producing a torque that is parallel to the asteroid surface (Golubov et al., 2014). The effect of those torques, so-called T-YORP, taken into account in thermophysical modelling, as they should be included in predictions of YORP strength. It might be important to take the T-YORP into account especially for targets like (85990) 1999 JV_6, for which radar observations suggest considerable decimetre-scale surface roughness. More YORP detections and detailed physical models are still required to better constrain the comprehensive theoretical YORP

determination. Especially considering that all YORP detections to date were accelerations of the spin-rate. Establishing whether a YORP-induced deceleration can be directly detected is considered to be top-priority in the investigation of this non-gravitational effect (recent THERMOPS conference, private communication).

Bibliography

C. H. Acton. Ancillary data services of NASA's Navigation and Ancillary Information Facility. *Planet. Space Sci.*, 44:65–70, January 1996. doi: 10.1016/0032-0633(95)00107-7.

J. Agarwal, D. Jewitt, M. Mutchler, H. Weaver, and S. Larson. A binary main-belt comet. *Nature*, 549:357–359, September 2017. doi: 10.1038/nature23892.

M. F. A'Hearn, S. Hoban, P. V. Birch, C. Bowers, R. Martin, and D. A. Klinglesmith, III. Cyanogen jets in comet Halley. *Nature*, 324:649–651, December 1986. doi: 10.1038/324649a0.

K. Altwegg, H. Balsiger, A. Bar-Nun, J. J. Berthelier, A. Bieler, P. Bochsler, C. Briois, U. Calmonte, M. Combi, J. De Keyser, P. Eberhardt, B. Fiethe, S. Fuselier, S. Gasc, T. I. Gombosi, K. C. Hansen, M. Hässig, A. Jäckel, E. Kopp, A. Korth, L. LeRoy, U. Mall, B. Marty, O. Mousis, E. Neefs, T. Owen, H. Rème, M. Rubin, T. Sémon, C.-Y. Tzou, H. Waite, and P. Wurz. 67P/Churyumov-Gerasimenko, a Jupiter family comet with a high D/H ratio. *Science*, 347(27):1261952, January 2015. ISSN 0036-8075. doi: 10.1126/science.1261952. URL `http://science.sciencemag.org/content/early/2014/12/09/science.1261952`.

K. Altwegg, H. Balsiger, A. Bar-Nun, J.-J. Berthelier, A. Bieler, P. Bochsler, C. Briois, U. Calmonte, M. R. Combi, H. Cottin, J. De Keyser, F. Dhooghe, B. Fiethe, S. A. Fuselier, S. Gasc, T. I. Gombosi, K. C. Hansen, M. Haessig, A. Ja ckel, E. Kopp, A. Korth, L. Le Roy, U. Mall, B. Marty, O. Mousis, T. Owen, H. Reme, M. Rubin, T. Semon, C.-Y. Tzou, J. H. Waite, and P. Wurz. Prebiotic chemicals–amino acid and phosphorus–in the coma of comet 67P/Churyumov-Gerasimenko. *Science Advances*, 2(5):e1600285–e1600285, May 2016. doi: 10.1126/sciadv.1600285. URL `http://advances.sciencemag.org/content/2/5/e1600285`.

M. Ashman, M. Barthélémy, L. O'Rourke, M. Almeida, N. Altobelli, M. Costa Sitjà, J. J. García Beteta, B. Geiger, B. Grieger, D. Heather, R. Hoofs, M. Küppers, P. Martin, R. Moissl, C. Múñoz Crego, M. Pérez-Ayúcar, E. Sanchez Suarez, M. Taylor, and C. Vallat. Rosetta science operations in support of the Philae mission. *Acta Astronautica*, 125:41–64, August 2016. doi: 10.1016/j.actaastro.2016.02.007.

C. Barbieri and I. Bertini. Comets. *Nuovo Cimento Rivista Serie*, 40:335–409, August 2017. doi: 10.1393/ncr/i2017-10138-4.

G. Beekman. I. o. yarkovsky and the discovery of 'his' effect. *Journal for the History of Astronomy*, 37:71–86, February 2006.

L. A. M. Benner, S. J. Ostro, C. Magri, M. C. Nolan, E. S. Howell, J. D. Giorgini, R. F. Jurgens, J.-L. Margot, P. A. Taylor, M. W. Busch, and M. K. Shepard. Near-Earth asteroid surface roughness depends on compositional class. *Icarus*, 198:294–304, December 2008. doi: 10.1016/j.icarus.2008.06.010.

L. A. M. Benner, M. W. Busch, J. D. Giorgini, P. A. Taylor, and J.-L. Margot. *Radar Observations of Near-Earth and Main-Belt Asteroids*, pages 165–182. 2015. doi: 10.2458/azu_uapress_9780816532131-ch009.

R. Berry and J. Burnell. *The Handbook of Astronomical Image Processing*. Willmann-Bell, 2005. ISBN 9780943396828. URL `https://books.google.co.uk/books?id=O0fPPAAACAAJ`.

J.-L. Bertaux. Estimate of the erosion rate from H_2O mass-loss measurements from SWAN/SOHO in previous perihelions of comet 67P/Churyumov-Gerasimenko and connection with observed rotation rate variations. *A&A*, 583:A38, November 2015. doi: 10.1051/0004-6361/201525992.

J. Biele, S. Ulamec, M. Maibaum, R. Roll, L. Witte, E. Jurado, P. Muñoz, W. Arnold, H.-U. Auster, C. Casas, C. Faber, C. Fantinati, F. Finke, H.-H. Fischer, K. Geurts, C. Güttler, P. Heinisch, A. Herique, S. Hviid, G. Kargl, M. Knapmeyer, J. Knollenberg, W. Kofman, N. Kömle, E. Kührt, V. Lommatsch, S. Mottola, R. Pardo de Santayana, E. Remetean, F. Scholten, K. J. Seidensticker, H. Sierks, and T. Spohn. The landing(s) of Philae and inferences about comet surface mechanical properties. *Science*, 349(1), July 2015. doi: 10.1126/science.aaa9816.

A. Bieler, K. Altwegg, H. Balsiger, J.-J. Berthelier, U. Calmonte, M. Combi, J. De Keyser, B. Fiethe, N. Fougere, S. Fuselier, S. Gasc, T. Gombosi, K. Hansen, M. Hässig, Z. Huang, A. Jäckel, X. Jia, L. Le Roy, U. A. Mall, H. Rème, M. Rubin, V. Tenishev, G. Tóth, C.-Y. Tzou, and P. Wurz. Comparison of 3D kinetic and hydrodynamic models to ROSINA-COPS measurements of the neutral coma of 67P/Churyumov-Gerasimenko. *A&A*, 583: A7, November 2015. doi: 10.1051/0004-6361/201526178.

R. P. Binzel and S. Xu. Chips off of asteroid 4 Vesta - Evidence for the parent body of basaltic achondrite meteorites. *Science*, 260:186–191, April 1993. doi: 10.1126/science.260.5105.186.

R. P. Binzel, A. W. Harris, S. J. Bus, and T. H. Burbine. Spectral Properties of Near-Earth Objects: Palomar and IRTF Results for 48 Objects Including Spacecraft Targets (9969) Braille and (10302) 1989 ML. *Icarus*, 151:139–149, June 2001. doi: 10.1006/icar.2001.6613.

R. P. Binzel, A. S. Rivkin, J. S. Stuart, A. W. Harris, S. J. Bus, and T. H. Burbine. Observed spectral properties of near-Earth objects: results for population distribution, source regions, and space weathering processes. *Icarus*, 170:259–294, August 2004. doi: 10.1016/j.icarus.2004.04.004.

R. P. Binzel, V. Reddy, and T. L. Dunn. *The Near-Earth Object Population: Connections to Comets, Main-Belt Asteroids, and Meteorites*, pages 243–256. 2015. doi: 10.2458/azu_uapress_9780816532131-ch013.

H. Boehnhardt and K. Birkle. Time variable coma structures in comet P/Swift-Tuttle. *A&AS*, 107:101–120, October 1994.

B. T. Bolin, M. Delbo, A. Morbidelli, and K. J. Walsh. Yarkovsky V-shape identification of asteroid families. *Icarus*, 282:290–312, January 2017. doi: 10.1016/j.icarus.2016.09.029.

W. F. Bottke, Jr., D. Vokrouhlický, D. P. Rubincam, and M. Broz. *The Effect of Yarkovsky Thermal Forces on the Dynamical Evolution of Asteroids and Meteoroids*, pages 395–408. March 2002.

W. F. Bottke, Jr., D. Vokrouhlický, D. P. Rubincam, and D. Nesvorný. The Yarkovsky and Yorp Effects: Implications for Asteroid Dynamics. *Annual Review of Earth and Planetary Sciences*, 34:157–191, May 2006. doi: 10.1146/annurev.earth.34.031405.125154.

S. Breiter and H. Michalska. YORP torque as the function of shape harmonics. *MNRAS*, 388: 927–944, August 2008. doi: 10.1111/j.1365-2966.2008.13471.x.

S. Breiter and M. Murawiecka. Tumbling asteroid rotation with the YORP torque and inelastic energy dissipation. *MNRAS*, 449:2489–2497, May 2015. doi: 10.1093/mnras/stv433.

S. Breiter, H. Michalska, D. Vokrouhlický, and W. Borczyk. Radiation-induced torques on spheroids. *A&A*, 471:345–353, August 2007. doi: 10.1051/0004-6361:20077313.

S. Breiter, A. Rożek, and D. Vokrouhlický. Yarkovsky-O'Keefe-Radzievskii-Paddack effect on tumbling objects. *MNRAS*, 417:2478–2499, November 2011. doi: 10.1111/j.1365-2966.2011.19411.x.

S. Breiter, A. Rożek, and D. Vokrouhlický. Stress field and spin axis relaxation for inelastic triaxial ellipsoids. *MNRAS*, 427:755–769, November 2012. doi: 10.1111/j.1365-2966.2012.21970.x.

B. Brugger, O. Mousis, A. Morse, U. Marboeuf, L. Jorda, A. Guilbert-Lepoutre, D. Andrews, S. Barber, P. Lamy, A. Luspay-Kuti, K. Mandt, G. Morgan, S. Sheridan, P. Vernazza, and I. P. Wright. Subsurface Characterization of 67P/Churyumov-Gerasimenko's Abydos Site. *ApJ*, 822:98, May 2016. doi: 10.3847/0004-637X/822/2/98.

S. J. Bus and R. P. Binzel. Phase II of the Small Main-Belt Asteroid Spectroscopic Survey. A Feature-Based Taxonomy. *Icarus*, 158:146–177, July 2002. doi: 10.1006/icar.2002.6856.

S.J. Bus. *Compositional Structure in the Asteroid Belt: Results of a Spectroscopic Survey.* PhD thesis, Massachusetts Institute of Technology, 1999.

C. Capanna, G. Gesquière, L. Jorda, P. Lamy, and D. Vibert. Three-dimensional reconstruction using multiresolution photoclinometry by deformation. *The Visual Computer*, 29(6):825–835, Jun 2013. ISSN 1432-2315. doi: 10.1007/s00371-013-0821-5. URL `https://doi.org/10.1007/s00371-013-0821-5`.

C. Capanna, L. Jorda, G. Gesquière, R. W. Gaskell, O. Groussin, P. Gutiérrez, S. F. Hviid, P. L. Lamy, F. Preusker, S. Rodionov, F. Scholten, and D. Vibert. Multi-Resolution Stereophotoclinometry by Deformation, a New 3D Shape Reconstruction Method Applied to ROSETTA/OSIRIS Images. *AGU Fall Meeting Abstracts*, December 2014.

D. Čapek and D. Vokrouhlický. The YORP effect with finite thermal conductivity. *Icarus*, 172:526–536, December 2004. doi: 10.1016/j.icarus.2004.07.003.

V. Carruba, B. Novaković, and S. Aljbaae. The Hoffmeister asteroid family. *MNRAS*, 465:4099–4105, March 2017. doi: 10.1093/mnras/stw3022.

B. Carry. Density of asteroids. *Planet. Space Sci.*, 73:98–118, December 2012. doi: 10.1016/j.pss.2012.03.009.

G. Chauvin, A.-M. Lagrange, C. Dumas, B. Zuckerman, D. Mouillet, I. Song, J.-L. Beuzit, and P. Lowrance. A giant planet candidate near a young brown dwarf. Direct VLT/NACO observations using IR wavefront sensing. *A&A*, 425:L29–L32, October 2004. doi: 10.1051/0004-6361:200400056.

S. R. Chesley, S. J. Ostro, D. Vokrouhlický, D. Čapek, J. D. Giorgini, M. C. Nolan, J.-L. Margot, A. A. Hine, L. A. M. Benner, and A. B. Chamberlin. Direct Detection of the Yarkovsky Effect by Radar Ranging to Asteroid 6489 Golevka. *Science*, 302:1739–1742, December 2003. doi: 10.1126/science.1091452.

S. R. Chesley, D. Farnocchia, M. C. Nolan, D. Vokrouhlický, P. W. Chodas, A. Milani, F. Spoto, B. Rozitis, L. A. M. Benner, W. F. Bottke, M. W. Busch, J. P. Emery, E. S. Howell, D. S. Lauretta, J.-L. Margot, and P. A. Taylor. Orbit and bulk density of the OSIRIS-REx target Asteroid (101955) Bennu. *Icarus*, 235:5–22, June 2014. doi: 10.1016/j.icarus.2014.02.020.

C. F. Chyba, C. Sagan, L. Brookshaw, and P. J. Thomas. Impact delivery of prebiotic organics to the early earth. *Origins of Life and Evolution of the Biosphere*, 19:467–468, May 1989. doi: 10.1007/BF02388954.

M. Ciarniello, F. Capaccioni, G. Filacchione, A. Raponi, F. Tosi, M. C. De Sanctis, M. T. Capria, S. Erard, D. Bockelee-Morvan, C. Leyrat, G. Arnold, A. Barucci, P. Beck, G. Bellucci, S. Fornasier, A. Longobardo, S. Mottola, E. Palomba, E. Quirico, and B. Schmitt. Photometric properties of comet 67P/Churyumov-Gerasimenko from VIRTIS-M onboard Rosetta. *A&A*, 583:A31, November 2015. doi: 10.1051/0004-6361/201526307.

S. Cicalò and D. J. Scheeres. Averaged rotational dynamics of an asteroid in tumbling rotation under the YORP torque. *Celestial Mechanics and Dynamical Astronomy*, 106:301–337, April 2010. doi: 10.1007/s10569-009-9249-7.

D. Cotto-Figueroa, T. S. Statler, D. C. Richardson, and P. Tanga. Coupled spin and shape evolution of small rubble-pile asteroids: Self-limitation of the yorp effect. *ApJ*, 803:25, April 2015. doi: 10.1088/0004-637X/803/1/25.

M. Ćuk and J. A. Burns. Effects of thermal radiation on the dynamics of binary NEAs. *Icarus*, 176:418–431, August 2005. doi: 10.1016/j.icarus.2005.02.001.

B. J. R. Davidsson, H. Sierks, C. Güttler, F. Marzari, M. Pajola, H. Rickman, M. F. A'Hearn, A.-T. Auger, M. R. El-Maarry, S. Fornasier, P. J. Gutiérrez, H. U. Keller, M. Massironi, C. Snodgrass, J.-B. Vincent, C. Barbieri, P. L. Lamy, R. Rodrigo, D. Koschny, M. A. Barucci, J.-L. Bertaux, I. Bertini, G. Cremonese, V. Da Deppo, S. Debei, M. De Cecco, C. Feller, M. Fulle, O. Groussin, S. F. Hviid, S. Höfner, W.-H. Ip, L. Jorda, J. Knollenberg, G. Kovacs, J.-R. Kramm, E. Kührt, M. Küppers, F. La Forgia, L. M. Lara, M. Lazzarin, J. J. Lopez Moreno, R. Moissl-Fraund, S. Mottola, G. Naletto, N. Oklay, N. Thomas, and C. Tubiana. The primordial nucleus of comet 67P/Churyumov-Gerasimenko. *A&A*, 592:A63, July 2016. doi: 10.1051/0004-6361/201526968.

M. C. De Sanctis, F. Capaccioni, M. Ciarniello, G. Filacchione, M. Formisano, S. Mottola, A. Raponi, F. Tosi, D. Bockelée-Morvan, S. Erard, C. Leyrat, B. Schmitt, E. Ammannito, G. Arnold, M. A. Barucci, M. Combi, M. T. Capria, P. Cerroni, W.-H. Ip, E. Kuehrt, T. B. Mccord, E. Palomba, P. Beck, and E. Quirico. The diurnal cycle of water ice on comet 67P/Churyumov-Gerasimenko. *Nature*, 525(7570), September 2015. ISSN 1476-4687.

M. Delbo', A. dell'Oro, A. W. Harris, S. Mottola, and M. Mueller. Thermal inertia of near-Earth asteroids and implications for the magnitude of the Yarkovsky effect. *Icarus*, 190: 236–249, September 2007. doi: 10.1016/j.icarus.2007.03.007.

M. Delbo, M. Mueller, J. P. Emery, B. Rozitis, and M. T. Capria. *Asteroid Thermophysical Modeling*, pages 107–128. 2015. doi: 10.2458/azu_uapress_9780816532131-ch006.

H. Demura, S. Kobayashi, E. Nemoto, N. Matsumoto, M. Furuya, A. Yukishita, N. Muranaka, H. Morita, K. Shirakawa, M. Maruya, H. Ohyama, M. Uo, T. Kubota, T. Hashimoto, J. Kawaguchi, A. Fujiwara, J. Saito, S. Sasaki, H. Miyamoto, and N. Hirata. Pole and Global Shape of 25143 Itokawa. *Science*, 312:1347–1349, June 2006. doi: 10.1126/science.1126574.

J. Ďurech, D. Vokrouhlický, M. Kaasalainen, D. Higgins, Y. N. Krugly, N. M. Gaftonyuk, V. G. Shevchenko, V. G. Chiorny, H. Hamanowa, H. Hamanowa, V. Reddy, and R. R. Dyvig. Detection of the YORP effect in asteroid (1620) Geographos. *A&A*, 489:L25–L28, October 2008. doi: 10.1051/0004-6361:200810672.

J. Ďurech, D. Vokrouhlický, A. R. Baransky, S. Breiter, O. A. Burkhonov, W. Cooney, V. Fuller, N. M. Gaftonyuk, J. Gross, R. Y. Inasaridze, M. Kaasalainen, Y. N. Krugly, O. I. Kvaratshelia, E. A. Litvinenko, B. Macomber, F. Marchis, I. E. Molotov, J. Oey, D. Polishook, J. Pollock, P. Pravec, K. Sárneczky, V. G. Shevchenko, I. Slyusarev, R. Stephens, G. Szabó, D. Terrell, F. Vachier, Z. Vanderplate, M. Viikinkoski, and B. D. Warner. Analysis of the rotation period of asteroids (1865) Cerberus, (2100) Ra-Shalom, and (3103) Eger - search for the YORP effect. *A&A*, 547:A10, November 2012. doi: 10.1051/0004-6361/201219396.

M. Ram El-Maarry, O. Groussin, N. Thomas, M. Pajola, A.-T. Auger, B. Davidsson, X. Hu, S. F. Hviid, J. Knollenberg, C. Güttler, C. Tubiana, S. Fornasier, C. Feller, P. Hasselmann, J.-B. Vincent, H. Sierks, C. Barbieri, P. Lamy, R. Rodrigo, D. Koschny, H. U. Keller, H. Rickman, M. F. A'Hearn, M. A. Barucci, J.-L. Bertaux, I. Bertini, S. Besse, D. Bodewits, G. Cremonese, V. Da Deppo, S. Debei, M. De Cecco, J. Deller, J. D. P. Deshapriya, M. Fulle, P. J. Gutierrez, M. Hofmann, W.-H. Ip, L. Jorda, G. Kovacs, J.-R. Kramm, E. Kührt, M. Küppers, L. M. Lara, M. Lazzarin, Z.-Yi Lin, J. J. Lopez Moreno, S. Marchi, F. Marzari, S. Mottola, G. Naletto, N. Oklay, A. Pommerol, F. Preusker, F. Scholten, and X. Shi. Surface changes on comet 67P/Churyumov-Gerasimenko suggest a more active past. *Science*, 355(6332):1392–1395, 2017. ISSN 0036-8075. doi: 10.1126/science.aak9384. URL `http://science.sciencemag.org/content/355/6332/1392`.

A. Erikson, S. Mottola, J. S. V. Lagerros, M. Lindgren, J. Piironen, T. Oja, G. Hahn, C.-I. Lagerkvist, A. W. Harris, A. Nathues, and G. Neukum. The Near-Earth Objects Follow-up Program. III. 32 Lightcurves for 12 Objects from 1992 and 1995. *Icarus*, 147:487–497, October 2000. doi: 10.1006/icar.2000.6457.

ESO. EFOSC intstrument website, 2016. URL `https://www.eso.org/sci/facilities/lasilla/instruments/efosc/inst/Efosc2Filters.html`.

P. Farinella, D. Vokrouhlický, and W. K. Hartmann. Meteorite delivery via yarkovsky orbital drift. *Icarus*, 132:378–387, April 1998. doi: 10.1006/icar.1997.5872.

D. Farnocchia, S. R. Chesley, D. Vokrouhlický, A. Milani, F. Spoto, and W. F. Bottke. Near earth asteroids with measurable yarkovsky effect. *Icarus*, 224:1–13, May 2013. doi: 10.1016/j.icarus.2013.02.004.

D. Farnocchia, S. R. Chesley, A. Milani, G. F. Gronchi, and P. W. Chodas. *Orbits, Long-Term Predictions, Impact Monitoring*, pages 815–834. 2015. doi: 10.2458/azu_uapress_9780816532131-ch041.

S. Fornasier, B. E. Clark, and E. Dotto. Spectroscopic survey of x-type asteroids. *Icarus*, 214:131–146, July 2011. doi: 10.1016/j.icarus.2011.04.022.

S. Fornasier, S. Mottola, H. U. Keller, M. A. Barucci, B. Davidsson, C. Feller, J. D. P. Deshapriya, H. Sierks, C. Barbieri, P. L. Lamy, R. Rodrigo, D. Koschny, H. Rickman, M. A'Hearn, J. Agarwal, J.-L. Bertaux, I. Bertini, S. Besse, G. Cremonese, V. Da Deppo, S. Debei, M. De Cecco, J. Deller, M. R. El-Maarry, M. Fulle, O. Groussin, P. J. Gutierrez, C. Güttler, M. Hofmann, S. F. Hviid, W.-H. Ip, L. Jorda, J. Knollenberg, G. Kovacs, R. Kramm, E. Kührt, M. Küppers, M. L. Lara, M. Lazzarin, J. J. L. Moreno, F. Marzari, M. Massironi, G. Naletto, N. Oklay, M. Pajola, A. Pommerol, F. Preusker, F. Scholten, X. Shi, N. Thomas, I. Toth, C. Tubiana, and J.-B. Vincent. Rosetta's comet 67P/Churyumov-Gerasimenko sheds its dusty mantle to reveal its icy nature. *Science*, 354:1566–1570, December 2016. doi: 10.1126/science.aag2671.

N. Fougere, K. Altwegg, J.-J. Berthelier, A. Bieler, D. Bockelée-Morvan, U. Calmonte, F. Capaccioni, M. R. Combi, J. De Keyser, V. Debout, S. Erard, B. Fiethe, G. Filacchione, U. Fink, S. A. Fuselier, T. I. Gombosi, K. C. Hansen, M. Hässig, Z. Huang, L. Le Roy, C. Leyrat, A. Migliorini, G. Piccioni, G. Rinaldi, M. Rubin, Y. Shou, V. Tenishev, G. Toth, and C.-Y. Tzou. Direct Simulation Monte Carlo modelling of the major species in the coma of comet 67P/Churyumov-Gerasimenko. *MNRAS*, 462:S156–S169, November 2016. doi: 10.1093/mnras/stw2388.

L. M. French and R. P. Binzel. CCD photometry of asteroids. In R. P. Binzel, T. Gehrels, and M. S. Matthews, editors, *Asteroids II*, pages 54–65, 1989.

R. Gaskell, J. Saito, M. Ishiguro, T. Kubota, T. Hashimoto, N. Hirata, S. Abe, O. Barnouin-Jha, and D. Scheeres. Gaskell Itokawa Shape Model V1.0. *NASA Planetary Data System*, 92, September 2008. URL `https://pdsquery.jpl.nasa.gov/query?Identifier=HAY-A-AMICA-5-ITOKAWASHAPE-V1.0&resclass=data.dataset`.

L. Giacomini, M. Massironi, M. R. El-Maarry, L. Penasa, M. Pajola, N. Thomas, S. C. Lowry, C. Barbieri, G. Cremonese, F. Ferri, G. Naletto, I. Bertini, F. La Forgia, M. Lazzarin, F. Marzari, H. Sierks, P. L. Lamy, R. Rodrigo, H. Rickman, D. Koschny, H. U. Keller, J. Agarwal, M. F. A'Hearn, A.-T. Auger, M. A. Barucci, J.-L. Bertaux, S. Besse, D. Bodewits, V. Da Deppo, B. Davidsson, M. De Cecco, S. Debei, S. Fornasier, M. Fulle, O. Groussin, P. J. Gutierrez, C. Güttler, S. F. Hviid, W.-H. Ip, L. Jorda, J. Knollenberg, G. Kovacs, J.-R. Kramm, E. Kührt, M. Küppers, L. M. Lara, J. J. L. Moreno, S. Magrin, H. Michalik, N. Oklay, A. Pommerol, F. Preusker, F. Scholten, C. Tubiana, and J.-B. Vincent. Geologic mapping of the Comet 67P/Churyumov-Gerasimenko's Northern hemisphere. *MNRAS*, 462:S352–S367, November 2016. doi: 10.1093/mnras/stw2848.

A. Gicquel, J.-B. Vincent, J. Agarwal, M. F. A'Hearn, I. Bertini, D. Bodewits, H. Sierks, Z.-Y. Lin, C. Barbieri, P. L. Lamy, R. Rodrigo, D. Koschny, H. Rickman, H. U. Keller, M. A. Barucci, J.-L. Bertaux, S. Besse, G. Cremonese, V. Da Deppo, B. Davidsson, S. Debei, J. Deller, M. De Cecco, E. Frattin, M. R. El-Maarry, S. Fornasier, M. Fulle, O. Groussin, P. J. Gutiérrez, P. Gutiérrez-Marquez, C. Güttler, S. Höfner, M. Hofmann, X. Hu, S. F. Hviid, W.-H. Ip, L. Jorda, J. Knollenberg, G. Kovacs, J.-R. Kramm, E. Kührt, M. Küppers, L. M. Lara, M. Lazzarin, J. J. L. Moreno, S. Lowry, F. Marzari, N. Masoumzadeh, M. Massironi, F. Moreno, S. Mottola, G. Naletto, N. Oklay, M. Pajola, A. Pommerol, F. Preusker, F. Scholten, X. Shi, N. Thomas, I. Toth, and C. Tubiana. Sublimation of icy aggregates in the coma of comet 67P/Churyumov-Gerasimenko detected with the OSIRIS cameras on board Rosetta. *MNRAS*, 462:S57–S66, November 2016. doi: 10.1093/mnras/stw2117.

J. D. Giorgini, P. A. Taylor, L. A. Rodriguez-Ford, A. Rozek, S. C. Lowry, M. C. Nolan, M. Brozovic, and L. A. M. Benner. (85990) 1999 JV_6. *CBET*, 4279, 2016. URL `http://www.cbat.eps.harvard.edu/iau/cbet/004200/CBET004279.txt`.

O. Golubov and Y. N. Krugly. Tangential Component of the YORP Effect. *ApJ*, 752:L11, June 2012. doi: 10.1088/2041-8205/752/1/L11.

O. Golubov and D. J. Scheeres. Equilibrium Rotation States of Doubly Synchronous Binary Asteroids. *ApJ*, 833:L23, December 2016. doi: 10.3847/2041-8213/833/2/L23.

O. Golubov, D. J. Scheeres, and Y. N. Krugly. A Three-dimensional Model of Tangential YORP. *ApJ*, 794:22, October 2014. doi: 10.1088/0004-637X/794/1/22.

O. Golubov, Y. Kravets, Y. N. Krugly, and D. J. Scheeres. Physical models for the normal YORP and diurnal Yarkovsky effects. *MNRAS*, March 2016. doi: 10.1093/mnras/stw540.

R. Gomes, H. F. Levison, K. Tsiganis, and A. Morbidelli. Origin of the cataclysmic Late Heavy Bombardment period of the terrestrial planets. *Nature*, 435:466–469, May 2005. doi: 10.1038/nature03676.

M. Granvik, A. Morbidelli, D. Vokrouhlický, W. F. Bottke, D. Nesvorný, and R. Jedicke. Escape of asteroids from the main belt. *A&A*, 598:A52, February 2017. doi: 10.1051/0004-6361/201629252.

A. Guilbert-Lepoutre, R. Schulz, A. Rożek, S. C. Lowry, G. P. Tozzi, and J. A. Stüwe. Pre-perihelion activity of comet 67P/Churyumov-Gerasimenko. *A&A*, 567:L2, July 2014. doi: 10.1051/0004-6361/201424186.

C. A. Gullixson. Two Dimensional Imagery. In S. B. Howell, editor, *Astronomical CCD Observing and Reduction Techniques*, volume 23 of *Astronomical Society of the Pacific Conference Series*, page 130, 1992.

P. J. Gutiérrez, L. Jorda, R. W. Gaskell, B. J. R. Davidsson, C. Capanna, S. F. Hviid, H. U. Keller, L. Maquet, S. Mottola, F. Preusker, F. Scholten, L. M. Lara, F. Moreno, R. Rodrigo, H. Sierks, C. Barbieri, P. Lamy, D. Koschny, H. Rickman, J. Agarwal, M. F. A'Hearn, A. T. Auger, M. A. Barucci, J. L. Bertaux, I. Bertini, G. Cremonese, V. Da Deppo, S. Debei, M. De Cecco, M. R. El-Maarry, S. Fornasier, M. Fulle, O. Groussin, P. Gutiérrez-Marques, C. Güttler, W. H. Ip, J. Knollenberg, J. R. Kramm, E. Kührt, M. Küppers, F. La Forgia, M. Lazzarin, J. J. López-Moreno, S. Magrin, S. Marchi, F. Marzari, G. Naletto, N. Oklay, M. Pajola, A. Pommerol, D. Sabau, N. Thomas, I. Toth, C. Tubiana, and J. B. Vincent. Possible interpretation of the precession of comet 67P/Churyumov-Gerasimenko. *A&A*, 590:A46, May 2016. doi: 10.1051/0004-6361/201528029.

J. Hanuš, J. Ďurech, M. Brož, A. Marciniak, B. D. Warner, F. Pilcher, R. Stephens, R. Behrend, B. Carry, D. Čapek, P. Antonini, M. Audejean, K. Augustesen, E. Barbotin, P. Baudouin, A. Bayol, L. Bernasconi, W. Borczyk, J.-G. Bosch, E. Brochard, L. Brunetto, S. Casulli, A. Cazenave, S. Charbonnel, B. Christophe, F. Colas, J. Coloma, M. Conjat, W. Cooney, H. Correira, V. Cotrez, A. Coupier, R. Crippa, M. Cristofanelli, C. Dalmas, C. Danavaro, C. Demeautis, T. Droege, R. Durkee, N. Esseiva, M. Esteban, M. Fagas, G. Farroni, M. Fauvaud, S. Fauvaud, F. Del Freo, L. Garcia, S. Geier, C. Godon, K. Grangeon, H. Hamanowa, H. Hamanowa, N. Heck, S. Hellmich, D. Higgins, R. Hirsch, M. Husarik, T. Itkonen, O. Jade, K. Kamiński, P. Kankiewicz, A. Klotz, R. A. Koff, A. Kryszczyńska, T. Kwiatkowski, A. Laffont, A. Leroy, J. Lecacheux, Y. Leonie, C. Leyrat, F. Manzini, A. Martin, G. Masi, D. Matter, J. Michałowski, M. J. Michałowski, T. Michałowski, J. Michelet, R. Michelsen, E. Morelle, S. Mottola, R. Naves, J. Nomen, J. Oey, W. Ogłoza, A. Oksanen, D. Oszkiewicz, P. Pääkkönen, M. Paiella, H. Pallares, J. Paulo, M. Pavic, B. Payet, M. Polińska, D. Polishook, R. Poncy, Y. Revaz, C. Rinner, M. Rocca, A. Roche, D. Romeuf, R. Roy, H. Saguin, P. A. Salom, S. Sanchez, G. Santacana, T. Santana-Ros, J.-P. Sareyan, K. Sobkowiak, S. Sposetti, D. Starkey, R. Stoss, J. Strajnic, J.-P. Teng, B. Trégon, A. Vagnozzi, F. P. Velichko, N. Waelchli, K. Wagrez, and H. Wücher. Asteroids' physical models from combined dense and sparse photometry and scaling of the YORP effect by the observed obliquity distribution. *A&A*, 551:A67, March 2013. doi: 10.1051/0004-6361/201220701.

J. K. Harmon, M. C. Nolan, E. S. Howell, J. D. Giorgini, and P. A. Taylor. Radar Observations of Comet 103P/Hartley 2. *ApJ*, 734:L2, June 2011. doi: 10.1088/2041-8205/734/1/L2.

A. W. Harris. A Thermal Model for Near-Earth Asteroids. *Icarus*, 131:291–301, February 1998. doi: 10.1006/icar.1997.5865.

A. W. Harris, J. W. Young, E. Bowell, L. J. Martin, R. L. Millis, M. Poutanen, F. Scaltriti, V. Zappala, H. J. Schober, H. Debehogne, and K. W. Zeigler. Photoelectric observations of asteroids 3, 24, 60, 261, and 863. *Icarus*, 77:171–186, January 1989. doi: 10.1016/0019-1035(89)90015-8.

A. W. Harris, M. Boslough, C. R. Chapman, L. Drube, P. Michel, and A. W. Harris. *Asteroid Impacts and Modern Civilization: Can We Prevent a Catastrophe?*, pages 835–854. 2015. doi: 10.2458/azu_uapress_9780816532131-ch042.

M. Hässig, K. Altwegg, H. Balsiger, A. Bar-Nun, J. J. Berthelier, A. Bieler, P. Bochsler, C. Briois, U. Calmonte, M. Combi, J. De Keyser, P. Eberhardt, B. Fiethe, S. A. Fuselier, M. Galand, S. Gasc, T. I. Gombosi, K. C. Hansen, A. Jäckel, H. U. Keller, E. Kopp, A. Korth, E. Kührt, L. Le Roy, U. Mall, B. Marty, O. Mousis, E. Neefs, T. Owen, H. Rème, M. Rubin, T. Sémon, C. Tornow, C.-Y. Tzou, J. H. Waite, and P. Wurz. Time variability and heterogeneity in the coma of 67P/Churyumov-Gerasimenko. *Science*, 347(1):aaa0276, January 2015. doi: 10.1126/science.aaa0276.

M. Hässig, K. Altwegg, H. Balsiger, J. J. Berthelier, A. Bieler, U. Calmonte, F. Dhooghe, B. Fiethe, S. A. Fuselier, S. Gasc, T. I. Gombosi, L. Le Roy, A. Luspay-Kuti, K. Mandt, M. Rubin, C.-Y. Tzou, S. F. Wampfler, and P. Wurz. Isotopic composition of CO_2 in the coma of 67P/Churyumov-Gerasimenko measured with ROSINA/DFMS. *A&A*, 605:A50, September 2017. doi: 10.1051/0004-6361/201630140.

M. Hirabayashi, D. J. Scheeres, S. R. Chesley, S. Marchi, J. W. McMahon, J. Steckloff, S. Mottola, S. P. Naidu, and T. Bowling. Fission and reconfiguration of bilobate comets as revealed by 67P/Churyumov-Gerasimenko. *Nature*, 534:352–355, June 2016. doi: 10.1038/nature17670.

M. Hoffmann, H. Rebhan, G. Neukum, and E. H. Geyer. Photometric observations of four near-earth asteroids. *Acta Astron.*, 43:61–67, January 1993.

S. A. Jacobson and D. J. Scheeres. Dynamics of rotationally fissioned asteroids: Source of observed small asteroid systems. *Icarus*, 214:161–178, July 2011. doi: 10.1016/j.icarus.2011.04.009.

S. A. Jacobson, F. Marzari, A. Rossi, and D. J. Scheeres. Matching asteroid population characteristics with a model constructed from the YORP-induced rotational fission hypothesis. *Icarus*, 277:381–394, October 2016. doi: 10.1016/j.icarus.2016.05.032.

A. Johansen, E. Jacquet, J. N. Cuzzi, A. Morbidelli, and M. Gounelle. *New Paradigms for Asteroid Formation*, pages 471–492. 2015. doi: 10.2458/azu_uapress_9780816532131-ch025.

L. Jorda, R. Gaskell, C. Capanna, S. Hviid, P. Lamy, J. Ďurech, G. Faury, O. Groussin, P. Gutiérrez, C. Jackman, S. J. Keihm, H. U. Keller, J. Knollenberg, E. Kührt, S. Marchi, S. Mottola, E. Palmer, F. P. Schloerb, H. Sierks, J.-B. Vincent, M. F. A'Hearn, C. Barbieri, R. Rodrigo, D. Koschny, H. Rickman, M. A. Barucci, J. L. Bertaux, I. Bertini, G. Cremonese, V. Da Deppo, B. Davidsson, S. Debei, M. De Cecco, S. Fornasier, M. Fulle, C. Güttler, W.-H. Ip, J. R. Kramm, M. Küppers, L. M. Lara, M. Lazzarin, J. J. Lopez Moreno, F. Marzari, G. Naletto, N. Oklay, N. Thomas, C. Tubiana, and K.-P. Wenzel. The global shape, density and rotation of Comet 67P/Churyumov-Gerasimenko from preperihelion Rosetta/OSIRIS observations. *Icarus*, 277:257–278, October 2016. doi: 10.1016/j.icarus.2016.05.002.

M. Jutzi and E. Asphaug. The shape and structure of cometary nuclei as a result of low-velocity accretion. *Science*, 348:1355–1358, June 2015. doi: 10.1126/science.aaa4747.

M. Kaasalainen and L. Lamberg. Inverse problems of generalized projection operators. *Inverse Problems*, 22:749–769, June 2006. doi: 10.1088/0266-5611/22/3/002.

M. Kaasalainen and J. Torppa. Optimization Methods for Asteroid Lightcurve Inversion. I. Shape Determination. *Icarus*, 153:24–36, September 2001. doi: 10.1006/icar.2001.6673.

M. Kaasalainen, J. Torppa, and K. Muinonen. Optimization Methods for Asteroid Lightcurve Inversion. II. The Complete Inverse Problem. *Icarus*, 153:37–51, September 2001. doi: 10.1006/icar.2001.6674.

M. Kaasalainen, S. Mottola, and M. Fulchignoni. *Asteroid Models from Disk-integrated Data*, pages 139–150. 2002.

M. Kaasalainen, J. Ďurech, B. D. Warner, Y. N. Krugly, and N. M. Gaftonyuk. Acceleration of the rotation of asteroid 1862 Apollo by radiation torques. *Nature*, 446:420–422, March 2007. doi: 10.1038/nature05614.

H. U. Keller, C. Barbieri, P. Lamy, H. Rickman, R. Rodrigo, K.-P. Wenzel, H. Sierks, M. F. A'Hearn, F. Angrilli, M. Angulo, M. E. Bailey, P. Barthol, M. A. Barucci, J.-L. Bertaux, G. Bianchini, J.-L. Boit, V. Brown, J. A. Burns, I. Büttner, J. M. Castro, G. Cremonese, W. Curdt, V. Da Deppo, S. Debei, M. De Cecco, K. Dohlen, S. Fornasier, M. Fulle, D. Germerott, F. Gliem, G. P. Guizzo, S. F. Hviid, W.-H. Ip, L. Jorda, D. Koschny, J. R. Kramm, E. Kührt, M. Küppers, L. M. Lara, A. Llebaria, A. López, A. López-Jimenez, J. López-Moreno, R. Meller, H. Michalik, M. D. Michelena, R. Müller, G. Naletto, A. Origné, G. Parzianello, M. Pertile, C. Quintana, R. Ragazzoni, P. Ramous, K.-U. Reiche, M. Reina, J. Rodríguez, G. Rousset, L. Sabau, A. Sanz, J.-P. Sivan, K. Stöckner, J. Tabero, U. Telljohann, N. Thomas, V. Timon, G. Tomasch, T. Wittrock, and M. Zaccariotto. Osiris – the scientific camera system onboard rosetta. *Space Science Reviews*, 128(1):433–506, 2007. ISSN 1572-9672. doi: 10.1007/s11214-006-9128-4. URL `http://dx.doi.org/10.1007/s11214-006-9128-4`.

H. U. Keller, C. Barbieri, D. Koschny, P. Lamy, H. Rickman, R. Rodrigo, H. Sierks, M. F. A'Hearn, F. Angrilli, M. A. Barucci, J.-L. Bertaux, G. Cremonese, V. Da Deppo, B. Davidsson, M. De Cecco, S. Debei, S. Fornasier, M. Fulle, O. Groussin, P. J. Gutierrez, S. F. Hviid, W.-H. Ip, L. Jorda, J. Knollenberg, J. R. Kramm, E. Kührt, M. Küppers, L.-M. Lara, M. Lazzarin, J. L. Moreno, F. Marzari, H. Michalik, G. Naletto, L. Sabau, N. Thomas, K.-P. Wenzel, I. Bertini, S. Besse, F. Ferri, M. Kaasalainen, S. Lowry, S. Marchi, S. Mottola, W. Sabolo, S. E. Schröder, S. Spjuth, and P. Vernazza. E-Type Asteroid (2867) Steins as Imaged by OSIRIS on Board Rosetta. *Science*, 327:190, January 2010. doi: 10.1126/science.1179559.

H. U. Keller, S. Mottola, B. Davidsson, S. E. Schröder, Y. Skorov, E. Kührt, O. Groussin, M. Pajola, S. F. Hviid, F. Preusker, F. Scholten, M. F. A'Hearn, H. Sierks, C. Barbieri, P. Lamy, R. Rodrigo, D. Koschny, H. Rickman, M. A. Barucci, J.-L. Bertaux, I. Bertini, G. Cremonese, V. Da Deppo, S. Debei, M. De Cecco, S. Fornasier, M. Fulle, P. J. Gutiérrez, W.-H. Ip, L. Jorda, J. Knollenberg, J. R. Kramm, M. Küppers, L. M. Lara, M. Lazzarin, J. J. Lopez Moreno, F. Marzari, H. Michalik, G. Naletto, L. Sabau, N. Thomas, J.-B. Vincent, K.-P. Wenzel, J. Agarwal, C. Güttler, N. Oklay, and C. Tubiana. Insolation, erosion, and morphology of comet 67P/Churyumov-Gerasimenko. *A&A*, 583:A34, November 2015a. doi: 10.1051/0004-6361/201525964.

H. U. Keller, S. Mottola, Y. Skorov, and L. Jorda. The changing rotation period of comet 67P/Churyumov-Gerasimenko controlled by its activity. *A&A*, 579:L5, July 2015b. doi: 10.1051/0004-6361/201526421.

H. U. Keller, S. Mottola, S. F. Hviid, J. Agarwal, E. Kührt, Y. Skorov, K. Otto, J.-B. Vincent, N. Oklay, S. E. Schröder, B. Davidsson, M. Pajola, X. Shi, D. Bodewits, I. Toth, F. Preusker, F. Scholten, H. Sierks, C. Barbieri, P. Lamy, R. Rodrigo, D. Koschny, H. Rickman, M. F. A'Hearn, M. A. Barucci, J.-L. Bertaux, I. Bertini, G. Cremonese, V. Da Deppo, S. Debei, M. De Cecco, J. Deller, S. Fornasier, M. Fulle, O. Groussin, P. J. Gutiérrez, C. Güttler, M. Hofmann, W.-H. Ip, L. Jorda, J. Knollenberg, J. R. Kramm, M. Küppers, L.-M. Lara, M. Lazzarin, J. J. Lopez-Moreno, F. Marzari, G. Naletto, C. Tubiana, and N. Thomas. Seasonal mass transfer on the nucleus of comet 67P/Chuyumov-Gerasimenko. *MNRAS*, 469: S357–S371, July 2017. doi: 10.1093/mnras/stx1726.

R. Kokotanekova, C. Snodgrass, P. Lacerda, S. F. Green, S. C. Lowry, Y. R. Fernández, C. Tubiana, A. Fitzsimmons, and H. H. Hsieh. Rotation of cometary nuclei: new light curves and an update of the ensemble properties of Jupiter-family comets. *MNRAS*, 471: 2974–3007, November 2017. doi: 10.1093/mnras/stx1716.

H. Krüger, K. J. Seidensticker, H.-H. Fischer, T. Albin, I. Apathy, W. Arnold, A. Flandes, A. Hirn, M. Kobayashi, A. Loose, A. Péter, and M. Podolak. Dust Impact Monitor (SESAME-DIM) measurements at comet 67P/Churyumov-Gerasimenko. *A&A*, 583:A15, November 2015. doi: 10.1051/0004-6361/201526400.

P. L. Lamy, I. Toth, H. A. Weaver, L. Jorda, M. Kaasalainen, and P. J. Gutiérrez. Hubble Space Telescope observations of the nucleus and inner coma of comet 67P/Churyumov-Gerasimenko. *A&A*, 458:669–678, November 2006. doi: 10.1051/0004-6361:20065253.

L. M. Lara, S. Lowry, J.-B. Vincent, P. J. Gutiérrez, A. Rożek, F. La Forgia, N. Oklay, H. Sierks, C. Barbieri, P. L. Lamy, R. Rodrigo, D. Koschny, H. Rickman, H. U. Keller, J. Agarwal, A.-T. Auger, M. F. A'Hearn, M. A. Barucci, J.-L. Bertaux, I. Bertini, S. Besse, D. Bodewits, G. Cremonese, B. Davidsson, V. Da Deppo, S. Debei, M. De Cecco, M. R. El-Maarry, F. Ferri, S. Fornasier, M. Fulle, O. Groussin, P. Gutiérrez-Marques, C. Güttler, S. F. Hviid, W.-H. Ip, L. Jorda, J. Knollenberg, G. Kovacs, J.-R. Kramm, E. Kührt, M. Küppers, M. Lazzarin, Z.-Y. Lin, J. J. López-Moreno, S. Magrin, F. Marzari, H. Michalik, R. Moissl-Fraund, F. Moreno, S. Mottola, G. Naletto, M. Pajola, A. Pommerol, N. Thomas, M. D. Sabau, and C. Tubiana. Large-scale dust jets in the coma of 67P/Churyumov-Gerasimenko as seen by the OSIRIS instrument onboard Rosetta. *A&A*, 583:A9, November 2015. doi: 10.1051/0004-6361/201526103.

D. S. Lauretta, S. S. Balram-Knutson, E. Beshore, W. V. Boynton, C. Drouet d'Aubigny, D. N. DellaGiustina, H. L. Enos, D. R. Golish, C. W. Hergenrother, E. S. Howell, C. A. Bennett, E. T. Morton, M. C. Nolan, B. Rizk, H. L. Roper, A. E. Bartels, B. J. Bos, J. P. Dworkin, D. E. Highsmith, D. A. Lorenz, L. F. Lim, R. Mink, M. C. Moreau, J. A. Nuth, D. C. Reuter, A. A. Simon, E. B. Bierhaus, B. H. Bryan, R. Ballouz, O. S. Barnouin, R. P. Binzel, W. F. Bottke, V. E. Hamilton, K. J. Walsh, S. R. Chesley, P. R. Christensen, B. E. Clark, H. C. Connolly, M. K. Crombie, M. G. Daly, J. P. Emery, T. J. McCoy, J. W. McMahon, D. J. Scheeres, S. Messenger, K. Nakamura-Messenger, K. Righter, and S. A. Sandford. OSIRIS-REx: Sample Return from Asteroid (101955) Bennu. *Space Sci. Rev.*, August 2017. doi: 10.1007/s11214-017-0405-1.

C. Lhotka, S. Reimond, J. Souchay, and O. Baur. Gravity field and solar component of the precession rate and nutation coefficients of Comet 67P/Churyumov-Gerasimenko. *MNRAS*, 455:3588–3596, February 2016. doi: 10.1093/mnras/stv2521.

Y. Liao, C. C. Su, R. Marschall, J. S. Wu, M. Rubin, I. L. Lai, W. H. Ip, H. U. Keller, J. Knollenberg, E. Kührt, Y. V. Skorov, and N. Thomas. 3D Direct Simulation Monte Carlo Modelling

of the Inner Gas Coma of Comet 67P/Churyumov-Gerasimenko: A Parameter Study. *Earth Moon and Planets*, 117:41–64, March 2016. doi: 10.1007/s11038-016-9486-1.

Z.-Y. Lin, W.-H. Ip, I.-L. Lai, J.-C. Lee, J.-B. Vincent, L. M. Lara, D. Bodewits, H. Sierks, C. Barbieri, P. L. Lamy, R. Rodrigo, D. Koschny, H. Rickman, H. U. Keller, J. Agarwal, M. F. A'Hearn, M. A. Barucci, J.-L. Bertaux, I. Bertini, G. Cremonese, V. Da Deppo, B. Davidsson, S. Debei, M. De Cecco, S. Fornasier, M. Fulle, O. Groussin, P. J. Gutiérrez, C. Güttler, S. F. Hviid, L. Jorda, J. Knollenberg, G. Kovacs, J.-R. Kramm, E. Kührt, M. Küppers, F. La Forgia, M. Lazzarin, J. J. López-Moreno, S. Lowry, F. Marzari, H. Michalik, S. Mottola, G. Naletto, N. Oklay, M. Pajola, A. Rożek, N. Thomas, Y. Liao, and C. Tubiana. Morphology and dynamics of the jets of comet 67P/Churyumov-Gerasimenko: Early-phase development. *A&A*, 583:A11, November 2015. doi: 10.1051/0004-6361/201525961.

Z.-Y. Lin, I.-L. Lai, C.-C. Su, W.-H. Ip, J.-C. Lee, J.-S. Wu, J.-B. Vincent, F. La Forgia, H. Sierks, C. Barbieri, P. L. Lamy, R. Rodrigo, D. Koschny, H. Rickman, H. U. Keller, J. Agarwal, M. F. A'Hearn, M. A. Barucci, J.-L. Bertaux, I. Bertini, D. Bodewits, G. Cremonese, V. Da Deppo, B. Davidsson, S. Debei, M. De Cecco, S. Fornasier, M. Fulle, O. Groussin, P. J. Gutiérrez, C. Güttler, S. F. Hviid, L. Jorda, J. Knollenberg, G. Kovacs, J.-R. Kramm, E. Kührt, M. Küppers, L. M. Lara, M. Lazzarin, J. J. López-Moreno, S. Lowry, F. Marzari, H. Michalik, S. Mottola, G. Naletto, N. Oklay, M. Pajola, A. Rożek, N. Thomas, and C. Tubiana. Observations and analysis of a curved jet in the coma of comet 67P/Churyumov-Gerasimenko. *A&A*, 588:L3, April 2016. doi: 10.1051/0004-6361/201527784.

S. C. Lowry, A. Fitzsimmons, P. Pravec, D. Vokrouhlický, H. Boehnhardt, P. A. Taylor, J.-L. Margot, A. Galád, M. Irwin, J. Irwin, and P. Kusnirák. Direct Detection of the Asteroidal YORP Effect. *Science*, 316:272–, April 2007. doi: 10.1126/science.1139040.

S. C. Lowry, S.R. Duddy, B. Rozitis, S.F. Green, A. Fitzsimmons, C. Snodgrass, H.H. Hsieh, and O. Hainaut. The nucleus of Comet 67P/Churyumov-Gerasimenko: A new shape model and thermophysical analysis. *Astronomy and Astrophysics*, 548:(A12) 1–15, December 2012. URL `http://kar.kent.ac.uk/52279/`.

S. C. Lowry, P. R. Weissman, S. R. Duddy, B. Rozitis, A. Fitzsimmons, S. F. Green, M. D. Hicks, C. Snodgrass, S. D. Wolters, S. R. Chesley, J. Pittichová, and P. van Oers. The internal structure of asteroid (25143) Itokawa as revealed by detection of YORP spin-up. *A&A*, 562:A48, February 2014. doi: 10.1051/0004-6361/201322602.

A. Luspay-Kuti, M. Hässig, S. A. Fuselier, K. E. Mandt, K. Altwegg, H. Balsiger, S. Gasc, A. Jäckel, L. Le Roy, M. Rubin, C.-Y. Tzou, P. Wurz, O. Mousis, F. Dhooghe, J. J. Berthelier, B. Fiethe, T. I. Gombosi, and U. Mall. Composition-dependent outgassing of comet 67P/Churyumov-Gerasimenko from ROSINA/DFMS. Implications for nucleus heterogeneity? *A&A*, 583:A4, November 2015. doi: 10.1051/0004-6361/201526205.

P. Magnusson, M. A. Barucci, J. D. Drummond, K. Lumme, S. J. Ostro, J. Surdej, R. C. Taylor, and V. Zappalà. Determination of pole orientations and shapes of asteroids. In R. P. Binzel, T. Gehrels, and M. S. Matthews, editors, *Asteroids II*, pages 66–97. University of Arizona Press, Tucson, 1989.

C. Magri, S. J. Ostro, D. J. Scheeres, M. C. Nolan, J. D. Giorgini, L. A. M. Benner, and J.-L. Margot. Radar observations and a physical model of Asteroid 1580 Betulia. *Icarus*, 186: 152–177, January 2007. doi: 10.1016/j.icarus.2006.08.004.

C. Magri, E. S. Howell, M. C. Nolan, P. A. Taylor, Y. R. Fernández, M. Mueller, R. J. Vervack, L. A. M. Benner, J. D. Giorgini, S. J. Ostro, D. J. Scheeres, M. D. Hicks, H. Rhoades, J. M.

Somers, N. M. Gaftonyuk, V. V. Kouprianov, Y. N. Krugly, I. E. Molotov, M. W. Busch, J.-L. Margot, V. Benishek, V. Protitch-Benishek, A. Galád, D. Higgins, P. Kušnirák, and D. P. Pray. Radar and photometric observations and shape modeling of contact binary near-Earth Asteroid (8567) 1996 HW1. *Icarus*, 214:210–227, July 2011. doi: 10.1016/j.icarus.2011.02.019.

K. A. Maher and D. J. Stevenson. Impact frustration of the origin of life. *Nature*, 331:612–614, February 1988. doi: 10.1038/331612a0.

F. Manzini and R. Behrend. Private communication, 2013. URL `http://obswww.unige.ch/~behrend/page_cou.html`.

U. Marboeuf, A. Bonsor, and J.-C. Augereau. Extrasolar comets: The origin of dust in exozodiacal disks? *Planet. Space Sci.*, 133:47–62, November 2016. doi: 10.1016/j.pss.2016.03.014.

B. G. Marsden. Orbital properties of Jupiter-family comets. *Planet. Space Sci.*, 57:1098–1105, August 2009. doi: 10.1016/j.pss.2008.12.007.

S. E. Marshall, E. S. Howell, C. Magri, R. J. Vervack, D. B. Campbell, Y. R. Fernández, M. C. Nolan, J. L. Crowell, M. D. Hicks, K. J. Lawrence, and P. A. Taylor. Thermal properties and an improved shape model for near-Earth asteroid (162421) 2000 ET70. *Icarus*, 292:22–35, August 2017. doi: 10.1016/j.icarus.2017.03.028.

M. Massironi, E. Simioni, F. Marzari, G. Cremonese, L. Giacomini, M. Pajola, L. Jorda, G. Naletto, S. Lowry, M. R. El-Maarry, F. Preusker, F. Scholten, H. Sierks, C. Barbieri, P. Lamy, R. Rodrigo, D. Koschny, H. Rickman, H. U. Keller, M. F. A'Hearn, J. Agarwal, A.-T. Auger, M. A. Barucci, J.-L. Bertaux, I. Bertini, S. Besse, D. Bodewits, C. Capanna, V. da Deppo, B. Davidsson, S. Debei, M. de Cecco, F. Ferri, S. Fornasier, M. Fulle, R. Gaskell, O. Groussin, P. J. Gutiérrez, C. Güttler, S. F. Hviid, W.-H. Ip, J. Knollenberg, G. Kovacs, R. Kramm, E. Kührt, M. Küppers, F. La Forgia, L. M. Lara, M. Lazzarin, Z.-Y. Lin, J. J. Lopez Moreno, S. Magrin, H. Michalik, S. Mottola, N. Oklay, A. Pommerol, N. Thomas, C. Tubiana, and J.-B. Vincent. Two independent and primitive envelopes of the bilobate nucleus of comet 67P. *Nature*, 526(7573):402–405, Oct 2015. ISSN 0028-0836. doi: 10.1038/nature15511. URL `http://dx.doi.org/10.1038/nature15511`. Letter.

K. J. Meech, B. Yang, J. Kleyna, O. R. Hainaut, S. Berdyugina, J. V. Keane, M. Micheli, A. Morbidelli, and R. J. Wainscoat. Inner solar system material discovered in the Oort cloud. *Science Advances*, 2:e1600038–e1600038, April 2016. doi: 10.1126/sciadv.1600038.

W. J. Merline, J. D. Drummond, B. Carry, A. Conrad, P. M. Tamblyn, C. Dumas, M. Kaasalainen, A. Erikson, S. Mottola, J. Ďurech, G. Rousseau, R. Behrend, G. B. Casalnuovo, B. Chinaglia, J. C. Christou, C. R. Chapman, and C. Neyman. The Resolved Asteroid Program - Size, shape, and pole of (52) Europa. *Icarus*, 225:794–805, July 2013. doi: 10.1016/j.icarus.2013.01.010.

M. Mitchell, B. Muftakhidinov, and T. Winchen. Engauge digitizer software, 2002. URL `http://digitizer.sourceforge.net`.

A. Morbidelli and D. Vokrouhlický. The Yarkovsky-driven origin of near-Earth asteroids. *Icarus*, 163:120–134, May 2003. doi: 10.1016/S0019-1035(03)00047-2.

A. Morbidelli, H. F. Levison, K. Tsiganis, and R. Gomes. Chaotic capture of Jupiter's Trojan asteroids in the early Solar System. *Nature*, 435:462–465, May 2005. doi: 10.1038/nature03540.

A. Morbidelli, K. J. Walsh, D. P. O'Brien, D. A. Minton, and W. F. Bottke. *The Dynamical Evolution of the Asteroid Belt*, pages 493–507. 2015. doi: 10.2458/azu_uapress_9780816532131-ch026.

F. Moreno, C. Snodgrass, O. Hainaut, C. Tubiana, H. Sierks, C. Barbieri, P. L. Lamy, R. Rodrigo, D. Koschny, H. Rickman, H. U. Keller, J. Agarwal, M. F. A'Hearn, M. A. Barucci, J.-L. Bertaux, I. Bertini, S. Besse, D. Bodewits, G. Cremonese, V. Da Deppo, B. Davidsson, S. Debei, M. De Cecco, F. Ferri, S. Fornasier, M. Fulle, O. Groussin, P. J. Gutiérrez, P. Gutiérrez-Marques, C. Güttler, S. F. Hviid, W.-H. Ip, L. Jorda, J. Knollenberg, G. Kovacs, J.-R. Kramm, E. Kührt, M. Küppers, L. M. Lara, M. Lazzarin, J. J. López-Moreno, F. Marzari, S. Mottola, G. Naletto, N. Oklay, M. Pajola, N. Thomas, J. B. Vincent, V. Della Corte, A. Fitzsimmons, S. Faggi, E. Jehin, C. Opitom, and G.-P. Tozzi. The dust environment of comet 67P/Churyumov-Gerasimenko from Rosetta OSIRIS and VLT observations in the 4.5 to 2.9 AU heliocentric distance range inbound. *A&A*, 587:A155, March 2016. doi: 10.1051/0004-6361/201527564.

S. Mottola, S. Lowry, C. Snodgrass, P. L. Lamy, I. Toth, A. Rożek, H. Sierks, M. F. A'Hearn, F. Angrilli, C. Barbieri, M. A. Barucci, J.-L. Bertaux, G. Cremonese, V. Da Deppo, B. Davidsson, M. De Cecco, S. Debei, S. Fornasier, M. Fulle, O. Groussin, P. Gutiérrez, S. F. Hviid, W. Ip, L. Jorda, H. U. Keller, J. Knollenberg, D. Koschny, R. Kramm, E. Kührt, M. Küppers, L. Lara, M. Lazzarin, J. J. Lopez Moreno, F. Marzari, H. Michalik, G. Naletto, H. Rickman, R. Rodrigo, L. Sabau, N. Thomas, K.-P. Wenzel, J. Agarwal, I. Bertini, F. Ferri, C. Güttler, S. Magrin, N. Oklay, C. Tubiana, and J.-B. Vincent. The rotation state of 67P/Churyumov-Gerasimenko from approach observations with the OSIRIS cameras on Rosetta. *A&A*, 569: L2, September 2014. doi: 10.1051/0004-6361/201424590.

O. Mousis, A. Guilbert-Lepoutre, B. Brugger, L. Jorda, J. S. Kargel, A. Bouquet, A.-T. Auger, P. Lamy, P. Vernazza, N. Thomas, and H. Sierks. Pits Formation from Volatile Outgassing on 67P/Churyumov-Gerasimenko. *ApJ*, 814:L5, November 2015. doi: 10.1088/2041-8205/814/1/L5.

M. Mueller, M. Delbo', J. L. Hora, D. E. Trilling, B. Bhattacharya, W. F. Bottke, S. Chesley, J. P. Emery, G. Fazio, A. W. Harris, A. Mainzer, M. Mommert, B. Penprase, H. A. Smith, T. B. Spahr, J. A. Stansberry, and C. A. Thomas. ExploreNEOs. III. Physical Characterization of 65 Potential Spacecraft Target Asteroids. *AJ*, 141:109, April 2011. doi: 10.1088/0004-6256/141/4/109.

K. Muinonen, I. N. Belskaya, A. Cellino, M. Delbò, A.-C. Levasseur-Regourd, A. Penttilä, and E. F. Tedesco. A three-parameter magnitude phase function for asteroids. *Icarus*, 209: 542–555, October 2010. doi: 10.1016/j.icarus.2010.04.003.

F. Murtagh. The European Southern Observatory: Into Its Second Quarter Century. *Irish Astronomical Journal*, 18:237, March 1988.

R. Nan, D. Li, C. Jin, Q. Wang, L. Zhu, W. Zhu, H. Zhang, Y. Yue, and L. Qian. The Five-Hundred Aperture Spherical Radio Telescope (fast) Project. *International Journal of Modern Physics D*, 20:989–1024, 2011. doi: 10.1142/S0218271811019335.

National Optical Astronomy Observatories. IRAF: Image Reduction and Analysis Facility. Astrophysics Source Code Library, November 1999.

H. Nilsson, G. Stenberg Wieser, E. Behar, C. S. Wedlund, E. Kallio, H. Gunell, N. J. T. Edberg, A. I. Eriksson, M. Yamauchi, C. Koenders, M. Wieser, R. Lundin, S. Barabash, K. Mandt, J. L. Burch, R. Goldstein, P. Mokashi, C. Carr, E. Cupido, P. T. Fox, K. Szego, Z. Nemeth,

A. Fedorov, J.-A. Sauvaud, H. Koskinen, I. Richter, J.-P. Lebreton, P. Henri, M. Volwerk, C. Vallat, and B. Geiger. Evolution of the ion environment of comet 67P/Churyumov-Gerasimenko. Observations between 3.6 and 2.0 AU. *A&A*, 583:A20, November 2015. doi: 10.1051/0004-6361/201526142.

M. C. Nolan, C. Magri, E. S. Howell, L. A. M. Benner, J. D. Giorgini, C. W. Hergenrother, R. S. Hudson, D. S. Lauretta, J.-L. Margot, S. J. Ostro, and D. J. Scheeres. Shape model and surface properties of the OSIRIS-REx target Asteroid (101955) Bennu from radar and lightcurve observations. *Icarus*, 226:629–640, September 2013. doi: 10.1016/j.icarus.2013.05.028.

M. C. Nolan, E. S. Howell, K. S. Noll, J. P. Emery, C. W. Hergenrother, and D. S. Lauretta. Detection of yorp spin-up for (101955) bennu. In *The 4th Workshop on Binaries in the Solar System (available on-line)*, June 2016. URL `https://www.asu.cas.cz/~binaries/contents/abstracts/pdf/abstracts_0023.pdf`.

C. Opitom, C. Snodgrass, A. Fitzsimmons, E. Jehin, J. Manfroid, G. P. Tozzi, S. Faggi, and M. Gillon. Ground-based monitoring of comet 67P/Churyumov-Gerasimenko gas activity throughout the Rosetta mission. *MNRAS*, 469:S222–S229, July 2017. doi: 10.1093/mnras/stx1591.

S. J. Ostro. *Radar Observations of Asteroids*, pages 151–168. 1989.

S. J. Ostro. *Planetary radar*, pages 773–807. Academic Press, 1999.

S. J. Ostro and R. Connelly. Convex profiles from asteroid lightcurves. *Icarus*, 57:443–463, March 1984. doi: 10.1016/0019-1035(84)90129-5.

S. J. Ostro and W. Z. Wisniewski. The shape of asteroid 1917 Cuyo. In A. W. Harris and E. Bowell, editors, *Asteroids, Comets, Meteors 1991*, pages 447–450, December 1992.

S. J. Ostro, R. Connelly, and L. Belkora. Asteroid shapes from radar echo spectra - A new theoretical approach. *Icarus*, 73:15–24, January 1988a. doi: 10.1016/0019-1035(88)90083-8.

S. J. Ostro, R. Connelly, and M. Dorogi. Convex-profile inversion of asteroid lightcurves - Theory and applications. *Icarus*, 75:30–63, July 1988b. doi: 10.1016/0019-1035(88)90126-1.

S. J. Ostro, R. S. Hudson, L. A. M. Benner, J. D. Giorgini, C. Magri, J. L. Margot, and M. C. Nolan. *Asteroid Radar Astronomy*, pages 151–168. University of Arizona Press, Tucson, 2002.

S. J. Ostro, L. A. M. Benner, M. C. Nolan, C. Magri, J. D. Giorgini, D. J. Scheeres, S. B. Broschart, M. Kaasalainen, D. Vokrouhlický, S. R. Chesley, J.-L. Margot, R. F. Jurgens, R. Rose, D. K. Yeomans, S. Suzuku, and E. M. de Jong. Radar observations of asteroid 25143 Itokawa (1998 SF36). *Meteoritics and Planetary Science*, 39:407–424, March 2004. doi: 10.1111/j.1945-5100.2004.tb00102.x.

S. J. Ostro, J.-L. Margot, L. A. M. Benner, J. D. Giorgini, D. J. Scheeres, E. G. Fahnestock, S. B. Broschart, J. Bellerose, M. C. Nolan, C. Magri, P. Pravec, P. Scheirich, R. Rose, R. F. Jurgens, E. M. De Jong, and S. Suzuki. Radar Imaging of Binary Near-Earth Asteroid (66391) 1999 KW4. *Science*, 314:1276–1280, November 2006. doi: 10.1126/science.1133622.

M. Pajola, J.-B. Vincent, C. Güttler, J.-C. Lee, I. Bertini, M. Massironi, E. Simioni, F. Marzari, L. Giacomini, A. Lucchetti, C. Barbieri, G. Cremonese, G. Naletto, A. Pommerol, M. R. El-Maarry, S. Besse, M. Küppers, F. La Forgia, M. Lazzarin, N. Thomas, A.-T. Auger,

H. Sierks, P. Lamy, R. Rodrigo, D. Koschny, H. Rickman, H. U. Keller, J. Agarwal, M. F. A'Hearn, M. A. Barucci, J.-L. Bertaux, V. Da Deppo, B. Davidsson, M. De Cecco, S. Debei, F. Ferri, S. Fornasier, M. Fulle, O. Groussin, P. J. Gutierrez, S. F. Hviid, W.-H. Ip, L. Jorda, J. Knollenberg, J.-R. Kramm, E. Kürt, L. M. Lara, Z.-Y. Lin, J. J. Lopez Moreno, S. Magrin, S. Marchi, H. Michalik, R. Moissl, S. Mottola, N. Oklay, F. Preusker, F. Scholten, and C. Tubiana. Size-frequency distribution of boulders $\geq$7 m on comet 67P/Churyumov-Gerasimenko. *A&A*, 583:A37, November 2015. doi: 10.1051/0004-6361/201525975.

M. Pajola, S. Mottola, M. Hamm, M. Fulle, B. Davidsson, C. Güttler, H. Sierks, G. Naletto, G. Arnold, H.-G. Grothues, R. Jaumann, H. Michaelis, J. P. Bibring, C. Barbieri, P. L. Lamy, R. Rodrigo, D. Koschny, H. Rickman, H. U. Keller, J. Agarwal, M. F. A'Hearn, M. A. Barucci, J. L. Bertaux, I. Bertini, S. Boudreault, G. Cremonese, V. Da Deppo, S. Debei, M. De Cecco, J. Deller, M. R. El Maarry, C. Feller, S. Fornasier, A. Gicquel, O. Groussin, P. J. Gutierrez, M. Hofmann, S. F. Hviid, W. H. Ip, L. Jorda, J. Knollenberg, J. R. Kramm, E. Kührt, M. Küppers, F. La Forgia, L. M. Lara, Z. Y. Lin, M. Lazzarin, J. J. Lopez Moreno, A. Lucchetti, F. Marzari, M. Massironi, H. Michalik, N. Oklay, A. Pommerol, F. Preusker, F. Scholten, N. Thomas, C. Tubiana, and J. B. Vincent. The Agilkia boulders/pebbles size-frequency distributions: OSIRIS and ROLIS joint observations of 67P surface. *MNRAS*, 462:S242–S252, November 2016a. doi: 10.1093/mnras/stw2720.

M. Pajola, N. Oklay, F. La Forgia, L. Giacomini, M. Massironi, I. Bertini, M. R. El-Maarry, F. Marzari, F. Preusker, F. Scholten, S. Höfner, J.-C. Lee, J.-B. Vincent, O. Groussin, G. Naletto, M. Lazzarin, C. Barbieri, H. Sierks, P. Lamy, R. Rodrigo, D. Koschny, H. Rickman, H. U. Keller, J. Agarwal, M. F. A'Hearn, M. A. Barucci, J.-L. Bertaux, G. Cremonese, V. Da Deppo, B. Davidsson, M. De Cecco, S. Debei, F. Ferri, S. Fornasier, M. Fulle, C. Güttler, P. J. Gutierrez, S. F. Hviid, W.-H. Ip, L. Jorda, J. Knollenberg, J.-R. Kramm, M. Küppers, E. Kürt, L. M. Lara, Z.-Y. Lin, J. J. Lopez Moreno, S. Magrin, H. Michalik, S. Mottola, N. Thomas, and C. Tubiana. Aswan site on comet 67P/Churyumov-Gerasimenko: Morphology, boulder evolution, and spectrophotometry. *A&A*, 592:A69, July 2016b. doi: 10.1051/0004-6361/201527865.

M. Pajola, S. Höfner, J. B. Vincent, N. Oklay, F. Scholten, F. Preusker, S. Mottola, G. Naletto, S. Fornasier, S. Lowry, C. Feller, P. H. Hasselmann, C. Güttler, C. Tubiana, H. Sierks, C. Barbieri, P. Lamy, R. Rodrigo, D. Koschny, H. Rickman, H. U. Keller, J. Agarwal, M. F. A'Hearn, M. A. Barucci, J.-L. Bertaux, I. Bertini, S. Besse, S. Boudreault, G. Cremonese, V. da Deppo, B. Davidsson, S. Debei, M. de Cecco, J. Deller, J. D. P. Deshapriya, M. R. El-Maarry, S. Ferrari, F. Ferri, M. Fulle, O. Groussin, P. Gutierrez, M. Hofmann, S. F. Hviid, W.-H. Ip, L. Jorda, J. Knollenberg, G. Kovacs, J. R. Kramm, E. Kührt, M. Küppers, L. M. Lara, Z.-Y. Lin, M. Lazzarin, A. Lucchetti, J. J. Lopez Moreno, F. Marzari, M. Massironi, H. Michalik, L. Penasa, A. Pommerol, E. Simioni, N. Thomas, I. Toth, and E. Baratti. The pristine interior of comet 67P revealed by the combined Aswan outburst and cliff collapse. *Nature Astronomy*, 1:0092, March 2017. doi: 10.1038/s41550-017-0092.

J. Piironen, C.-I. Lagerkvist, J. Torppa, M. Kaasalainen, and B. Warner. Standard Asteroid Photometric Catalogue. In *AAS/Division for Planetary Sciences Meeting Abstracts #33*, volume 33 of *Bulletin of the American Astronomical Society*, page 1562, December 2001.

M. Popescu, M. Birlan, R. Binzel, P. Vernazza, A. Barucci, D. A. Nedelcu, F. DeMeo, and M. Fulchignoni. Spectral properties of eight near-Earth asteroids. *A&A*, 535:A15, November 2011. doi: 10.1051/0004-6361/201117118.

P. Pravec and A. W. Harris. Fast and Slow Rotation of Asteroids. *Icarus*, 148:12–20, November 2000. doi: 10.1006/icar.2000.6482.

P. Pravec, D. Vokrouhlický, D. Polishook, D. J. Scheeres, A. W. Harris, A. Galád, O. Vaduvescu, F. Pozo, A. Barr, P. Longa, F. Vachier, F. Colas, D. P. Pray, J. Pollock, D. Reichart, K. Ivarsen, J. Haislip, A. Lacluyze, P. Kušnirák, T. Henych, F. Marchis, B. Macomber, S. A. Jacobson, Y. N. Krugly, A. V. Sergeev, and A. Leroy. Formation of asteroid pairs by rotational fission. *Nature*, 466:1085–1088, August 2010. doi: 10.1038/nature09315.

F. Preusker, F. Scholten, K.-D. Matz, T. Roatsch, K. Willner, S. F. Hviid, J. Knollenberg, L. Jorda, P. J. Gutiérrez, E. Kührt, S. Mottola, M. F. A'Hearn, N. Thomas, H. Sierks, C. Barbieri, P. Lamy, R. Rodrigo, D. Koschny, H. Rickman, H. U. Keller, J. Agarwal, M. A. Barucci, J.-L. Bertaux, I. Bertini, G. Cremonese, V. Da Deppo, B. Davidsson, S. Debei, M. De Cecco, S. Fornasier, M. Fulle, O. Groussin, C. Güttler, W.-H. Ip, J. R. Kramm, M. Küppers, L. M. Lara, M. Lazzarin, J. J. Lopez Moreno, F. Marzari, H. Michalik, G. Naletto, N. Oklay, C. Tubiana, and J.-B. Vincent. Shape model, reference system definition, and cartographic mapping standards for comet 67P/Churyumov-Gerasimenko - Stereo-photogrammetric analysis of Rosetta/OSIRIS image data. *A&A*, 583:A33, November 2015. doi: 10.1051/0004-6361/201526349.

S. N. Raymond and A. Izidoro. Origin of water in the inner Solar System: Planetesimals scattered inward during Jupiter and Saturn's rapid gas accretion. *Icarus*, 297:134–148, November 2017. doi: 10.1016/j.icarus.2017.06.030.

A. S. Rivkin and J. P. Emery. Detection of ice and organics on an asteroidal surface. *Nature*, 464(7293):1322–1323, Apr 2010. ISSN 0028-0836. doi: 10.1038/nature09028. URL `http://dx.doi.org/10.1038/nature09028`.

A. Rożek, S. Lowry, B. Rozitis, S. Wolters, M. Hicks, S. Duddy, A. Fitzsimmons, S. Green, C. Snodgrass, and P. Weissman. Spin-state and thermophysical analysis of the near-Earth asteroid (8567) 1996 HW1. In K. Muinonen, A. Penttilä, M. Granvik, A. Virkki, G. Fedorets, O. Wilkman, and T. Kohout, editors, *Asteroids, Comets, Meteors 2014*, July 2014.

A. Rożek, S. Lowry, and et al. Asteroid (1917) Cuyo physical modelling from optical and thermal observations. *In Preparation*, 2017.

B. Rozitis and S. F. Green. Directional characteristics of thermal-infrared beaming from atmosphereless planetary surfaces - a new thermophysical model. *MNRAS*, 415:2042–2062, August 2011. doi: 10.1111/j.1365-2966.2011.18718.x.

B. Rozitis and S. F. Green. The influence of rough surface thermal-infrared beaming on the Yarkovsky and YORP effects. *MNRAS*, 423:367–388, June 2012. doi: 10.1111/j.1365-2966.2012.20882.x.

B. Rozitis and S. F. Green. The influence of global self-heating on the Yarkovsky and YORP effects. *MNRAS*, 433:603–621, July 2013. doi: 10.1093/mnras/stt750.

B. Rozitis, E. Maclennan, and J. P. Emery. Cohesive forces prevent the rotational breakup of rubble-pile asteroid (29075) 1950 DA. *Nature*, 512:174–176, August 2014. doi: 10.1038/nature13632.

D. P. Rubincam. Radiative Spin-up and Spin-down of Small Asteroids. *Icarus*, 148:2–11, November 2000. doi: 10.1006/icar.2000.6485.

H. N. Russell. On the light variations of asteroids and satellites. *ApJ*, 24:1–18, July 1906. doi: 10.1086/141361.

T. Saiki, H. Imamura, M. Arakawa, K. Wada, Y. Takagi, M. Hayakawa, K. Shirai, H. Yano, and C. Okamoto. The Small Carry-on Impactor (SCI) and the Hayabusa2 Impact Experiment. *Space Sci. Rev.*, 208:165–186, July 2017. doi: 10.1007/s11214-016-0297-5.

D. P. Sánchez and D. J. Scheeres. DEM simulation of rotation-induced reshaping and disruption of rubble-pile asteroids. *Icarus*, 218:876–894, April 2012. doi: 10.1016/j.icarus.2012.01.014.

P. Santos-Sanz, J. L. Ortiz, N. Morales, R. Duffard, F. Pozuelos, F. Moreno, and E. Fernández-Valenzuela. Short-term variability of comet C/2012 S1 (ISON) at 4.8 AU from the Sun. *A&A*, 575:A52, March 2015. doi: 10.1051/0004-6361/201425265.

D. J. Scheeres, E. G. Fahnestock, S. J. Ostro, J.-L. Margot, L. A. M. Benner, S. B. Broschart, J. Bellerose, J. D. Giorgini, M. C. Nolan, C. Magri, P. Pravec, P. Scheirich, R. Rose, R. F. Jurgens, E. M. De Jong, and S. Suzuki. Dynamical Configuration of Binary Near-Earth Asteroid (66391) 1999 KW4. *Science*, 314:1280–1283, November 2006. doi: 10.1126/science.1133599.

D. J. Scheeres, D. Britt, B. Carry, and K. A. Holsapple. *Asteroid Interiors and Morphology*, pages 745–766. 2015. doi: 10.2458/azu_uapress_9780816532131-ch038.

L. D. Schmadel. *(1917) Cuyo*, pages 154–154. Springer Berlin Heidelberg, Berlin, Heidelberg, 2007. ISBN 978-3-540-29925-7. doi: 10.1007/978-3-540-29925-7_1918. URL `http://dx.doi.org/10.1007/978-3-540-29925-7_1918`.

M. I. Schmitt, C. Tubiana, C. Güttler, H. Sierks, J.-B. Vincent, M. R. El-Maarry, D. Bodewits, S. Mottola, S. Fornasier, M. Hofmann, C. Barbieri, P. L. Lamy, R. Rodrigo, D. Koschny, H. Rickman, M. F. A'Hearn, J. Agarwal, M. A. Barucci, J.-L. Bertaux, I. Bertini, G. Cremonese, V. Da Deppo, B. Davidsson, S. Debei, M. De Cecco, J. Deller, M. Fulle, A. Gicquel, O. Groussin, P. J. Gutiérrez, S. F. Hviid, W.-H. Ip, L. Jorda, H. U. Keller, J. Knollenberg, J. R. Kramm, E. Kührt, M. Küppers, L. M. Lara, M. Lazzarin, J. J. López-Moreno, F. Marzari, G. Naletto, N. Oklay, M. Pajola, D. Prasanna, X. Shi, F. Scholten, I. Toth, and N. Thomas. Long-term monitoring of comet 67P/Churyumov-Gerasimenko's jets with OSIRIS onboard Rosetta. *MNRAS*, 469:S380–S385, July 2017. doi: 10.1093/mnras/stx1780.

R. Schödel, T. Ott, R. Genzel, R. Hofmann, M. Lehnert, A. Eckart, N. Mouawad, T. Alexander, M. J. Reid, R. Lenzen, M. Hartung, F. Lacombe, D. Rouan, E. Gendron, G. Rousset, A.-M. Lagrange, W. Brandner, N. Ageorges, C. Lidman, A. F. M. Moorwood, J. Spyromilio, N. Hubin, and K. M. Menten. A star in a 15.2-year orbit around the supermassive black hole at the centre of the Milky Way. *Nature*, 419:694–696, October 2002. doi: 10.1038/nature01121.

P. Schulte, L. Alegret, I. Arenillas, J. A. Arz, P. J. Barton, P. R. Bown, T. J. Bralower, G. L. Christeson, P. Claeys, C. S. Cockell, G. S. Collins, A. Deutsch, T. J. Goldin, K. Goto, J. M. Grajales-Nishimura, R. A. F. Grieve, S. P. S. Gulick, K. R. Johnson, W. Kiessling, C. Koeberl, D. A. Kring, K. G. MacLeod, T. Matsui, J. Melosh, A. Montanari, J. V. Morgan, C. R. Neal, D. J. Nichols, R. D. Norris, E. Pierazzo, G. Ravizza, M. Rebolledo-Vieyra, W. U. Reimold, E. Robin, T. Salge, R. P. Speijer, A. R. Sweet, J. Urrutia-Fucugauchi, V. Vajda, M. T. Whalen, and P. S. Willumsen. The Chicxulub Asteroid Impact and Mass Extinction at the Cretaceous-Paleogene Boundary. *Science*, 327:1214, March 2010. doi: 10.1126/science.1177265.

D. W. G. Sears. The Explored Asteroids: Science and Exploration in the Space Age. *Space Sci. Rev.*, 194:139–235, November 2015. doi: 10.1007/s11214-015-0202-7.

M. Sekiya and A.A. Shimoda. An iterative method for obtaining a nonlinear solution for the temperature distribution of a rotating spherical body revolving in a circular orbit around a star. *Planetary and Space Science*, 84(Supplement C):112 – 121, 2013. ISSN 0032-0633. doi: https://doi.org/10.1016/j.pss.2013.05.015. URL http://www.sciencedirect.com/science/article/pii/S0032063313001323.

M. Sekiya and A.A. Shimoda. An iterative method for obtaining a nonlinear solution for the temperature distribution of a rotating spherical body revolving in an eccentric orbit. *Planetary and Space Science*, 97(Supplement C):23 – 33, 2014. ISSN 0032-0633. doi: https://doi.org/10.1016/j.pss.2014.04.006. URL http://www.sciencedirect.com/science/article/pii/S0032063314001032.

E. M. Shoemaker and E. F. Helin. Earth-approaching asteroids as targets for exploration. In D. Morrison and W. C. Wells, editors, *NASA Conference Publication*, volume 2053 of *NASA Conference Publication*, 1978.

H. Sierks, C. Barbieri, P. L. Lamy, R. Rodrigo, D. Koschny, H. Rickman, H. U. Keller, J. Agarwal, M. F. A'Hearn, F. Angrilli, A.-T. Auger, M. A. Barucci, J.-L. Bertaux, I. Bertini, S. Besse, D. Bodewits, C. Capanna, G. Cremonese, V. Da Deppo, B. Davidsson, S. Debei, M. De Cecco, F. Ferri, S. Fornasier, M. Fulle, R. Gaskell, L. Giacomini, O. Groussin, P. Gutierrez-Marques, P. J. Gutiérrez, C. Güttler, N. Hoekzema, S. F. Hviid, W.-H. Ip, L. Jorda, J. Knollenberg, G. Kovacs, J. R. Kramm, E. Kührt, M. Küppers, F. La Forgia, L. M. Lara, M. Lazzarin, C. Leyrat, J. J. Lopez Moreno, S. Magrin, S. Marchi, F. Marzari, M. Massironi, H. Michalik, R. Moissl, S. Mottola, G. Naletto, N. Oklay, M. Pajola, M. Pertile, F. Preusker, L. Sabau, F. Scholten, C. Snodgrass, N. Thomas, C. Tubiana, J.-B. Vincent, K.-P. Wenzel, M. Zaccariotto, and M. Pätzold. On the nucleus structure and activity of comet 67P/Churyumov-Gerasimenko. *Science*, 347(1):aaa1044, January 2015. doi: 10.1126/science.aaa1044.

M. A. Slade, L. A. M. Benner, and A. Silva. Goldstone Solar System Radar Observatory: Earth-based planetary mission support and unique science results. In *IEEE*, volume 99, pages 757–769, 2011.

S. M. Slivan. Spin vector alignment of Koronis family asteroids. *Nature*, 419:49–51, September 2002.

S. M. Slivan, R. P. Binzel, L. D. Crespo da Silva, M. Kaasalainen, M. M. Lyndaker, and M. Krčo. Spin vectors in the Koronis family: comprehensive results from two independent analyses of 213 rotation lightcurves. *Icarus*, 162:285–307, April 2003. doi: 10.1016/S0019-1035(03)00029-0.

S. J. Smartt, T.-W. Chen, A. Jerkstrand, M. Coughlin, E. Kankare, S. A. Sim, M. Fraser, C. Inserra, K. Maguire, K. C. Chambers, and et al. A kilonova as the electromagnetic counterpart to a gravitational-wave source. *Nature*, Oct 2017. ISSN 1476-4687. doi: 10.1038/nature24303. URL http://dx.doi.org/10.1038/nature24303.

C. Snodgrass and B. Carry. Automatic Removal of Fringes from EFOSC Images. *The Messenger*, 152:14–16, June 2013.

C. Snodgrass, E. Jehin, J. Manfroid, C. Opitom, A. Fitzsimmons, G. P. Tozzi, S. Faggi, B. Yang, M. M. Knight, B. C. Conn, T. Lister, O. Hainaut, D. M. Bramich, S. C. Lowry, A. Rozek, C. Tubiana, and A. Guilbert-Lepoutre. Distant activity of 67P/Churyumov-Gerasimenko in 2014: Ground-based results during the Rosetta pre-landing phase. *A&A*, 588:A80, April 2016. doi: 10.1051/0004-6361/201527834.

T. S. Statler. Extreme sensitivity of the yorp effect to small-scale topography. *Icarus*, 202: 502–513, August 2009. doi: 10.1016/j.icarus.2009.03.003.

G. H. Stokes, J. B. Evans, H. E. M. Viggh, F. C. Shelly, and E. C. Pearce. Lincoln Near-Earth Asteroid Program (LINEAR). *Icarus*, 148:21–28, November 2000. doi: 10.1006/icar.2000.6493.

D. Sunday. Geometry algorithms, 2012. URL `http://geomalgorithms.com/`.

P. Sánchez and D. J. Scheeres. Disruption patterns of rotating self-gravitating aggregates: A survey on angle of friction and tensile strength. *Icarus*, 271(Supplement C):453 – 471, 2016. ISSN 0019-1035. doi: https://doi.org/10.1016/j.icarus.2016.01.016. URL `http://www.sciencedirect.com/science/article/pii/S0019103516000208`.

M. Tarenghi and R. N. Wilson. The ESO NTT (New Technology Telescope) - The first active optics telescope. In F. J. Roddier, editor, *Active telescope systems*, volume 1114 of *Proc. SPIE*, pages 302–313, September 1989. doi: 10.1117/12.960835.

P. A. Taylor, J.-L. Margot, D. Vokrouhlický, D. J. Scheeres, P. Pravec, S. C. Lowry, A. Fitzsimmons, M. C. Nolan, S. J. Ostro, L. A. M. Benner, J. D. Giorgini, and C. Magri. Spin Rate of Asteroid (54509) 2000 PH5 Increasing Due to the YORP Effect. *Science*, 316:274–, April 2007. doi: 10.1126/science.1139038.

C. A. Thomas, J. P. Emery, D. E. Trilling, M. Delbó, J. L. Hora, and M. Mueller. Physical characterization of Warm Spitzer-observed near-Earth objects. *Icarus*, 228:217–246, January 2014. doi: 10.1016/j.icarus.2013.10.004.

N. Thomas, H. Sierks, C. Barbieri, P. L. Lamy, R. Rodrigo, H. Rickman, D. Koschny, H. U. Keller, J. Agarwal, M. F. A'Hearn, F. Angrilli, A.-T. Auger, M. A. Barucci, J.-L. Bertaux, I. Bertini, S. Besse, D. Bodewits, G. Cremonese, V. Da Deppo, B. Davidsson, M. De Cecco, S. Debei, M. R. El-Maarry, F. Ferri, S. Fornasier, M. Fulle, L. Giacomini, O. Groussin, P. J. Gutierrez, C. Güttler, S. F. Hviid, W.-H. Ip, L. Jorda, J. Knollenberg, J.-R. Kramm, E. Kührt, M. Küppers, F. La Forgia, L. M. Lara, M. Lazzarin, J. J. L. Moreno, S. Magrin, S. Marchi, F. Marzari, M. Massironi, H. Michalik, R. Moissl, S. Mottola, G. Naletto, N. Oklay, M. Pajola, A. Pommerol, F. Preusker, L. Sabau, F. Scholten, C. Snodgrass, C. Tubiana, J.-B. Vincent, and K.-P. Wenzel. The morphological diversity of comet 67P/Churyumov-Gerasimenko. *Science*, 347(6220), 2015. ISSN 0036-8075. doi: 10.1126/science.aaa0440. URL `http://science.sciencemag.org/content/347/6220/aaa0440`.

P. C. Thomas, J. W. Parker, L. A. McFadden, C. T. Russell, S. A. Stern, M. V. Sykes, and E. F. Young. Differentiation of the asteroid Ceres as revealed by its shape. *Nature*, 437:224–226, September 2005. doi: 10.1038/nature03938.

D. Tody. The IRAF Data Reduction and Analysis System. In D. L. Crawford, editor, *Instrumentation in astronomy VI*, volume 627 of *Proc. SPIE*, page 733, January 1986. doi: 10.1117/12.968154.

D. Tody. IRAF in the Nineties. In R. J. Hanisch, R. J. V. Brissenden, and J. Barnes, editors, *Astronomical Data Analysis Software and Systems II*, volume 52 of *Astronomical Society of the Pacific Conference Series*, page 173, January 1993.

D. E. Trilling, M. Mueller, J. L. Hora, A. W. Harris, B. Bhattacharya, W. F. Bottke, S. Chesley, M. Delbo, J. P. Emery, G. Fazio, A. Mainzer, B. Penprase, H. A. Smith, T. B. Spahr, J. A. Stansberry, and C. A. Thomas. Exploreneos. i. description and first results from the warm spitzer near-earth object survey. *AJ*, 140:770–784, September 2010. doi: 10.1088/0004-6256/140/3/770.

K. Tsiganis, R. Gomes, A. Morbidelli, and H. F. Levison. Origin of the orbital architecture of the giant planets of the Solar System. *Nature*, 435:459–461, May 2005. doi: 10.1038/nature03539.

C. Tubiana, L. Barrera, M. Drahus, and H. Boehnhardt. Comet 67P/Churyumov-Gerasimenko at a large heliocentric distance. *A&A*, 490:377–386, October 2008. doi: 10.1051/0004-6361:20078792.

C. Tubiana, H. Böhnhardt, J. Agarwal, M. Drahus, L. Barrera, and J. L. Ortiz. 67P/Churyumov-Gerasimenko at large heliocentric distance. *A&A*, 527:A113, March 2011. doi: 10.1051/0004-6361/201016027.

C. Tubiana, C. Snodgrass, I. Bertini, S. Mottola, J.-B. Vincent, L. Lara, S. Fornasier, J. Knollenberg, N. Thomas, M. Fulle, J. Agarwal, D. Bodewits, F. Ferri, C. Güttler, P. J. Gutierrez, F. La Forgia, S. Lowry, S. Magrin, N. Oklay, M. Pajola, R. Rodrigo, H. Sierks, M. F. A'Hearn, F. Angrilli, C. Barbieri, M. A. Barucci, J.-L. Bertaux, G. Cremonese, V. Da Deppo, B. Davidsson, M. De Cecco, S. Debei, O. Groussin, S. F. Hviid, W. Ip, L. Jorda, H. U. Keller, D. Koschny, R. Kramm, E. Kührt, M. Küppers, M. Lazzarin, P. L. Lamy, J. J. Lopez Moreno, F. Marzari, H. Michalik, G. Naletto, H. Rickman, L. Sabau, and K.-P. Wenzel. 67P/Churyumov-Gerasimenko: Activity between March and June 2014 as observed from Rosetta/OSIRIS. *A&A*, 573:A62, January 2015. doi: 10.1051/0004-6361/201424735.

J. Ďurech, V. Sidorin, and M. Kaasalainen. DAMIT: a database of asteroid models. *A&A*, 513:A46, April 2010. doi: 10.1051/0004-6361/200912693.

J. Ďurech, B. Carry, M. Delbo, M. Kaasalainen, and M. Viikinkoski. *Asteroid Models from Multiple Data Sources*, pages 183–202. 2015. doi: 10.2458/azu_uapress_9780816532131-ch010.

J. Ďurech, D. Vokrouhlicky, P. Pravec, J. Hanus, P. Kusnirak, K. Hornoch, A. Galad, and G. Masi. Detection of the YORP effect in asteroid (161989) Cacus. In *AAS/Division for Planetary Sciences Meeting Abstracts*, volume 48 of *AAS/Division for Planetary Sciences Meeting Abstracts*, page 504.02, October 2016.

F. P. Velichko, D. F. Lupishko, and V. G. Shevchenko. 1917 Cuyo - One More Asteroid with Fast Rotation. *Astronomicheskij Tsirkulyar*, 1541:35, December 1989.

D. Veras, S. Eggl, and B. T. Gänsicke. Sublimation-induced orbital perturbations of extrasolar active asteroids and comets: application to white dwarf systems. *MNRAS*, 452:1945–1957, September 2015. doi: 10.1093/mnras/stv1417.

P. Vereš, R. Jedicke, A. Fitzsimmons, L. Denneau, M. Granvik, B. Bolin, S. Chastel, R. J. Wainscoat, W. S. Burgett, K. C. Chambers, H. Flewelling, N. Kaiser, E. A. Magnier, J. S. Morgan, P. A. Price, J. L. Tonry, and C. Waters. Absolute magnitudes and slope parameters for 250,000 asteroids observed by Pan-STARRS PS1 - Preliminary results. *Icarus*, 261:34–47, November 2015. doi: 10.1016/j.icarus.2015.08.007.

M. Viikinkoski, M. Kaasalainen, and J. Durech. ADAM: a general method for using various data types in asteroid reconstruction. *A&A*, 576:A8, April 2015. doi: 10.1051/0004-6361/201425259.

J.-B. Vincent, D. Bodewits, S. Besse, H. Sierks, C. Barbieri, P. Lamy, R. Rodrigo, D. Koschny, H. Rickman, H. U. Keller, J. Agarwal, M. F. A'Hearn, A.-T. Auger, M. A. Barucci, J.-L. Bertaux, I. Bertini, C. Capanna, G. Cremonese, V. da Deppo, B. Davidsson, S. Debei, M. de Cecco, M. R. El-Maarry, F. Ferri, S. Fornasier, M. Fulle, R. Gaskell, L. Giacomini, O. Groussin, A. Guilbert-Lepoutre, P. Gutierrez-Marques, P. J. Gutiérrez, C. Güttler, N. Hoekzema, S. Höfner, S. F. Hviid, W.-H. Ip, L. Jorda, J. Knollenberg, G. Kovacs,

R. Kramm, E. Kührt, M. Küppers, F. La Forgia, L. M. Lara, M. Lazzarin, V. Lee, C. Leyrat, Z.-Y. Lin, J. J. Lopez Moreno, S. Lowry, S. Magrin, L. Maquet, S. Marchi, F. Marzari, M. Massironi, H. Michalik, R. Moissl, S. Mottola, G. Naletto, N. Oklay, M. Pajola, F. Preusker, F. Scholten, N. Thomas, I. Toth, and C. Tubiana. Large heterogeneities in comet 67P as revealed by active pits from sinkhole collapse. *Nature*, 523(7558):63–66, July 2015. ISSN 0028-0836. doi: 10.1038/nature14564.

D. Vokrouhlicky. Diurnal Yarkovsky effect as a source of mobility of meter-sized asteroidal fragments. I. Linear theory. *A&A*, 335:1093–1100, July 1998.

D. Vokrouhlicky and W. F. Bottke. Yarkovsky and YORP effects. *Scholarpedia*, 7(5):10599, 2012. doi: 10.4249/scholarpedia.10599. revision #122352.

D. Vokrouhlický and P. Farinella. Efficient delivery of meteorites to the Earth from a wide range of asteroid parent bodies. *Nature*, 407:606–608, October 2000. doi: 10.1038/35036528.

D. Vokrouhlický and D. Čapek. YORP-Induced Long-Term Evolution of the Spin State of Small Asteroids and Meteoroids: Rubincam's Approximation. *Icarus*, 159:449–467, October 2002. doi: 10.1006/icar.2002.6918.

D. Vokrouhlický, D. Nesvorný, and W. F. Bottke. The vector alignments of asteroid spins by thermal torques. *Nature*, 425:147–151, September 2003.

D. Vokrouhlický, M. Brož, W. F. Bottke, D. Nesvorný, and A. Morbidelli. Yarkovsky/YORP chronology of asteroid families. *Icarus*, 182:118–142, May 2006a. doi: 10.1016/j.icarus.2005.12.010.

D. Vokrouhlický, D. Nesvorný, and W. F. Bottke. Secular spin dynamics of inner main-belt asteroids. *Icarus*, 184:1–28, September 2006b. doi: 10.1016/j.icarus.2006.04.007.

D. Vokrouhlický, S. Breiter, D. Nesvorný, and W. F. Bottke. Generalized YORP evolution: Onset of tumbling and new asymptotic states. *Icarus*, 191:636–650, November 2007. doi: 10.1016/j.icarus.2007.06.002.

D. Vokrouhlický, W. F. Bottke, S. R. Chesley, D. J. Scheeres, and T. S. Statler. *The Yarkovsky and YORP Effects*, pages 509–531. 2015a. doi: 10.2458/azu_uapress_9780816532131-ch027.

D. Vokrouhlický, D. Farnocchia, D. Čapek, S. R. Chesley, P. Pravec, P. Scheirich, and T. G. Müller. The Yarkovsky effect for 99942 Apophis. *Icarus*, 252:277–283, May 2015b. doi: 10.1016/j.icarus.2015.01.011.

D. Vokrouhlický, A. Milani, and S.R. Chesley. Yarkovsky effect on small near-earth asteroids: Mathematical formulation and examples. *Icarus*, 148(1):118 – 138, 2000. ISSN 0019-1035. doi: http://dx.doi.org/10.1006/icar.2000.6469. URL `http://www.sciencedirect.com/science/article/pii/S0019103500964698`.

J. V. Wall. Practical Statistics for Astronomers - II. Correlation, Data-modelling and Sample Comparison. *QJRAS*, 37:519, December 1996.

K. J. Walsh, D. C. Richardson, and P. Michel. Rotational breakup as the origin of small binary asteroids. *Nature*, 454:188–191, July 2008. doi: 10.1038/nature07078.

K. J. Walsh, A. Morbidelli, S. N. Raymond, D. P. O'Brien, and A. M. Mandell. A low mass for Mars from Jupiter's early gas-driven migration. *Nature*, 475:206–209, July 2011. doi: 10.1038/nature10201.

K. J. Walsh, D. C. Richardson, and P. Michel. Spin-up of rubble-pile asteroids: Disruption, satellite formation, and equilibrium shapes. *Icarus*, 220:514–529, August 2012. doi: 10.1016/j.icarus.2012.04.029.

B. D. Warner. Near-Earth Asteroid Lightcurve Analysis at CS3-Palmer Divide Station: 2014 January-March. *Minor Planet Bulletin*, 41:157–168, July 2014a.

B. D. Warner. Near-Earth Asteroid Lightcurve Analysis at CS3-Palmer Divide Station: 2014 March-June. *Minor Planet Bulletin*, 41:213–224, October 2014b.

B. D. Warner. Near-Earth Asteroid Lightcurve Analysis at CS3-Palmer Divide Station: 2014 June-October. *Minor Planet Bulletin*, 42:41–53, January 2015a.

B. D. Warner. Near-Earth Asteroid Lightcurve Analysis at CS3-Palmer Divide Station: 2015 January - March. *Minor Planet Bulletin*, 42:172–183, July 2015b.

B. D. Warner, A. W. Harris, and P. Pravec. The asteroid lightcurve database. *Icarus*, 202:134–146, July 2009. doi: 10.1016/j.icarus.2009.02.003.

O. Wilkman and K. Muinonen. Asteroid lightcurve phase shift from rough-surface shadowing. *Meteoritics and Planetary Science*, 49:1–7, January 2014. doi: 10.1111/maps.12061.

W. Z. Wisniewski, T. M. Michałowski, A. W. Harris, and R. S. McMillan. Photometric Observations of 125 Asteroids. *Icarus*, 126:395–449, April 1997. doi: 10.1006/icar.1996.5665.

Appendix A

Supplementary figures and tables

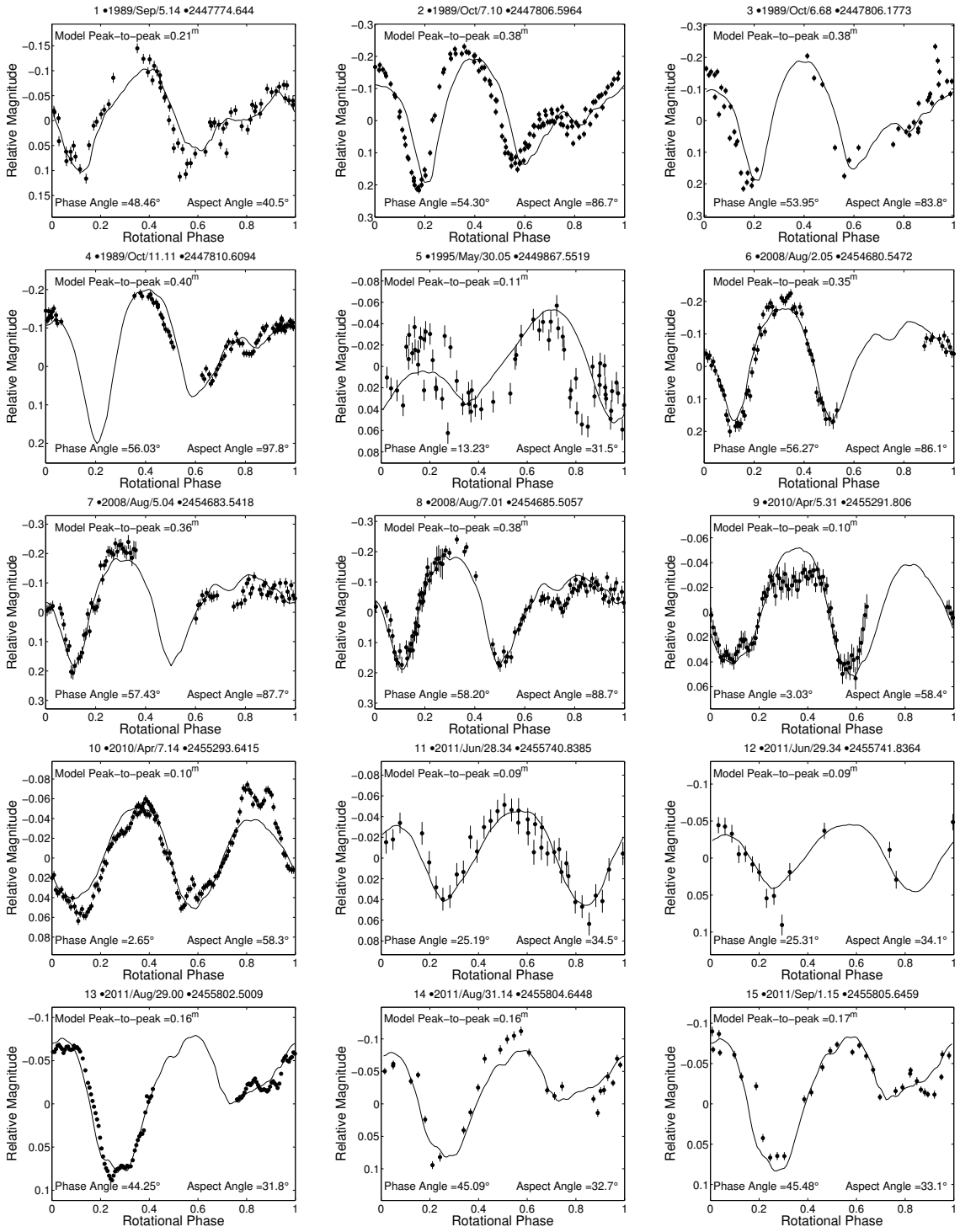

Figure A.1: Lightcurve fits of model A of asteroid (1917) Cuyo to all available lightcurves using the T_0 and P_0 developed with the convex model summarised in Table 4.3. The lightcurves are labelled chronologically and the numerical IDs match those in Table 4.1 as well as Table 4.2. One lightcurve has been usually gathered per night, but lightcurves 1,2,4,5, and 28 are composites of multiple observing nights.

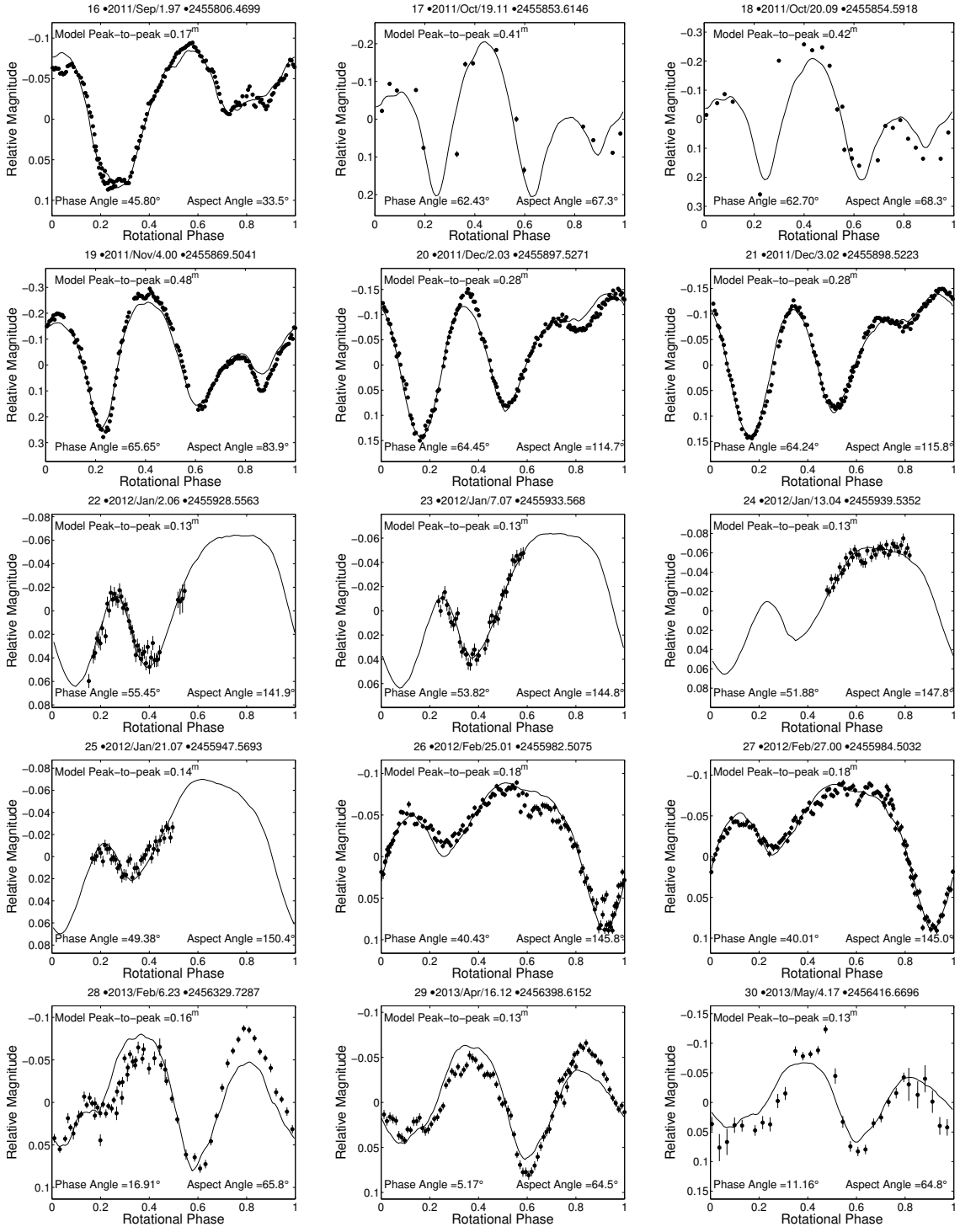

Figure A.1: Continued from page 183

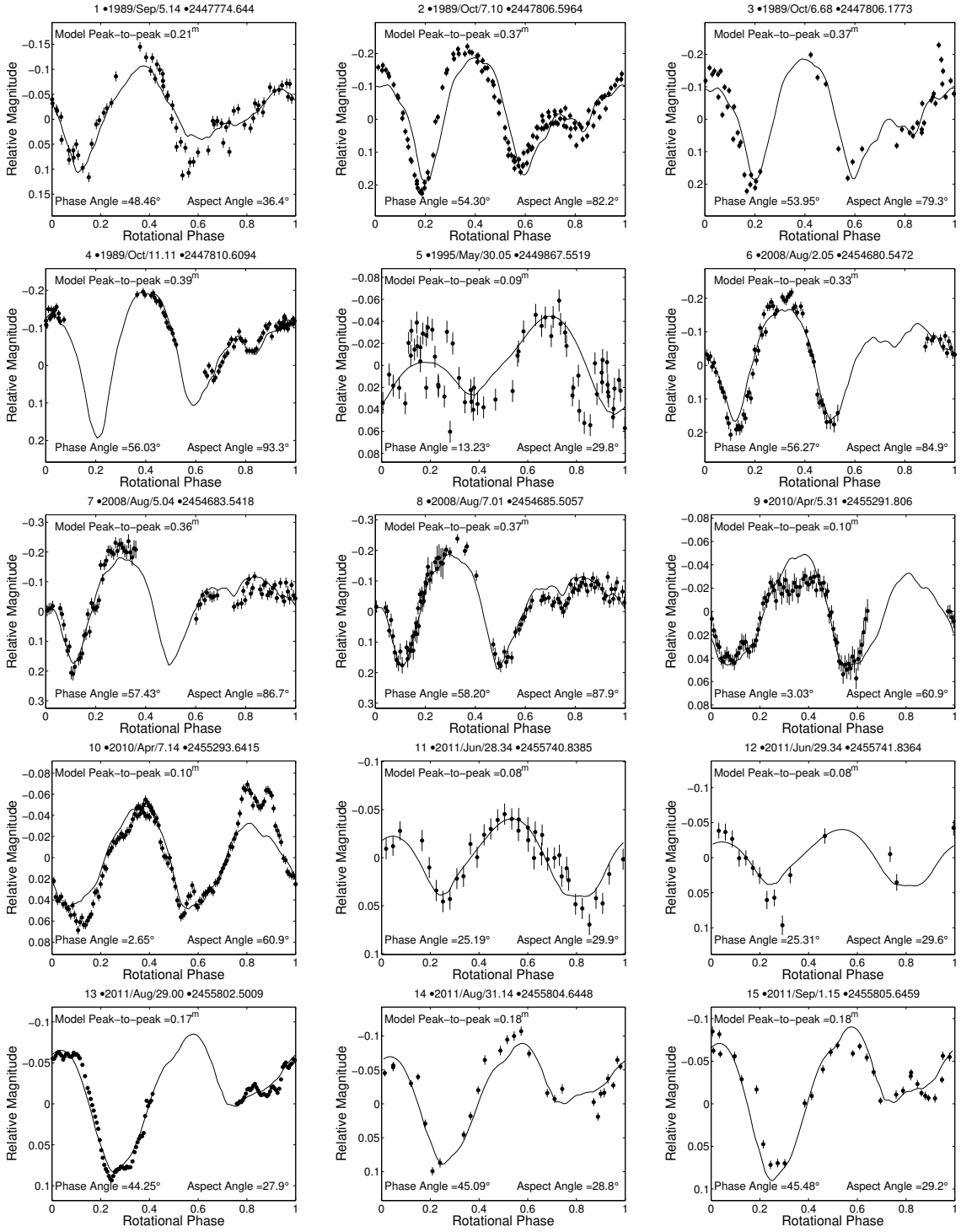

Figure A.2: Lightcurve fits of model B of asteroid (1917) Cuyo to all available lightcurves using the T_0 and P_0 developed with the convex model summarised in Table 4.3 (see description of fig. A.1).

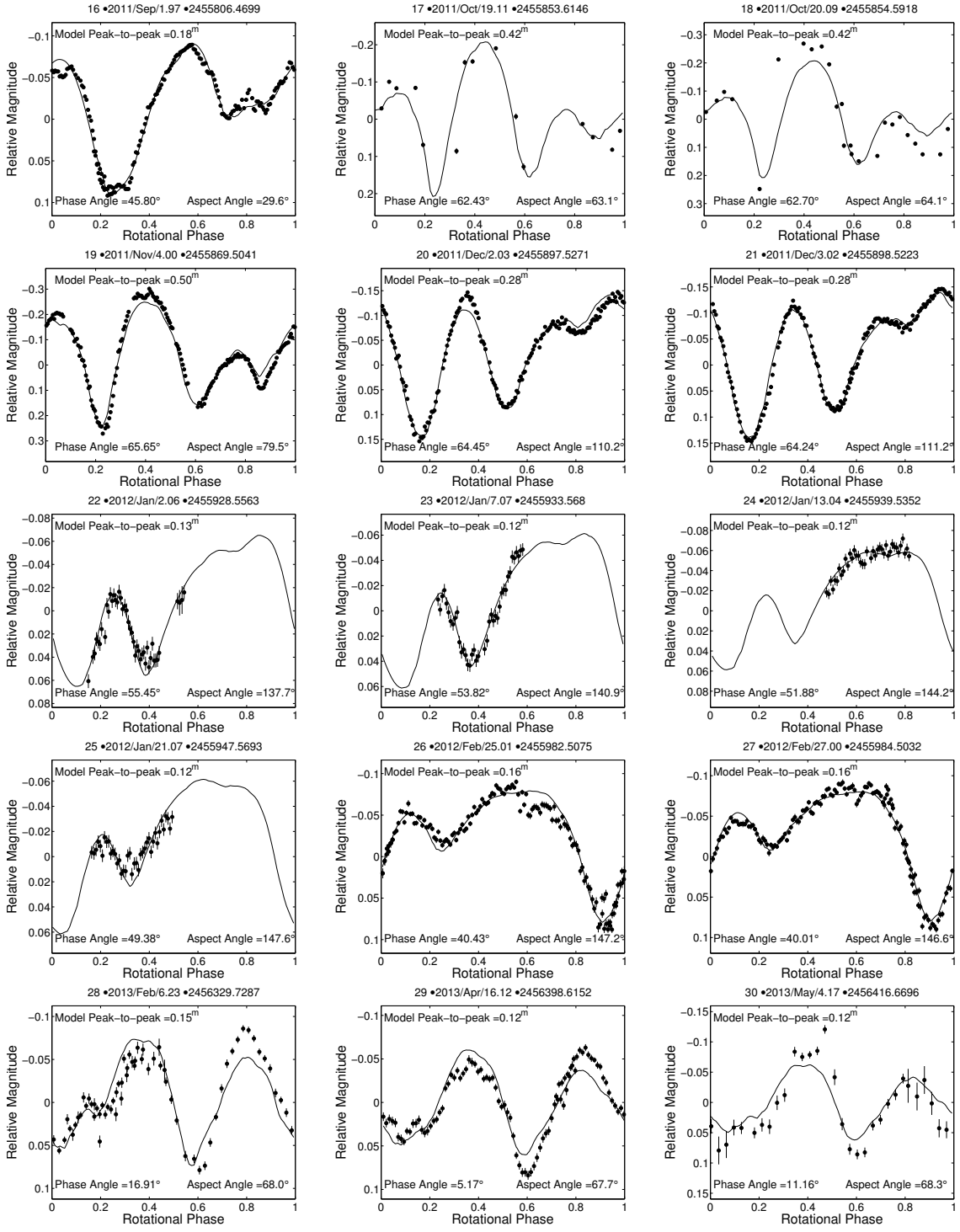

Figure A.2: Continued from page 185

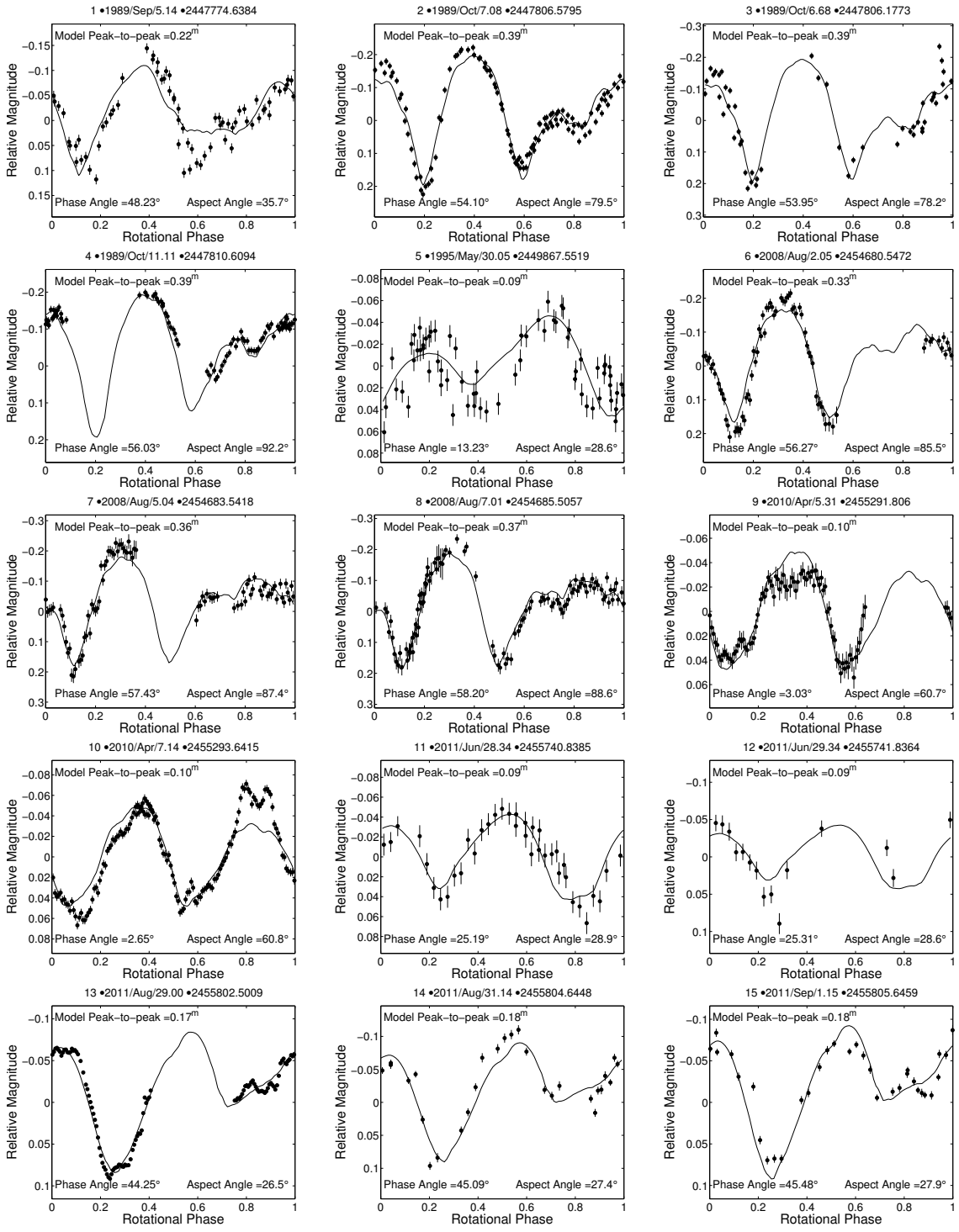

Figure A.3: Lightcurve fits of model A of asteroid (1917) Cuyo to all available lightcurves using the T_1 and P_1 developed with the convex model summarised in Table 4.3. The lightcurves are labelled chronologically and the numerical IDs match those in Table 4.1 as well as Table 4.2. One lightcurve has been usually gathered per night, but lightcurves 1,2,4,5, and 28 are composites of multiple observing nights.

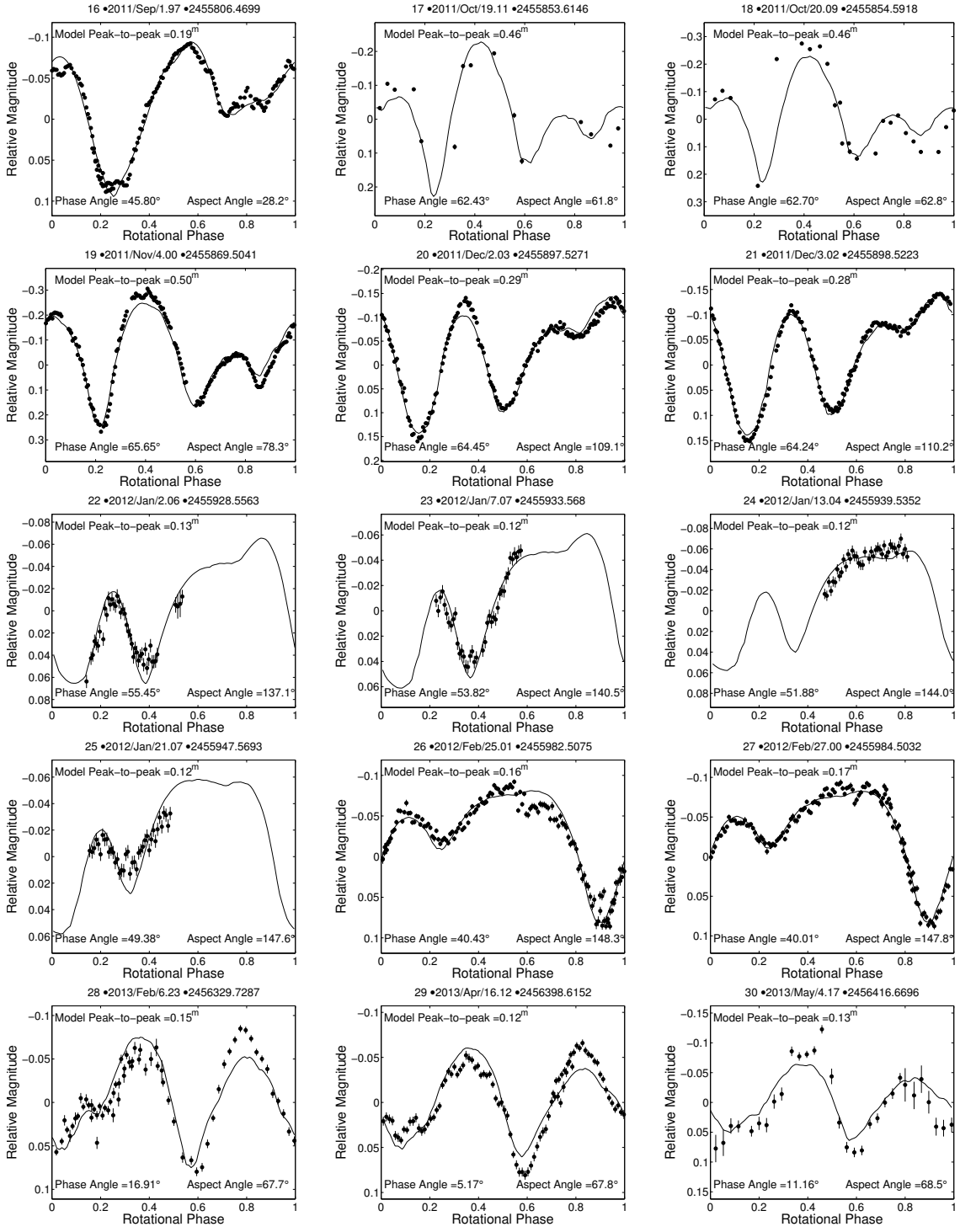

Figure A.3: Continued from page 187

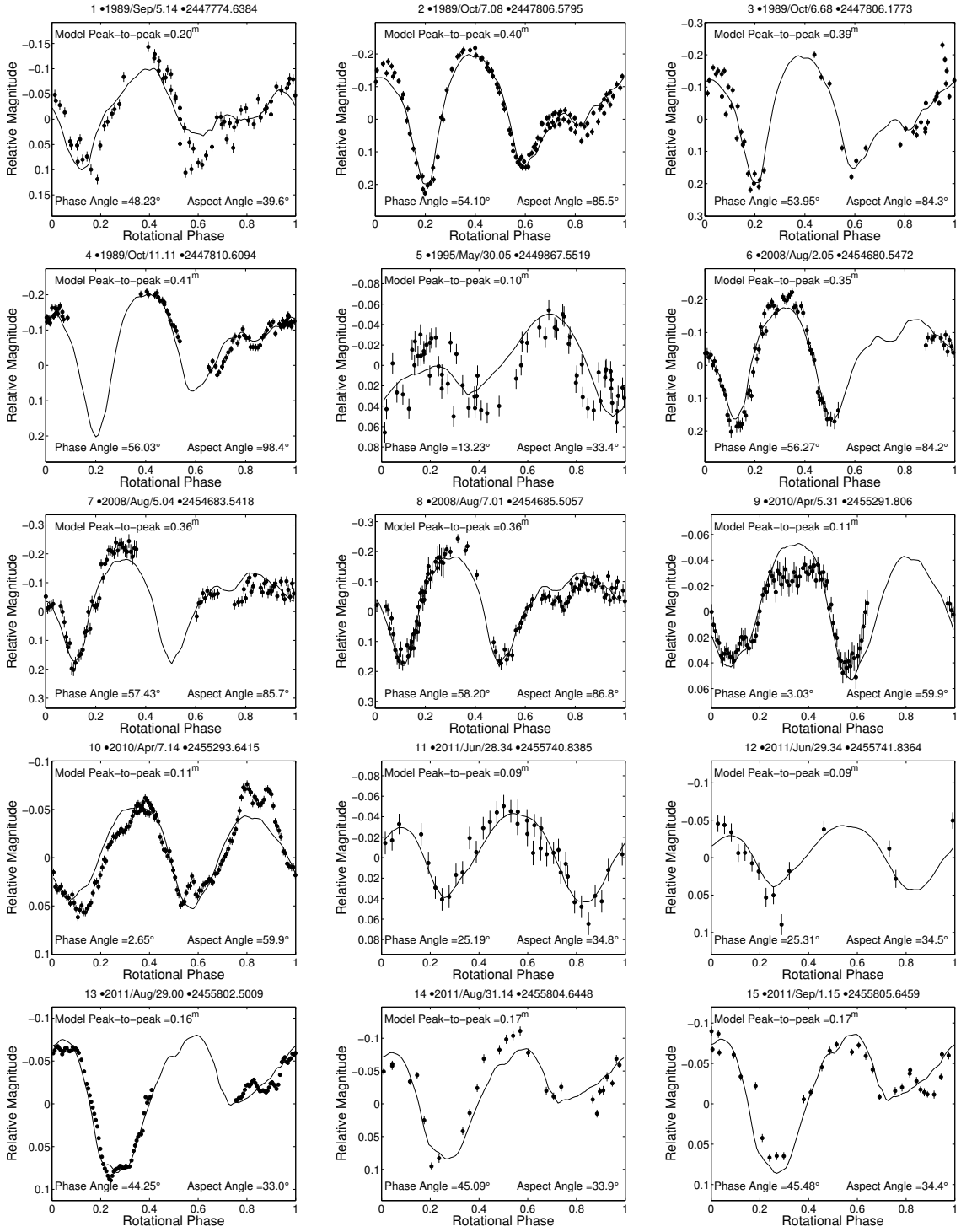

Figure A.4: Lightcurve fits of model B of asteroid (1917) Cuyo to all available lightcurves using the T_1 and P_1 developed with the convex model summarised in Table 4.3 (see description of fig. A.3).

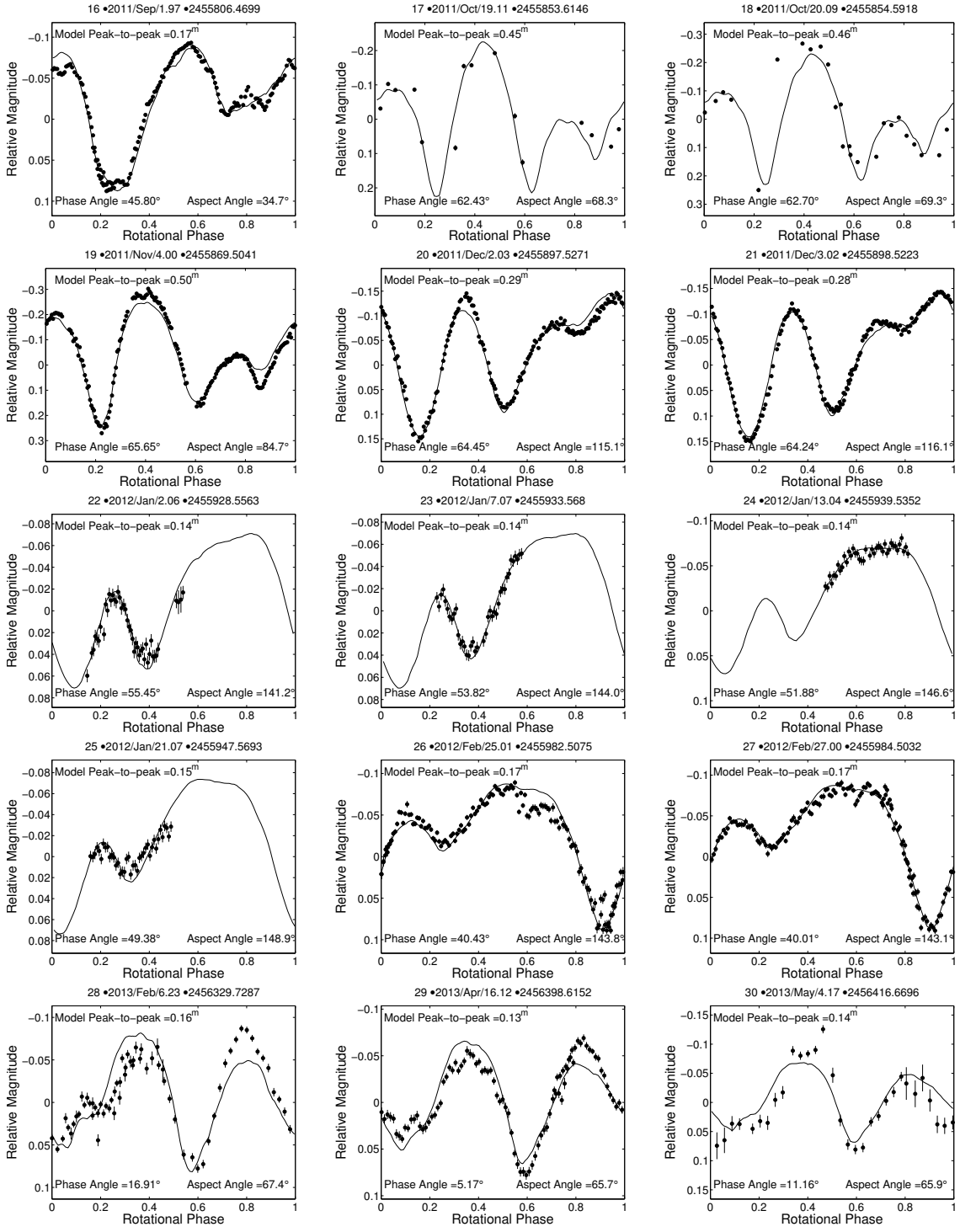

Figure A.4: Continued from page 189

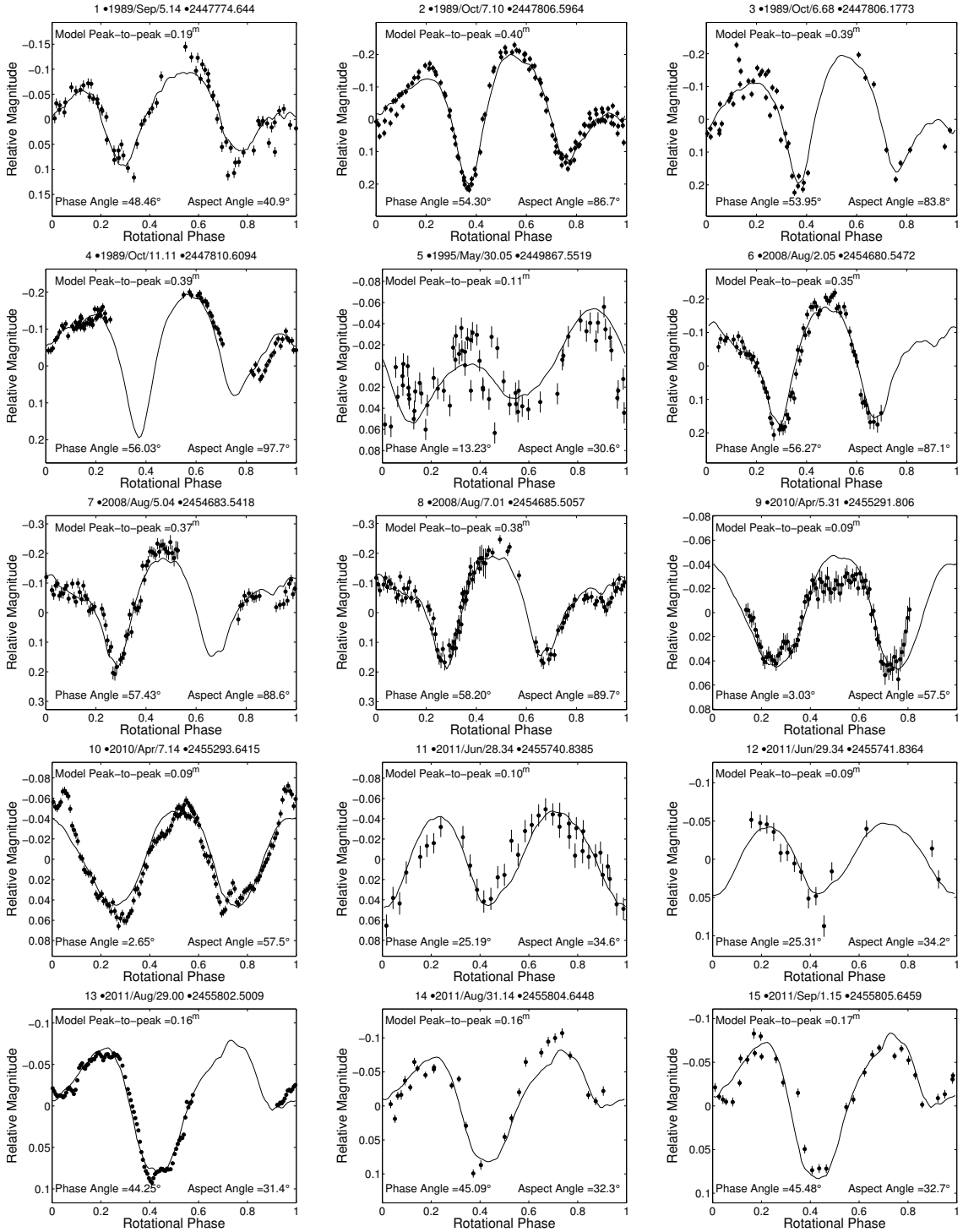

Figure A.5: Lightcurve fits of model C of asteroid (1917) Cuyo to all available lightcurves using the T_0 and P_0 developed with the convex model summarised in Table 4.3 (see description of fig. A.1).

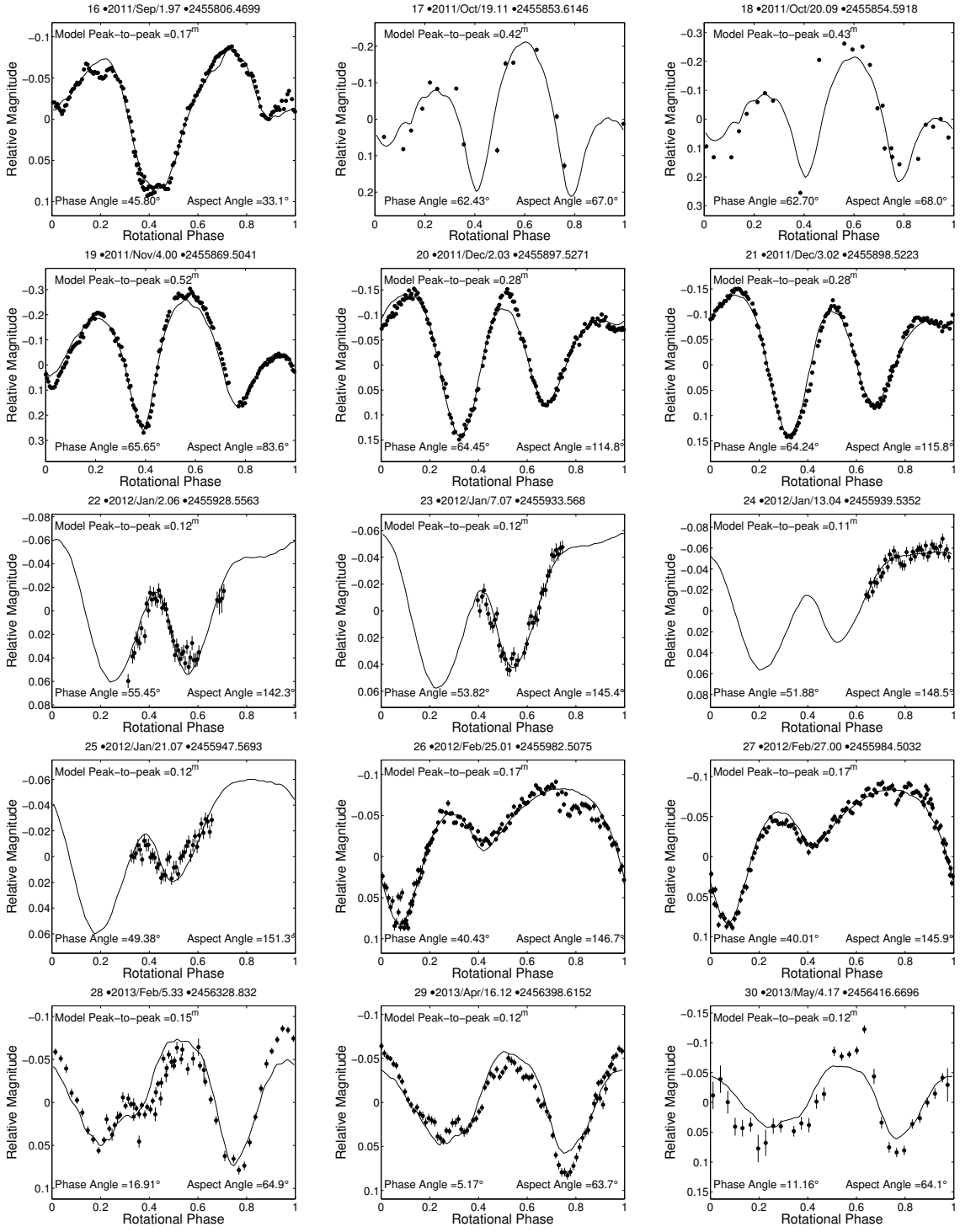

Figure A.5: Continued from page 191

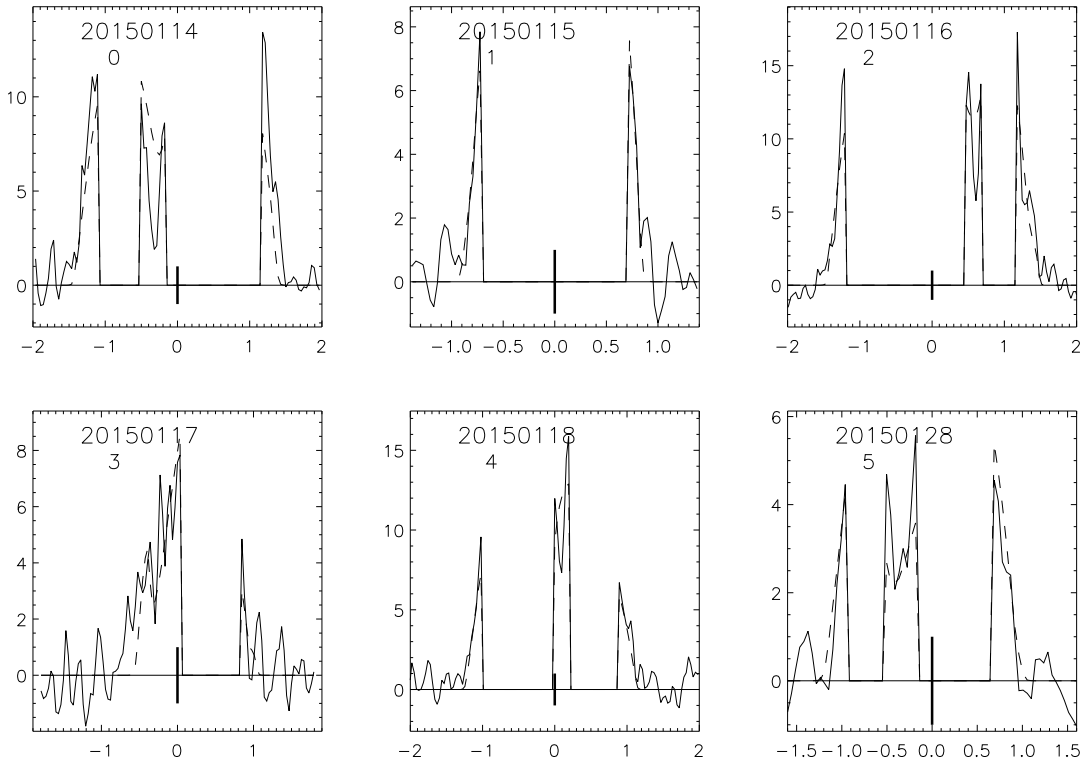

(a) Arecibo 2015, masked *cw* spectra (as used in the modelling procedure)

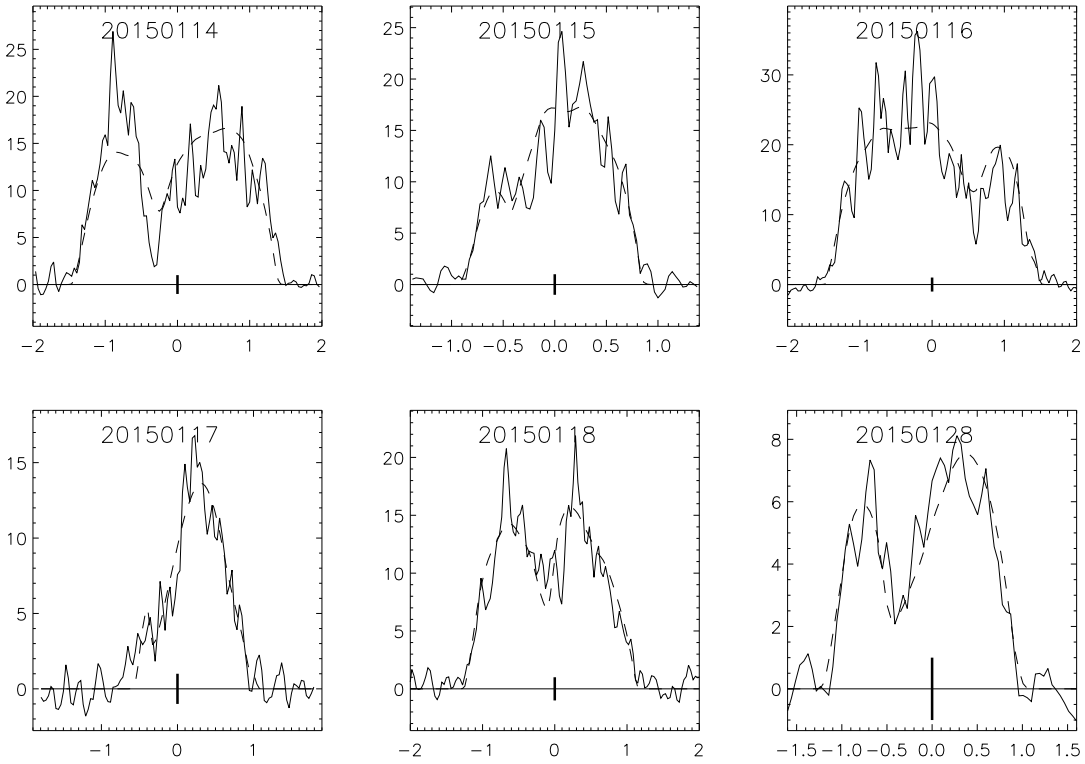

(b) Arecibo 2015, full *cw* spectra (illustration only)

Figure A.6: Description in page 195

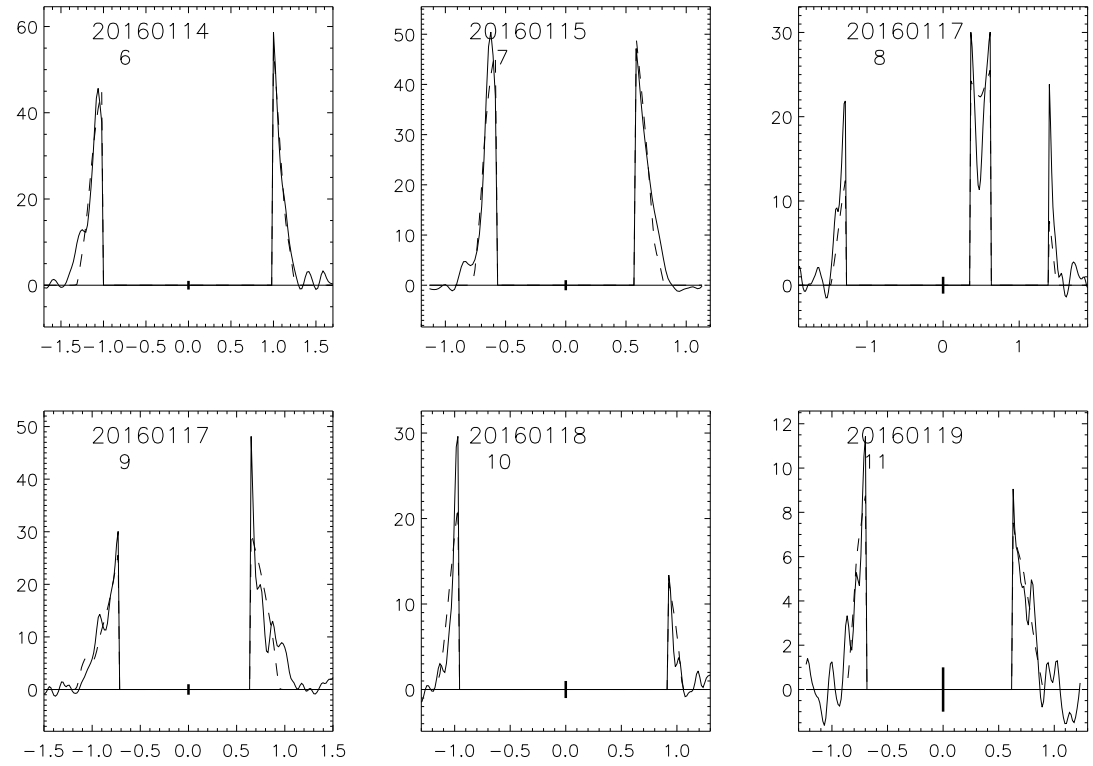

(c) Arecibo 2016, masked *cw* spectra (as used in the modelling procedure)

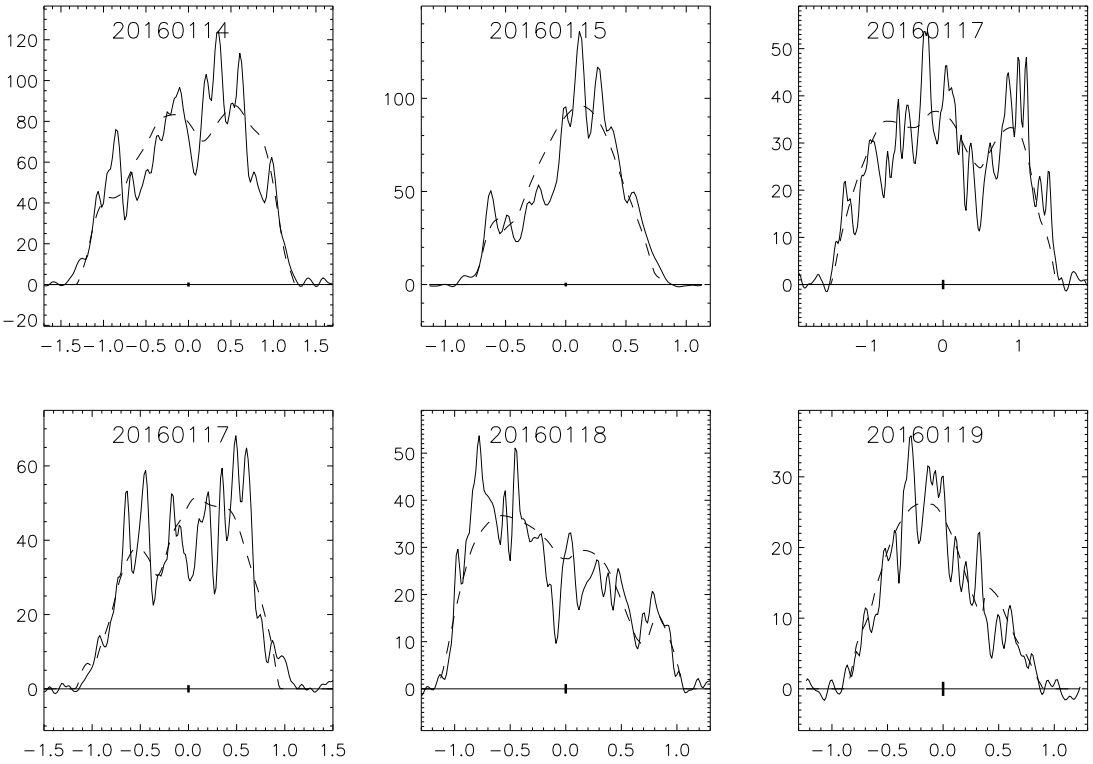

(d) Arecibo 2016, full *cw* spectra (illustration only)

Figure A.6: Description in page 195

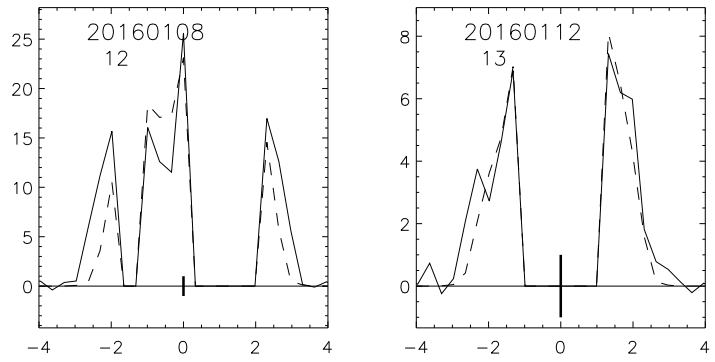

(e) Goldstone, masked *cw* spectra (as used in the modelling procedure)

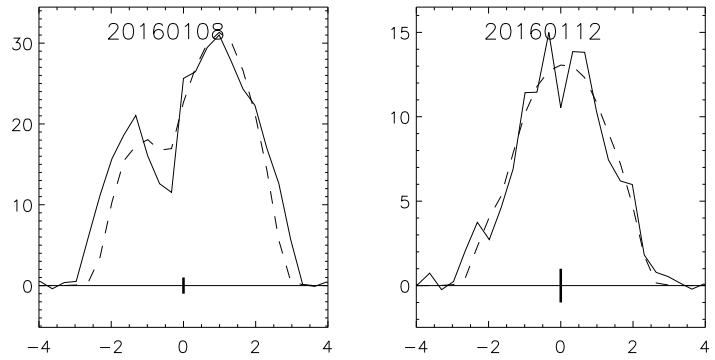

(f) Goldstone, full *cw* spectra (illustration only)

Figure A.6: Fit of the final shape model of asteroid (85990) 1999 JV_6 to the full continuous-wave data set. Each panel is a graph of echo power in units of standard deviation of the noise against Doppler frequency offset in Hz (relative to centre of mass). The black bar at the 0 Hz frequency has a unit length. Each panel is labelled with the date of observations in *yyyymmdd* format and the unique set number in `SHAPE`. Solid lines represent observations (received OC spectra), and the dashed line is a simulated echo based on the best-fit model with $\lambda = 96°$ and $\beta = -88°$. Different sub-figures represent different observing runs: panels (a), and (b) – 2015 run at Arecibo, panels (c), and (d) – 2016 run at Arecibo, and panels (e), and (f) – the run at Goldstone. Also, in panels (a), (c), and (e) the cropped spectra are shown, masked to only show the bandwidth and significant drops in the echo power. This is how the spectra are input to the `SHAPE` modelling procedures and it is from those cropped spectra that the contribution to the χ^2 goodness-of-fit is calculated. The panels (b), (d), and (f) are included for illustration purposes only, to show how the full modelled spectra look like relative to the observations.

Set	Obs.	UT Date	UT Time	Pix. width	Looks	Phase
00	A1	2015-01-14	06:11:55	0.036	5	0.82
01	A1	2015-01-15	05:58:29	0.034	5	0.45
02	A1	2015-01-16	06:33:03	0.034	5	0.21
03	A1	2015-01-17	07:15:03	0.033	5	0.98
04	A1	2015-01-18	07:05:53	0.032	7	0.62
05	A1	2015-01-28	04:36:37	0.046	7	0.91
06	A2	2016-01-14	03:12:35	0.021	4	0.35
07	A2	2016-01-15	02:55:30	0.019	5	0.97
08	A2	2016-01-17	02:26:48	0.016	4	0.24
09	A2	2016-01-17	03:37:00	0.016	4	0.42
10	A2	2016-01-18	03:43:18	0.015	4	0.10
11	A2	2016-01-19	02:15:07	0.014	4	0.55
12	G	2016-01-08	06:33:53	0.330	63	0.88
13	G	2016-01-12	06:14:28	0.330	75	0.47

Table A.1: Full details of continuous-wave spectra used for detailed modelling of (85990) 1999 JV_6. *Set* column lists the number of set as it appears in the `SHAPE` observations file. *Obs.* is a designation of the observing run, *A1* for Arecibo 2015, *A2* for Arecibo 2016, and *G* for Goldstone. *UT Date* is the UT date at which the observation was taken. *UT Time* is the mid-receive time. *Freq. res.* is the frequency (Doppler) resolution in Hz. *Looks* is the total number of independent measurements (looks) in each frame. *Phase* is the rotation phase, assuming the spin-state of the refined radar model with $\lambda = 96°$ and $\beta = -88°$, as a fraction of full rotation.

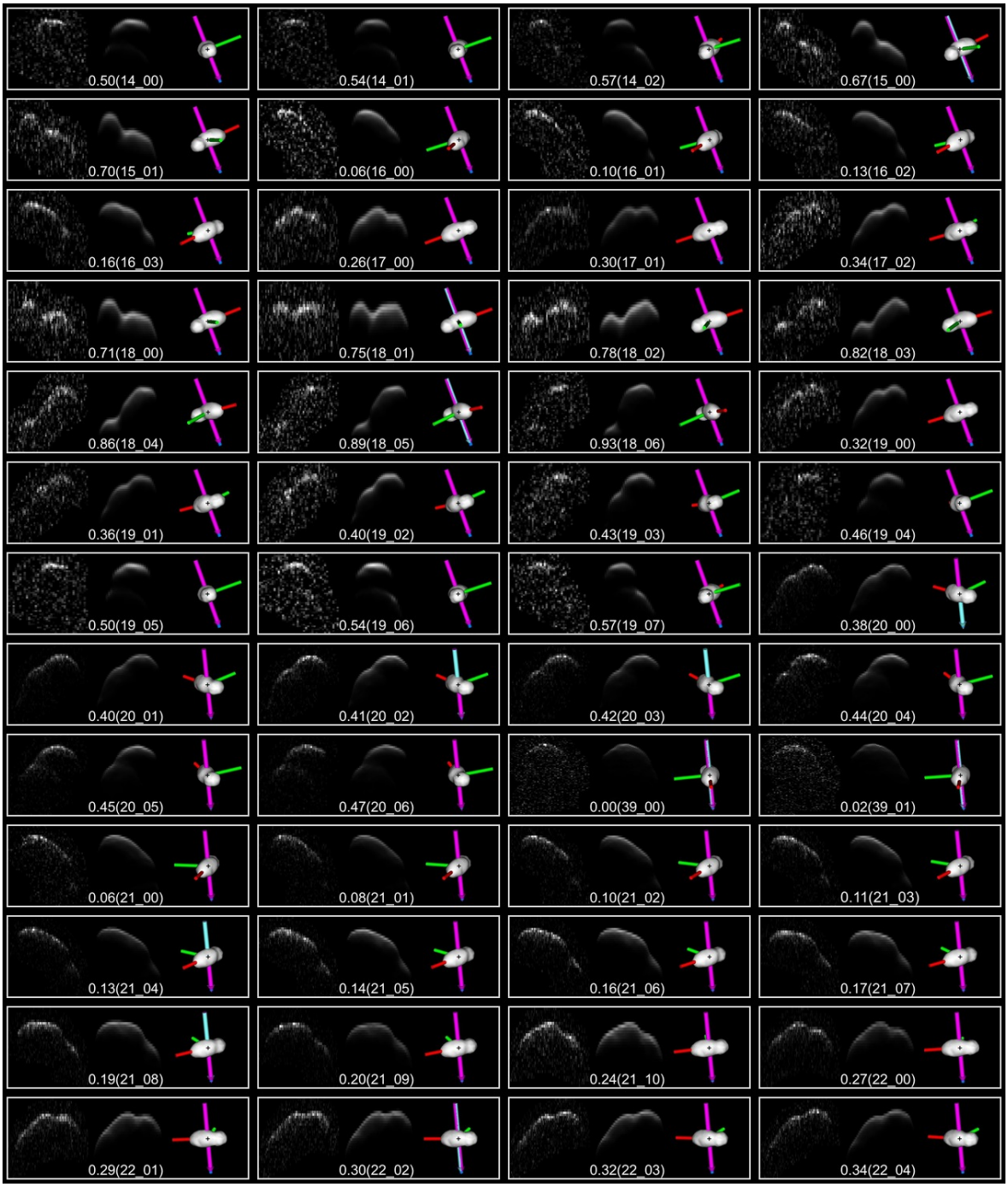

Figure A.7: Fit of the final shape model of asteroid (85990) 1999 JV_6 to the full radar data set. Each set of three panels represents one imaging frame and is made of the actual observation (left panel), echo simulation based on the model (middle panel), and plane-of-sky projection of the model (right panel). On the observation and simulation images the delay increases downwards and the frequency (Doppler) to the right. The plane-of-sky image is orientated with north to the top and east to the left. The principal axes of inertia are marked with coloured rods (red, green and blue), and the rotation vector (z-axis of fixed body coordinate system) is marked with a purple arrow.

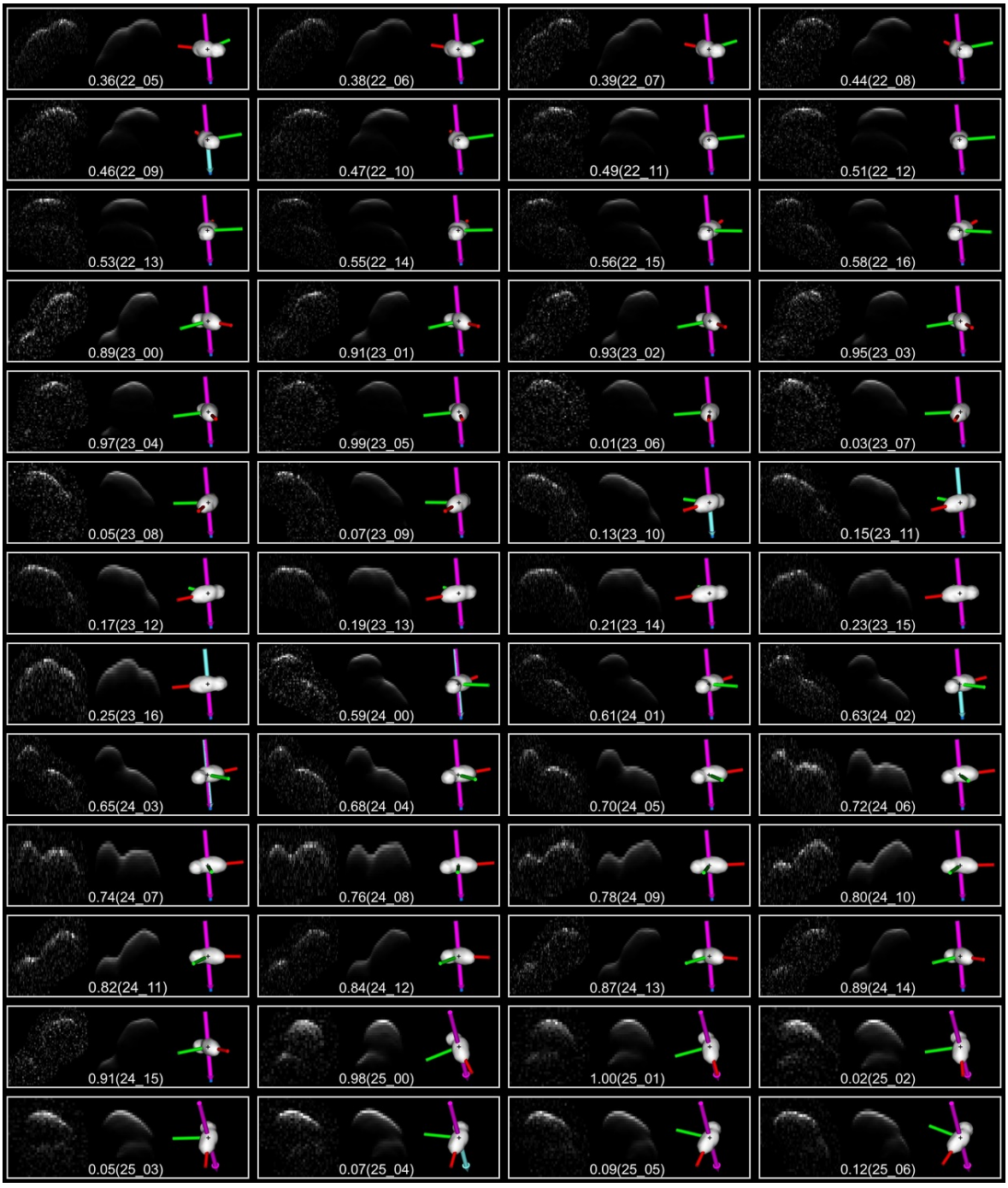

Figure A.7: Continued from Page 197

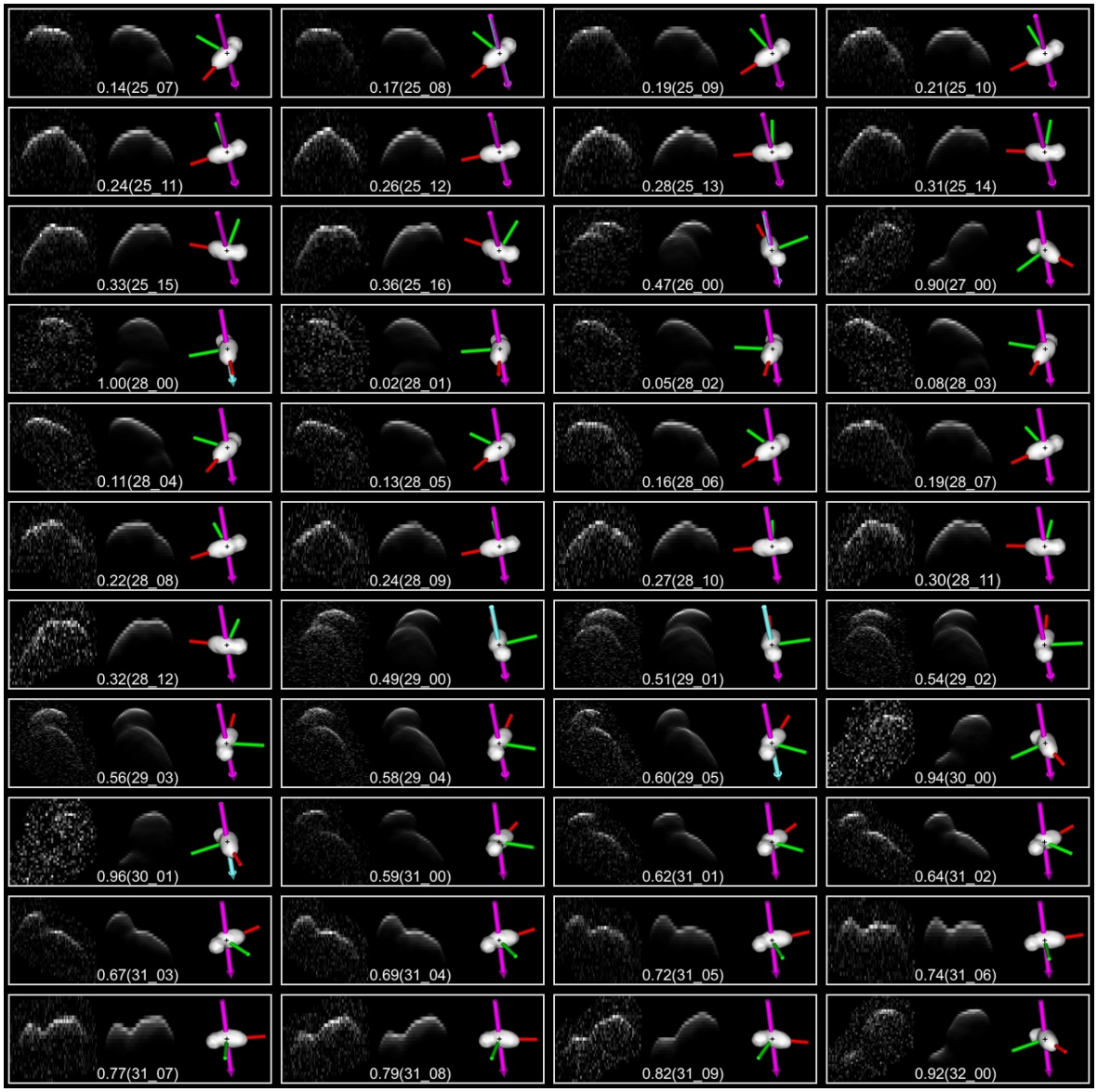

Figure A.7: Continued from Page 197

Set	Frame	Obs.	UT Date	UT Time	Baud	Pix. height	Pix. width	Looks	Phase
14	00	A1	2015-01-15	06:18:26	0.200	0.100	0.068	24	0.50
14	01	A1	2015-01-15	06:31:06	0.200	0.100	0.068	24	0.54
14	02	A1	2015-01-15	06:44:19	0.200	0.100	0.068	24	0.57
15	00	A1	2015-01-15	07:22:01	0.200	0.100	0.068	24	0.67
15	01	A1	2015-01-15	07:34:41	0.200	0.100	0.068	24	0.70
16	00	A1	2015-01-16	05:35:46	0.200	0.100	0.067	24	0.06
16	01	A1	2015-01-16	05:49:48	0.200	0.100	0.067	24	0.10
16	02	A1	2015-01-16	06:02:44	0.200	0.100	0.067	24	0.13
16	03	A1	2015-01-16	06:15:40	0.200	0.100	0.067	24	0.16
17	00	A1	2015-01-16	06:54:26	0.200	0.100	0.067	24	0.26
17	01	A1	2015-01-16	07:08:59	0.200	0.100	0.067	30	0.30
17	02	A1	2015-01-16	07:25:09	0.200	0.100	0.067	30	0.34
18	00	A1	2015-01-17	05:31:40	0.200	0.100	0.065	24	0.71
18	01	A1	2015-01-17	05:45:25	0.200	0.100	0.065	24	0.75
18	02	A1	2015-01-17	05:58:37	0.200	0.100	0.065	24	0.78
18	03	A1	2015-01-17	06:11:49	0.200	0.100	0.065	24	0.82
18	04	A1	2015-01-17	06:27:44	0.200	0.100	0.065	24	0.86
18	05	A1	2015-01-17	06:41:56	0.200	0.100	0.065	24	0.89
18	06	A1	2015-01-17	06:56:56	0.200	0.100	0.065	30	0.93
19	00	A1	2015-01-18	05:08:29	0.200	0.100	0.074	28	0.32
19	01	A1	2015-01-18	05:23:57	0.200	0.100	0.074	28	0.36
19	02	A1	2015-01-18	05:37:43	0.200	0.100	0.074	28	0.40
19	03	A1	2015-01-18	05:51:18	0.200	0.100	0.074	28	0.43
19	04	A1	2015-01-18	06:04:55	0.200	0.100	0.074	28	0.46
19	05	A1	2015-01-18	06:18:35	0.200	0.100	0.074	28	0.50
19	06	A1	2015-01-18	06:32:51	0.200	0.100	0.074	28	0.54
19	07	A1	2015-01-18	06:46:54	0.200	0.100	0.074	28	0.57
20	00	A2	2016-01-14	03:26:09	0.100	0.100	0.042	6	0.38
20	01	A2	2016-01-14	03:31:45	0.100	0.100	0.042	6	0.40
20	02	A2	2016-01-14	03:37:21	0.100	0.100	0.042	6	0.41
20	03	A2	2016-01-14	03:42:01	0.100	0.100	0.042	4	0.42
20	04	A2	2016-01-14	03:49:41	0.100	0.100	0.042	4	0.44
20	05	A2	2016-01-14	03:54:21	0.100	0.100	0.042	6	0.45
20	06	A2	2016-01-14	03:59:57	0.100	0.100	0.042	6	0.47
39	00	A2	2016-01-15	03:06:49	0.050	0.050	0.038	6	0.00
39	01	A2	2016-01-15	03:12:54	0.050	0.050	0.038	6	0.02
21	00	A2	2016-01-15	03:31:27	0.100	0.100	0.038	4	0.06
21	01	A2	2016-01-15	03:36:31	0.100	0.100	0.038	6	0.08

Table A.2: Full details of radar imaging frames spectra used for detailed modelling of (85990) 1999 JV_6 (see Figure A.7). *Set* column lists the number of set as it appears in the `SHAPE` observations file. *Frame* column contains the frame number in the `SHAPE` file. The set and frame numbers are given as they are unique labels and are convenient for identification of images in the figures. *Obs.* is a designation of the observing run, *A1* for Arecibo 2015, *A2* for Arecibo 2016, and *G* for Goldstone. *UT Date* is the UT date at which the observation was taken. *UT Time* is the mid-receive time. *Baud* is the signal code baud length in µs. *Pix. height* is the pixel size in the delay domain in µs. *Pix. width* is the pixel size in the frequency (Doppler) domain in Hz. *Looks* is the total number of independent measurements (looks) in each frame. *Phase* is the rotation phase, assuming the spin-state of the refined radar model with $\lambda = 96°$ and $\beta = -88°$, as a fraction of full rotation. The observations are listed chronologically.

Set	Frame	Obs.	UT Date	UT Time	Baud	Pix. height	Pix. width	Looks	Phase
21	02	A2	2016-01-15	03:43:54	0.100	0.100	0.038	6	0.10
21	03	A2	2016-01-15	03:50:01	0.100	0.100	0.038	6	0.11
21	04	A2	2016-01-15	03:56:06	0.100	0.100	0.038	6	0.13
21	05	A2	2016-01-15	04:02:12	0.100	0.100	0.038	6	0.14
21	06	A2	2016-01-15	04:08:19	0.100	0.100	0.038	6	0.16
21	07	A2	2016-01-15	04:14:24	0.100	0.100	0.038	6	0.17
21	08	A2	2016-01-15	04:20:31	0.100	0.100	0.038	6	0.19
21	09	A2	2016-01-15	04:26:36	0.100	0.100	0.038	6	0.20
21	10	A2	2016-01-15	04:41:41	0.100	0.100	0.038	6	0.24
22	00	A2	2016-01-17	02:38:12	0.100	0.100	0.032	6	0.27
22	01	A2	2016-01-17	02:45:18	0.100	0.100	0.032	6	0.29
22	02	A2	2016-01-17	02:52:24	0.100	0.100	0.032	6	0.30
22	03	A2	2016-01-17	02:59:29	0.100	0.100	0.032	6	0.32
22	04	A2	2016-01-17	03:06:35	0.100	0.100	0.032	6	0.34
22	05	A2	2016-01-17	03:13:41	0.100	0.100	0.032	6	0.36
22	06	A2	2016-01-17	03:20:48	0.100	0.100	0.032	6	0.38
22	07	A2	2016-01-17	03:27:54	0.100	0.100	0.032	6	0.39
22	08	A2	2016-01-17	03:46:12	0.100	0.100	0.032	4	0.44
22	09	A2	2016-01-17	03:52:07	0.100	0.100	0.032	6	0.46
22	10	A2	2016-01-17	03:59:12	0.100	0.100	0.032	6	0.47
22	11	A2	2016-01-17	04:06:18	0.100	0.100	0.032	6	0.49
22	12	A2	2016-01-17	04:13:24	0.100	0.100	0.032	6	0.51
22	13	A2	2016-01-17	04:20:31	0.100	0.100	0.032	6	0.53
22	14	A2	2016-01-17	04:27:37	0.100	0.100	0.032	6	0.55
22	15	A2	2016-01-17	04:34:43	0.100	0.100	0.032	6	0.56
22	16	A2	2016-01-17	04:41:48	0.100	0.100	0.032	6	0.58
23	00	A2	2016-01-18	02:21:15	0.100	0.100	0.044	9	0.89
23	01	A2	2016-01-18	02:28:51	0.100	0.100	0.044	9	0.91
23	02	A2	2016-01-18	02:36:27	0.100	0.100	0.044	9	0.93
23	03	A2	2016-01-18	02:44:03	0.100	0.100	0.044	9	0.95
23	04	A2	2016-01-18	02:51:39	0.100	0.100	0.044	9	0.97
23	05	A2	2016-01-18	02:59:15	0.100	0.100	0.044	9	0.99
23	06	A2	2016-01-18	03:06:51	0.100	0.100	0.044	9	0.01
23	07	A2	2016-01-18	03:14:27	0.100	0.100	0.044	9	0.03
23	08	A2	2016-01-18	03:22:03	0.100	0.100	0.044	9	0.05
23	09	A2	2016-01-18	03:29:39	0.100	0.100	0.044	9	0.07
23	10	A2	2016-01-18	03:54:24	0.100	0.100	0.044	9	0.13
23	11	A2	2016-01-18	04:02:00	0.100	0.100	0.044	9	0.15
23	12	A2	2016-01-18	04:09:36	0.100	0.100	0.044	9	0.17
23	13	A2	2016-01-18	04:17:12	0.100	0.100	0.044	9	0.19
23	14	A2	2016-01-18	04:24:48	0.100	0.100	0.044	9	0.21
23	15	A2	2016-01-18	04:32:24	0.100	0.100	0.044	9	0.23
23	16	A2	2016-01-18	04:40:00	0.100	0.100	0.044	9	0.25
24	00	A2	2016-01-19	02:31:52	0.100	0.100	0.041	9	0.59
24	01	A2	2016-01-19	02:40:12	0.100	0.100	0.041	9	0.61
24	02	A2	2016-01-19	02:48:46	0.100	0.100	0.041	9	0.63
24	03	A2	2016-01-19	02:56:51	0.100	0.100	0.041	9	0.65
24	04	A2	2016-01-19	03:04:58	0.100	0.100	0.041	9	0.68
24	05	A2	2016-01-19	03:13:03	0.100	0.100	0.041	9	0.70
24	06	A2	2016-01-19	03:21:10	0.100	0.100	0.041	9	0.72
24	07	A2	2016-01-19	03:29:21	0.100	0.100	0.041	9	0.74
24	08	A2	2016-01-19	03:37:33	0.100	0.100	0.041	9	0.76
24	09	A2	2016-01-19	03:45:45	0.100	0.100	0.041	9	0.78
24	10	A2	2016-01-19	03:53:57	0.100	0.100	0.041	9	0.80
24	11	A2	2016-01-19	04:02:09	0.100	0.100	0.041	9	0.82

Table A.2: Continued from Page 200

Set	Frame	Obs.	UT Date	UT Time	Baud	Pix. height	Pix. width	Looks	Phase
24	12	A2	2016-01-19	04:10:21	0.100	0.100	0.041	9	0.84
24	13	A2	2016-01-19	04:20:40	0.100	0.100	0.041	9	0.87
24	14	A2	2016-01-19	04:29:55	0.100	0.100	0.041	9	0.89
24	15	A2	2016-01-19	04:38:07	0.100	0.100	0.041	9	0.91
25	00	G	2016-01-08	07:13:03	0.125	0.125	0.158	40	0.98
25	01	G	2016-01-08	07:22:25	0.125	0.125	0.158	40	1.00
25	02	G	2016-01-08	07:31:45	0.125	0.125	0.158	40	0.02
25	03	G	2016-01-08	07:41:08	0.125	0.125	0.158	40	0.05
25	04	G	2016-01-08	07:50:29	0.125	0.125	0.158	40	0.07
25	05	G	2016-01-08	07:59:50	0.125	0.125	0.158	40	0.09
25	06	G	2016-01-08	08:09:11	0.125	0.125	0.158	40	0.12
25	07	G	2016-01-08	08:18:33	0.125	0.125	0.158	40	0.14
25	08	G	2016-01-08	08:27:56	0.125	0.125	0.158	40	0.17
25	09	G	2016-01-08	08:37:17	0.125	0.125	0.158	40	0.19
25	10	G	2016-01-08	08:46:38	0.125	0.125	0.158	40	0.21
25	11	G	2016-01-08	08:56:00	0.125	0.125	0.158	40	0.24
25	12	G	2016-01-08	09:05:21	0.125	0.125	0.158	40	0.26
25	13	G	2016-01-08	09:14:43	0.125	0.125	0.158	40	0.28
25	14	G	2016-01-08	09:24:05	0.125	0.125	0.158	40	0.31
25	15	G	2016-01-08	09:34:02	0.125	0.125	0.158	45	0.33
25	16	G	2016-01-08	09:44:32	0.125	0.125	0.158	45	0.36
26	00	G	2016-01-09	06:07:31	0.125	0.125	0.158	40	0.47
27	00	G	2016-01-10	04:36:25	0.125	0.125	0.158	53	0.90
28	00	G	2016-01-10	05:16:44	0.125	0.125	0.158	45	1.00
28	01	G	2016-01-10	05:27:26	0.125	0.125	0.158	45	0.02
28	02	G	2016-01-10	05:38:09	0.125	0.125	0.158	47	0.05
28	03	G	2016-01-10	05:48:51	0.125	0.125	0.158	46	0.08
28	04	G	2016-01-10	05:59:32	0.125	0.125	0.158	45	0.11
28	05	G	2016-01-10	06:10:14	0.125	0.125	0.158	46	0.13
28	06	G	2016-01-10	06:20:56	0.125	0.125	0.158	47	0.16
28	07	G	2016-01-10	06:31:36	0.125	0.125	0.158	48	0.19
28	08	G	2016-01-10	06:42:16	0.125	0.125	0.158	48	0.22
28	09	G	2016-01-10	06:52:57	0.125	0.125	0.158	44	0.24
28	10	G	2016-01-10	07:03:39	0.125	0.125	0.158	46	0.27
28	11	G	2016-01-10	07:14:20	0.125	0.125	0.158	47	0.30
28	12	G	2016-01-10	07:22:20	0.125	0.125	0.158	24	0.32
29	00	G	2016-01-09	06:18:39	0.050	0.050	0.144	70	0.49
29	01	G	2016-01-09	06:26:49	0.050	0.050	0.144	70	0.51
29	02	G	2016-01-09	06:34:59	0.050	0.050	0.144	70	0.54
29	03	G	2016-01-09	06:43:09	0.050	0.050	0.144	70	0.56
29	04	G	2016-01-09	06:51:19	0.050	0.050	0.144	70	0.58
29	05	G	2016-01-09	06:59:29	0.050	0.050	0.144	70	0.60
30	00	G	2016-01-10	04:54:51	0.125	0.125	0.158	77	0.94
30	01	G	2016-01-10	05:03:35	0.125	0.125	0.158	77	0.96
31	00	G	2016-01-12	06:58:17	0.125	0.125	0.160	98	0.59
31	01	G	2016-01-12	07:10:03	0.125	0.125	0.160	96	0.62
31	02	G	2016-01-12	07:20:03	0.125	0.125	0.160	96	0.64
31	03	G	2016-01-12	07:30:03	0.125	0.125	0.160	96	0.67
31	04	G	2016-01-12	07:40:03	0.125	0.125	0.160	96	0.69
31	05	G	2016-01-12	07:50:03	0.125	0.125	0.160	96	0.72
31	06	G	2016-01-12	08:00:03	0.125	0.125	0.160	96	0.74
31	07	G	2016-01-12	08:10:03	0.125	0.125	0.160	96	0.77
31	08	G	2016-01-12	08:20:03	0.125	0.125	0.160	96	0.79
31	09	G	2016-01-12	08:30:03	0.125	0.125	0.160	96	0.82
32	00	G	2016-01-13	04:48:26	0.125	0.125	0.160	96	0.92

Table A.2: Continued from Page 200

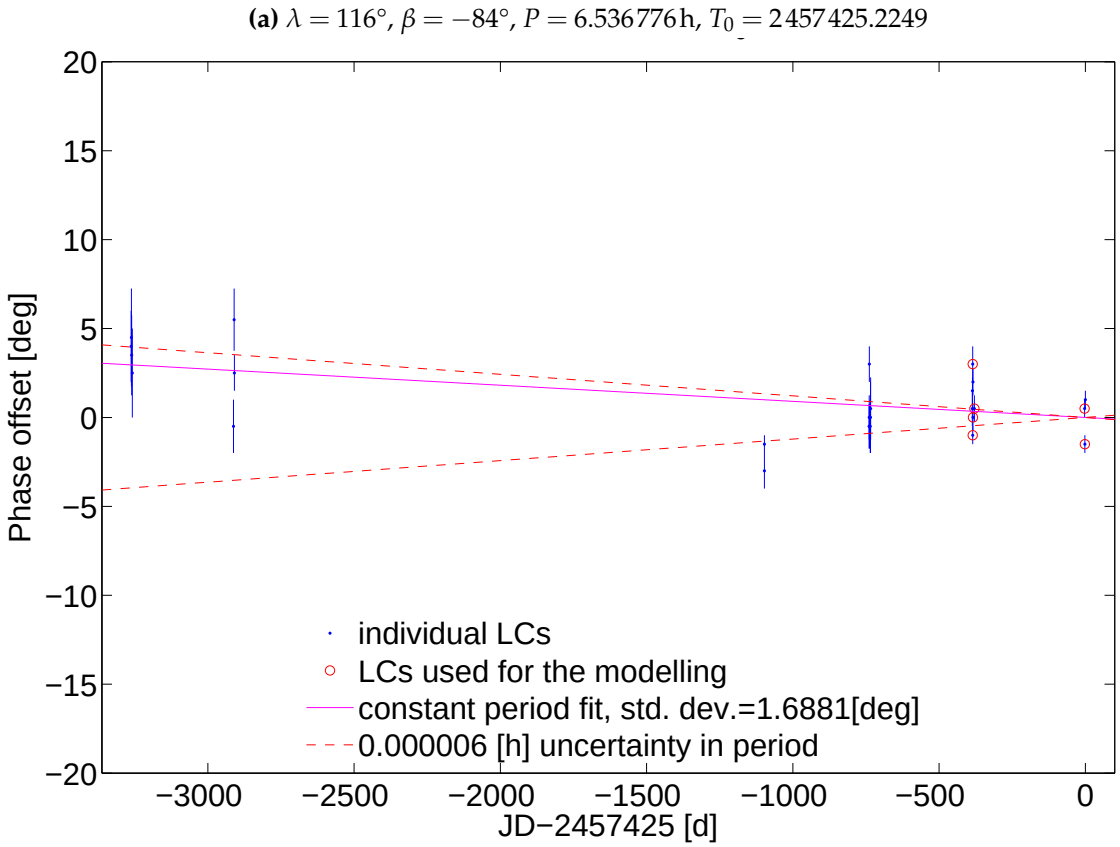

Figure A.8: Phase offset measurements for (85990) 1999 JV_6 faceted models. The blue points represent individual lightcurves with error in the phase offset measurement marked with the vertical bars. The lightcurves utilised in SHAPE modelling are circled in red. Purple solid line marks best-fit, assuming a constant-period solution (the σ of the fit is given in the legend). The red dashed lines mark possible spread in phase offsets due to uncertainty in the measured period alone.

(b) $\lambda = 120°$, $\beta = -84°$, $P = 6.536786\,\mathrm{h}$, $T_0 = 2457425.2226$

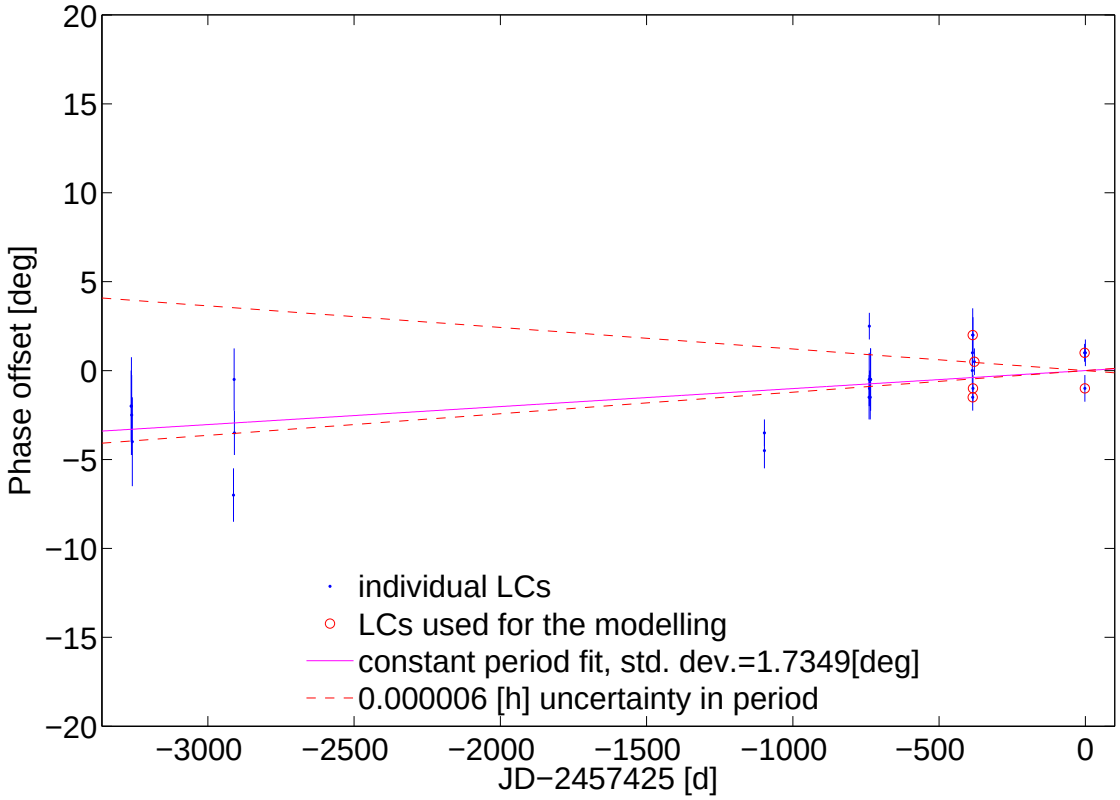

(c) $\lambda = 140°$, $\beta = -84°$, $P = 6.536783\,\mathrm{h}$, $T_0 = 2457425.2072$

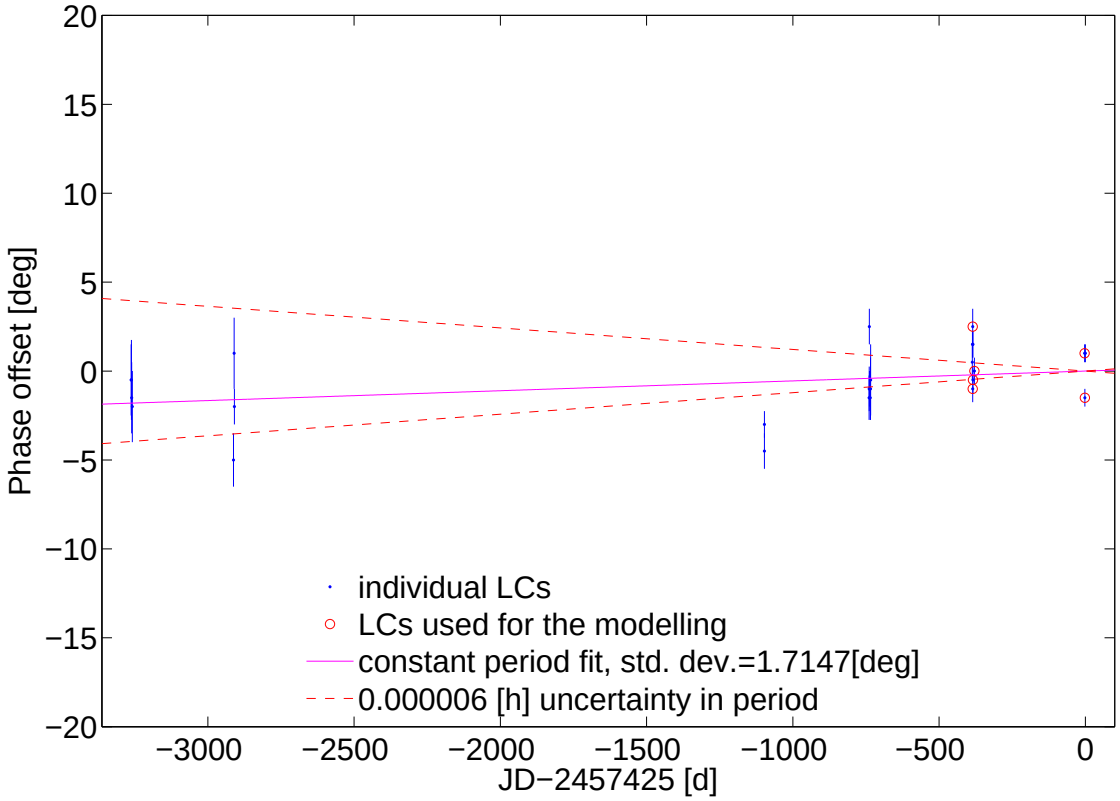

Figure A.8: Continued from Page 203

(d) $\lambda = 144°$, $\beta = -84°$, $P = 6.536783\,\mathrm{h}$, $T_0 = 2457425.2045$

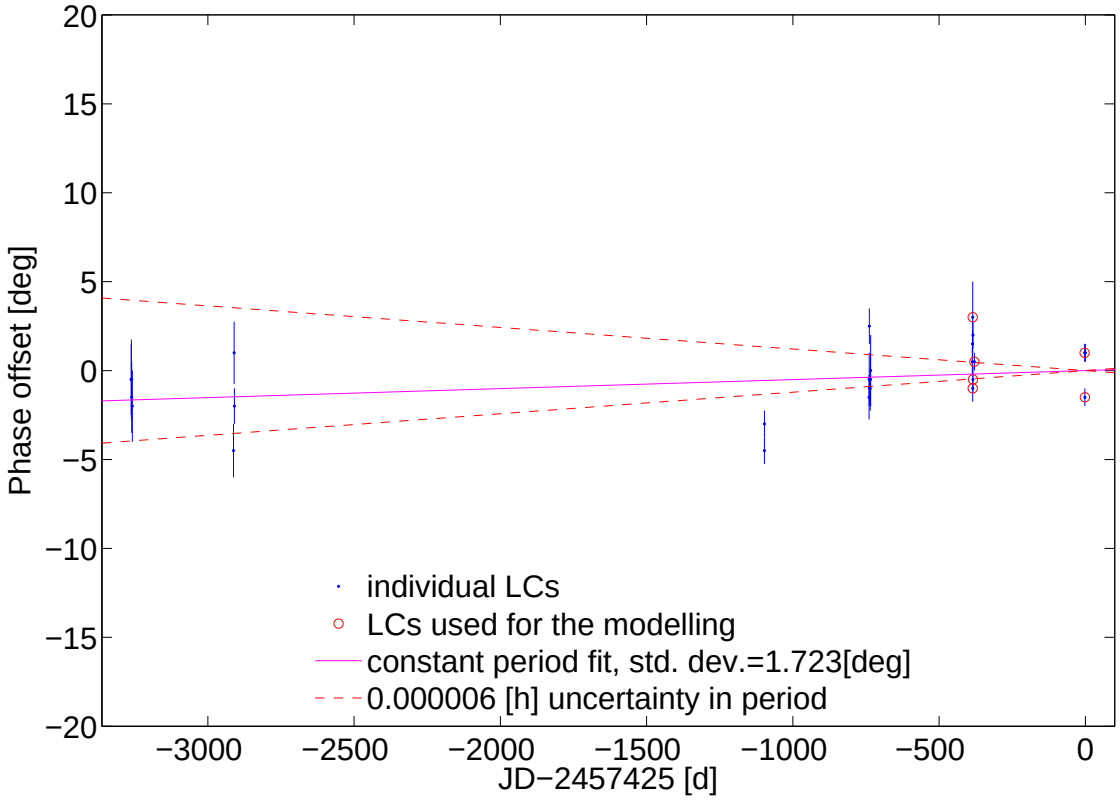

(e) $\lambda = 156°$, $\beta = -84°$, $P = 6.536783\,\mathrm{h}$, $T_0 = 2457425.1951$

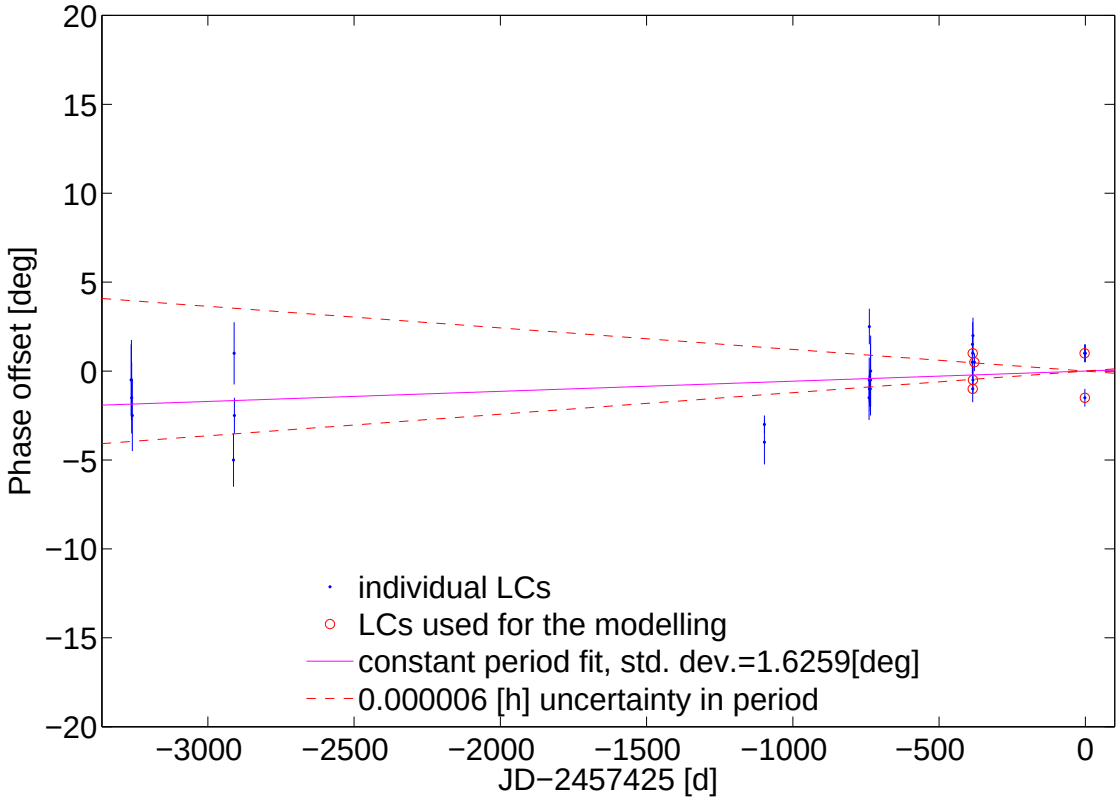

Figure A.8: Continued from Page 203

(f) $\lambda = 40°$, $\beta = -86°$, $P = 6.536794\,\mathrm{h}$, $T_0 = 2457425.2843$

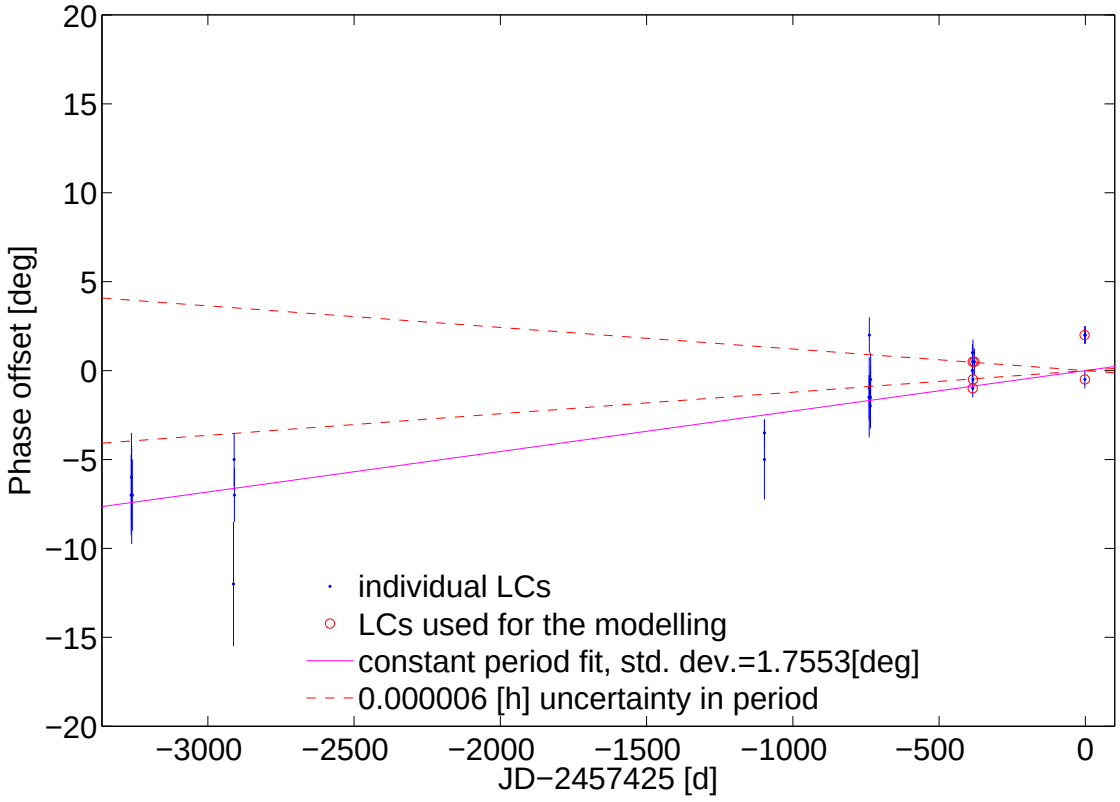

(g) $\lambda = 96°$, $\beta = -86°$, $P = 6.536788\,\mathrm{h}$, $T_0 = 2457425.2404$

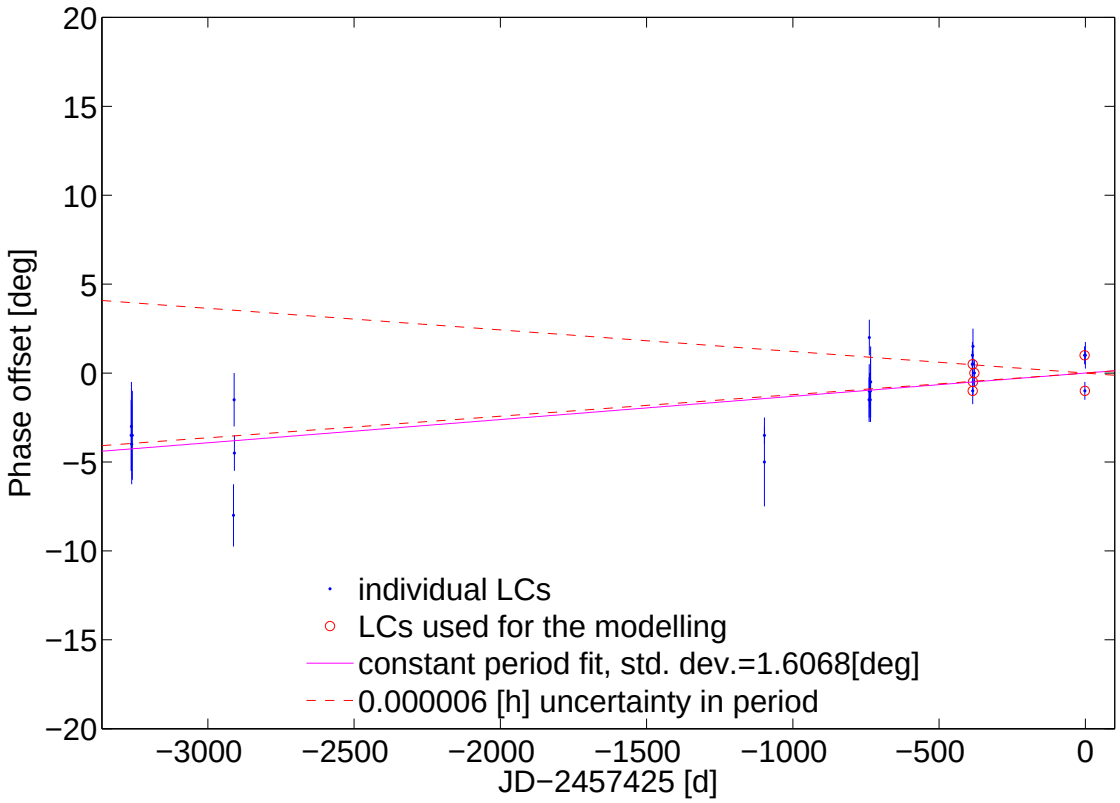

Figure A.8: Continued from Page 203

(h) $\lambda = 132°$, $\beta = -86°$, $P = 6.536\,800\,\mathrm{h}$, $T_0 = 2\,457\,425.2148$

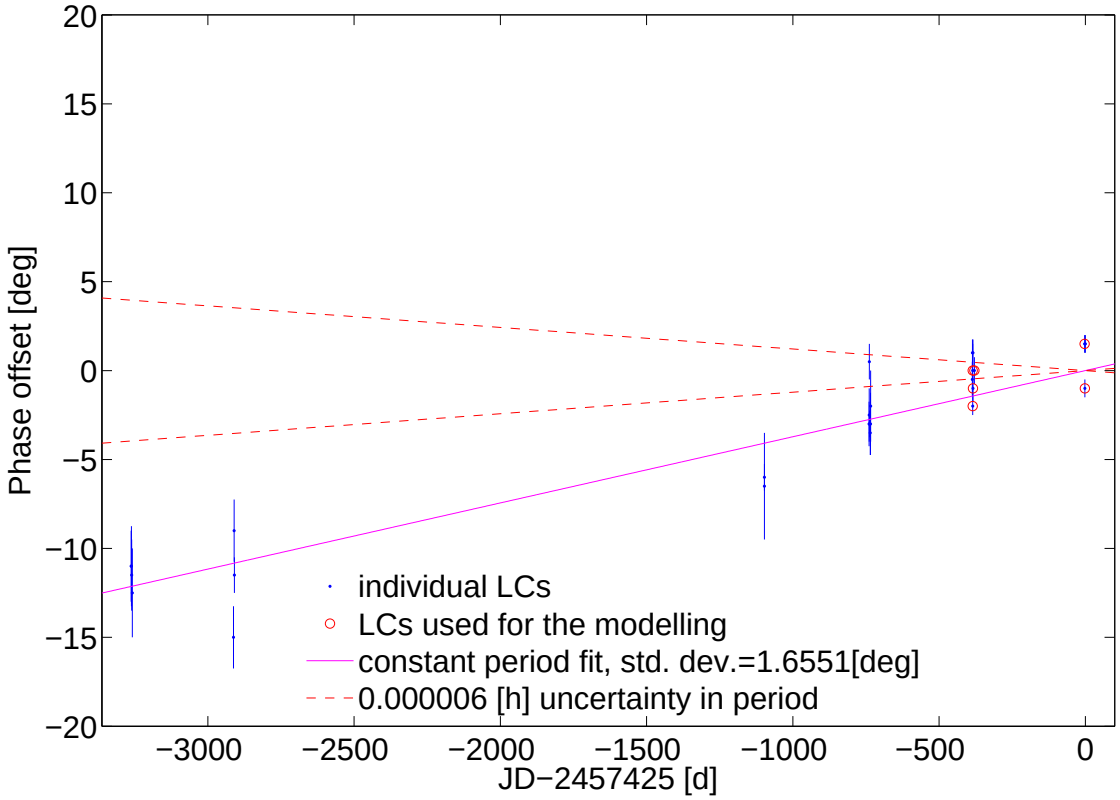

(i) $\lambda = 140°$, $\beta = -86°$, $P = 6.536\,789\,\mathrm{h}$, $T_0 = 2\,457\,425.2072$

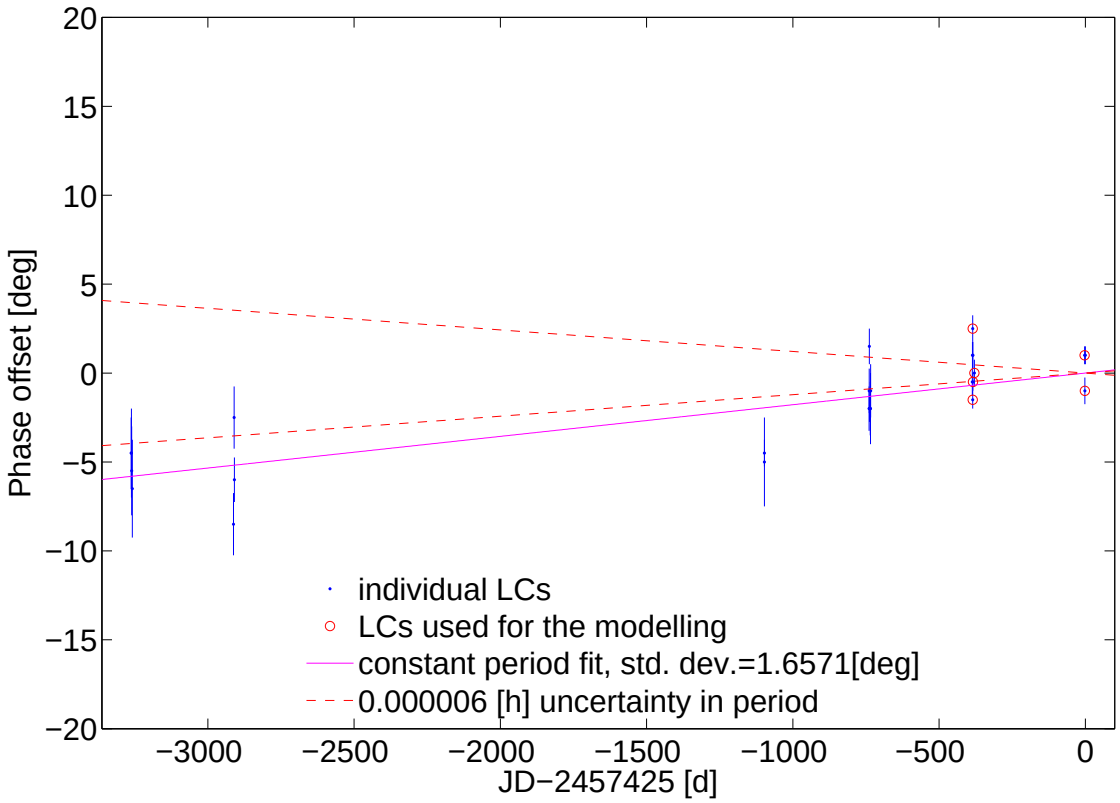

Figure A.8: Continued from Page 203

(j) $\lambda = 148°$, $\beta = -86°$, $P = 6.536787\,\mathrm{h}$, $T_0 = 2457425.2012$

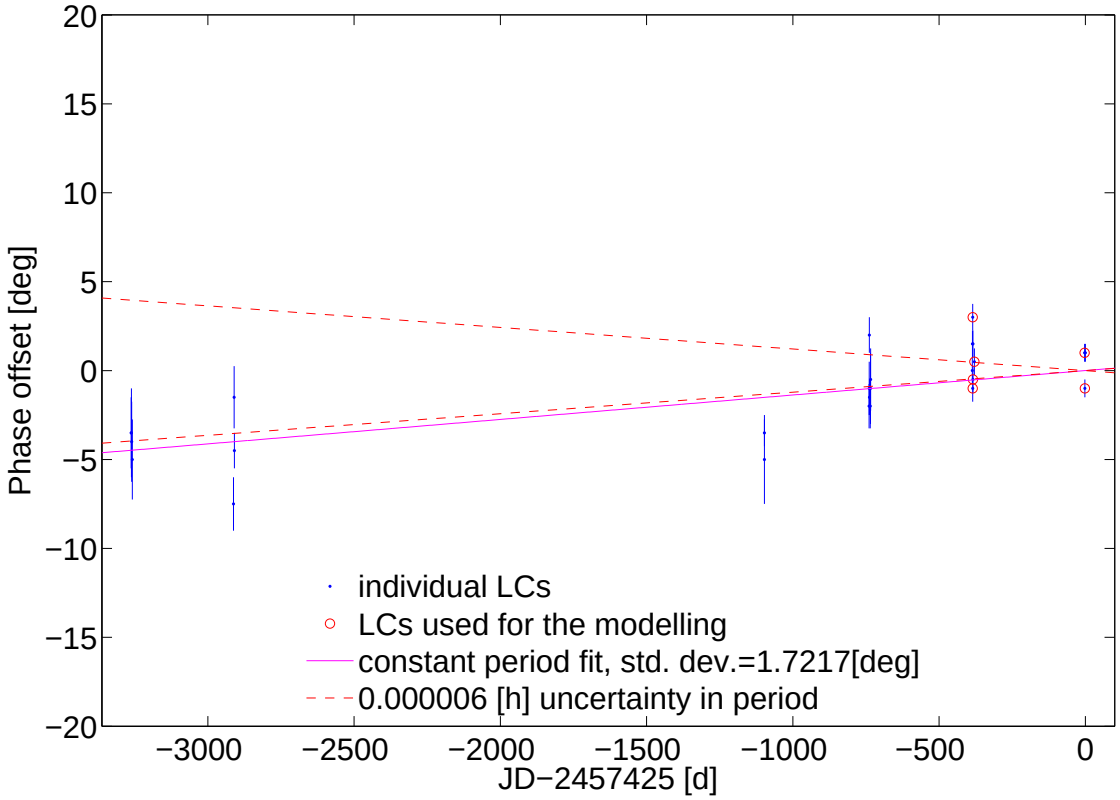

(k) $\lambda = 164°$, $\beta = -86°$, $P = 6.536791\,\mathrm{h}$, $T_0 = 2457425.1904$

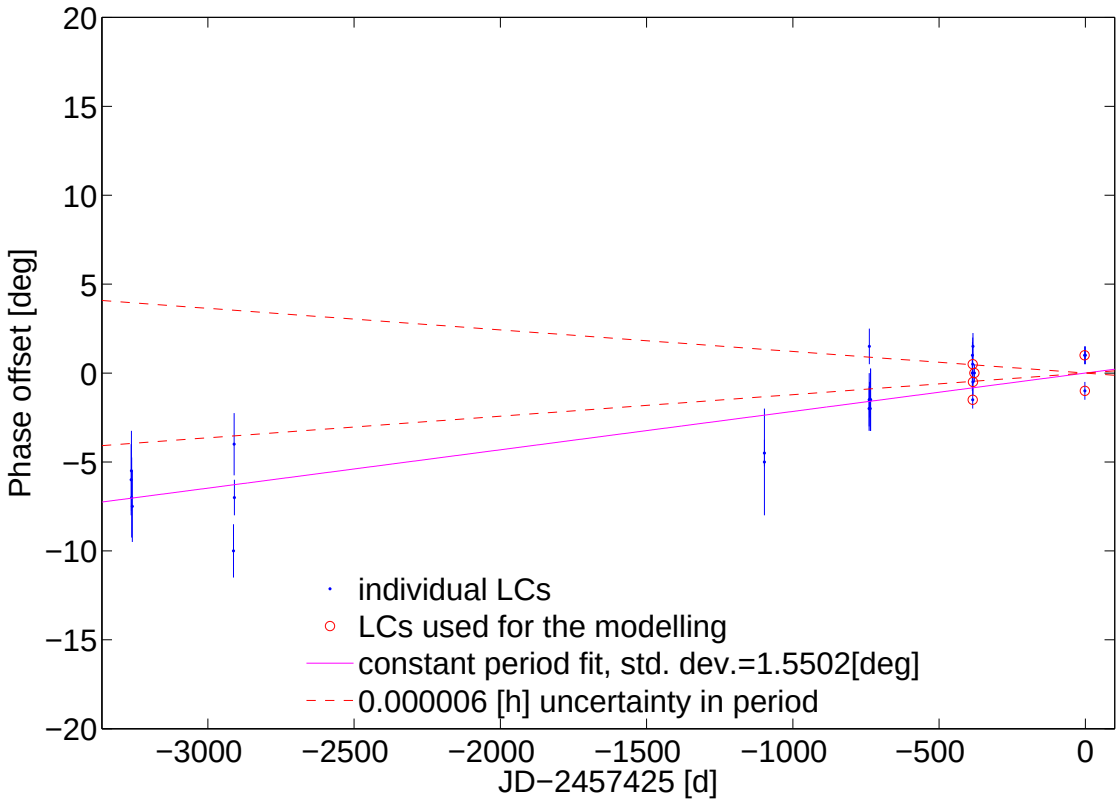

Figure A.8: Continued from Page 203

(l) $\lambda = 168°$, $\beta = -86°$, $P = 6.536793\,\mathrm{h}$, $T_0 = 2457425.1863$

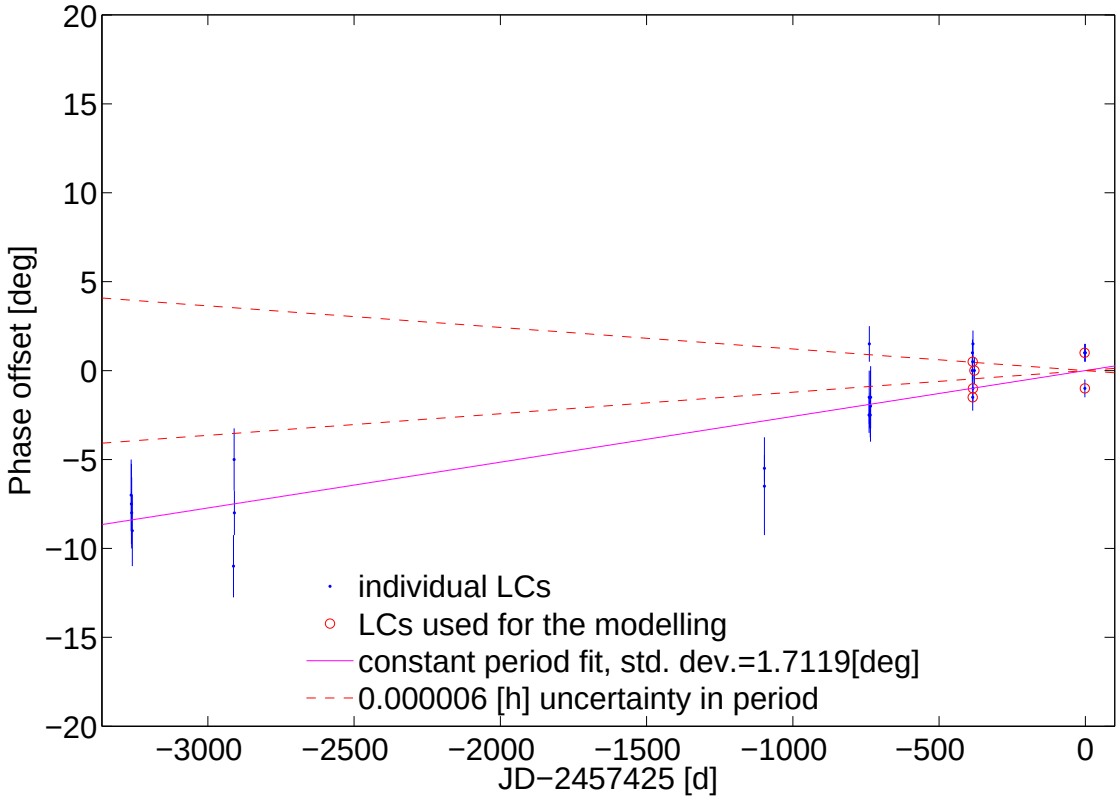

(m) $\lambda = 172°$, $\beta = -86°$, $P = 6.536782\,\mathrm{h}$, $T_0 = 2457425.1838$

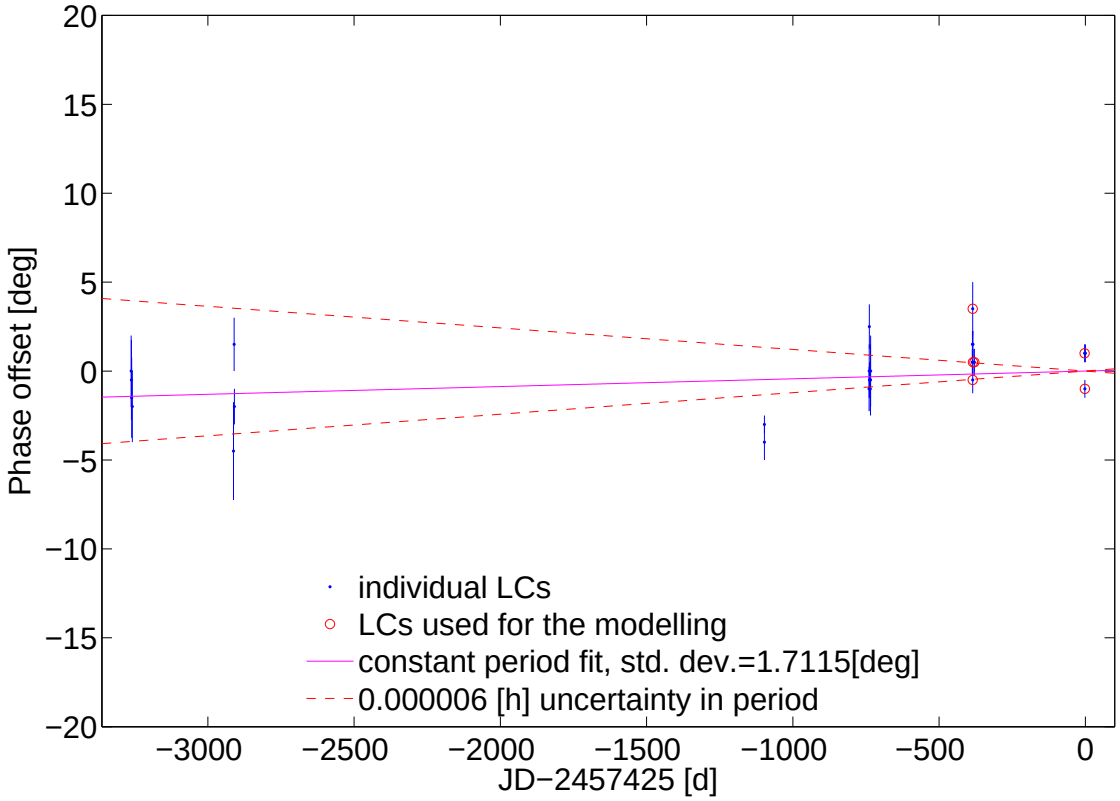

Figure A.8: Continued from Page 203

(n) $\lambda = 96°$, $\beta = -88°$, $P = 6.536781\,\mathrm{h}$, $T_0 = 2457425.2413$

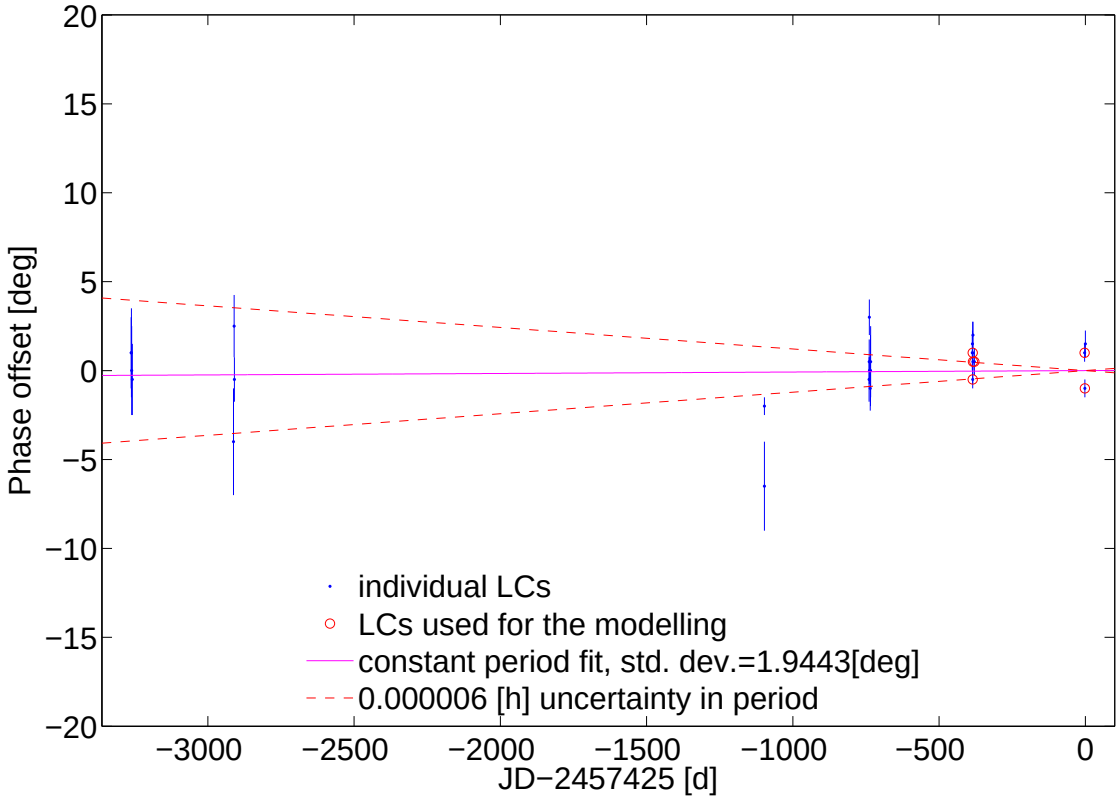

(o) $\lambda = 104°$, $\beta = -88°$, $P = 6.536781\,\mathrm{h}$, $T_0 = 2457425.2344$

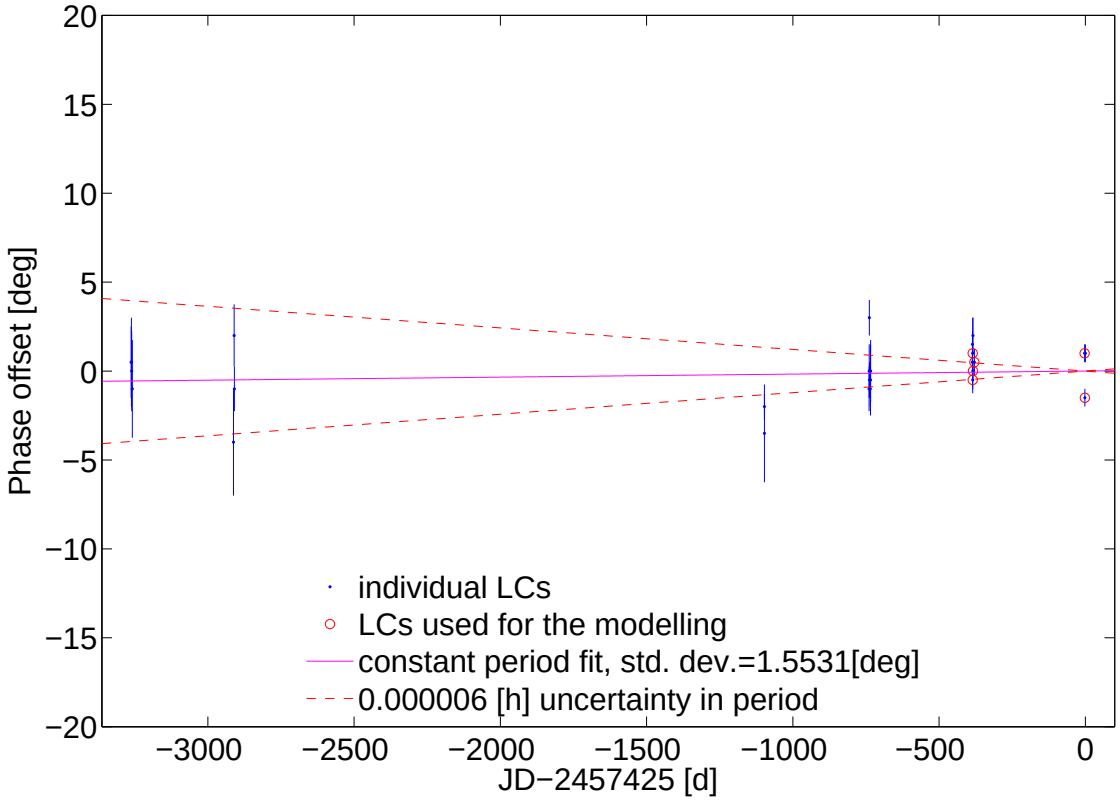

Figure A.8: Continued from Page 203

Appendix B

Coordinate systems and schematics

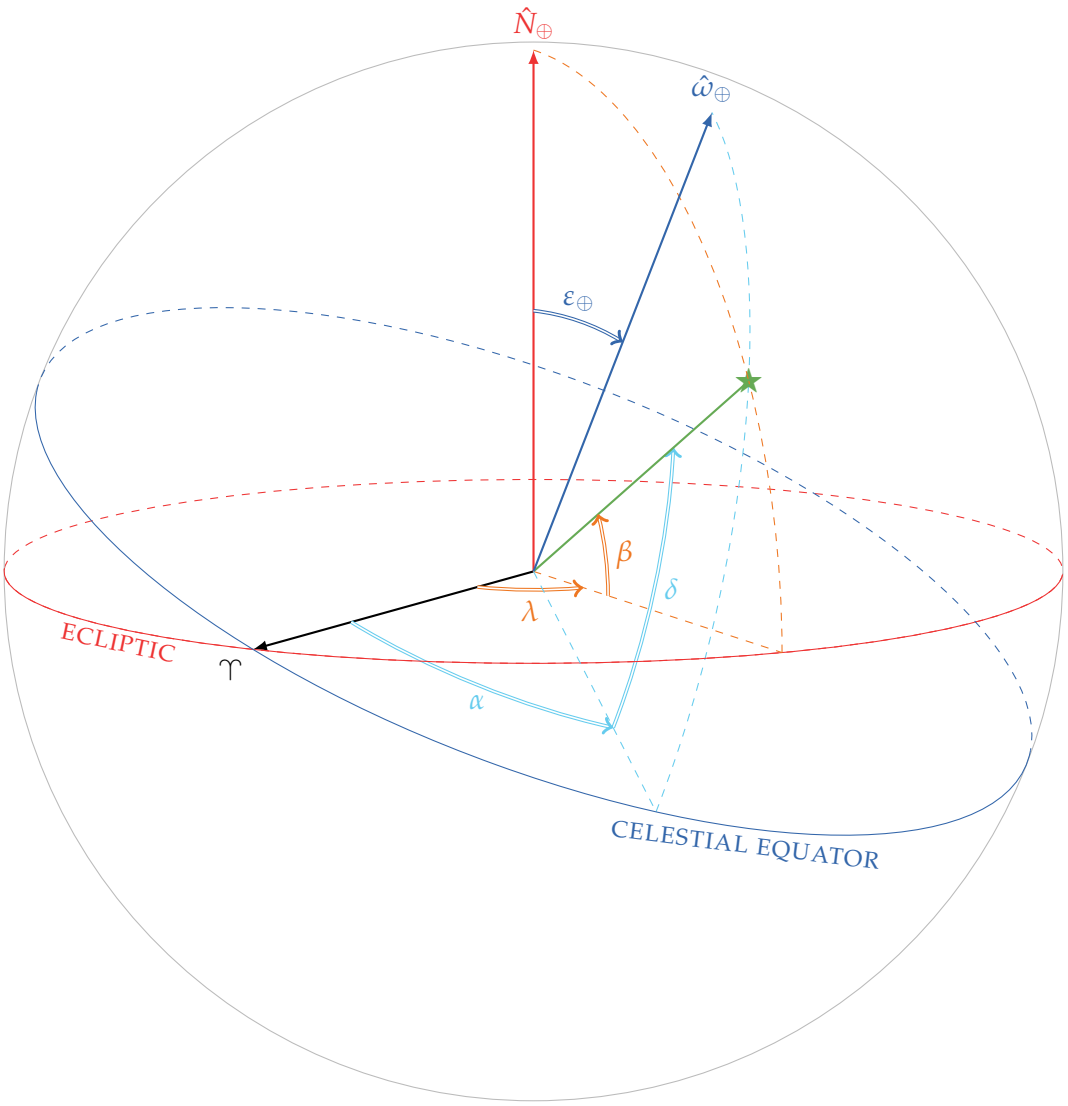

Figure B.1: The schematic shows the relation between the ecliptic and equatorial coordinate systems. The two coordinate systems are rotated relative to each other around the common x axis, by the angle $\varepsilon_\oplus$, which is the obliquity of Earths spin axis. The x-axis of both coordinate systems is defined with the vernal equinox point – marked traditionally with the astronomical sign of Aires Υ as it lays within this constellation. The z-axis of the ecliptic coordinate system is defined by the Earth orbital momentum versor, unit vector perpendicular to the plane of Eartgs orbit, the ecliptic, marked here with $\hat{N}_\oplus$, The elevation angle in ecliptic coordinate system is called the ecliptic latitude, β, and is measured from the plane of the Earths orbit and $\beta \in [-90°, 90]$. The azimuth angle is the ecliptic longitude, λ and is measured counter-clock-wise between the semi-plane stretching from the orbital momentum containing the vernal equinox, and semi-plane containing the position of the target, and $\lambda \in [0, 360]$. The z-axis of the equatorial coordinate system (also called J2000 from the epoch for which it was defined) is defined by the angular momentum versor of Earth, unit vector along the Earths spin axis at the epoch for which the system was defined, marked here with $\hat{\omega}_\oplus$. The celestial equator is the projection of Earth equator on the celestial sphere, and the plane containing it is perpendicular to the spin axis. The celestial equator plane serves as a reference plane for the elevation angle called declination, δ, and $\delta \in [-90°, 90°]$. The azimuth angle is the right ascension, α, and is measured between semi-plane stretching from the spin axis containing the vernal equinox, and semi-plane containing the position of the target, and $\alpha \in [0^h, 24^h]$. Coordinates of an example target which position is marked with a star, are marked in the graph.

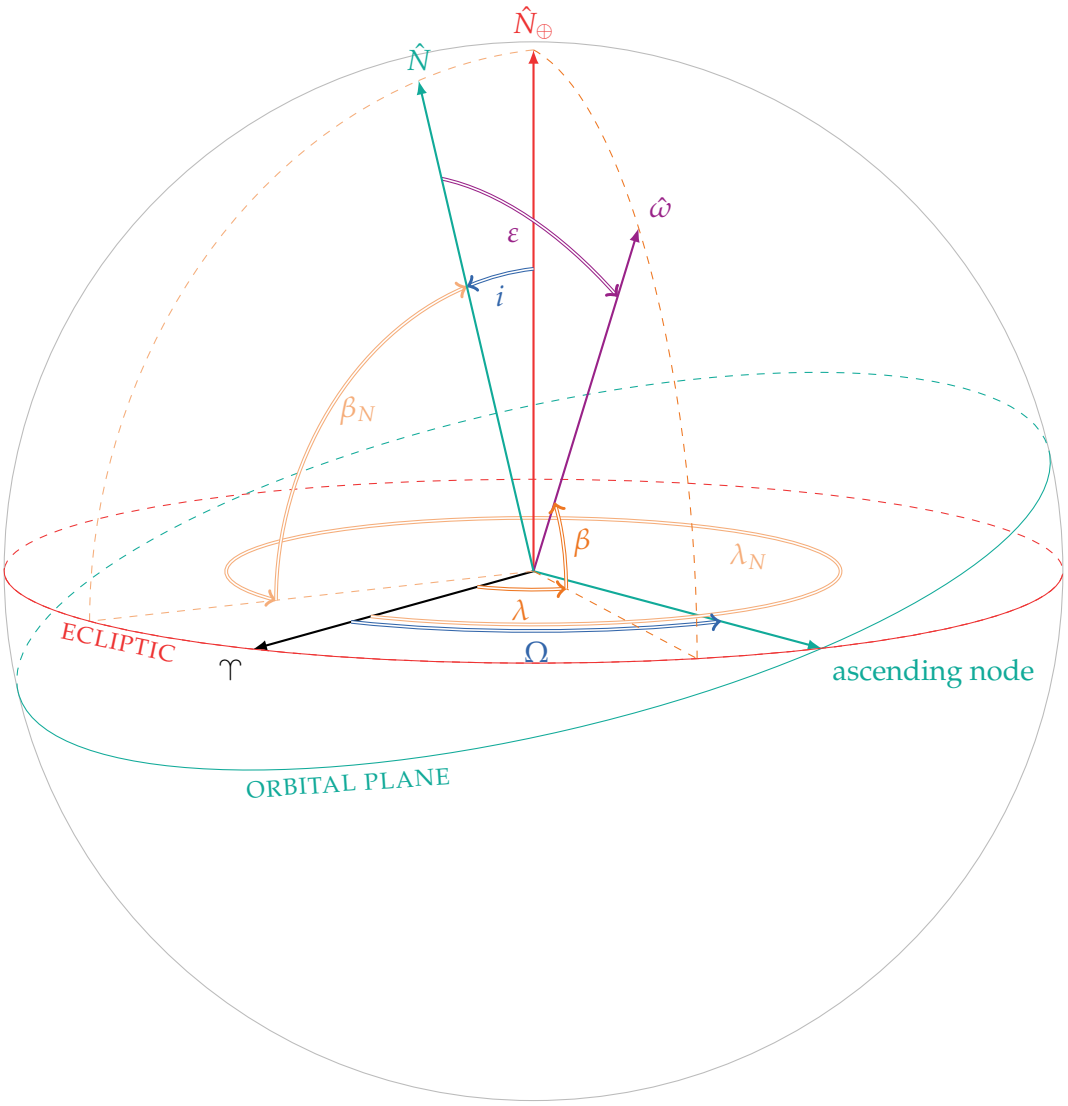

Figure B.2: The schematic shows how obliquity is calculated for a small body. The spin-axis obliquity, ε, is the angle between rotation axis $\hat{\omega}$ and the orbital momentum $\hat{N}$. The position of spin-axis, or pole, is defined by the ecliptic coordinates, longitude λ and latitude β. It can be expressed as
$\hat{\omega} = (\cos\beta\cos\lambda, \cos\beta\sin\lambda, \sin\beta)^T$.
The position of the orbital momentum is defined by two Keplerian elements, i and Ω. The inclination, i, is the angle between the orbital plane of the small body, and the ecliptic. In ecliptic coordinate system the latitude of $\hat{N}$ can be expressed as $\beta_N = 90° - i$. The second element, Ω, is the ecliptic longitude of the ascending node of the orbit. A node is an intersection of orbital plane of the object with the ecliptic. An orbit with a non-0° inclination has two nodes, the ascending node is the one where the object would pass from below to above the plane of the ecliptic in its orbital motion. The ecliptic longitude of $\hat{N}$ can be expressed as $\lambda_N = \Omega + 270°$. The vector $\hat{N}$ in ecliptic coordinate system is then
$\hat{N} = (\cos\beta_N\cos\lambda_N, \cos\beta_N\sin\lambda_N, \sin\beta_N)^T$, or
$\hat{N} = (\sin i\sin\Omega, -\sin i\cos\Omega, \cos i)^T$,

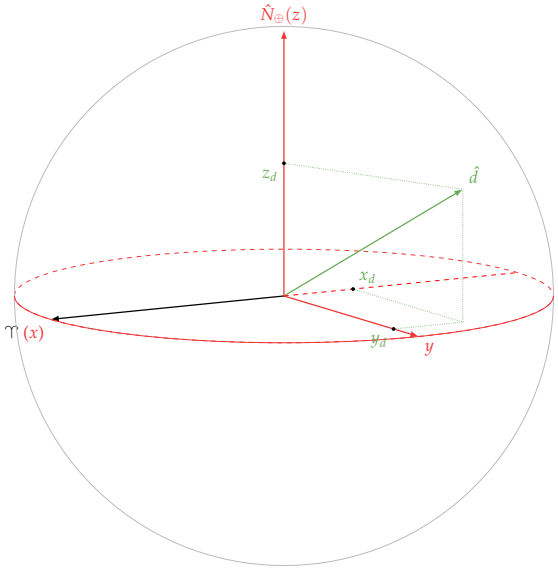

(a) The unit vector $\hat{d}$ is given in ecliptic coordinate system

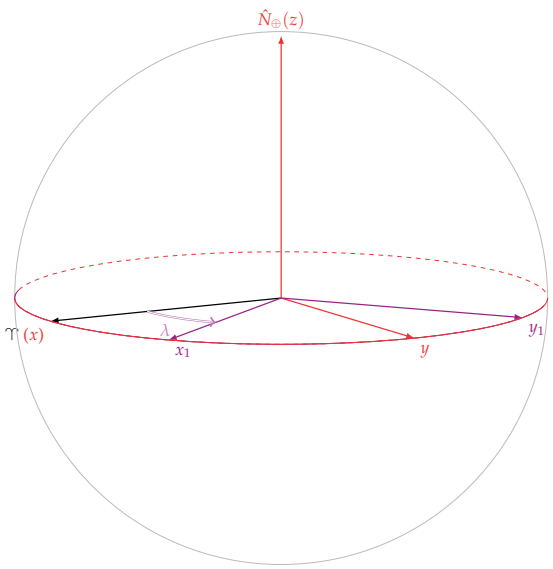

(b) First rotation: around the z axis by λ

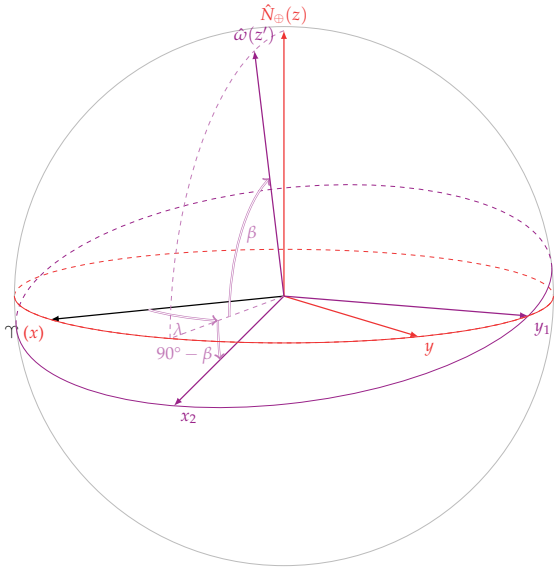

(c) Second rotation: around the y_1 axis by $90^\circ - \beta$

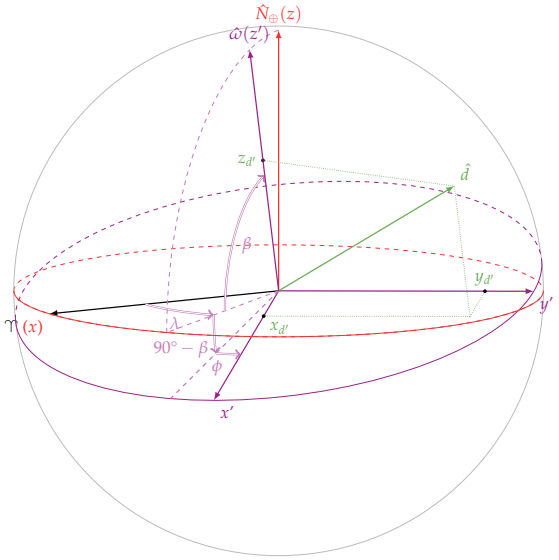

(d) Third rotation: around the $\hat{\omega}$ by ϕ

Figure B.3: The schematic shows how a vector is transformed from ecliptic to body-centric coordinate system. he position of Sun, $\hat{d}_\odot$, and Earth, $\hat{d}_\oplus$, are given in the ecliptic coordinate system, with x-axis pointing towards the vernal equinox, Υ, and z-axis parallel to orbital momentum of the Earth ($\hat{N}_\oplus$). The first panel (a) is included to show the initial coordinates of vector $\hat{d}$ in the ecliptic coordinate system, with $\hat{d} = (x_d, y_d, z_d)^T$.During lightcurve calculations this position vector needs to be transformed to the body-centric coordinate system, for a given moment of time, or rotation phase ϕ, calculated for that moment. For principal-axis rotators the body-centric frame is defined by z-axis aligned with spin-axis, $\hat{\omega}$, and with the axis of maximum inertia. The x axis might be aligned with the minimum moment of inertia, or arbitrarily shifted to have 0° rotation phase occur at a specific moment in time. The rotation of the coordinate system from ecliptic to body-centric frame can be described with 3 steps, illustrated in panels (b-d). Panel (b) shows the first rotation around the initial z-axis by ecliptic longitude of the pole, λ. Panel (c) shows rotation about the new y_1 axis by angle $(90^\circ - \beta)$, where β is the ecliptic latitude of the rotation pole. Panel (d) shows the final rotation by the phase ϕ calculated for the given epoch (see for example Equation (3.4)). To obtain the coordinates of vector $\hat{d}$ in the new coordinate system the original position has to be rotated by the three angles $(\lambda, 90^\circ - \beta, \phi)$, as discussed in Section 3.3.1. The final coordinates of the vector in the rotated frame are shown in panel (d), they are $\hat{d} = (x_{d'}, y_{d'}, z_{d'})$.

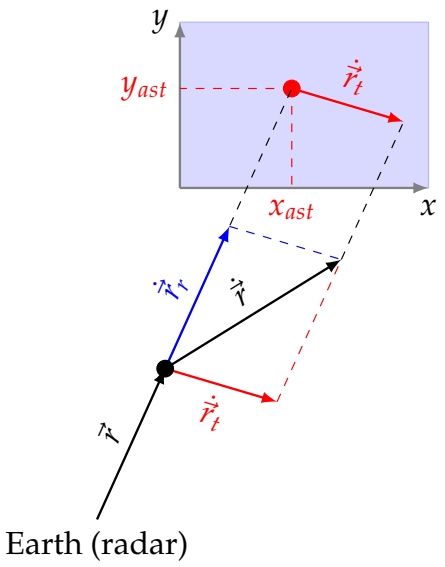

Figure B.4: A schematic of the complementary nature of radar and optical astrometry. The asteroid (black circle) is in the position $\vec{r}$ moving with a velocity $\dot{\vec{r}}$ relative to Earth. The optical astrometry is performed on the image of the asteroid (red circle) projected onto the plane of sky (blue rectangle). The coordinates of the target can be measured relative to the background stars in the selected reference system. Here the coordinates x_{ast} and y_{ast} are measured for the target. Having multiple observations also allows to determine the asteroids plane-of-sky or transversal rate of motion $\dot{\vec{r}}_t$, which is orthogonal to the line-of-sight component.
Using radar observations it is possible to determine the distance to the target, $r \equiv \|\vec{r}\|$, as well as the radial component of its velocity, $\dot{\vec{r}}_r$, where $\dot{\vec{r}} = \dot{\vec{r}}_r + \dot{\vec{r}}_t$.

The orbital properties of asteroids are determined thanks to complementary use of optical and radar astrometry, illustrated in Figure B.4. The optical astrometry measures the position of the asteroid in the plane of sky relative to catalogue positions of background stars. A few measurements are necessary for determination of orbital elements. The radar astrometry is performed by estimating the position of the asteroid centre-of-mass in delay-Doppler image (the radar images are discussed in Section 2.2). Due to the nature of the radar images, this kind of astrometry is performed along the observers line-of-sight. One of the measured quantities is the distance to the target, inferred from the delay of the signal. The second quantity is the radial velocity (velocity along the line-of-sight), obtained from the Doppler shift of received radar echo. Combining both types of observations allows to significantly reduce the uncertainties of orbit determination, and, over sufficiently long periods of time, allowing for detection of non-gravitational effects (Benner et al., 2015).

Appendix C

Mathematical formulation of the Yarkovsky effect

Contemporary numerical and analytical models of the Yarkovsky forces tackle intricacies like various kinds of heat transfer, inhomogeneities of the asteroid building material, or shape-dependence. Here, a formula for a simplified case, taken from Vokrouhlický et al. (2015a), is discussed. The expressions below are developed assuming a spherical body on a circular orbit, with fixed orientation of the spin-axis in the ecliptic reference frame, and uniform linear heat transfer. The orbitally-averaged change of semi-major axis for the diurnal effect can be expressed as (Vokrouhlický et al., 2015a, Equation 1),

$$\dot{a}_{\mathrm{D}} = -\frac{8}{9}\frac{(1-A)\,\Phi}{n} W_{\omega}\left(R_{\omega}, \Theta_{\omega}\right) \cos\varepsilon, \tag{C.1}$$

and for the seasonal effect (Vokrouhlický et al., 2015a, Equation 2)

$$\dot{a}_{\mathrm{S}} = \frac{4}{9}\frac{(1-A)\,\Phi}{n} W_{n}\left(R_{n}, \Theta_{n}\right) \sin^2\varepsilon, \tag{C.2}$$

with the symbols defined as follows

- $\dot{a}$ semi-major axis drift (time derivative), with D denoting the diurnal and S – the seasonal component,
- A the Bond albedo,
- Φ radiation pressure coefficient,
- n mean motion, one of the Keplerian elements of the orbit,
- R_{ν} scaled radius of the body, frequency dependent,
- Θ_{ν} thermal parameter, frequency dependent,
- W_{ν} analytical function combining the above parameters,
- ν frequency dominating the effect, either ω or n
- ω the sidereal spin rate, $\omega = 2\pi/P$, where P is the sidereal rotation period,
- ε the obliquity, angle between the direction of spin-axis – $\hat{\omega}$ and orbit normal – $\hat{N}$, $\cos\varepsilon = \hat{\omega}\cdot\hat{N}$ (see Figure B.1).

The primary difference between the two types of semi-major axis drift, as can be deduced from those equations, and as illustrated in Figure 1.4, are in their dependence on the spin-axis obliquity. The W_{ν} functions will be discussed later, but they are defined in such a manner that they are always negative, and all other factors are positive. Hence it is the $\cos\varepsilon$ dependence in the diurnal component, expressed with Equation (C.1), that makes it sensitive to the sense of rotation of the body. It will cause the orbit to expand when $\varepsilon \in [0°, 90°)$, disappear for $\varepsilon = 90°$, and cause a decrease of semi-major axis for $\varepsilon \in (90°, 180°]$. The seasonal component depends on $\sin^2\varepsilon$, as formulated by Equation (C.2), so it is always negative, therefore causing the orbital decay, and vanishes for bodies with spin-axis perpendicular to the orbital plane ($\varepsilon = 0°$ or $\varepsilon = 180°$).

Both aspects of the Yarkovsky effect depend on the thermal properties of the asteroid surface in a similar manner. The common factor Φ in Equations (C.1) and (C.2) is typical to any phenomena related to the absorption and scattering of Solar radiation by a surface, defined as

$$\Phi = \frac{\pi R^2 F}{mc}, \tag{C.3}$$

It combines the radius of the body – R, solar flux at the body – F (ratio of the solar constant to the square of heliocentric distance), with mass – m, and speed of light – c. With

the mass of the body proportional to R^3 the Φ is a factor inversely proportional to the body density and R.

The Yarkovsky force depends not only on the solar radiation flux received by the target, and its size, but also on the thermal response of the surface. The physical parameters of the asteroid material that are important here are K – the thermal conductivity of the surface, C_p – the heat capacity, or specific heat of the surface, and ρ – density at the surface. The thermal inertia, Γ, combines those parameters into

$$\Gamma \equiv \sqrt{K\rho C_p}. \tag{C.4}$$

The thermal inertia can be considered a measure of the rate at which the surface of the body would accumulate heat. The larger the value of Γ, the larger is the lag between absorption and thermal re-emission of radiation, and hence smaller surface temperature variation between the day and night side of the asteroid. When used in the reference to asteroid surfaces, high thermal inertia is considered an indication of coarse regolith, as opposed to a fine-grained material with a low value of Γ (Delbo et al., 2015). Typical value of thermal inertia for kilometer-sized NEAs is $(200 \pm 40)\,\mathrm{Jm^{-2}\,s^{-0.5}\,K}$ (Delbo' et al., 2007).

The dependence of the Yarkovsky strength on thermal parameters is not straightforward, but rather contained in the analytical functions, $W_\nu\left(R_\nu, \Theta_\nu\right)$. The W_ν for both effects, diurnal and seasonal, have the same form and only differ in which frequency, rotational ($\nu = \omega$) or orbital ($\nu = n$), they are defined. Those functions depend on two arguments, the first one is $R_\nu = R/\ell_\nu$, or body radius scaled by the heat wave penetration depth, which is

$$\ell_\nu = \sqrt{K/\rho C_p \nu}. \tag{C.5}$$

This scaling means, for example, that for large bodies with $R \gg \ell_\nu$ only a thin surface layer is heated up by radiation. In this case the dependence on size vanishes from W_ν and the semi-major axis drift becomes inversely proportional to R (coming from the definition of Φ), becoming negligible for very large asteroids or planets. For bodies that have radii comparable to ℓ_ν the Yarkovsky drift is proportional to R_ν^2. However, for very small R_ν the heat is transferred across the small body, balancing the temperature throughout the surface and causing the Yarkovsky to disappear.

The next thermal parameter Θ_ν, is related to the ratio of the time required to emit in the form of thermal radiation the heat absorbed during one rotation ($\nu = \omega$) or orbit ($\nu = n$), as defined for example by Farinella et al. (1998); Vokrouhlicky (1998). The parameter includes the thermal inertia in its definition

$$\Theta_\nu = \frac{\Gamma\sqrt{\nu}}{\epsilon\sigma {T_\star}^3} \tag{C.6}$$

the new quantities are

- ϵ thermal emissivity of the small body surface,
- σ the Stefan–Boltzmann constant,
- $T_\star$ the sub-solar temperature, defined as $\varepsilon\sigma {T_\star}^4 = (1 - A)\,F$.

The Yarkovsky effect is most efficient when the Θ_ν is of the order of unity. When it is too small, there is little delay between absorption and emission of thermal radiation and the effect

vanishes. On the other hand, when the Θ_ν grows too large there is no temperature difference between the day/night, or summer/winter sides of the object and the effect vanishes as well.

Appendix D

Exaple input files for the shape modelling programs

```
41
70 0
2447774.63841083 0.02538166 -1.077309 0.437201 -0.263421 -0.114713 0.137317
    -0.263387
2447774.64045667 0.02506340 -1.077316 0.437166 -0.263406 -0.114709 0.137315
    -0.263372
2447774.64341875 0.02431756 -1.077325 0.437115 -0.263384 -0.114703 0.137313
    -0.263350
2447774.64592375 0.02377497 -1.077333 0.437072 -0.263366 -0.114699 0.137311
    -0.263332
2447774.64797167 0.02340346 -1.077340 0.437037 -0.263351 -0.114695 0.137310
    -0.263317
2447774.65002000 0.02301018 -1.077346 0.437002 -0.263336 -0.114691 0.137308
    -0.263302
2447774.65006000 0.02155361 -1.077347 0.437001 -0.263335 -0.114691 0.137308
    -0.263301
2447774.65258333 0.02044561 -1.077355 0.436958 -0.263317 -0.114686 0.137306
    -0.263283
2447774.65529708 0.02057406 -1.077363 0.436911 -0.263297 -0.114681 0.137304
    -0.263263
2447774.66027375 0.02074340 -1.077379 0.436826 -0.263260 -0.114672 0.137301
    -0.263227
...
```

Figure D.1: A fragment of an example input lightcurve of asteroid (1917) Cuyo (see Chapter 4). The file is formatted for the `CONVEXINV` shape modelling software, as described in Section 2.3.

```
41
70 0
2447774.63841083 0.02538166 -1.077309 0.437201 -0.263421 -0.114713 0.137317
    -0.263387 0.01
2447774.64045667 0.02506340 -1.077316 0.437166 -0.263406 -0.114709 0.137315
    -0.263372 0.01
2447774.64341875 0.02431756 -1.077325 0.437115 -0.263384 -0.114703 0.137313
    -0.263350 0.01
2447774.64592375 0.02377497 -1.077333 0.437072 -0.263366 -0.114699 0.137311
    -0.263332 0.01
2447774.64797167 0.02340346 -1.077340 0.437037 -0.263351 -0.114695 0.137310
    -0.263317 0.01
2447774.65002000 0.02301018 -1.077346 0.437002 -0.263336 -0.114691 0.137308
    -0.263302 0.01
2447774.65006000 0.02155361 -1.077347 0.437001 -0.263335 -0.114691 0.137308
    -0.263301 0.01
2447774.65258333 0.02044561 -1.077355 0.436958 -0.263317 -0.114686 0.137306
    -0.263283 0.01
2447774.65529708 0.02057406 -1.077363 0.436911 -0.263297 -0.114681 0.137304
    -0.263263 0.01
2447774.66027375 0.02074340 -1.077379 0.436826 -0.263260 -0.114672 0.137301
    -0.263227 0.01
...
```

Figure D.2: A fragment of an example input lightcurve of asteroid (1917) Cuyo (see Chapter 4). The file is formatted for the `MATLAB` spin-state modelling routines, as described in Section 2.3.

```
{DATA FILE FOR SHAPE.C}

7 {number of sets}


{SET 0}

-1 {is mpi node responsible for this set}

c   0.000000e+00 c   0.000000e+00 c   0.000000e+00 {Euler angle offsets}
c   0.000000e+00 c   0.000000e+00 c   0.000000e+00 {spin vector offsets}

lightcurve {set type}

0 {optical scattering law for this set}

7 {number of asteroid ephemeris points}
{ yr mo dd hh mm ss         ra        dec       dist}
2014  1 28  4  0  0 151.06437  16.06319 0.16660260
2014  1 28  5  0  0 151.01199  16.09954 0.16669546
2014  1 28  6  0  0 150.95936  16.13559 0.16679121
2014  1 28  7  0  0 150.90674  16.17133 0.16688994
2014  1 28  8  0  0 150.85438  16.20676 0.16699157
2014  1 28  9  0  0 150.80254  16.24190 0.16709582
2014  1 28 10  0  0 150.75142  16.27680 0.16720226

7 {number of solar ephemeris points}
{ yr mo dd hh mm ss         ra        dec       dist}
2014  1 28  4  0  0 310.55977 -18.22742 0.98488950
2014  1 28  5  0  0 310.60348 -18.21645 0.98489516
2014  1 28  6  0  0 310.64718 -18.20551 0.98489822
2014  1 28  7  0  0 310.69083 -18.19462 0.98489882
2014  1 28  8  0  0 310.73437 -18.18376 0.98489728
2014  1 28  9  0  0 310.77779 -18.17292 0.98489406
2014  1 28 10  0  0 310.82105 -18.16209 0.98488974

-1 {number of calculated points}

63 {number of samples in lightcurve}
./1999JV6Palmer2014.lc01.dat f 1.000000e+00 1.000000e+00 {name, calfact,
    weight}
```

(a) Formatted SHAPE input file.

```
2456685.71984 17.951 0.049
2456685.73122 18.27 0.068
2456685.7335 18.303 0.06
```

(b) Formatted SHAPE lightcurve file.

Figure D.3: A fragment of a formatted SHAPE input file (a) along with a fragment of the corresponding lightcurve (b) of asteroid (85990) 1999 JV_6 (see Chapter 5). The file is formatted for the SHAPE modelling software, as described in Section 2.3.

```
{SET 0}

-1 {is mpi node responsible for this set}

c   0.000000e+00 c   0.000000e+00 c   0.000000e+00 {Euler angle offsets}
c   0.000000e+00 c   0.000000e+00 c   0.000000e+00 {spin vector offsets}

delay-doppler {set type}

0 {radar scattering law for this set}

3 {number of ephemeris points}
{ yr mo dd hh mm ss         ra        dec       dist}
2015  1 15  6  0  0 147.86486   4.99616 0.09423055
2015  1 15  7  0  0 147.77992   5.06939 0.09432347
2015  1 15  8  0  0 147.69523   5.14233 0.09441955

2380.000000 {transmitter frequency (MHz)}

200 0.100000 4 2 short {delay: # rows, pixel height (usec), spb, stride, code
     method}

200 0.068242 101.307251 72.000000 1118 {dop: # cols, pixel width (Hz), COM
    col, DC col, fftlen}

2015  1 15  6  0  0 {t0 of delcor poly}
1 {order of polynomial}
f -2.041386e+00 {coefficient 0}
f -1.393239e+01 {coefficient 1}

c  1.000000e+00 {Doppler scaling factor}

/share/rserv00/radar/1999JV6/2015/jan15/p2b {data directory}

2 {number of frames}
{                    name year mo dd hh mm ss          sdev         calfact
    looks   COM del row        weight mask}
dec1.oc.fits 2015  1 15  7 22  1 1.000000e+00 f 1.460969e+04    24.0
    149.231720 1.500000e+00    1
dec2.oc.fits 2015  1 15  7 34 41 1.000000e+00 f 1.079905e+04    24.0
    148.952576 1.500000e+00    1
```

Figure D.4: A fragment of a formatted SHAPE input file for a *cw* observation of asteroid (85990) 1999 JV_6 (see Chapter 5). The file is formatted for the SHAPE modelling software, as described in Section 2.3.

```
{SET 1}

-1 {is mpi node responsible for this set}

c   0.000000e+00 c   0.000000e+00 c   0.000000e+00 {Euler angle offsets}
c   0.000000e+00 c   0.000000e+00 c   0.000000e+00 {spin vector offsets}

doppler {set type}

0 {radar scattering law for this set}

4 {number of ephemeris points}
{ yr mo dd hh mm ss         ra        dec       dist}
2015  1 15  4  0  0 148.03372   4.84888 0.09405387
2015  1 15  5  0  0 147.94960   4.92265 0.09414076
2015  1 15  6  0  0 147.86486   4.99616 0.09423055
2015  1 15  7  0  0 147.77992   5.06939 0.09432348

2380.000000 {transmitter frequency (MHz)}

233 0.034483 117.000000 {dop: # bins, bin width (Hz), COM bin}

2015  1 15  4  0  0 {t0 of delcor poly}
1 {order of polynomial}
c  0.000000e+00 {coefficient 0}
f  0.000000e+00 {coefficient 1}

c  1.000000e+00 {Doppler scaling factor}

/share/rserv00/radar/1999JV6/2015/jan15/cw {data directory}

1 {number of frames}
{                                name year mo dd hh mm ss          sdev
    calfact    looks        weight mask}
1999JV6.2015Jan15.s0p08Hz.d3.sum.rdf 2015  1 15  5 58 29 3.098411e-05 c
    1.000000e+00      5.0 1.000000e+00    0
```

Figure D.5: A fragment of a formatted SHAPE input file for a delay-Doppler imaging of asteroid (85990) 1999 JV_6 (see Chapter 5). The file is formatted for the SHAPE modelling software, as described in Section 2.3.

Appendix E

Acronyms

ADU analog-to-digital unit

APC Asteroid Photometric Catalogue

ATPM Advanced Thermophysical Model

CCD charge-coupled device

CPU central processing unit

cw continuous-wave

DAMIT Database of Asteroid Models from Inversion Techniques

dD delay-Doppler

DFOSC Danish Faint Object Spectrograph and Camera

EFOSC ESO Faint Object Spectrograph and Camera (version 2)

ESA European Space Agency

ESO European Southern Observatory

ESO LP ESO Large Programme

FFT fast Fourier transform

FOAM13 Fondazione Osservatorio Astronomico di Tradate Messier 13

GPU graphics processing unit

IAC Instituto de Astrofísica de Canarias

ICRF International Celestial Reference Frame

ING Isaac Newton Group of telescopes

INT Isaac Newton Telescope

JD Julian date

JFC Jupiter family comet

JPL Jet Propulsion Laboratory

LCOGTN Las Cumbres Observatory Global Telescope Network

LFC Large Format Camera

LJMU Liverpool John Moores University

MBA main-belt asteroid

MPC Minor Planet Centre

MPI Max-Planck Institute

NAC Narrow Angle Camera

NAIC National Astronomy and Ionosphere Center

NEA near-Earth asteroid

NTT New Technology Telescope

NWO Nederlanse Organisatie voor Wetenschappelijk Onderzoek

OSIRIS Optical, Spectroscopic, and Infrared Remote Imaging System

OU Open University, Milton Keynes

PHA potentially hazardous asteroid

PSF point-spread function

QUB Queens University, Belfast

R-C Ritchey-Chrétien

RTT round-trip time

SPICE Spacecraft ephemeris, Planet, satellite, comet, or asteroid ephemeris, Instrument description, C-matrix, Events

SSSB small Solar System body

STFC Science and Technology Facilities Council

TMO Table Mountain Observatory

VIMOS VIsible MultiObject Spectrograph

VISIR VLT Imager and Spectrometer for mid-InfraRed

VLT Very Large Telescope

WAC Wide Angle Camera

WFC Wide Field Camera

WFI Wide Field Image

YORP Yarkovsky, O'Keefe, Radzievskii, and Paddack